



**UNIVERSIDAD NACIONAL AUTÓNOMA DE MÉXICO**  
**PROGRAMA DE POSGRADO EN CIENCIAS DE LA TIERRA**  
**INSTITUTO DE GEOFÍSICA**

**DEFINICIÓN DE LA CUENCA DE SAN BLAS Y EL BLOQUE DE JALISCO, Y DETERMINACIÓN DE LA PLOMERÍA DE VOLCANES, MEDIANTE GRAVIMETRÍA SATELITAL**

**TESIS**

**QUE PARA OPTAR POR EL GRADO DE:**  
**DOCTOR EN CIENCIAS DE LA TIERRA**

**PRESENTA:**  
**M.Sc. MIGUEL ALEJANDRO CAMACHO ASCANIO**

**TUTOR:**

**DR. ROMÁN ÁLVAREZ BÉJAR**

**(UNAM, Instituto de Investigaciones en Matemáticas Aplicadas y en Sistemas)**

**MIEMBROS DEL COMITÉ TUTOR:**

**DR. LUCA FERRARI**

**(UNAM, Centro de Geociencias)**

**Dr. Fernando Corbo Camargo**

**(UNAM, Centro de Geociencias)**

**Dr. Vsevolod Yutis (IPICYT; Inst. Potosino de Investigación científica y Tecnológica)**

**Dr. Marco Antonio Pérez Flores**

**(CICESE; Centro de Investigación**

**Científica y de Educación Superior de Ensenada, Baja California )**

**Ciudad de México, abril de 2024**



Universidad Nacional  
Autónoma de México



**UNAM – Dirección General de Bibliotecas**  
**Tesis Digitales**  
**Restricciones de uso**

**DERECHOS RESERVADOS ©**  
**PROHIBIDA SU REPRODUCCIÓN TOTAL O PARCIAL**

Todo el material contenido en esta tesis esta protegido por la Ley Federal del Derecho de Autor (LFDA) de los Estados Unidos Mexicanos (México).

El uso de imágenes, fragmentos de videos, y demás material que sea objeto de protección de los derechos de autor, será exclusivamente para fines educativos e informativos y deberá citar la fuente donde la obtuvo mencionando el autor o autores. Cualquier uso distinto como el lucro, reproducción, edición o modificación, será perseguido y sancionado por el respectivo titular de los Derechos de Autor.

## AGRADECIMIENTOS

Al Posgrado en Ciencias de la Tierra-UNAM por la formación académica.

Un Agradecimiento especial al consejo Nacional de Ciencia y Tecnología (CONACYT), ahora bautizado Consejo Nacional de Humanidades ciencias y Tecnologías (CONAHCyT), por la oportunidad de ganarme la beca, para desarrollar mis estudios de posgrado en Ciencias de la Tierra.

Un agradecimiento especial ¡A México! Una nación hermosa y pintoresca que me acogió en su seno y me brindó la oportunidad de crecer en muchos aspectos, y que me dio la felicidad de conocer a mi primogénito.

En primer lugar, quisiera agradecer a mi esposa, la mecenas de mis sonrisas y alegría. Gracias por estos años de esfuerzo y de paciencia, gracias por el apoyo que me has dado todos estos años. Gracias por creer en mí, y por impulsarme a llegar a nuevos retos que a veces ni yo mismo creía capaz de terminar. Gracias por darme el amor que todo lo puede y que todo lo cura, el bálsamo perfecto para mi alma. Gracias por ser el motor que me impulsa para querer ser mejor cada día. Y gracias por darme ese pedacito de cielo llamado Ethan.

A mi tutor y amigo, el Dr, Román, gracias por su tiempo y la paciencia ejercida. Gracias por su apoyo, y la gran calidad humana que ha demostrado desde que lo conozco, que ha sido inequívocamente crucial para lograr este trabajo y las otras investigaciones que hemos completado; y quien me ha logrado sembrar en mí la pasión de investigar.

A la Dr. Claudia Arango que ha sido sinodal y amiga (y sin duda tutora tacita), un gran agradecimiento de mi parte. Gracias por su gran calidad docente y profesional, y por su gran calidad humana, de la que he logrado aprender muchísimo. Muchas gracias por su apoyo.

A Ethan... por ser la luz y el motivo, a quien le debo todo y por quien todo (y quien no ayudo para nada en a lograr esta obra jajaja). Gracias por tu sonrisa “Sr. Bebe”. Es curioso como la vida pasa, y como los ciclos y las etapas se van sucediendo, iniciando y culminando. Hoy finalizando estas líneas, comienzan las líneas de la tuya, una vida que espero con que sea larga y maravillosa, copada de aquello que sueñes. Una vida de la que disfrutes las rosas de la alegría, pero con las suficientes espinas para que no carezca de sentido, una vida de la que espero estar a la altura de ser el mentor y el guía que necesites. En resumen, una vida de la que espero “ser valiente no salga tan caro, y ser cobarde no valga la pena” (Sabina, 1999).

A los que amigos o compañeros que me apoyaron con la realización de estos trabajos, y todo el trabajo anterior que son los cimientos de estos, cual iceberg del cual no se observa más que la punta. Gracias por su oportuna ayuda y consejo: Gracias Nestor “Agazapin” Cahuana por ser un compañero en l distancia y un consultor afín y paciente, y un opinador bien entendido sobre mis “ideas disparatadas”. Al Doctor “Control” (el Dr. Alejandro González) gracias por sus oportunas asistencias en gramática de inglés. Y finalmente, gracias a la futura Dra. Elizabeth Rivera-Calderón, tus aportes en geología y varios ámbitos de vida han sido muy esclarecedores y oportunos, espero que tengamos oportunidad de seguir colaborando.

A mi abuelita Myriam, ahora ya elevada Bisabuelita, gracias por todo... infinitas gracias... gracias por ser la piedra fundamental y fundacional del sentido común en mi vida; es muy posible que más del 80% de las cosas buenas que pueda tener en mi carácter sean debido a ti, o profundamente influidas de ti. Gracias por siempre estar allí, y por creer en mí y amarme como lo has hecho.

A mi tía Isolia, un millón de gracias. Sin duda una de las personas más importantes en mi vida. Gracias a ti no me perdí, y gracias a ti encontré las herramientas para comenzar y recorrer esa carrera profesional. Nuevamente es muy probable que más del 50% de las cosas buenas que pueda tener en mi carácter sean debido a ti, o profundamente influidas de ti. Y muy especialmente gracias porque no tenías por qué haber hecho nada por mí, y aun así lo hiciste... y aun a contra consejo, me ayudaste como nadie más me ayudó. Infinitas gracias, por darme la oportunidad y por creer en mí.

Gracias a mi hermano Samuel "Shishy" por millones de cosas, pero principalmente mantenerme cuerdo en los meses de la pandemia, de no ser por ti, no habría podido comenzar con buen pie los dos primeros años del doctorado. Estoy feliz y orgulloso del hombre que te convertiste.

A mi hermanita Ana, gracias por mostrarme que el amor sigue existiendo. Que se puede ganar aun con las derrotas más definitivas. Que el amor, y el sacrificio prevalecen sobre los mal entendido, y que se puede influir positivamente sobre alguien, que se puede romper la cadena de dolor siendo el eslabón de cambio. Estoy feliz y orgulloso de la mujer que te convertiste.

A María "La Suegris", gracias por estar allí. Por ser un apoyo y alguna forma de madre para conmigo. Has sido una gran ayuda en todo momento, y en especial a lo largo de este proyecto tan especial llamado "Ethan".

Al "Cuñis" Samuel, francamente uno jamás cree que va a haber alguien que sea digna pareja de su hermanita. Pero como toda regla hay excepciones y tu eres claramente la regla de la excepción. Te doy unas gracias infinitas por tu temple, por el bonito hogar que lograste con Ana y por hacerme sentir parte de tu familia. Muchas gracias por tu trato y por todo lo bien que te has portado... considero que debo escribirte más xD.

A todos los amigos, a los personajes y héroes "anónimos" a estas líneas. Los que de una u otra forma lograr aportar de maneras directas y a veces no vinculantes sobre la obra, pero que en muchos casos logran ser tan determinantes, por las situaciones de vida, que sin ustedes sería difícil o improbable llegar al final. A Mariana y Raúl por ser los buenos amigos que son, los más longevos que tengo en México y por estar allí brindando su amistad en esos momentos en que el camino se hace más

estrecho, y estar pendientes en los tiempos de necesidad, como en la pandemia; gracias por ser de los amigos que se convierten en familia. A mi “primo” Adrian, gracias por estar allí bro, es bueno tener a la familia cerca, con poca gente se puede hablar sin mascarar. Muchas gracias a Tania, has sido muy buena amiga y has probado ser de esas amistades “patria o muerte”, de esas que se quieren conservar a lo largo de la vida. Adal, muchas gracias por su amistad y todos tus apoyos logísticos, eres de las amistades más nuevas y verdaderamente se siente que uno te conoce una vida, francamente una de las mejores personas que conozco.

Por supuesto al “Gusgus”, el hermano mayor que nunca tuve. Gracias por un sin fin de cosas y apoyos, y una mención especial por ser “El Alamo” de mi conciencia y rescatarme de mi, cuando mi sentido común sucumbe a las vicisitudes; además un gran compañero de juergas.

Y finalmente gracias a los anónimos todos los que pusieron su granito de arena en diversos momentos, que de una u otra forma ayudaron el camino tendiendo su mano y obsequiándome la motivación que en ocasiones me impulso, lamento que mi memoria y el tiempo de entrega de esto no dé para listarlos a todos, pero aun así gracias por su apoyo.

A mí mismo, por transitar el camino de lo inexplorado. Por soñar y tener el valor o la temeridad de perseguir esos sueños. Por no rendirme cuando todos parecía perdidos, por no aparcar cuando parecía lo único sensato.

Y Finalmente gracias a mis enemigos y a mis demonios, por darme la oportunidad de superarme una vez más.

## RESUMEN

Este trabajo es un compendio de 5 artículos publicados durante el doctorado, el cual se realiza como tesis en modo artículos. El primer capítulo (Capítulo 1: Geophysical Modeling with Satellite Gravity Data: Eigen-6C4 vs. GGM Plus) se centra en una comparación entre los dos principales modelos de datos gravimétricos satelitales: el EIGEN-6C4 y el modelo GGMplus, en función de su calidad espectral y su calidad de resolución, para la exploración geofísica en escala regional y local. Además, se desarrolla la importancia del DEM (modelo de elevación digital) a la hora del procesado de los datos satelitales, y cuáles son los principales artificios matemáticos surgidos a partir de la utilización de *DEMs* subóptimos.

El segundo capítulo (Capítulo 2: Delineation of the Boundaries of San Blas Basin, Mexico, Merging Gravity, Magnetic, and Seismic Data), aborda la delimitación de la Cuenca de San Blas a través del modelo EIGEN-6C4, en conjunción con datos magnéticos del NA\_Mag y diferentes sísmicas interpretadas en la región. Adicionalmente, se realizó una inversión 3D gravimétrica y una inversión 3D magnética, con el fin de determinar cuerpos intrusivos en el área, logrando obtener evidencias que respaldan el proceso de evolución de la apertura de baja california.

El tercer capítulo (Capítulo 3: Gravimetric analysis of the rifts and volcanic fields of the Jalisco block, Mexico), trata del estudio en el Bloque de Jalisco. En dicho capítulo, se realizó un estudio geofísico que integra: modelos gravimétricos satelitales (Eigen-6C4), modelos magnéticos (NA\_mag), datos sísmicos interpretados y perfiles magnetoteléuricos interpretados; para definir con exactitud las fronteras del bloque y sus principales rasgos estructurales desde un punto de vista gravimétrico/tectónico.

Los Capítulos 4 (Applying High-Resolución Gravity Analysis to Volcanic Plumbing Systems: The Case of Nevado De Toluca Volcano, Mexico) y 5 (Plumbing System of Hunga Tonga Hunga Ha'apai Volcano) plantean una nueva aplicación para el modelo de datos GGMplus en el estudio de dos importantes volcanes del mundo: El Nevado de Toluca y el volcán Hunga Tonga Hunga Ha'apai. En ambos casos se realizó un modelo de inversión 3D sobre los datos gravimétricos, en cada estudio nos centramos en los procesos que ocurren en los primeros 5-6 km de la litosfera, con el fin de analizar el sistema plomería de ambos volcanes.



## ABSTRACT

This work is a compilation of 5 papers developed during the doctoral program, carried out as a thesis in article format. The first chapter (Chapter 1: Geophysical Modeling with Satellite Gravity Data: Eigen-6C4 vs. GGM Plus) focuses on a comparison between the two main models of satellite gravity data: EIGEN-6C4 and the GGMplus model, based on their spectral and resolution quality, for regional and local-scale geophysical exploration. Additionally, it delves into the importance of DEM (digital elevation model) in satellite data processing and discusses the main mathematical artifacts arising from using sub-optimal DEMs.

The second chapter (Chapter 2: Delineation of the Boundaries of San Blas Basin, Mexico, Merging Gravity, Magnetic, and Seismic Data) addresses the delineation of the San Blas Basin using the EIGEN-6C4 model, in conjunction with magnetic data from NA\_Mag and various seismic interpretations in the region. Additionally, a 3D gravimetric inversion and a 3D magnetic inversion were conducted to determine intrusive bodies in the area, successfully obtaining evidence that supports the evolution process of the opening of Baja California.

The third chapter (Chapter 3: Gravimetric Analysis of the Rifts and Volcanic Fields of the Jalisco Block, Mexico) focuses on studying the Jalisco Block. In this chapter, a geophysical study was conducted, integrating satellite gravity models (Eigen-6C4), magnetic models (NA\_mag), interpreted seismic data, and interpreted magnetotelluric profiles, to accurately define the boundaries of the block and its main structural features from a gravimetric/tectonic perspective.

Chapters 4 (Applying High-Resolution Gravity Analysis to Volcanic Plumbing Systems: The Case of Nevado De Toluca Volcano, Mexico) and 5 (Plumbing System of Hunga Tonga Hunga Ha'apai Volcano) propose a new application for the GGMplus data model in the study of two significant volcanoes in the world: Nevado de Toluca and Hunga Tonga Hunga Ha'apai volcano. In both cases, a 3D inversion model was performed on the gravity data, focusing on the processes occurring in the first 5-6 km of the lithosphere to analyze the plumbing system of both volcanoes.

# CONTENIDO

1. INTRODUCCIÓN .....	1
1.1. MODELOS DE DATOS GRAVÍMETROS SATELITALES DE ALTA RESOLUCIÓN .....	1
1.2. TECTÓNICA DEL OESTE DE MÉXICO .....	3
1.2.1 LA CUENCA DE SAN BLAS.....	6
1.2.2 BLOQUE DE JALSICO .....	9
1.3. ANÁLISIS GRAVIMÉTRICO DEL SISTEMA DE PLOMERIA DE VOLCANES: .....	11
2. Capítulo 1: <i>Geophysical Modeling with Satellite Gravity Data: Eigen-6C4 vs. GGM Plus.</i> .....	12
3. Capítulo 2: <i>Delineation of the Boundaries of San Blas Basin, Mexico, Merging Gravity, Magnetic, and Seismic Data.</i> .....	13
4. Capítulo 3: <i>Gravimetric analysis of the rifts and volcanic fields of the Jalisco block, Mexico.</i> ..	14
5. Capítulo 4: <i>Applying High-Resolution Gravity Analysis to Volcanic Plumbing Systems: The Case of Nevado De Toluca Volcano, Mexico</i> .....	15
6. Capítulo 5: <i>Plumbing System of Hunga Tonga Hunga Ha 'apai Volcano</i> .....	16
7. CONCLUSIONES .....	17
7.1. Capítulo 1 (Geophysical Modeling with Satellite Gravity Data: Eigen-6C4 vs. GGM Plus)	17
7.2. Capítulo 2 (Delineation of the Boundaries of San Blas Basin, Mexico, Merging Gravity, Magnetic, and Seismic Data) .....	19
7.3. Capítulo 3 ( <i>Gravimetric analysis of the rifts and volcanic fields of the Jalisco block, Mexico</i> )	22
7.4. Capítulo 4 (Volcanic Plumbing Systems: The Case of Nevado De Toluca Volcano) .....	24
7.5. Capítulo 5 (Plumbing System of Hunga Tonga Hunga Ha'apai Volcano).....	26
REFERENCIAS.....	30

## INDICE DE FIGURAS

FIGURA 1. MAPAS DE ANOMALÍA DE AIRE LIBRE SOBRE UNA MISMA REGIÓN GEOGRÁFICA. (A) MAPA DE ANOMALÍA DE AIRE LIBRE DEL MODELO GGMPPLUS. (B) MAPA DE ANOMALÍA DE AIRE LIBRE DEL MODELO EMG2008. (C) MAPA DE ANOMALÍA DE AIRE LIBRE DEL MODELO EIGEN-6C4. TOMADO DE CAMACHO Y ALVAREZ (2021); CAPÍTULO 1	2
FIGURA 2. HISTOGRAMA DE FRECUENCIA DE LA ANOMALÍA DE AIRE LIBRE PARA LOS MODELOS: (A) GGMPPLUS, (B) EMG2008 Y (C) EIGEN-6C4. EL COMPORTAMIENTO DE LOS HISTOGRAMAS REVELA SUTILES PERO RELEVANTES DIFERENCIAS ENTRE LOS MODELOS. DEMOSTRANDO LO SIMILAR DEL COMPORTAMIENTO ESTADÍSTICO DE LOS DATOS DEL MODELO EIGEN-6C4 Y EL MODELO GGMPPLUS. TOMADO DE CAMACHO Y ALVAREZ (2021); CAPÍTULO 1.	3
FIGURA 3. MODELO TECTÓNICO DE LA APERTURA DEL GOLFO DE CALIFORNIA. TOMADO DE FERRARI ET AL. (2013).	5
FIGURA 4. RECONSTRUCCIÓN TECTÓNICA DE LA POSICIÓN DE BAJA CALIFORNIA ENTRE LOS 19 Y 16 MA. TOMADO DE FERRARI ET AL. (2018).	6
FIGURA 5. CONFIGURACIÓN TECTÓNICA DE LA SBB, INCLUYENDO LOS LÍMITES DE LA PLACA DE RIVERA Y UNA PORCIÓN DE LOS LÍMITES CONOCIDOS DE LA SBB (REPRESENTADOS POR UN CUADRADO VERDE). CTP: PUNTO TRIPLE DE COMPOSTELA. JB: BLOQUE DE JALISCO. GTP: PUNTO TRIPLE DE GUADALAJARA. LOS LÍMITES DEL BLOQUE DE JALISCO ESTÁN REPRESENTADOS POR LÍNEAS ROJAS (ADAPTADO DE CAMACHO Y ALVAREZ, 2020). NS: ESCARPES DE NAYARIT. MI: ISLAS MARÍAS. TB: BANCO TAMAYO. TT: TRINCHERA TAMAYO. MP: PLATAFORMA MAGDALENA. MF: ABANICO MAGDALENA. SBG: DESFILADERO DE SAN BLAS. LAS ESTRUCTURAS OCEÁNICAS FUERON ADAPTADAS DE DEMETS Y TRAYLEN (2000) Y FLETCHER ET AL. (2007). C: COMPOSTELA. CSL: CABO SAN LUCAS. CH: CHAMELA. MZ: MANZANILLO. PV: PUERTO VALLARTA. MZT: MAZATLÁN. SB: SAN BLAS. T: TEPIC. Z: ZACOALCO. TOMADO DE CAMACHO Y ALVAREZ (2024); CAPÍTULO 2.	7
FIGURA 6. PERFIL SÍSMICO DE LA CUENCA DE SAN BLAS. TOMADO DE SUTHERLAND ET AL. (2012). EN AZUL OBSCURO EL BASAMENTO INTERPRETADO. EN ROJO LAS FALLAS INTERPRETADAS.	8
FIGURA 7. LÍMITES DEL BOQUE DE JALISCO (JB). LA LÍNEA AMARILLA ES EL LÍMITE PROPUESTO POR ALVAREZ Y YUTSIS (2015). BATIMETRÍA (DE AZUL A MARRÓN CLARO) Y TOPOGRAFÍA (DE VERDE A BLANCO) SON DE RYAN ET AL (2009). MAT: TRINCHERA CENTRO AMERICANA. MB: BLOQUE DE MICHOACÁN. CVC: COMPLEJO VOLCÁNICO DE COLIMA. GTP: PUNTO TRIPLE DE GUADALAJARA. BB: BAHÍA DE BANDERAS, NCG: GRABEN NORTE DE COLIMA. CHG: GRABEN DE CHAPALA. TZG: GRABEN DE TEPIC-ZACOALCO. PUNTO NARANJA CORRESPONDE A CIUDADES: SB, SAN BLAS. TP, TEPIC. CM, COMPOSTELA. GD, GUADALAJARA. CH, CHAMELA. CO, COLIMA. MZ, MANZANILLO. TOMADO DE CAMACHO Y ALVAREZ (2020). CAPÍTULO 3.	10

- FIGURA 8. COMPARACIÓN DE  $G_{OBS}$  ENTRE (A) GGMPLUS Y (B) EIGEN-6C4. OBSERVA LA GRAN SIMILITUD ENTRE LOS RANGOS DE GRAVEDAD EN AMBOS MAPAS. TOMADO DE CAMACHO Y ALVAREZ (2021); CAPÍTULO 1 17
- FIGURA 9. (A) MALLA DE AB CALCULADA CON EL MODELO DE EIGEN-6C4 Y UN DEM DE IGUAL RESOLUCION. (B) MALLA DE AB CALCULADA CON EIGEN-6C4 Y CON EL STRM15 (DE APROX. EL DOBLE DE RESOLUCIÓN). (C) EN LA MALLA C SE OBSERVA UNA MALLA DE AB CALCULADA CON EL MODELO GGMPLUS Y UN DEM DE IGUAL RESOLUCIÓN. (D) MALLA DE AB CALCULADA CON EL MODELO GGMPLUS UN DEM DE LA MITAD DE RESOLUCIÓN (SRTM15). TOMADO Y MODIFICADO DE CAMACHO Y ALVAREZ (2021); CAPÍTULO 1. 18
- FIGURA 10. COMPARACION DEL ESPECTRO DE POTENCIA DEL MODELO EIGEN-6C4 Y EL MODELO GGMPLUS. TOMADO DE CAMACHO Y ALVAREZ (2021); CAPÍTULO 1 19
- FIGURA 11. MAPA DE  $AB_{DZ}$ . EN LÍNEAS GRISES, LOS CONTORNOS DE LA ANOMALÍA. EN LÍNEAS DELGADAS NEGRAS, LAS FALLAS MÁS REPRESENTATIVAS EN LA ZONA EN TIERRA FIRME. LA LÍNEA NEGRA CONTINUA REPRESENTA LA LÍNEA DE COSTA, Y LAS LÍNEAS GRISES CONTINUAS REPRESENTAN LOS CONTORNOS DE LA AB. LA LÍNEA BLANCA CONTINUA DELINEA LA CUENCA DE MAZATLÁN. SBG: DESFILADERO DE SAN BLAS. ARB: ENSANCHAMIENTO DE ARAMARA. LA LÍNEA SEGMENTADA NEGRA UBICA LOS LÍMITES PROPUESTOS DE LA CSB. TOMADO DE CAMACHO Y ALVAREZ (2024); CAPÍTULO 2. 20
- FIGURA 12. MAPA DE GEO-VOLÚMENES DE ISO-DENSIDADES. EN ROJO, CUERPOS CON DENSIDADES DE 0.025 G/CM<sup>3</sup>, EN VERDE CUERPOS CON -0.025 G/CM<sup>3</sup> Y EN AZUL CUERPOS CON -0.050 (EN RELACIÓN CON LA DENSIDAD DE REDUCCIÓN DEL MEDIO DE 2.67 G/CM<sup>3</sup>). EN NEGRO, LA LÍNEA DE COSTA, EN GRIS CLARO LOS CONTORNOS BATIMÉTRICOS. LAS SECCIONES EN AZUL CLARO REPRESENTAN SUPERFICIES DENTRO DE LAS VERDES. TOMADO DE CAMACHO Y ALVAREZ (2024); CAPÍTULO 2. 21
- FIGURA 13. DESARROLLO TECTÓNICO DEL ÁREA DE LA SBB ENTRE 30 MILLONES DE AÑOS Y EL PRESENTE. EN EL PANEL A, OBSERVAMOS LA POSICIÓN DE LA PLACA NORTEAMERICANA CUANDO COMENZÓ EL MOVIMIENTO DE SEPARACIÓN DE LA BC HACE APROXIMADAMENTE 30 MILLONES DE AÑOS. EL PANEL B SE REFIERE AL PROCESO DE CAMBIO EN LA DIRECCIÓN DEL MOVIMIENTO, OCURRIDO ENTRE 19 Y 16 MILLONES DE AÑOS ATRÁS, SOBRE ÁREAS DE EXTENSIÓN Y ADELGAZAMIENTO CORTICAL, CAUSANDO SU ROTACIÓN. EL PANEL C INDICA LA CONSOLIDACIÓN DEL MOVIMIENTO Y LA POSICIÓN FINAL ROTADA DE LOS CUERPOS ASOCIADOS CON ZONAS DE ADELGAZAMIENTO CORTICAL. EL PANEL D MUESTRA LA APARICIÓN DE ZONAS DE MATERIAL DE ALTA DENSIDAD ASOCIADAS CON INTRUSIONES FORMADAS POR EL RÉGIMEN CONTINUO DE EXTENSIÓN. EN EL PANEL E APARECE UN SISTEMA DE FALLAS SOBRE LA ZONA, QUE LA ATRAVIESA. EL PANEL F MUESTRA LA CONFIGURACIÓN ACTUAL DEL GEO-VOLUMEN, OBTENIDA A PARTIR DE LA INVERSIÓN. TOMADO DE CAMACHO Y ALVAREZ (2024); CAPÍTULO 2. 22
- FIGURA 14. PRINCIPALES ELEMENTOS Y LIMITES TECTÓNICOS DEL BLOQUE DE JALISCO, Y LOS DOMINIOS TOPOGRÁFICOS (EL ESTÁTICO Y EL LEVANTADO). EN NARANJA LOS LÍMITES Y LAS FALLAS GEOLÓGICAS.

- LOS TRIÁNGULOS REPRESENTAN LOS CAMPOS VOLCÁNICOS: CVC, COMPLEJO VOLCÁNICO DE COLIMA; LINEAMIENTO VOLCÁNICO CENTRAL DE JALISCO (CJVL, EN LÍNEA NEGRA) QUE INCLUYE LOS CAMPOS VOLCÁNICOS DE SAN SEBASTIÁN (SSVF); MASCOTA (MVF); AYUTLA, (AVF); LOS VOLCANES (LVVF). OTROS VOLCANES NOTABLES: SJ, SAN JUAN; SGG, SANGANGUEY; CB, CEBORUCO. LOS PUNTOS CORRESPONDEN A LAS CIUDADES: SB, SAN BLAS. TP, TEPIC. CM, COMPOSTELA. GD, GUADALAJARA. CH, CHAMELA. CO, COLIMA. MZ, MANZANILLO. BN, BARRA DE NAVIDAD. GTP, GUADALAJARA TRIPLE POINT. LCH, LAGO CHAPALA. LOS PUNTOS ROJOS REFIEREN A EL PUNTO TRIPLE DE GUADALAJARA (GTP) Y EL PUNTO TRIPLE DE COMPOSTELA (CTP). TOMADO DE CAMACHO Y ALVAREZ (2020); CAPITULO 3. 23
- FIGURA 15. INVERSIÓN GRAVIMÉTRICA 3D DE DIMENSIONES APROXIMADAS A 25 X 25 X 5 KM; LA RESOLUCIÓN DE LA MALLA ES DE 500 M. EL VOLUMEN FUE CORTADO A LO LARGO DE UN AZIMUT DE 65 GRADOS A TRAVÉS DEL EDIFICIO VOLCÁNICO PARA MOSTRAR LA ANOMALÍA DE BAJA DENSIDAD (EN AZUL) BAJO EL VOLCÁN NT. LA CAJA SUPERIOR MUESTRA EL MODELO DIGITAL DE ELEVACIÓN ASOCIADO AL VOLCÁN. LAS LÍNEAS PUNTEADAS AMARILLAS INDICAN LOS LÍMITES DEL SISTEMA DE CONDUCTOS DEL VOLCÁN. TOMADO DE ALVAREZ Y CAMACHO (2023A); CAPÍTULO 4. 25
- FIGURA 16. A) SUPERFICIE QUE ENCIERRA LA REGIÓN DE DENSIDADES MÁS BAJAS (EN ROJO), OBTENIDA A PARTIR DE LA INVERSIÓN 3D CON UNA RESOLUCIÓN DE 500 M, EXTENDIÉNDOSE VERTICALMENTE DESDE ELEVACIONES DE +4210 HASTA 2200 M. LA PARTE SUPERIOR DE LA SUPERFICIE MUESTRA CLARAMENTE LA FORMA DE LA BIFURCACIÓN. B) CUANDO SE RETIRA LA SUPERFICIE ROJA, SE EXPONEN LAS DENSIDADES MÁS BAJAS, REVELANDO UN ÚNICO CONDUCTO VOLCÁNICO AL OESTE DE LA CIMA. TOMADO DE ALVAREZ Y CAMACHO (2023A); CAPÍTULO 4. 26
- FIGURA 17. ANOMALÍA DE BOUGUER DEL VOLCÁN HUNGA TONGA HUNGA HA'APAI VOLCANO. TOMADO DE ALVAREZ Y CAMACHO (2023B); CAPÍTULO 4. 27
- FIGURA 18. MODELO DE INVERSIÓN GRAVIMÉTRICA 3D DEL VOLCÁN HUNGA TONGA HUNGA HA'APAI VOLCANO. EN LA SUPERFICIE 3D SE ENCUENTRA LA BATIMETRÍA CIRCUNDANTE AL VOLCÁN. RESALTADO EN LA LÍNEA PESPUNTEADA BLANCA SE SEÑALA EL SISTEMA DE PLOMERÍA ENCONTRADO. TOMADO DE ALVAREZ Y CAMACHO (2023B); CAPÍTULO 4. 28
- FIGURA 19. MODELO DE INVERSIÓN DE 500 M DE RESOLUCIÓN. (A) VISTA SUR DE LA GEO-SUPERFICIE; ALCANZA HASTA LA PARTE INFERIOR DEL MODELO (-6,000 M); (B) VISTA VERTICAL DE LA GEO-SUPERFICIE; CUBRE PREDOMINANTEMENTE LA PORCIÓN CENTRAL-ORIENTAL. EL POLÍGONO AMARILLO SEÑALA EL ÁREA (14 KM<sup>2</sup>). (B) GEO-SUPERFICIE OBTENIDA EN EL RANGO DE DENSIDAD DE 2.47 A 2.57 G/CM<sup>3</sup>, ESTIMADA DE PRODUCTOS DE ERUPCIÓN INTERACTUANDO CON AGUA DE MAR. TOMADO DE ALVAREZ Y CAMACHO (2023B); CAPÍTULO 4. 29

# 1. INTRODUCCIÓN

Este trabajo es un compendio de 5 trabajos desarrollados y publicados durante el doctorado, el cual se realiza como tesis en modo artículos. A continuación, se explicará como están distribuidos.

## 1.1. LOS DOS PRINCIPALES MODELOS DE DATOS GRAVÍMETROS SATELITALES DE ALTA RESOLUCIÓN

El uso de modelos de datos gravimétricos satelitales está revolucionando el campo de la exploración geofísica a niveles regionales y tectónicos; ya que estos datos cuentan con una distribución regular y uniforme en todo el globo terráqueo (dependiendo del modelo de datos satelitales), lo cual convierte los modelos de datos satelitales en un tipo de dato excelente para cubrir enormes extensiones de terreno, que con otros métodos requerirían enormes costos. Si bien este tipo de datos tiene en servicio alrededor 30 años, comenzaron como modelos de datos de baja resolución y poca precisión que, con el pasar de los años, siguen avanzando y refinándose a modelos que poseen cada vez mayor precisión (Álvarez et al, 2016). Actualmente entre los modelos más precisos se encuentran: el modelo de datos satelitales EIGEN-6C4 que cuenta con una cobertura global y con un máximo de resolución de  $0.009^\circ$  o aprox. 1km (Förste et al, 2014); y el modelo de datos satelitales GGMplus, que cuenta con una resolución de 7.2 arcosegundo, pero con una cobertura de  $\pm 60^\circ$  de latitud (Hirt et al., 2013).

Durante los últimos años, diversos estudios han comprobado su buen ajuste con respecto a datos terrestres, que pueden rondar cerca de 1 mGal (e.g: Garzón *et al.*, 2011; Förste et al, 2014; Linares et al, 2016). Es observable también que los datos de origen satelital se han usado en una gran diversidad de estudios tales como: Generación de mapas de basamento cristalino a través datos satelitales (e.g: Linares *et al.*, 2014; Espinoza et al., 2023); Estudio de la estructura cortical, mediante el análisis de flexión de placas (Arnaiz-Rodríguez *et al.*, 2011; Ughi, 2014); mapas de Anomalía de Bouguer sobre Venezuela y el Caribe (e.g: Linares *et al.*, 2016; Arnaiz-Rodríguez y Garzón, 2012); estudios de delimitación de estructuras tectónicas (Camacho y Alvarez et al, 2020; Ekka et al, 2022; Ghomsí et al, 2022; Espinosa et al, 2023; Camacho-Ascanio y Alvarez, 2024) e incluso hasta para la prospección de asentamientos arqueológicos (Klokočník et al, 2020). De esta forma, se aprecia que este tipo de datos son idóneos para cubrir grandes extensiones y destacar estructuras regionales.

Este trabajo, es una compilación de 5 trabajos publicados a lo largo del Doctorado (los cuales serán descritos a continuación). Por lo tanto, las referencias y figuras usada en el desarrollo de este texto

compilatorio, se mantendrán indexadas de forma tradicional; mientras que las referencias y figuras usadas en cada uno de los artículos publicados, se mantendrán dentro de cada uno de los capítulos correspondientes a cada trabajo y se citaran según su correspondiente trabajo.

En el Capítulo 1 (Geophysical Modeling with Satellite Gravity Data: Eigen-6C4 vs. GGM Plus; Camacho & Alvarez, 2021; <https://doi.org/10.4236/eng.2021.1312050>), se aborda una comparación de los modelos de mayor resolución en la actualidad: modelo EGM2008, el modelo Eigen-6C4 y el modelo GGMplus (Figura 1). En dicho capítulo 1, se comparan sus características de los principales modelos gravimétricos satelitales, en función de su calidad espectral y su calidad de resolución, para la exploración geofísica en escala regional y local. Además, se realizó un estudio estadístico para evaluar el comportamiento de dichos datos en diferentes regiones (e.g: Figura 2) y se analizaron los espectros de potencia de los modelos sobre la región, para determinar cuál era la profundidad de fuente dominante en cada modelo, comparando su respuesta con una inversión gravimétrica 3D a fin de diagnosticar si podía discriminar prácticamente lo encontrado en la comparación de los espectros de potencia. Adicionalmente, se desarrolla la importancia del *DEM* (modelo de elevación digital; siglas en inglés) a la hora del procesado de los datos satelitales y cuáles son los principales artificios matemáticos surgidos a partir de la utilización de DEMs sub-óptimos.

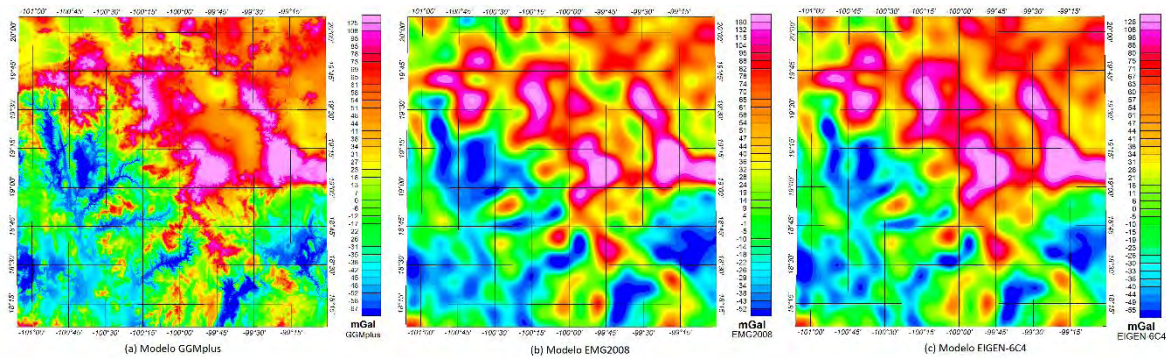


Figura 1. Mapas de anomalía de Aire libre sobre una misma región geográfica. (a) Mapa de Anomalía de Aire libre del modelo GGMplus. (b) Mapa de anomalía de Aire libre del modelo EGM2008. (c) Mapa de anomalía de Aire libre del modelo EIGEN-6C4. Tomado de Camacho y Alvarez (2021); Capítulo 1.

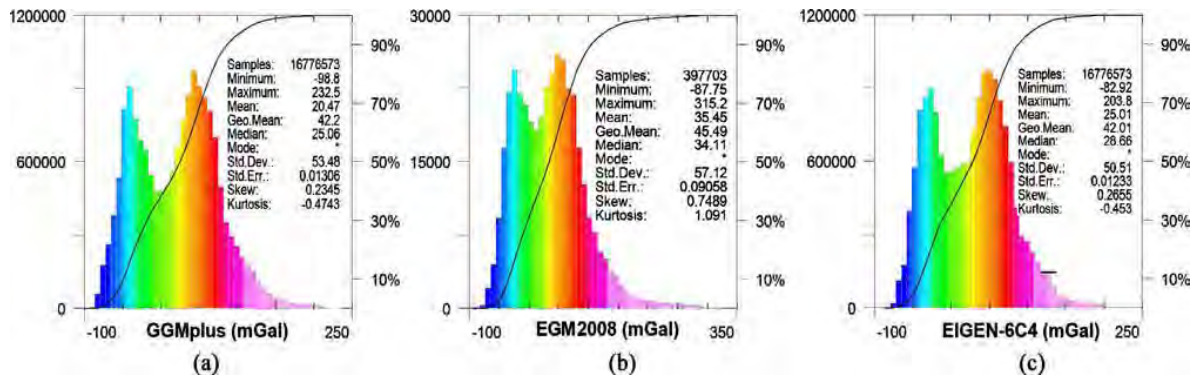


Figura 2. Histograma de frecuencia de la Anomalía de Aire libre para los modelos: (a) GGMplus, (b) EGM2008 y (c) EIGEN-6C4. El comportamiento de los histogramas revela sutiles pero relevantes diferencias entre los modelos. Demostrando lo similar del comportamiento estadístico de los datos del modelo EIGEN-6C4 y el modelo GGMplus. Tomado de Camacho y Alvarez (2021); Capítulo 1.

De toda esta información, se concluye en el capítulo 1 que los mejores modelos para estudios gravimétricos satelitales son los modelos EIGEN-6C4 y GGMplus. Además, se confirma que el comportamiento del modelo GGMplus es coherente al del EIGEN-6C4, pero con una resolución 4 veces mayor; lo cual demuestra la capacidad de este modelo para ser usado en estudios regionales, pero también que puede definir estructuras 4 veces menores en resolución espacial a los que define el modelo EIGEN-6C4. Dentro de este estudio se encontró que los datos del modelo EIGEN-6C4 poseen un contenido espectral más nutrido, para fuentes que poseen profundidades superiores a 10 km.

## 1.2. TECTÓNICA DEL OESTE DE MÉXICO

La tectónica del Oeste de México es muy compleja. La historia tectónica de la Cuenca de San Blas y el Bloque de Jalisco están íntimamente ligados a la evolución tectónica de Baja California y el Golfo de California; ya que dicha cuenca se encuentra en un límite de placa que ha sufrido gran actividad volcánica, procesos de subducción, procesos de extensión de la corteza y procesos transtensivos durante los últimos 100 Ma de años (por ejemplo; Karig y Jensky, 1972; Moore, 1973; Gastil et al., 1979; Stock y Hodges, 1989; Ferrari et al., 2013; Ortega-Gutiérrez et al., 2014; Duque-Trujillo et al., 2015; Ferrari et al., 2018). Además, la cuenca de San Blas se ha estudiado relativamente poco y no se han delimitado con precisión sus fronteras; de hecho, la geometría de la cuenca de San Blas es bastante compleja y aún no está bien determinada en su geometría, ni en su relación tectónica con el Bloque de Jalisco. Mientras que, por el contrario, el Bloque de Jalisco cuenta con una variedad de estudios que tratan de determinar sus fronteras de manera local, sin establecer claramente los límites tectónicos del bloque.



En la literatura existe un largo debate que aún sigue en desarrollo, sobre el modelo de separación de Baja California y apertura del Golfo de California. Desde el primero modelo planteado por Stock y Hodges (1989) a finales de la década de los 80's, se ha ido refinando a través del descubrimiento de diversas evidencias científicas que fueron desarrollándose a través del tiempo, como lo son por ejemplo los modelos de Gans (1997) Fletcher et al. (2007) y Sutherland et al. (2012), hasta llegar al modelo más actual presentado por el equipo de Ferrari *et al.* (2013). En este modelo se observa la posición de Baja California antes de la extensión que ocurrió hace 30 Ma (líneas de color verde; Figura 3), en la cual se realinean los batolitos del Cretácico Tardío de Bahía de Banderas (Bloque Jalisco), Los Cabos y Sinaloa, así como se reposiciona la paleo-trinchera a su posición más probable hace 30 Ma, al O de Baja California y al O de Bahía de Banderas (Figura 3). En su etapa inicial, ellos plantean que se movió cerca de 85 km en dirección N10°O hasta hace 18 Ma (7.7 mm/año), en donde cambió la dirección del movimiento, de N10°O a S10°O aproximadamente, completando unos 50 km de desplazamiento en 6 Ma (8.3mm/año). En esta reconstrucción, el extremo sur de Baja California está a 475 km al sureste de su posición actual. La posición de Baja California a 12 Ma se obtiene al eliminar los 245 km de corteza oceánica acumulada en la Dorsal del Pacífico Este, más 110 km de extensión a ambos lados de la corteza oceánica: 35 km en la corteza estirada al sureste del bloque Los Cabos y 75 km de extensión en el área de corteza estirada de 200 km de largo entre Bahía de Banderas y la vertiente continental al oeste de las Islas Tres Marías. Con lo cual los autores (Ferrari *et al.*; 2013) calcularon que el movimiento de Baja California entre los 30 y 12 Ma equivaldría a 135 km, en función de la edad y la geometría de las fallas.

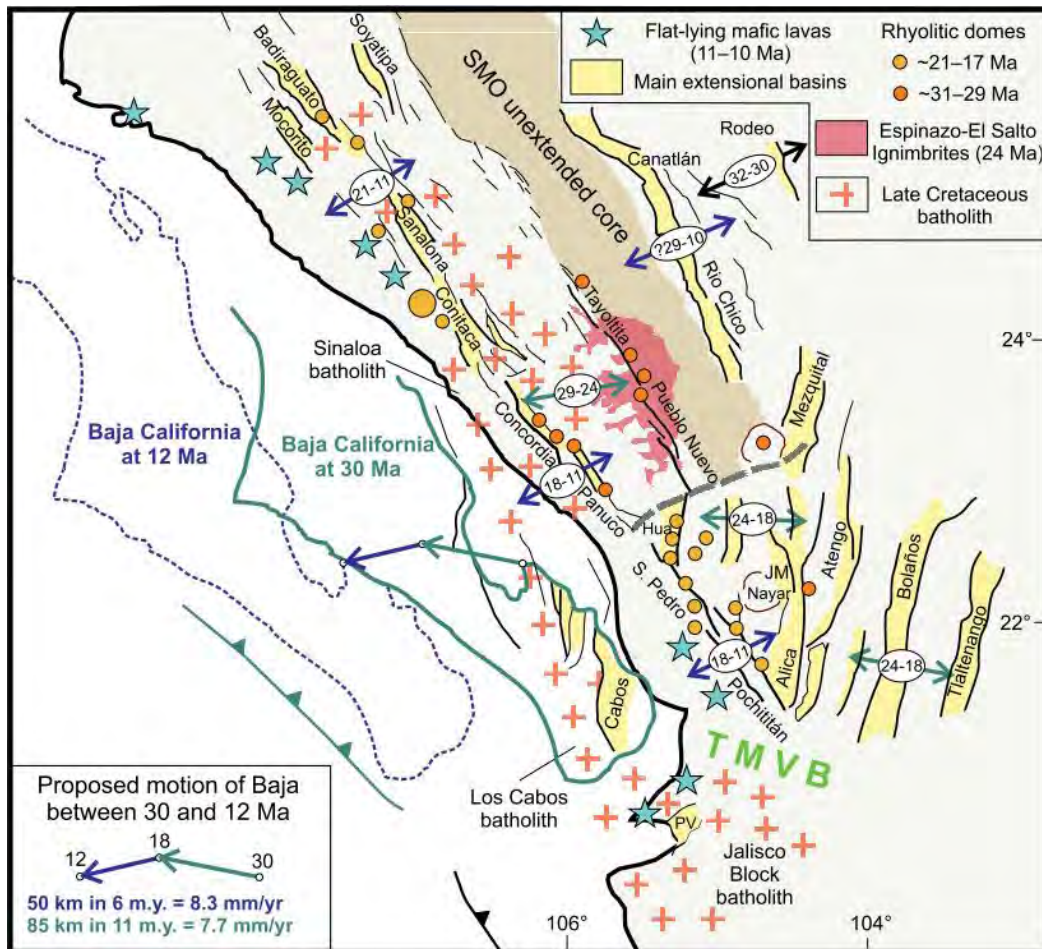


Figura 3. Modelo Tectónico de la apertura del Golfo de California. Tomado de Ferrari et al. (2013). Posteriormente ese modelo es complementado por Ferrari *et al.* (2018), añadiendo una reconstrucción del movimiento entre los 19 y 16 Ma (Figura 4) en donde se muestran las principales cuencas extensionales de ese periodo y la posición de las principales características tectónicas y geodinámicas del O de México entre los 19 y 16 Ma, cuando el rift estaba enfocado en el área del Golfo de California. Baja California es reconstruida según su posición pre-rift (Ferrari *et al.*, 2013) y la posición de las placas del Pacífico, Magdalena y Guadalupe según (Atwater y Stock, 1998), las estimaciones de la posición de la trinchera están construidas según las estimaciones de Lonsdale (1991) y en esa reconstrucción (Figura 4), se muestra que la extensión activa ocurrió en un cinturón de alrededor de 80 km de ancho en un ángulo agudo a la franja y ubicado entre 50 y 75 km del límite de la placa en su extremo sur. Este cinturón extensional comprende las cuencas Baucarit de Sonora y su continuación en Sinaloa, así como la cuenca Comondú en el sur de Baja California y otras cuencas similares ahora sumergidas en el sur del Golfo de California (Foca-Cerralvo y San Blas; Figura 4), por lo que para Ferrari *et al.* (2018) “la cuenca Foca-Cerralvo representa el remanente occidental

de una cuenca de rift axial, cuya contraparte oriental puede ser la cuenca de San Blas". Y el vulcanismo dentro de 19 a 16 Ma dentro de la estrecha banda de la grieta, fue el producto de la fusión de la litosfera del manto hidratado y/o astenósfera modificada por subducción con composiciones más intermedias que reflejan contribuciones variables de la fusión parcial de la corteza por procesos de mezcla de magma. Entonces, a partir de 16 Ma, el entorno geodinámico se caracterizó por la desaparición de la subducción ya que la edad de la placa de subducción no era en ningún caso mayor a 7 Ma para la placa de Guadalupe, y 4 MA para la micro-placa Magdalena.

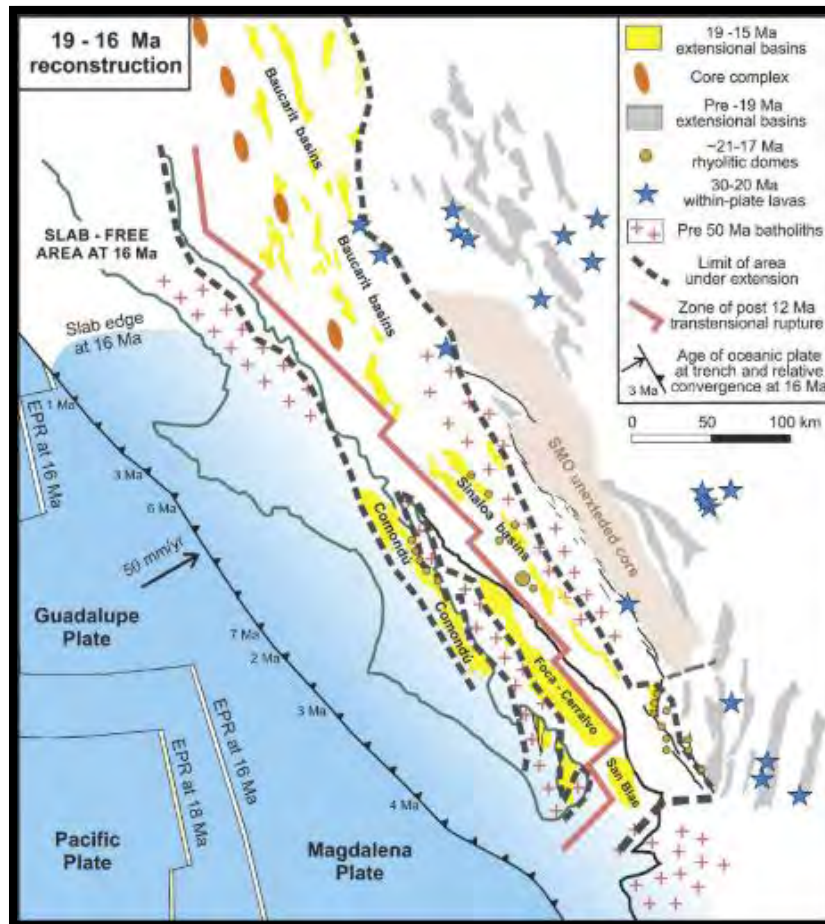


Figura 4. Reconstrucción tectónica de la posición de Baja California entre los 19 y 16 Ma. Tomado de Ferrari et al. (2018).

### 1.2.1 LA CUENCA DE SAN BLAS

De la Cuenca de San Blas, hay poca información. Se sabe que es la cuenca más grande del sector SE del basamento de Mazatlán (Sánchez-Barra *et al.*, 2023), está ubicada en el Golfo de California y se encuentra sumergida a una profundidad promedio de 50 m formando parte de la plataforma

continental Norteamericana (Sutherland *et al.*, 2012; Ferrari *et al.*, 2018; Sánchez-Barra *et al.*, 2023). En la *Figura 5*, se puede observar la zona que ocupa la cuenca en la plataforma continental Norteamericana, además se entiende encuentra su límite O entre el fin ; hacia el SE limita con el Bloque de Jalisco. Según lo visto anteriormente, la cuenca de San Blas podría ser la contraparte oriental de la cuenca Foca-Cerralvo, la cual habría sido una cuenca extensional temprana producida durante el desarrollo de la Provincia de Extensión del Golfo de California, que luego fue deformada por el movimiento transtensional y el sistema de fallas Tamayo y Pescadero (Ferrari *et al.*, 2018).

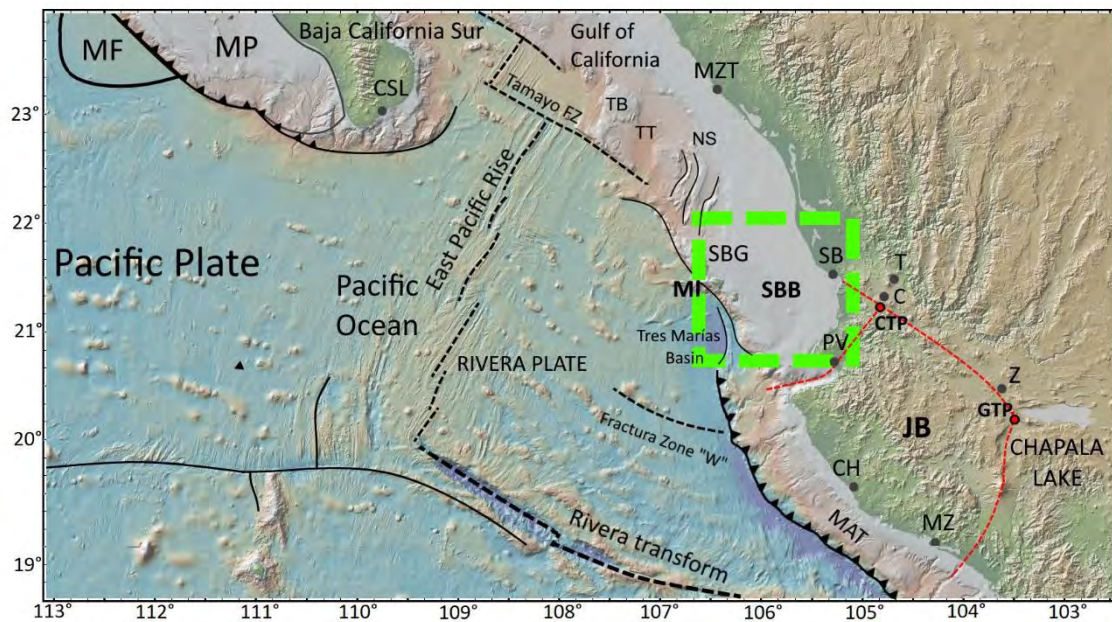


Figura 5. Configuración tectónica de la SBB, incluyendo los límites de la placa de Rivera y una porción de los límites conocidos de la SBB (representados por un cuadrado verde). CTP: Punto triple de Compostela. JB: Bloque de Jalisco. GTP: Punto triple de Guadalajara. Los límites del bloque de Jalisco están representados por líneas rojas (adaptado de Camacho y Alvarez, 2020). NS: Escarpes de Nayarit. MI: Islas Marías. TB: Banco Tamayo. TT: Trinchera Tamayo. MP: Plataforma Magdalena. MF: Abanico Magdalena. SBG: Desfiladero de San Blas. Las estructuras oceánicas fueron adaptadas de Demets y Traylen (2000) y Fletcher *et al.* (2007). Las Ciudades en puntos grises. C: Compostela. CSL: Cabo San Lucas. CH: Chamela. MZ: Manzanillo. PV: Puerto Vallarta. MZT: Mazatlán. SB: San Blas. T: Tepic. Z: Zacoalco. Tomado de Camacho-Ascanio y Alvarez (2024); Capítulo 2.

El principal estudio presente sobre la cuenca de San Blas, fue realizado a través del experimento de líneas sísmicas PESCADOR, en el cual esta cuenca fue la más grande registrada en el trazado (alrededor de 70 km de ancho). De este estudio se obtuvo un perfil sísmico que cruzó a través de la Cuenca de San Blas, en el que sin embargo no se alcanzó su límite SE. En el perfil de la Figura 2, que Sutherland *et al.* (2012) reportan, está claro que el basamento está muy fallado. Sin embargo, no se

reporta un fallamiento que destaque como falla principal del basamento, aunque los autores mencionan que es de tener en cuenta que: “en otras líneas sísmicas del experimento PESCADOR hay fallas normales de gran desplazamiento al sur del extremo sureste del tramo de Alarcón en la plataforma (Brown, 2007)”. Además, mencionan en ese trabajo (Sutherland et al., 2012), que hay variaciones en el carácter del basamento, desde una secuencia de basamento inferior altamente reflexiva en el borde septentrional poco profundo de la cuenca, hasta áreas sin un reflector claro del basamento; como el centro de la cuenca en donde los sedimentos alcanzan un grosor de 2.0 s (interpretado en tiempo) y revelan una deformación a pequeña escala de las fallas que cortan la estratigrafía a través de la cuenca, pero no tienen una fuerte indicación de depósito sincrónico. De esta forma, de acuerdo a este registro sísmico y lo mencionado anteriormente, Sutherland *et al.* (2012) afirman que la cuenca debe haberse formado hace al menos 14 Ma.

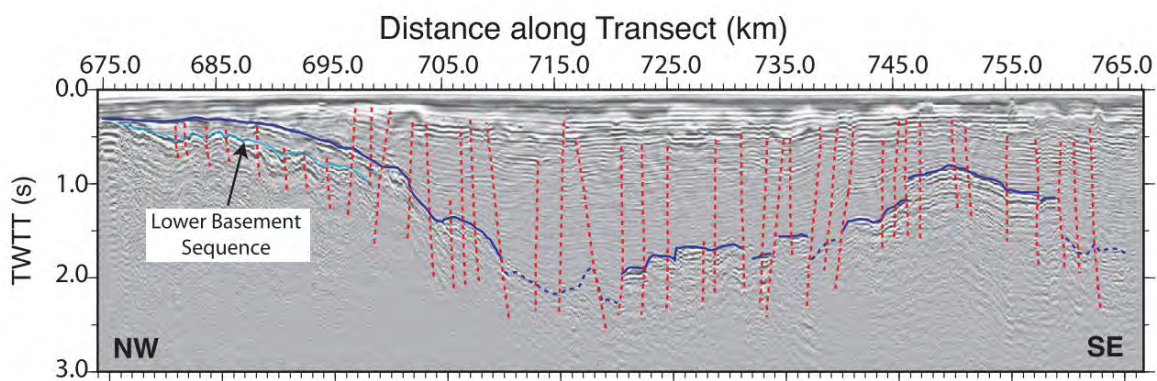


Figura 6. Perfil sísmico de la Cuenca de San Blas. Tomado de Sutherland et al. (2012). En azul oscuro el basamento interpretado. En rojo las fallas interpretadas.

En el capítulo 2 (DELINEATION OF THE BOUNDARIES OF SAN BLAS BASIN, MEXICO, MERGING GRAVITY, MAGNETIC, AND SEISMIC DATA; Camacho-Ascanio y Alvarez (2024); <https://doi.org/10.1016/j.jsames.2024.104818>). Utilizamos la exploración geofísica, principalmente a través de datos de modelos gravimétricos satelitales (en este caso el modelo EIGEN-6C4), en conjunción con datos magnéticos del NA\_Mag y diferentes sísmicas interpretadas en la región para delimitar los límites de la Cuenca de San Blas. Además, se realizó una inversión 3D gravimétrica y una inversión 3D magnética, con el fin de determinar cuerpos intrusivos en el área.

### 1.2.2 BLOQUE DE JALISCO

Inmediatamente en la frontera oriental de la Cuenca de San Blas, encontramos el Bloque de Jalisco. Dicho Bloque presenta una tectónica muy compleja: en él existen zona de subducción, zonas de graben, campos volcánicos y zonas de rift. Razón por la cual el Bloque de Jalisco es una zona tan fascinante para los investigadores de todas partes del mundo. Diversos autores (e.g: DeMets et al., 1990; Stock, 1993; Pardo y Suárez, 1993; DeMets et al., 1997; Bandy, 2005; Pardo y Suarez, 1995; Ferrari, 2000) han definido al Bloque de Jalisco como una microplaca tectónica que se mueve independientemente de las placas circundantes (Placa Rivera, placa de Cocos y Placa Norteamericana). Este movimiento de esta placa involucra importantes estructuras geológicas como lo son: el Rift de Tepic-Zacoalco, el Rift de Colima Rivera (Stock, 1993); además de la geometría de subducción de la placa Rivera (Alvarez et al., 2021).

En esencia se pueden observar los bordes del Bloque de Jalisco en la Figura 7, dicho bloque está delimitado por la Trinchera Mesoamericana hacia el occidente, la zona del Rift de Colima en la parte meridional y la zona del Rift de Tepic-Zacoalco en la parte nororiental (Allan, 1986; DeMets et al., 1990). El borde noroccidental ha sido propuesto por Camacho y Alvarez (2020), desde el Punto Triple de Compostela siguiendo al sur por el Valle de Banderas y hacia la Bahía de Banderas (Figura 7). La mayor parte del Bloque de Jalisco está constituido por el Batolito de Puerto Vallarta (Schaaf et al., 1995; Ferrari y Rosas-Elguera, 2000).

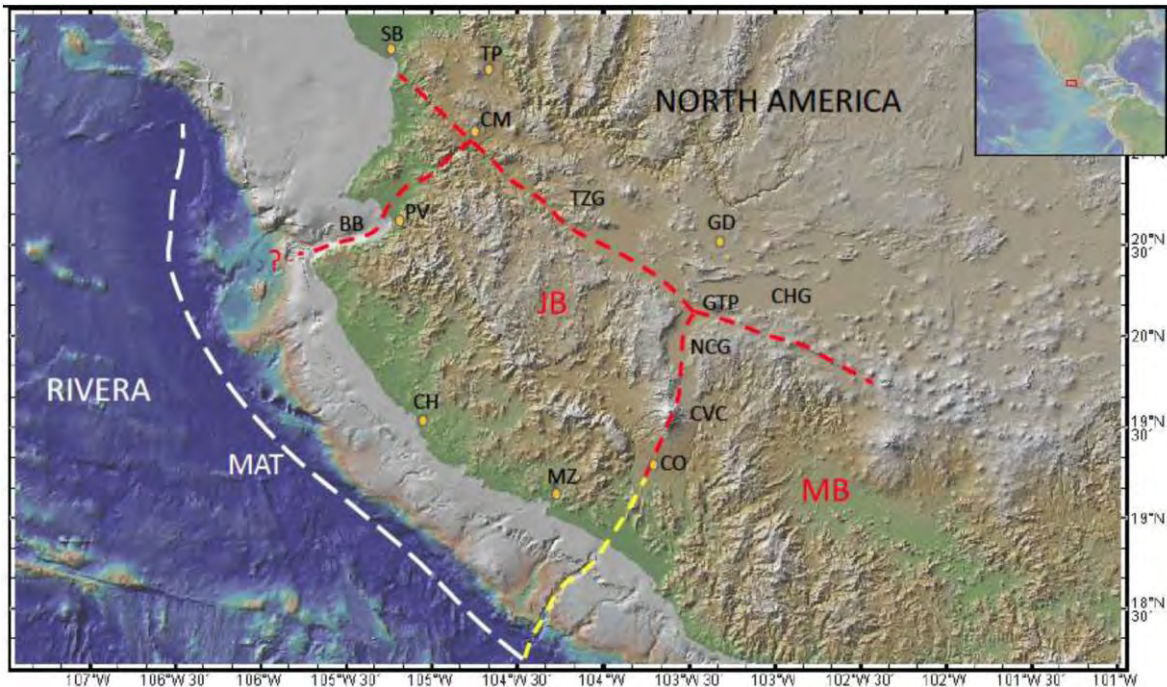


Figura 7. Límites del Boque de Jalisco (JB). La línea amarilla es el límite propuesto por Alvarez y Yutsis (2015). Batimetría (de azul a marrón claro) y topografía (de verde a blanco) son de Ryan et al (2009). MAT: Trincheras centro americanas. MB: Bloque de Michoacán. CVC: Complejo volcánico de Colima. GTP: Punto triple de Guadalajara. BB: Bahía de Banderas, NCG: Graben norte de Colima. CHG: Graben de Chapala. TZG: Graben de Tepic-Zacoalco. Punto naranja corresponde a ciudades: SB, San Blas. TP, Tepic. CM, Compostela. GD, Guadalajara. CH, Chamela. CO, Colima. MZ, Manzanillo. Tomado de Camacho y Alvarez (2020); Capítulo 3.

Según lo visto, el Bloque de Jalisco al ser una zona tan amplia y compleja, ha dado cabida a numerosas investigaciones. Se han tratado temas sobre geodesia (e.g: Hutton et al., 2001; Schmitt et al., 2007; Melbourne et al., 1997), petrología (e.g: Wallace y Carmichael, 2004), geología (e.g: Allan, 1986; Ferrari and Rosas-Elguera, 2000), paleomagnetismo (e.g: Nieto-Obregón et al., 1992; Goguitchaichvili et al., 2007), gravimetría y magnetometría (e.g: Campos-Enríquez et al., 1990; Alatorre-Zamora y Campos-Enríquez, 1991; Campos-Enríquez y Alatorre-Zamora, 1998; Arzate et al., 2006; Álvarez et al., 2010; Álvarez y Yutsis, 2015; Alatorre-Zamora et al., 2015; entre otros) y estudios sísmicos (e.g: Núñez-Cornú, 2004; Pacheco et al., 2003; León-Soto et al., 2009; Yang et al., 2009) entre otros.

Sin embargo, debido principalmente a las dimensiones del Bloque de Jalisco, su complejidad y la imposibilidad de dar una cobertura apropiada con los métodos tradicionales; la mayoría de los estudios realizados se efectuaron en zonas relativamente pequeñas comparadas a su extensión (e.g:

Campos-Enríquez y Alatorre-Zamora, 1998; Alvarez y Yutsis, 2015), dificultando una interpretación apropiada del contexto tectónico-estructural en su un marco regional. Es por ello que en el Capítulo 3 (*Gravimetric analysis of the rifts and volcanic fields of the Jalisco block, Mexico*; Camacho y Alvarez (2020); <https://doi.org/10.1016/j.tecto.2020.228577>) abordamos el análisis gravimétrico de los rifts presentes y sus principales campos volcánicos en un estudio geofísico que integra: modelos gravimétricos satelitales (Eigen-6C4), modelos magnéticos NA\_mag, datos sísmicos interpretados y perfiles magnetotélúricos interpretados. Todo esto con el suficiente alcance en extensión y detalle, para definir con exactitud sus fronteras y sus rasgos estructurales desde un punto de vista gravimétrico/tectónico. En dicho trabajo, se lograron precisar los límites tectónicos del Bloque de Jalisco: La Trinchera Mesoamericana para la región suroccidental; el Rift de Colima para la frontera oriental; el Graben del Gordo para el borde suroriental; el Rift de Tepic-Zacoalco para la región nororiental, y el Rift de Compostela-Banderas para la región noroccidental. Además, se precisó a través de información geofísica la posición del punto triple de Guadalajara, y se determinó y precisó el punto triple de Compostela.

### 1.3. ANÁLISIS GRAVIMÉTRICO DEL SISTEMA DE PLOMERÍA DE VOLCANES:

Interpretaciones y modelos gravimétricos y magnéticos, son usados para asociar anomalías de densidad y susceptibilidad magnética con las características estructurales en regiones volcánicas. Por lo tanto, los estudios gravimétricos ayudan a determinar las características de los campos volcánicos (e.g. Kauahikaua et al., 2000; Camacho et al., 2018; Camacho y Alvarez, 2020; Guevara et al. 2021) y pueden ayudar a identificar sus sistemas de conductos (e.g. Alvarez y Yutsis, 2015; Camacho et al., 2018; Alvarez y Camacho, 2023a; Alvarez y Camacho, 2023b; Guevara et al., 2023). Las determinaciones magnéticas a menudo complementan los estudios de gravedad (e.g. Guevara et al., 2021; Guevara et al., 2023). Los Capítulos 4 (*Applying High-Resolución Gravity Analysis to Volcanic Plumbing Systems: The Case of Nevado De Toluca Volcano, Mexico*; Alvarez y Camacho, 2023a; <https://doi.org/10.14738/tecs.114.15392>) y 5 (*Plumbing System of Hunga Tonga Hunga Ha'apai Volcano*; Alvarez y Camacho, 2023b; <https://doi.org/10.1007/s12583-022-1792-0>) plantean una nueva aplicación para el modelo de datos GGMplus en el estudio de dos importantes volcanes del mundo: El Nevado de Toluca y el volcán Hunga Tonga Hunga Ha'apai. En ambos casos se realizó un modelo de inversión 3D sobre los datos gravimétricos, nos centramos en los procesos que ocurren en los primeros 5-6 km de la litosfera, con el fin de analizar el sistema plomería de ambos volcanes.



Capitulo 1: *Geophysical Modeling with Satellite Gravity Data:  
Eigen-6C4 vs. GGM Plus.*

# Geophysical Modeling with Satellite Gravity Data: Eigen-6C4 vs. GGM Plus

Miguel Camacho<sup>1</sup>, Román Alvarez<sup>2</sup>

<sup>1</sup>Posgrado en Ciencias de la Tierra, Universidad Nacional Autónoma de México, Mexico City, Mexico

<sup>2</sup>Román Alvarez, Instituto de Investigaciones en Matemáticas Aplicadas y en Sistemas (IIMAS), Universidad Nacional Autónoma de México, CDMX, Mexico City, Mexico

Email: miguelcamacho.geofisica@gmail.com, Roman.alvarez@iimas.unam.mx

**How to cite this paper:** Camacho, M. and Alvarez, R. (2021) Geophysical Modeling with Satellite Gravity Data: Eigen-6C4 vs. GGM Plus. *Engineering*, 13, 690-706.  
<https://doi.org/10.4236/eng.2021.1312050>

**Received:** November 1, 2021

**Accepted:** December 27, 2021

**Published:** December 30, 2021

Copyright © 2021 by author(s) and Scientific Research Publishing Inc. This work is licensed under the Creative Commons Attribution International License (CC BY 4.0).

<http://creativecommons.org/licenses/by/4.0/>



Open Access

## Abstract

Satellite data sets are an asset in global gravity collections; their characteristics vary in coverage and resolution. New collections appear often, and the user must adapt fast to their characteristics. Their use in geophysical modeling is rapidly increasing; with this in mind we compare two of the most densely populated sets: EIGEN-6C4 and GGMplus. We characterize them in terms of their frequency histograms, Free Air anomalies, power spectrum, and simple Bouguer anomalies. The nature of the digital elevation models used for data reduction is discussed. We conclude that the GGMplus data set offers a better spatial resolution. To evaluate their effect in geophysical modelling, we chose an inland region with a prominent volcanic structure in which we perform 3D inversions of the respective Bouguer anomalies, obtaining density variations that in principle can be associated with the geologic materials and the structure of the volcanic edifice. Model results are analyzed along sections of the inverted data; we conclude that the GGMplus data set offers higher resolution in the cases analyzed.

## Keywords

EIGEN-6C4, GGMplus, Satellite Gravity Data, 3D inversions, Nevado de Toluca

## 1. Introduction

Modeling in Geophysics is a permanent exercise, trying to reproduce, as close as possible, the Earth systems and processes that scientists try to understand. Here we are concerned with one of the Potential Methods used for this purpose: the gravity method. As technology has progressed, determination of the gravity field of the

Earth at given locations has also changed. For most of last century gravimetric determinations were mainly performed on the surface of the Earth, with oceanic measurements occurring along ships' navigation trajectories, including a few aerial acquisitions. The process was usually slow, expensive, and limited in extent. By the end of the century a radical change occurred, and satellites were incorporated to gravimetric data acquisition, introducing global data coverage [1] [2] [3] [4] [5]. Presently there is a wide variety of satellites from which gravity data can be obtained, however, there is not much information on how much scope they can have as regional study tools, and it is not clear among them, which may be the most appropriate for certain type of study. We will focus on two of the most recent data sets, having greater spatial definition; they are the EIGEN-6C4 model (ICGEM, [6]) the EGM2008 model [7] and the GGMplus model [8].

The EIGEN-6C4 gravimetric satellite data model is the highest resolution model with the highest coverage worldwide. Many studies have proven the value of their data for numerous regional tectonic studies, e.g., [9]. Studies that otherwise would have been impossible or immensely costly for the area of acquisition. Recently the GGMplus model has been available, with an unprecedented resolution (200 m). However, there is no systematic comparison of its performance versus the EIGEN-6C4 model, or whether it manages to determine the regional structures as well as the EIGEN-6C4 model. Its high-resolution is generated mainly using the interpolations of a finer topography, combining it with a database of a previous gravimetric model [10] achieving an effective use in the determination of geological structures of shorter wavelength. To resolve this doubt, we will compare both models in a real situation and observe their behavior.

## 2. Materials and Methods

The gravimetric satellite models used for evaluation in this study are: the EIGEN-6C4 model, made available through International Centre for Global Earth Models (ICGEM, [6]) it was sampled to  $0.009^\circ$  (approximately 1 km; the maximum resolution for the EIGEN-6C4); the EGM2008 model [7], made available from [https://topex.ucsd.edu/cgi-bin/get\\_data.cgi](https://topex.ucsd.edu/cgi-bin/get_data.cgi) (Topex data; Scripps Institution of Oceanography, University of California San Diego), with 1 arc-minute resolution ( $1' = 1.85$  km); and finally, the GGMplus, available from <http://ddfe.curtin.edu.au/gravitymodels/GGMplus/> with 7.5 arc-sec (220 m) resolution [8].

For the calculation of the Bouguer Anomaly (AB) at a given location, it is necessary to use the elevation at the given point. The elevation is provided by a digital elevation model (DEM). In this work we used 3 DEMs with different resolutions. The ETOPO1 topography model (National Center for Environmental Information; NOAA; <https://ngdc.noaa.gov/mgg/global/global.html>), with 1 arc-minute resolution, sampled to  $0.009^\circ$  resolution (approximately 1 km), the maximum resolution for the EIGEN-6C4. The SRTM15 topography model [https://topex.ucsd.edu/cgi-bin/get\\_srtm15.cgi](https://topex.ucsd.edu/cgi-bin/get_srtm15.cgi); [9], has a resolution 15 arc-second (approximately 450 m); finally, the SRTM90

(<https://srtm.csi.cgiar.org/srtmdata/>; [10]) with a 7.5 arc-sec resolution. This was done to make the comparison more realistic, and to diminish the DEM's influence to a minimum. The DEM used was SRTM15, which has an intermediate resolution between the EIGEN-6C4 and the GGMplus.

### 2.1. Free Air Anomalies

For the direct comparison of the GGMplus model it is necessary to obtain the Free Air (FA) anomaly of the EIGEN-6C4; to this end, we will use the ETOPO DEM, and the EIGEN-6C4 data. We calculate the FA anomaly of Model EIGEN-6C4 with:

$$FA = G_{obs} - G_{theo} \pm C_{alt} \quad (1)$$

### 2.2. Obtaining $G_{obs}$

For a direct comparison of the  $G_{obs}$  of the EIGEN-6C4 model with the GGMplus model, it is necessary to convert the GGMplus model (FA anomaly) to an observed gravity value at ground surface ( $G_{obs}$ ); this is done using the elevation of the station or, in general, the elevation provided by a DEM. The precision of the  $G_{obs}$  will depend, thus, on the precision of the DEM used to obtain it. In the case of the GGMplus model, the DEM has a resolution of approximately 7.5 arc-sec (or 200 m approximately [8]), for this reason we will use the DEM of the SRTM90. In this way, we get  $G_{obs}$

$$G_{obs} = FA - G_{theo} \pm C_{alt} \quad (2)$$

Gravity on Earth is distributed in a similar way as it would be in a sphere, but with a slight increase towards the geographical poles, due to the flattening of the terrestrial spheroid [11] [12]. In this way, the gravity of the Earth varies according to the latitude, it is what is known as theoretical gravity ( $G_{theo}$ ). To calculate the theoretical gravity at any point on the planet we need Equation (2) (Geodetic Reference System of 1980, GRS80).

$$G_{theo} = 978032.7(1 + 0.0053024 \sin^2 \lambda + 0.000058 \sin^4 \lambda) \text{ mGal} \quad (3)$$

The altitude correction ( $C_{alt}$ ) is applied to correct the distance of the measurement to the reference level; therefore, it has a + or - sign depending on whether the altitude is less or greater than the reference level. The equation for calculating the simplified height correction is [13]:

$$C_{alt} = -0.3086 * h \quad (4)$$

where  $h$  is the station elevation of the DEM. From (3) and (4) in (2) we obtain the value of  $G_{obs}$ :

$$G_{obs} = \pm 0.3086 * h + FA + G_{theo} \quad (5)$$

### 2.3. Calculation of Bouguer Anomaly

Since satellites acquire data at several hundred kilometers above the ground sur-

face, when computing the gravity field, a new type of correction must be included, corresponding to the weight of the column of air between ground and the satellite position, and it is also necessary to consider the sphericity of the Earth in the calculation. In [14] the procedure to obtain the Bouguer anomaly from EIGEN-6C4 data was explained, where such a correction was included according to the new gravimetric standard of the USGS; e.g., [15].

## 2.4. Modelling

We perform 3D gravity inversions using the method described by [16], based in turn on the theoretical considerations of [17]. The inversion results are densities in  $\text{g}/\text{cm}^3$ . The code is implemented in the Oasis Montaj program of Seequent. To represent geologic volumes, the program uses a Cartesian Cut Cell algorithm (CCC); to match the observed result with the calculated one, within established error limits, the inversion program uses an Iterative Reweighting Inversion algorithm (IRI) [18]. The program can also perform magnetic data inversions, although this is not relevant to the present problem. The model requires a DEM; we use the same geographic area and the same DEM (SRTM15) to perform the GGMplus and EIGEN-6C4 Bouguer anomaly inversions to better evaluate the inherent differences between the gravity data of each set. The term *voxel*, derived from *pixel*, but representing a volume, contains the results of the 3D inversion. We selected a volcanic area in central Mexico to compare 3D inversions with the two data sets. Additional examples of the inversion process can be found in [19]-[21].

## 3. Results

### 3.1. Free Air Anomalies

Since GGMplus is a Free Air anomaly model (FA), we shall start by comparing it with other FA models, for a preliminary evaluation. **Figure 1(a)** shows the one corresponding to GGMplus, **Figure 1(b)** shows the EGM2008 FA anomaly, and **Figure 1(c)** the EIGEN-6C4 FA anomaly. The higher resolution of the former

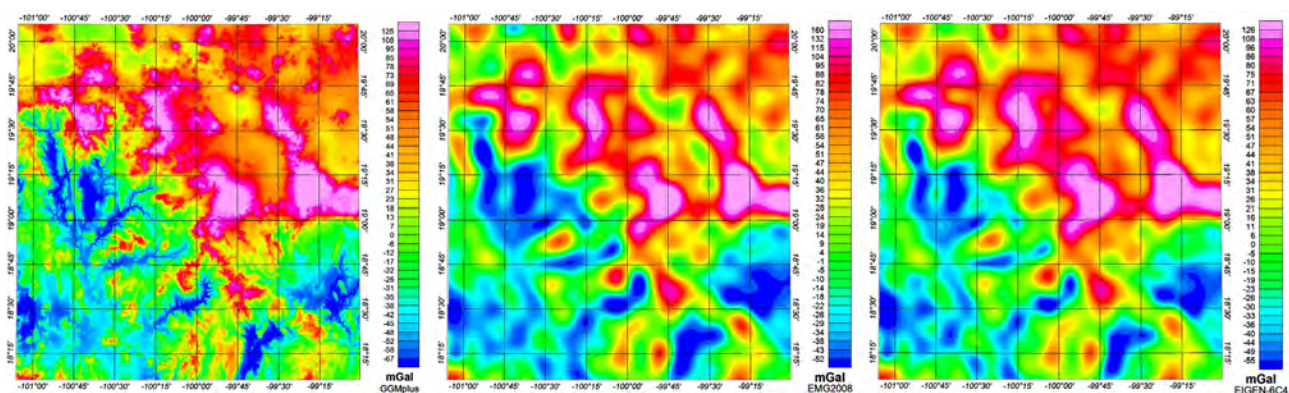


**Figure 1.** Free Air Anomaly maps obtained over the same geographic region, illustrating (a) the GGMplus, (b) the EGM2008, and (c) the EIGEN-6C4, FA corresponding anomalies. The better definition of the FA anomaly of the GGMplus data is neatly observed.

can be readily appreciated comparing the low-gravity regions on the west side of the maps.

The general aspect of the anomaly (**Figure 1(c)**) is quite similar to that of model EGM2008 (**Figure 1(b)**), although the anomaly range (125.8 to  $-55.3$  mGal) is somewhat smaller than that of EGM2008 model (148.1 to  $-55.3$  mGal). In **Fig 1** the resolution of the anomalies is clearly observed, reflecting smoother contours in the anomalies of the EIGEN-6C4 and EGM2008 models. Between the EIGEN-6C4 model and the EGM2008 we observed differences in the values of the anomalies, the negative values of FA being the most affected. In the EGM2008 model, more marked transitions between anomalies are observed, while in the EIGEN-6C4 model registers a less marked transition between the anomalies, better resembling the transition obtained in the GGMplus model. The range of GGMplus varies from 125.5 to  $-66.6$  mGal, enhancing details in the negative portion (**Figure 1(a)**), and being more similar to the behavior of the data distribution of the model EIGEN-6C4 (**Figure 2**). The distribution histograms (**Figure 2**), show a greater correlation between the GGMplus models and the EIGEN-6C4 model, in both we observed a bimodal distribution with modes close to  $-50$  and  $50$  mGal, and with a minimum between modes less than 50% of the accumulated data. In addition, the range of the histogram data varies from  $-90$  mGal to 215 mGal, while the range for the EGM2008 model is  $-87$  to 315 mGal, extending the upper range by about 70 mGal.

### 3.2. $G_{obs}$

The Observed Gravity ( $G_{obs}$ ) is the gravity that is measured in the surface of the Earth, which is the value of the GGMplus model we compared with the EIGEN-6C4 model. We calculate the  $G_{obs}$  of the GGMplus model according to Equation (5) (**Figure 3(a)**) and compare it to the corresponding EIGEN-6C4 (**Figure 3(b)**). A general similitude of results is observed although differences appear at closer inspection. The statistical data is very similar and the behavior of the data distribution in the histograms is quite similar.

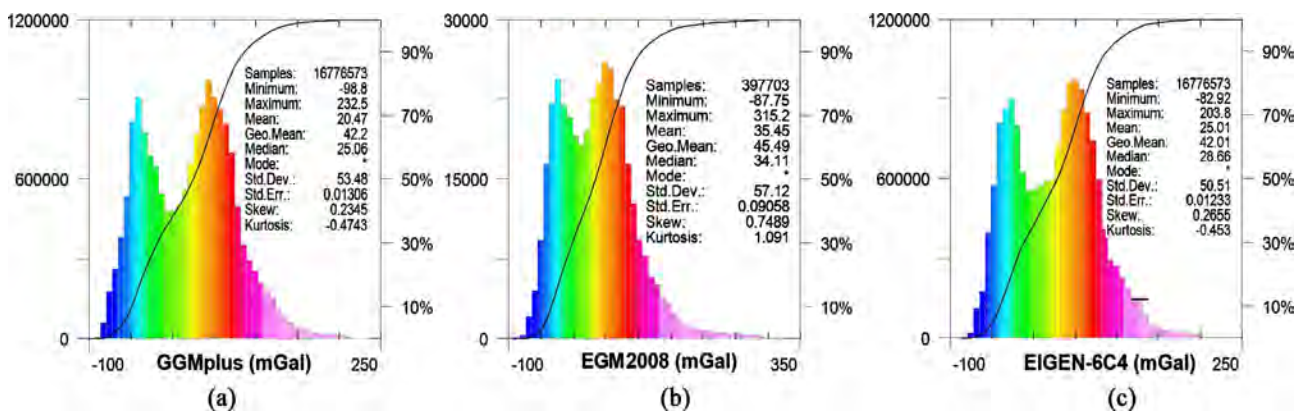


**Figure 2.** Frequency histograms for FA models (a) GGMplus, (b) EGM2008, and (c) EIGEN-6C4. There are subtle but relevant differences among them, revealing a greater similitude between EIGEN and GGMplus distributions and their cumulative frequencies (black line).

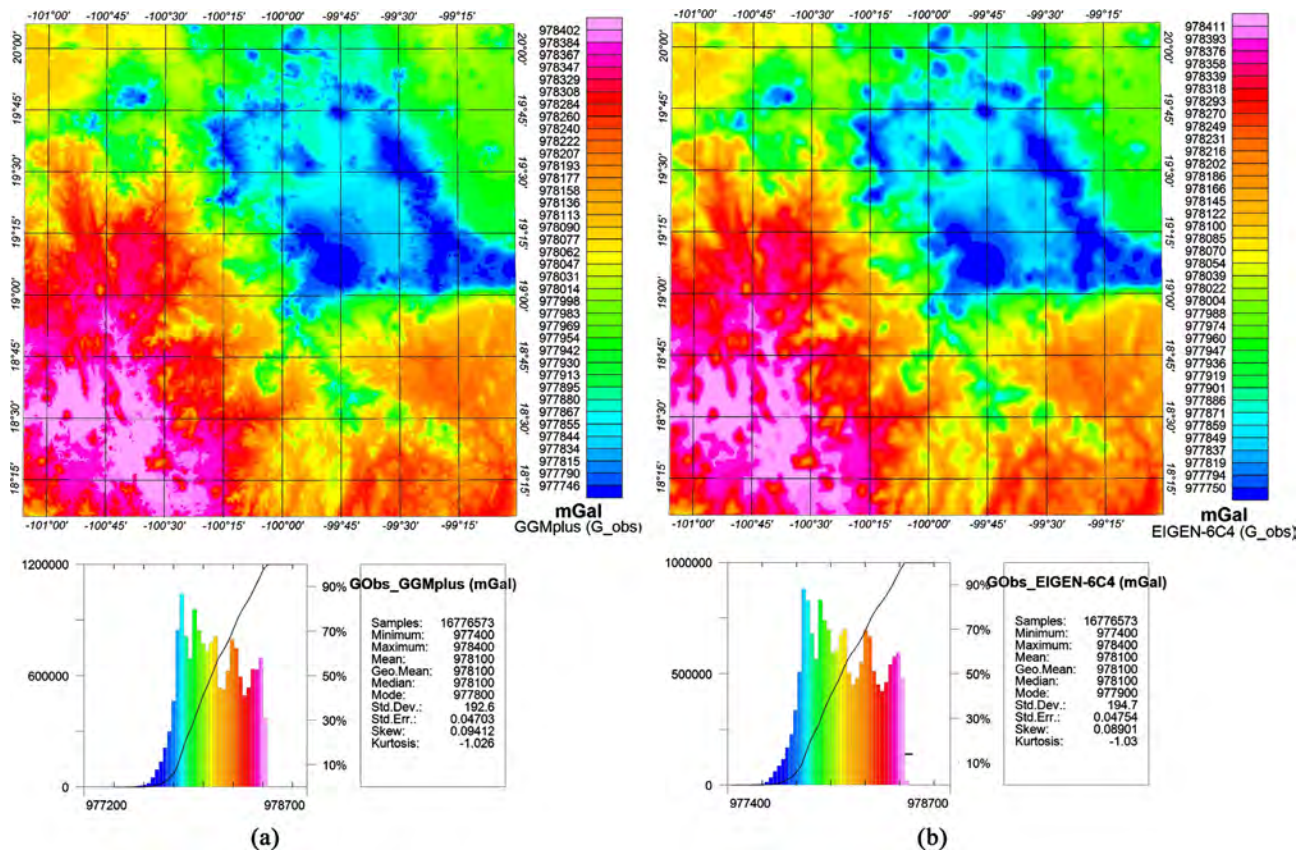


**Figure 3.** Comparison of  $G_{\text{obs}}$  between (a) GGMplus and, (b) EIGEN-6C4. Notice the great similarity between the gravity ranges in both maps.

### 3.3. Radial Power Spectrum

A comparison of the radial power spectrum of GGMplus and EIGEN-6C4 on a land region, shows additional differences between the depth sources of the anomalies as shown in **Figure 4**. And although it is not the purpose of this study to clarify the implications of these variations, this result shows that there is an important difference between them that must be considered when defining the objective of the study. This change occurs between the arrows of **Figure 4**, in the range of the spectrum 5 - 3.5 CYL/K\_unit, which is the range in these areas for structures of less than 10 km.

**Figure 5** Comparison between simple Bouguer anomalies of GGMplus and EIGEN-6C4 of the same land region, where no filters have been applied. Whilst the latter shows high-frequency variations, the former shows smooth regions. These differences affect 2D and 3D gravity models. This high-frequency variation has a low impact in the distribution of the histograms, with similar behavior, even though there is a greater content of high-frequencies in the GGMplus model.

## 4. Modelling

### 4.1. Inversions

Inversions corresponding to EIGEN-6C4 and GGMplus data sets are in the black

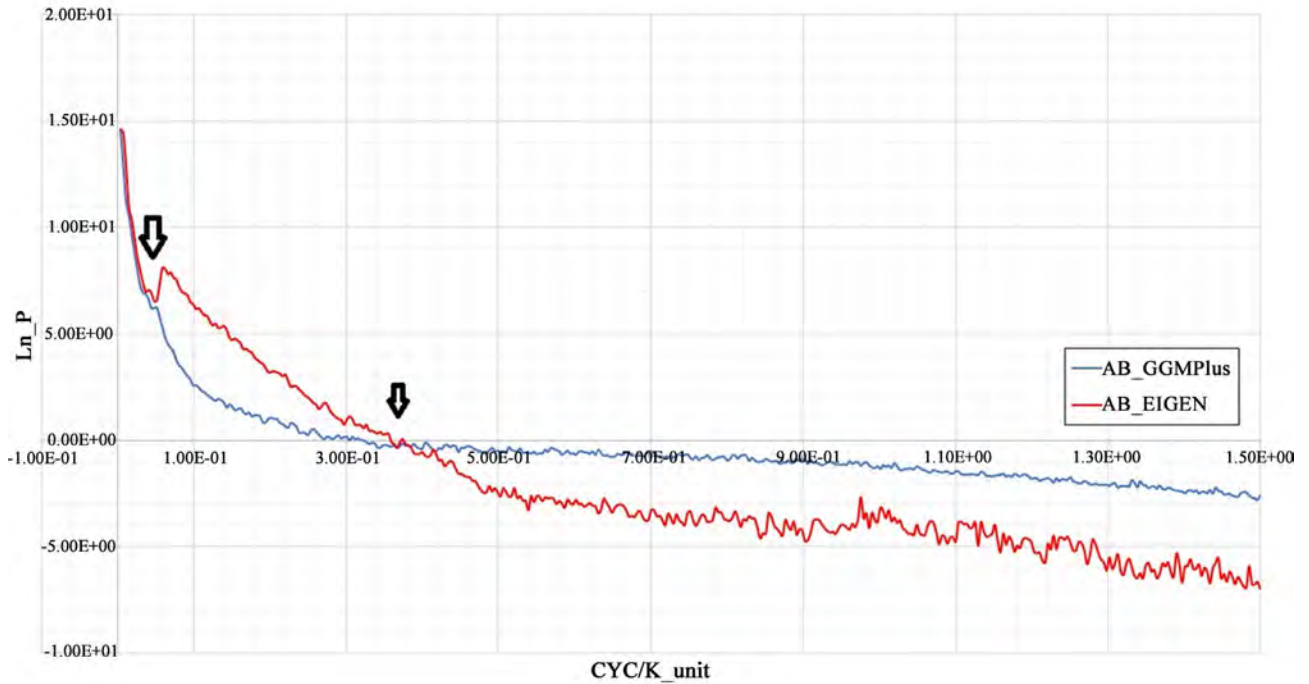


Figure 4. Power spectrum of GGMplus and EIGEN-6C4. The arrows indicate where the spectrum behavior changes for structures located shallower than 10 km.

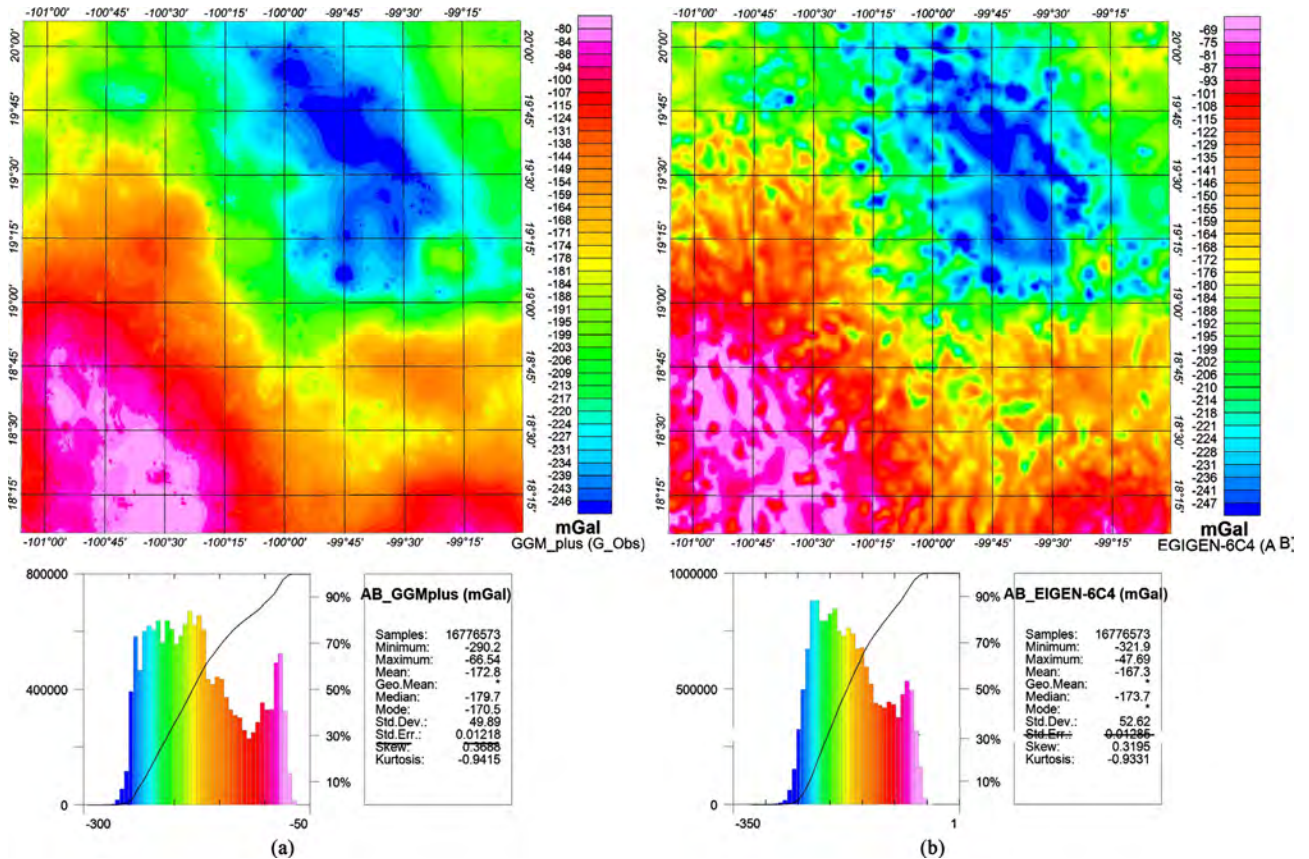
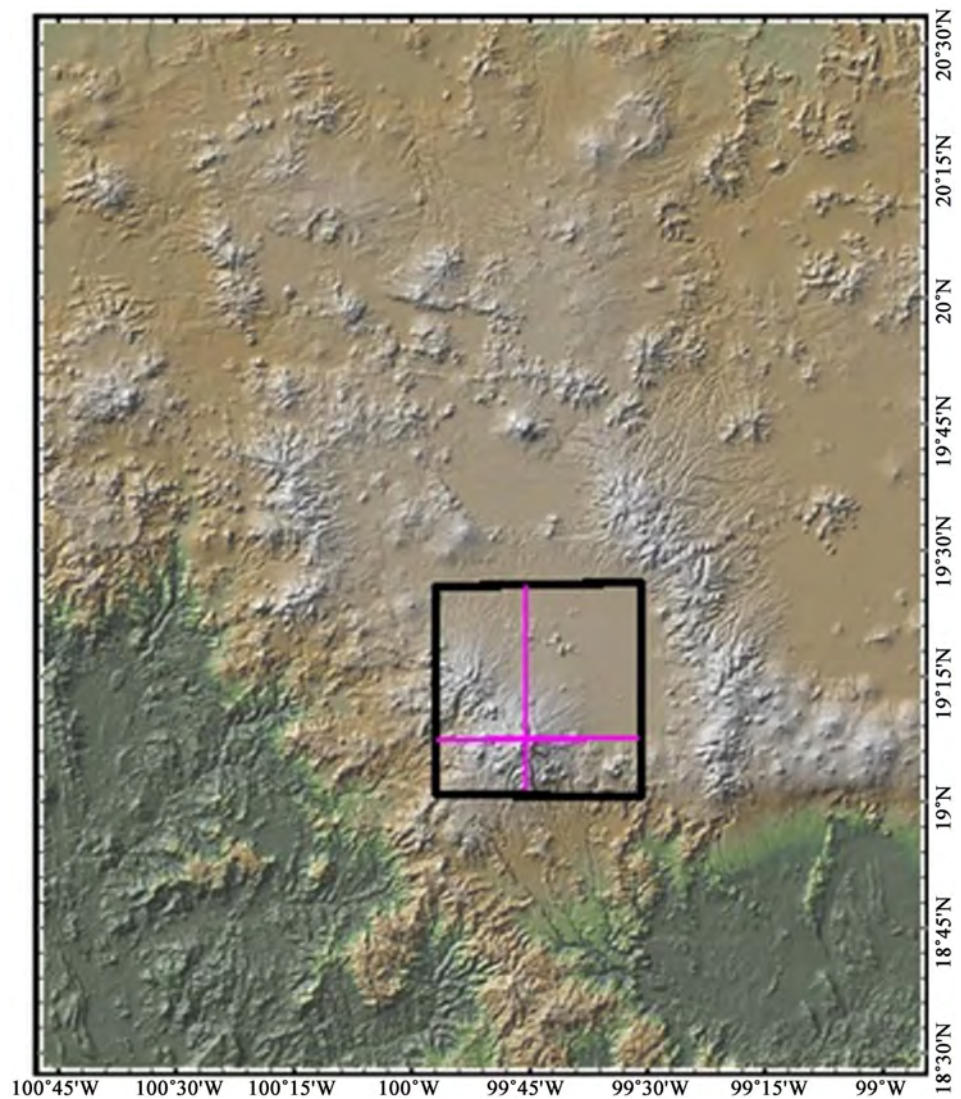


Figure 5. Comparison between simple Bouguer anomalies of GGMplus and EIGEN-6C4. The full anomaly range is comparable, the difference in standard deviation is 3 mGal, and the difference between their means is 5 mGal.



polygon of **Figure 6** and **Figure 7** are displayed in **Figure 8**. All inversion parameters were the same, with exception of the BA data sets; thus, differences observed are to be attributed to differences between those data sets. The inversion resolution is 1000 m. We use the region containing Nevado de Toluca volcano to exemplify the differences between the two data sets; it was chosen since it contains a variety of geologic structures [22] that help enhance the differences between them. The recent activity of this Quaternary volcano indicates that additional activity cannot be discarded [23]. Although the present study provides valuable insights about the structures in this volcanic area, it is not intended as a volcanic study.



**Figure 6.** Topography of the geographic area where 3D gravity inversions are performed. Nevado de Toluca volcano is located at  $99^{\circ}45'W$ ,  $19^{\circ}07'N$  and Sierra Las Cruces runs NW-SE along the NE side of the map. The black polygon represents the region where inversions are performed. The magenta lines correspond to the cross-sections of the inversions, to be presented below. Figure made with GeoMapApp ([www.geomapapp.org](http://www.geomapapp.org)) /CC BY/CC BY (Ryan *et al.*, 2009).

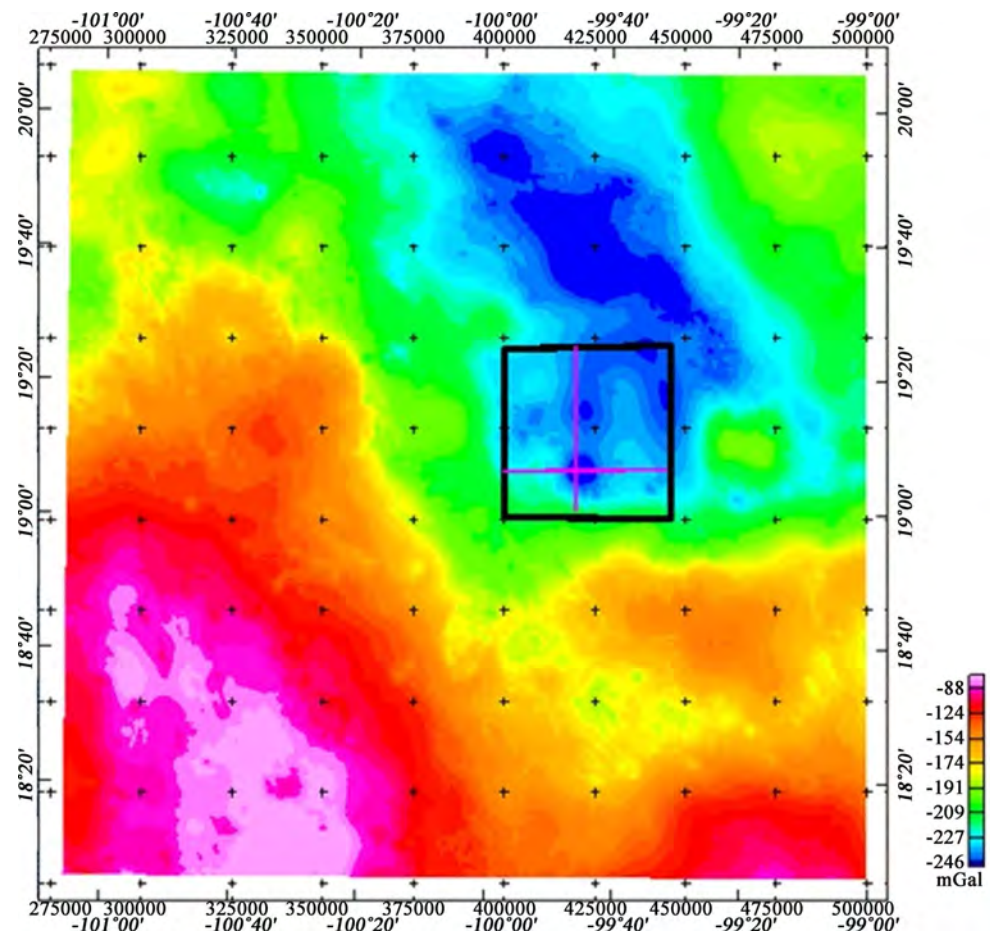


**Figure 7.** GGMplus Bouguer Anomaly map showing the region in which 3D inversions are performed (black polygon). Cross-sections are obtained from the respective inversions along lines N-S and E-W (magenta).

A preliminary assessment can be made considering the front sections along the X-axis (**Figure 8**). Both sections show two regions of higher densities (red); the higher definition of the section corresponding to GGMplus is quite clear. Whilst a diffuse red portion occupying about half of the EIGEN section is observed, the corresponding area in the GGMplus section shows the region divided in two, by a gap of material of lower density; that is, a diffuse region is substituted by a sharp boundary, made possible along the complete vertical range by the higher resolution of the GGMplus data set.

Another difference is appreciated in the surface distribution of density not shadowed by the displayed DEM. The EIGEN model shows rather uniform portions of green, whilst the GGMplus model shows a speckled surface with a distribution of cells with lower density values (blue).

Sections along the Y-axis of EIGEN-6C4 and GGMplus appear in **Figure 9**, where the greater resolution of the GGMplus inversion again shows important structural differences with respect to that of EIGEN-6C4. In the former, the low-density anomaly associated with Nevado de Toluca volcano, in the north portion of the section (red arrows), is continuous and of larger dimensions, whilst

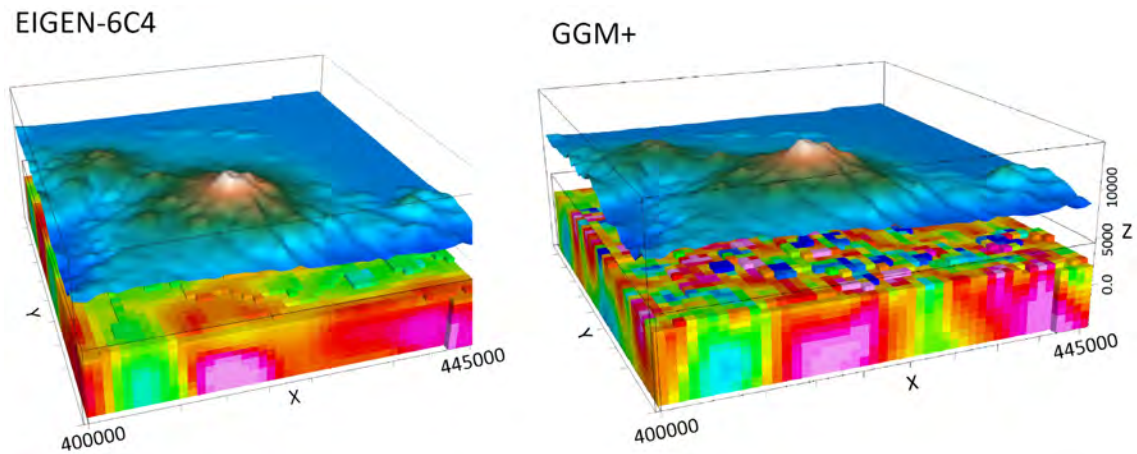


**Figure 8.** 3D inversions of the EIGEN-6C4 and GGMplus BA maps. The DEM used in the calculation is the same in both cases [24]. The voxel contains cells in the X and Y directions of 1 km, respectively; the Z-dimensions are variable, increasing in size downwards. The respective voxels have the same vertical extent:  $-1185$  to  $3340$  m, as well as the same cell distribution.

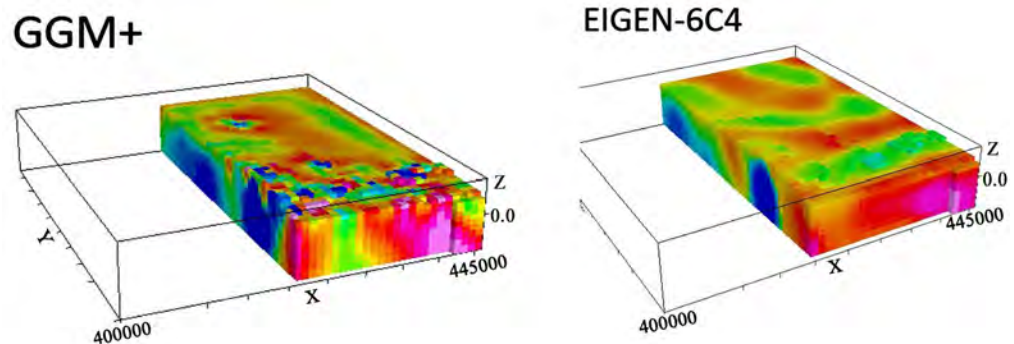


**Figure 9.** Same inversions as those in **Figure 8**, showing a section through Nevado de Toluca volcano (yellow arrows). To the N of the line, EIGEN-6C4 model displays a faint low (blue) at the bottom of the section, separated from a wider, shallower one to the north (red arrows). GGMplus shows instead a wide, continuous region of low densities not reaching the surface, associated with the same location. A much larger anomalous region of low density is observed to the south (yellow arrows) corresponding to NT volcano. Regarding the low-density anomaly at the volcano surface EIGEN-6C4 shows an elliptic anomaly, whereas GGMplus shows a divided upper portion and more detail in the anomaly reaching the surface. The inversion is performed at 1000 m resolution.

in the latter it appears of smaller size and fragmented. In the south portion of the sections appears an unexpected, low-density anomaly of large dimensions (yellow arrows); we shall discuss the volcanic implications of this anomaly elsewhere. In this study, we will only compare its manifestations in the two cases under comparison. The EIGEN-6C4 section shows the anomaly as an ellipse, whilst the GGMplus section shows a wider anomaly, divided in the surface by a higher density region.

#### 4.2. Cross-Sections

To inspect in more detail the results of the inversions, we compare cross-sections along lines N-S and E-W of **Figure 7**; the N-S line intersects the edifice of

Nevado de Toluca volcano [22]; the EIGEN-6C4 cross-section (**Figure 10**) shows a single negative anomaly in the southern portion of the section; the center of this negative anomaly is located at  $-2000$  m approximately, corresponding to NT volcano. On the north side, a deeper anomaly of higher density than that observed under the volcano appears with its center at approximately  $-3000$  m; it may correspond to intruded material.

The cross-section corresponding to GGMplus exhibits important differences. The volcano anomaly shows its center closer to the surface by almost 2 km (*i.e.*, at sea level) and a high-density gradient underneath the center; this may have important implications for the location of a magma chamber. The verticality of the anomaly is modified to a south-dipping anomaly. In addition, a bifurcation is observed, divided by a small, higher-density region in the surface, in agreement with the observation made in **Figure 9**. The elongated anomaly to the north has now been displaced southwardly and its center is shallower. The northernmost density-low diminished its value, although the region maintains its general shape.

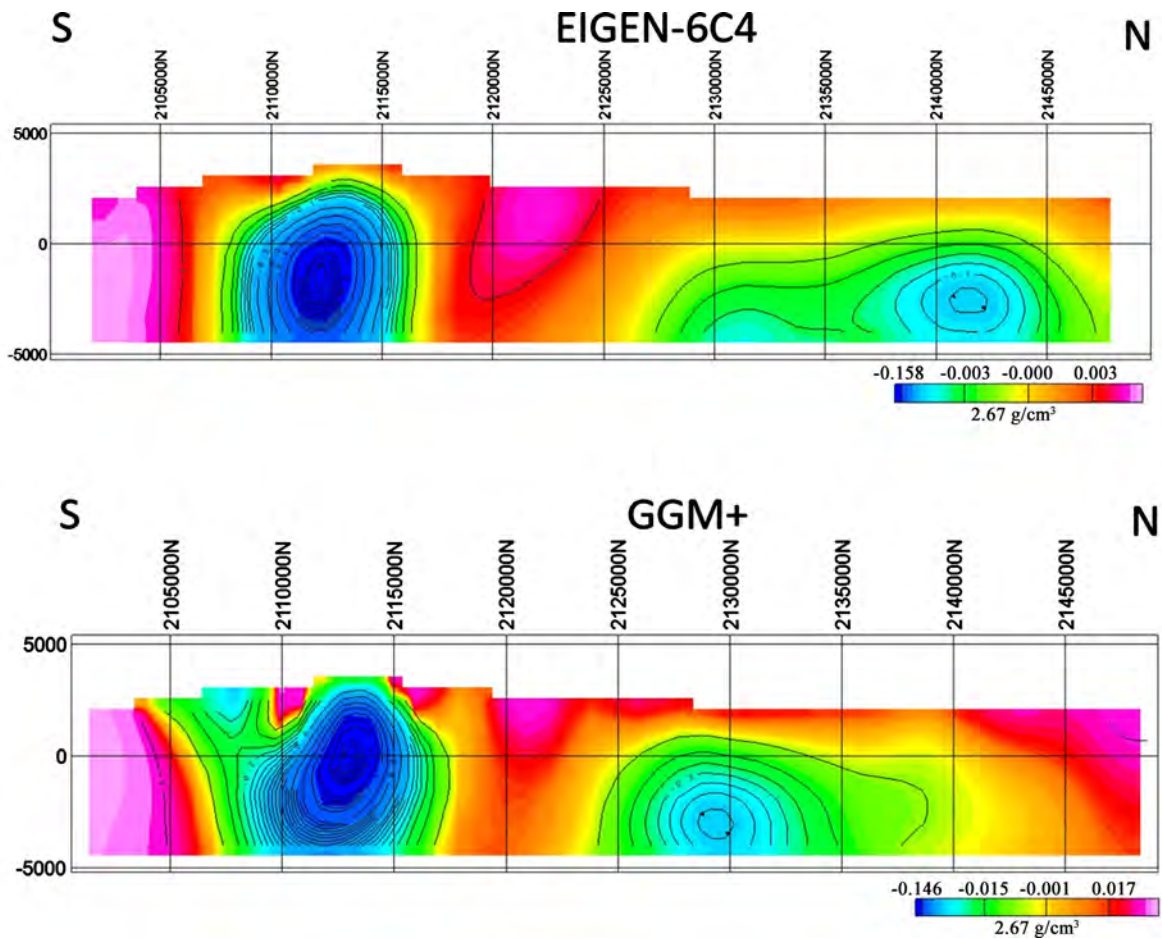


**Figure 10.** Cross-sections extracted from the voxels corresponding to EIGEN-6C4 and GGMplus along line N-S in **Figure 7**. Contours enhance the differences between the two sections. The vertical axis ranges from 5000 to  $-5000$  m. Notice that the averaged topographic profiles are the same in both cross-sections, and so are the voxel characteristics in the vertical direction. The inversion resolution is 1000 m. The coordinates are UTM northings.

Cross-sections corresponding to line E-W appear in **Figure 11**, they are perpendicular to line N-S and go across the structure of Nevado de Toluca volcano. The EIGEN-6C4 section presents a low-density anomaly at the center, corresponding to the position of the volcanic structure. The result is similar to that obtained for the N-S section above. Together they suggest that the volcanic anomaly has the shape of a conus, with a rounded apex on top, and its center at  $-2$  km. The section corresponding to GGMplus shows instead a more compact structure, with a division at the top of the low-density anomaly, like the one observed in the N-S section. The differences observed on the flanking portions of the low-density anomaly are more drastic than those observed in the N-S section, tending to emphasize the presence of finer geologic structures.

## 5. Discussion

### 5.1 Importance of DEM

In the use of the gravity satellite model, the correct choice of the DEM allows to

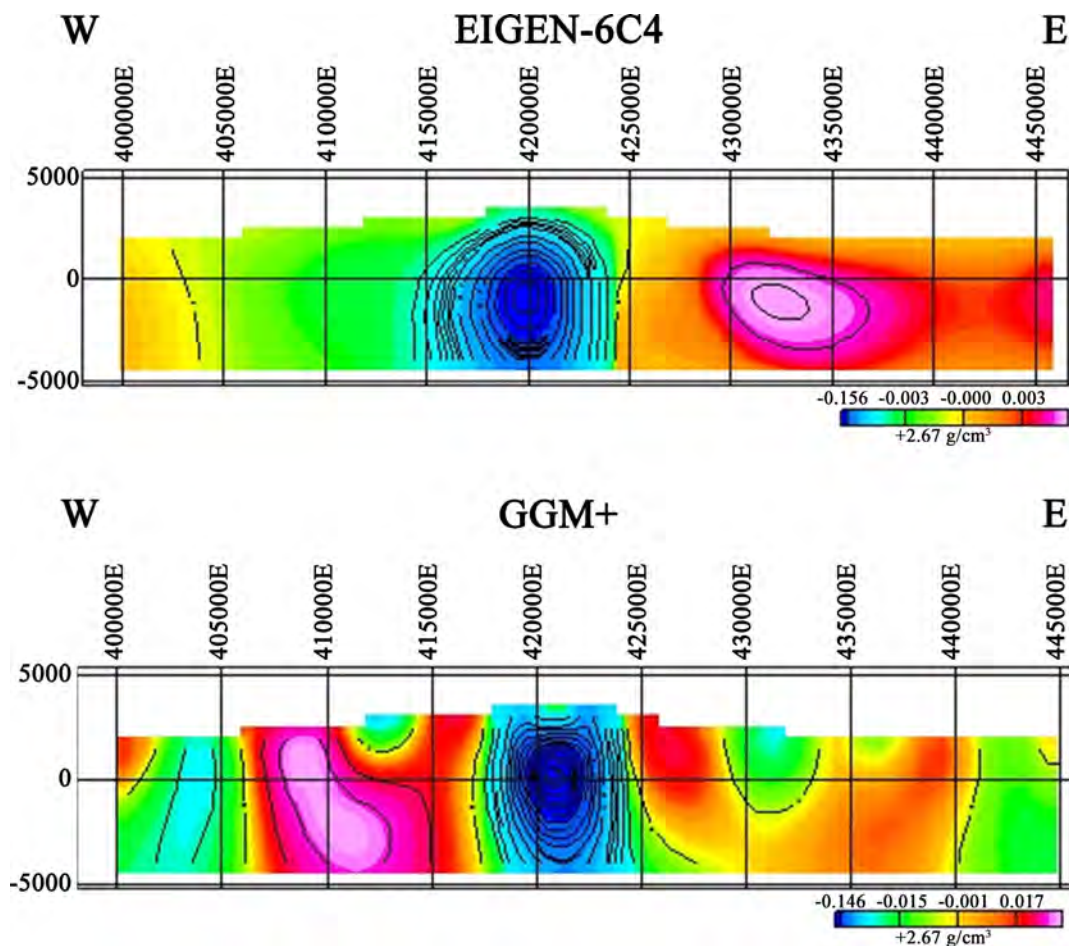


**Figure 11.** Cross-sections extracted from the voxels corresponding to EIGEN-6C4 and GGMplus along line E-W (**Figure 7**). The central, low-density anomaly corresponds to the location of Nevado de Toluca. Contours enhance the differences between the two sections. Notice that the averaged topographic profiles are the same in both cross-sections, and so are the voxel characteristics in the vertical direction.

get the most out of the data. For example, the ideal case is to use a DEM that has the same spatial resolution as the gravimetric model. **Figure 12** shows a comparison between simple Bouguer anomalies of GGMplus with DEM 7.5 arc-sec (the same resolution of model GGMplus), and simple Bouguer anomalies of GGMplus with DEM 15 arc-sec (half the resolution of model GGMplus). The full anomaly range is comparable, and the statistical data is very close, nonetheless the anomaly is slightly distorted, a small distortion difficult to appreciate which blurs the focus of the anomalies without changing its behavior.

In the use of the gravity satellite model, the correct choice of the DEM allows to get the most out of the data. For example, the ideal case is to use a DEM that has the same spatial resolution as the gravimetric model. In **Figure 13** show how comparison between simple Bouguer anomalies of EIGEN-6C4 model with DEM with the same resolution of model, and simple Bouguer anomalies of EIGEN-6C4 model with DEM with 15 arc-sec (the double resolution of model). The full anomaly range is comparable, and the statistical data is very close, nonetheless the anomaly presented a high frequency noise, because when using a higher resolution DEM, the C<sub>alt</sub> and CB corrections are sampled at twice the resolution of the gravimetric model. Although these discrepancies can be corrected with filters that remove high frequencies.

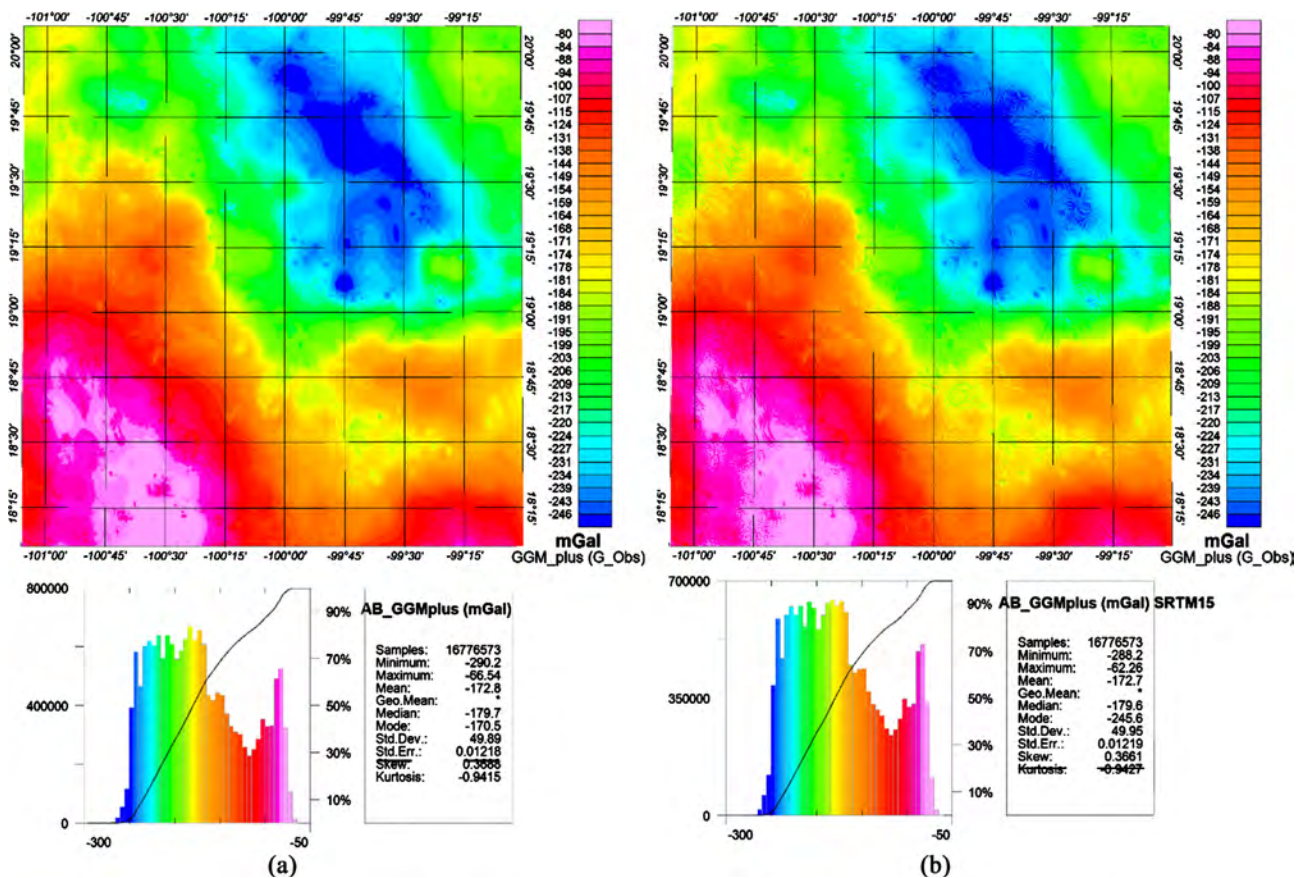


**Figure 12.** Comparison between simple Bouguer anomalies of the model GGMplus processed with two DEM: in case (a) with 7.5 arc-sec (220 m) resolution; in case (b) with a 15 arc-sec (450 m) resolution.

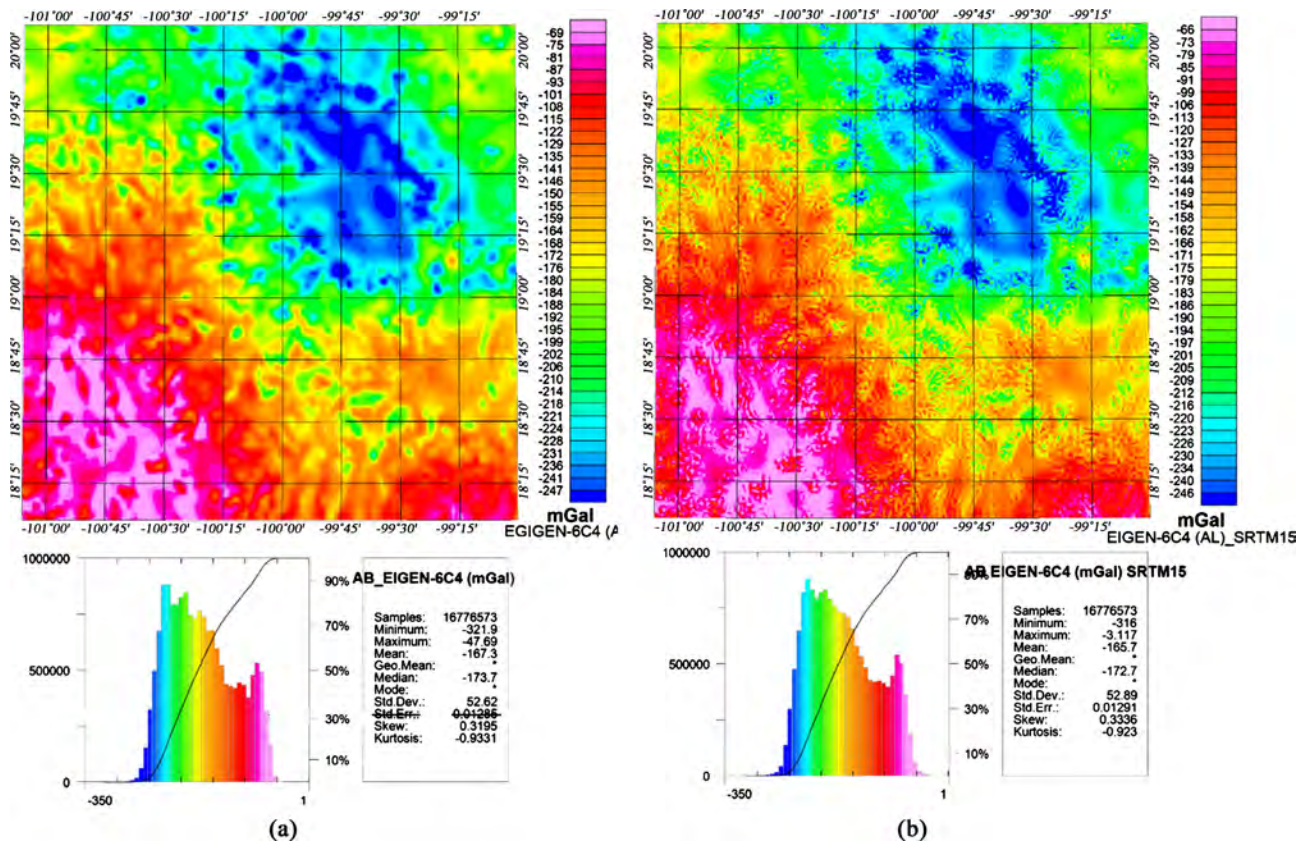


**Figure 13.** Comparison between simple Bouguer anomalies of the model EIGEN-6C4 processed with two DEMs: (a) with a 60 arc-sec (1 km; ETOPO1) resolution; (b) with a 15 arc-sec (450 m; SRTM15) resolution.

## 5.2. Comparison

A brief discussion of the BA in **Figure 7** helps explain some of the observations made regarding the cross-sections. We first note that the shape of the BA in the vicinity of Nevado de Toluca volcano has a horseshoe shape; Nevado de Toluca and an adjacent anomaly to the N, are in its western branch. Although the main traits are maintained between the two cross-sections under comparison (**Figure 10** and **Figure 11**), the anomalies are more sharply exposed by GGMplus. The BA map in **Figure 7** shows a low-density anomaly on the eastern portion of the E-W line; the cross-section of EIGEN-6C4 in **Figure 11** shows only a small decrement of the prevailing positive anomaly, the GGMplus more precisely reflects the low-density region, showing a clearly defined negative region. Additional differences are evident on the west end of the line; a strong difference is observed between the single anomaly on the EIGEN-6C4 with its center at  $-2000$  m, and an anomaly of a quite different shape in the GGMplus, where the surface is divided into two low-density anomalies, with density increasing with depth.

We selected a region in which geologic differences are present, expecting that they would be reflected in the rock-density variations associated with the intervening geologic sources. We selected a voxel for the inversion with cells of 1 km on the side. The results obtained belong to this spatial resolution; they can be increased or diminished varying those dimensions. We would expect that the

larger the cell dimensions the smaller the differences between the 3D inversions with the BA of both data sets. If cell dimensions are diminished, the better resolution of GGMplus is expected to yield more accurate results.

## 6. Conclusions

After evaluation of the frequency histograms, the Free Air anomalies, the radial power spectrum, and the simple Bouguer anomalies of the EIGEN-6C4 and GGMplus data sets, we concluded that the latter has a better spatial resolution. We infer that for wavelengths of 5 - 3.5 CYL/K\_unit, the former can produce better results with respect to the location of the deep sources of the gravitational field, while the GGMplus model could represent better results for shallower sources. The effects on models built from 3D inversions were evaluated under conditions of complete equality, except for the BA for each data set. The GGMplus model indicated that its resolution advantages are maintained in the modeling process.

The GGMplus model indisputably demonstrated that it achieves a higher spectral resolution in shallow cortical elements, which is reflected in a better identification of local elements. In addition, it is observed that it maintains the regional tectonic trends presented by the EIGEN-6C4 model, which makes it ideal for regional and local gravimetric studies. The biggest problem with the GGMplus model is still its limited coverage, since it only presents data up to 10 km from the coastline, which is why it is suggested to be combined with the EIGEN-6C4 model for study areas that include marine regions.

The use of DEMs with a higher sampling resolution than the resolution of the gravimetric model, allows the overestimation of AB of the model to be reduced by a fraction. However, they generate a random and chaotic high-frequency noise pattern, for this reason their use is discouraged, although it can be corrected using band-pass filters. The use of DEMs of lower resolution than the gravimetric model is discouraged since it generates blurring of the anomalies.

A comparison of the radial power spectrum of GGMplus and EIGEN-6C4, on a land region, shows additional differences between the depth sources of the anomalies; the difference is particularly relevant for the depth sources between approximately 15 and 1 km. This change between spectra is of interest in studies that try to model the depths of sources according to the power spectrum radial average method [25]; for this reason, we suggest the GGMplus model for shallow structures and the EIGEN-6C4 for deep structures.

## Acknowledgements

During development of this work, MC received support from Consejo Nacional de Ciencia y Tecnología (CONACYT, México. This study has been supported by IIMAS, UNAM; we acknowledge material support from both institutions. Comments of one anonymous reviewer helped improve the original manuscript. This research did not receive any specific grant from funding agencies in the public,



commercial, or not-for-profit sectors.

## Conflicts of Interest

The authors declare no conflicts of interest regarding the publication of this paper.

## References

- [1] Smith, W.H.F. and Sandwell, D.T. (1997) Global Sea Floor Topography from Satellite Altimetry and Ship Depth Soundings. *Science*, **277**, 1956-1962. <https://doi.org/10.1126/science.277.5334.1956>
- [2] Becker, J.J., Sandwell, D.T., Smith, W.H.F. and Braud, J. (2009) Global Bathymetry and Elevation Data at 30 Arc Seconds Resolution : Global Bathymetry and Elevation Data at 30 Arc Seconds Resolution: SRTM30\_PLUS. *Marine Geodesy*, **32**, 355-371. <https://doi.org/10.1080/01490410903297766>
- [3] Sandwell, D.T. and Smith, W.H.F. (2009) Global Marine Gravity from Retracked Geosat and ERS-1 Altimetry: Ridge Segmentation versus Spreading Rate. *Journal of Geophysical Research: Solid Earth*, **114**, 1-18. <https://doi.org/10.1029/2008JB006008>
- [4] Sandwell, D., Garcia, E., Soofi, K., Wessel, P., Chandler, M. and Smith, W.H.F. (2013) Toward 1-mGal Accuracy in Global Marine Gravity from CryoSat-2, Envisat, and Jason-1. *Leading Edge*, **32**, 892-899. <https://doi.org/10.1190/le32080892.1>
- [5] Sandwell, D.T., Müller, R.D., Smith, W.H.F., Garcia, E. and Francis, R. (2014) New Global Marine Gravity Model from CryoSat-2 and Jason-1 Reveals Buried Tectonic Structure. *Science*, **346**, 65-67. <https://doi.org/10.1126/science.1258213>
- [6] Ince, E.S., Barthelmes, F., Reißland, S., Elger, K., Förste, C., Flechtner, F. and Schuh, H. (2019) ICGEM—15 Years of Successful Collection and Distribution of Global Gravitational Models, Associated Services, and Future Plans. *Earth System Science Data*, **11**, 647-674. <https://doi.org/10.5194/essd-11-647-2019>
- [7] Pavlis, N.K., Holmes, S.A., Kenyon, S.C. and Factor, J.K. (2012) The Development and Evaluation of the Earth Gravitational Model 2008 (EGM2008). *Journal of Geophysical Research: Solid Earth*, **117**, 1-38. <https://doi.org/10.1029/2011JB008916>
- [8] Hirt, C., Claessens, S., Fecher, T., Kuhn, M., Pail, R. and Rexer, M. (2013) New Ultrahigh-Resolution Picture of Earth's Gravity Field. *Geophysical Research Letters*, **40**, 4279-4283. <https://doi.org/10.1002/grl.50838>
- [9] Tozer, B., Sandwell, D.T., Smith, W.H.F., Olson, C., Beale, J.R. and Wessel, P. (2019) Global Bathymetry and Topography at 15 Arc Sec: SRTM15+. *Earth and Space Science*, **6**, 1847-1864. <https://doi.org/10.1029/2019EA000658>
- [10] Jarvis, A., Reuter, H.I., Nelson, A., and Guevara, E. (2008) Hole-Filled SRTM for the Globe Version 4. CGIAR-CSI SRTM 90m Database. <http://srtm.csi.cgiar.org/>
- [11] Telford, W.M., Geldart, L.P. and Sheriff, R.E. (1991) Applied Geophysics. 2nd Edition, Cambridge University Press, Cambridge. [https://doi.org/10.1016/0031-9201\(91\)90163-C](https://doi.org/10.1016/0031-9201(91)90163-C)
- [12] Milsom, J. (2003) Magnetic Methods. *Field Geophysics: The Geological Field Guide Series (Issue C)*, John Wiley & Sons, Chichester, 51-67.
- [13] Götze, H.J. and Li, X. (1996) Topography and Geoid Effects on Gravity Anomalies in Mountainous Areas as Inferred from the Gravity Field of the Central Andes. *Physics and Chemistry of the Earth*, **21**, 295-297.

- [https://doi.org/10.1016/S0079-1946\(97\)00051-7](https://doi.org/10.1016/S0079-1946(97)00051-7)
- [14] Camacho, M. and Alvarez, R. (2020) Gravimetric Analysis of the Rifts and Volcanic Fields of the Jalisco Block, Mexico. *Tectonophysics*, **791**, Article ID: 228577. <https://doi.org/10.1016/j.tecto.2020.228577>
- [15] Hildenbrand, T.G., Briesacher, A., Flanagan, G. and Hinze, W.J. (2002) Rationale and Operational Plan to Upgrade the U.S. Gravity Database. USGS Open File Report, 12 p. <https://doi.org/10.3133/ofr02463>
- [16] Macleod, I.N. and Ellis, R.G. (2013) Magnetic Vector Inversion, a Simple Approach to the Challenge of Varying Direction of Rock Magnetization. 2013 *Australian Society of Exploration Geophysicists, Petroleum Exploration Society of Australia (ASEG-PESA) 23rd International Geophysical Conference and Exhibition*, Melbourne, 11-14 August 2013, 6 p. <https://doi.org/10.1071/PVv2012n159news>
- [17] Ellis, R.G., de Wet, B. and Macleod, I.N. (2012) Inversion of Magnetic Data from Remnant and Induced Sources. 2012 *Australian Society of Exploration Geophysicists (ASEG) 22nd International Geophysical Conference and Exhibition*, Brisbane, 26-29 February 2012, 4 p.
- [18] Ingram, D.M., Causon, D.M. and Mingham, C.G. (2003) Developments in Cartesian Cut Cell Methods. *Mathematics and Computers in Simulation*, **61**, 561-572. [https://doi.org/10.1016/S0378-4754\(02\)00107-6](https://doi.org/10.1016/S0378-4754(02)00107-6)
- [19] Alvarez, R. and Yutsis, V. (2015) Southward Migration of Magmatic Activity in the Colima Volcanic Complex, Mexico: An Ongoing Process. *International Journal of Geosciences*, **6**, 1077-1099. <https://doi.org/10.4236/ijg.2015.69085>
- [20] Alvarez, R. (2017) Mapping Geologic Interfaces that May Alter Seismic Wave Propagation in the Mexico City Basin. *Geofísica Internacional*, **56**, 37-56. <https://doi.org/10.22201/igeof.00167169p.2017.56.1.1733>
- [21] Guevara, R., Yutsis, V., Varley, N., Almaguer, J., Calderón-Moctezuma, A. and Guevara-Mansilla, O. (2021) Geophysical Determination of the Jalisco and Michoacán Blocks Boundary along the Colima Graben. *Journal of South American Earth Sciences*, **109**, Article ID: 103208. <https://doi.org/10.1016/j.jsames.2021.103208>
- [22] García-Palomo, A., Macías, J.L., Arce, J.L., Capra, L., Garduño, V.H. and Espindola, J.M. (2002) Geology of Nevado de Toluca Volcano and Surrounding Areas, Central Mexico. Geological Society of America: Map and Chart Series MCH089.
- [23] Martínez-Serrano, R.G., Schaaf, P., Solís-Pichardo, G., Hernández-Bernal, M.S., Hernández-Treviño, T., Morales-Contreras, J.J. and Macías, J.L. (2004) Sr, Nd and Pb Isotope and Geochemical Data from the Quaternary Nevado de Toluca Volcano, a Source of Recent Adakitic Magmatism, and the Tenango Volcanic Field, Mexico. *Journal of Volcanology and Geothermal Research*, **138**, 77-110. <https://doi.org/10.1016/j.jvolgeores.2004.06.007>
- [24] Ryan, W.B.F., Carbotte, S.M., Coplan, J., O'Hara, S., Melkonian, A., Arko, R., Weiszel, R.A., Ferrini, V., Goodwillie, A., Nitsche, F., Bonczkowski, J. and Zemsky, R. (2009) Global Multi-Resolution Topography (GMRT) Synthesis Data Set. *Geochimistry Geophysics Geosystems*, **10**, Article ID: Q03014.
- [25] Spector, A. and Grant, F.S. (1970) Statistical Models for Interpreting Aeromagnetic Data. *Geophysics*, **35**, 293-302. <https://doi.org/10.1190/1.1440092>

*Capítulo 2: Delineation of the Boundaries of San Blas Basin, Mexico,  
Merging Gravity, Magnetic, and Seismic Data.*



# Delineation of the boundaries of San Blas basin, Mexico, merging gravity, magnetic, and seismic data

M. Camacho-Ascanio<sup>a,\*</sup>, R. Alvarez<sup>b</sup>

<sup>a</sup> Posgrado en Ciencias de La Tierra, Instituto de Geofísica, Universidad Nacional Autónoma de México, Cuauhtémoc, 06900, CDMX, Mexico

<sup>b</sup> Instituto de Investigaciones en Matemáticas Aplicadas y en Sistemas (IIMAS), Universidad Nacional Autónoma de México, Mexico

## ARTICLE INFO

### Keywords:

San blas basin  
Satellite model date  
Satellite gravity data  
3D inversions  
High-resolution gravity  
Gravimetry

## ABSTRACT

The San Blas Basin (SBB) is located within what is referred to as the Mazatlán Basin, in the offshore west of Mexico. The SBB is positioned in the southern part of the Mazatlán Basin, within a region that remains poorly understood. Specifically, details about its shape and size are currently unknown, and only a few studies have provided some understanding of its limits. To ascertain the extent of the SBB and define its boundaries, we employed satellite-derived gravity and magnetic models, along with analyses linked to these fields. We established structural continuity through spectral analyses of gravimetric and magnetic data and the interpretation of various published seismic profiles in the near area. We also applied various filtering techniques, including the removal of regional trends and the regional Gaussian filter. Some anomalies of the potential fields are repeatedly reproduced in the different processed maps. These features allow for a comprehensive geophysical interpretation of the area under consideration, which leads to the proposal of the boundaries of the SBB. Additionally, 3D inversions of gravimetric and magnetic data were carried out in the study area. From these data, a more detailed response was observed in the 3D gravimetry than in the 3D magnetometry. In the former, it was possible to characterize a series of high-density and low-density bodies that were arranged in defined orientations, which were associated with the migration processes of Baja California from its position 30 Ma to its current position. A pattern of progressive evolution of the basin is given, from 30 Ma to the Present.

## 1. Introduction

Baja California (BC) was to the North American continent approximately 30 million years ago when a series of tectonic processes began to cause it to drift to its current position (Ferrari et al., 2013). This drifting process had significant consequences for the border area with the North American continent in the region known as the Mazatlán basin. Within this area, the San Blas Basin (SBB) stands out. The SBB is the largest basin in the southeastern sector of the Gulf of California, and it is submerged at an average depth of 500 m on the North American continental shelf. However, it remains a poorly explored basin, where its boundaries and geometry have not been well defined.

Today, the tectonic situation of the SBB is quite complex. As seen in Fig. 1, the SBB is situated at the W border of the North American Plate, in an area where the Rivera Plate meets the North American Plate, but according to the chron record (DeMets and Traylen, 2000) and the seismicity in the area (Madrigo et al., 2021), subduction of the Rivera Plate has not yet begun under SBB. Moreover, this location is affected by

the end of the Mesoamerican trench and is somehow controlled by the Tamayo and Pescadero fault systems. Additionally, the E edge along the Jalisco Block and the nature of their interaction are not precisely known. According to Ferrari et al. (2018), the SBB may have been an early extensional basin formed during the development of the Gulf of California Extensional Province between approximately 19 and 16 Ma.

### 1.1. Tectonic evolution of the SBB and the Gulf of California

The tectonic history of the SBB is closely linked to the tectonic evolution of Baja California and the Gulf of California. The SBB is situated in the vicinity a plate boundary that has undergone significant volcanic activity, subduction processes, extension processes of the crust, and transtensive processes over the last 100 Ma (e.g.: Karig and Jensky, 1972; Moore, 1973; Gastil et al., 1979; Stock and Hodges, 1989; Ferrari et al., 2013; Ortega-Gutiérrez et al., 2014; Duque-Trujillo et al., 2015; Ferrari et al., 2018).

At the end of the 1980s, Stock and Hodges (1989) proposed a

\* Corresponding author.

E-mail addresses: [miguelcamacho.geofisico@comunidad.unam.mx](mailto:miguelcamacho.geofisico@comunidad.unam.mx) (M. Camacho-Ascanio), [roman.alvarez@iimas.unam.mx](mailto:roman.alvarez@iimas.unam.mx) (R. Alvarez).

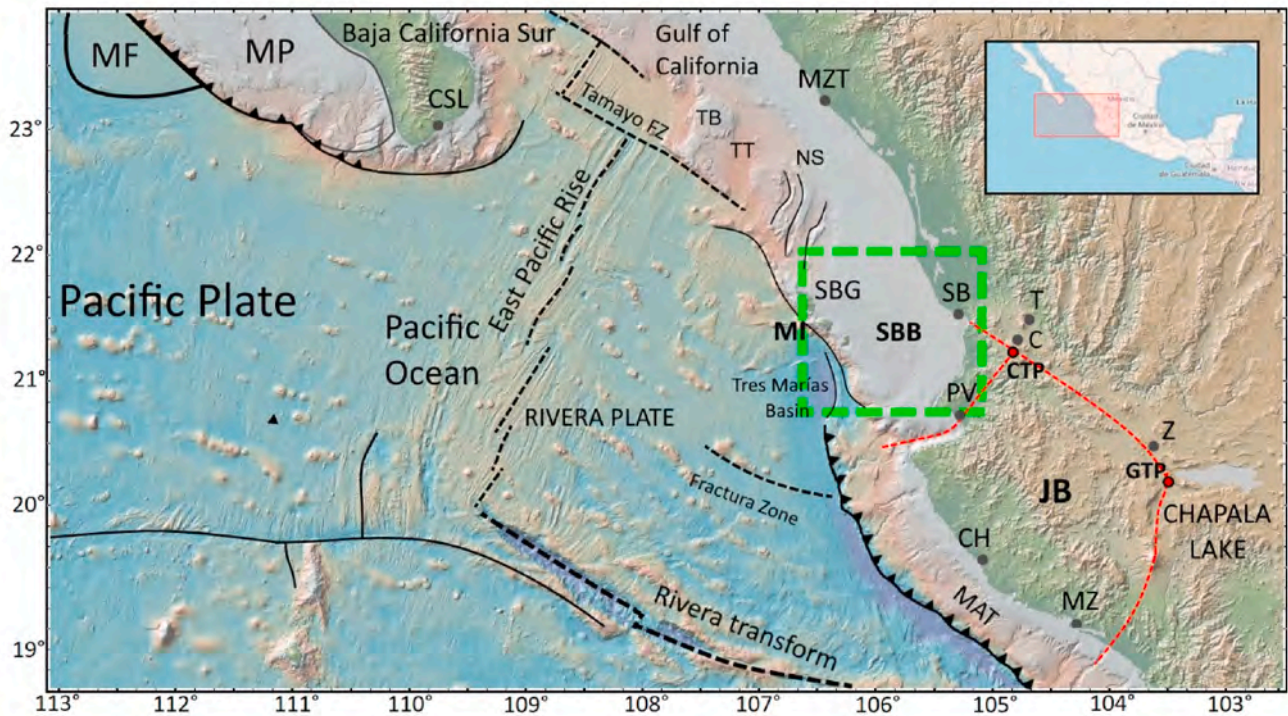


**Fig. 1.** Tectonic setting of the SBB, including the boundaries of the Rivera plate and a portion of the known boundaries of the SBB (represented by a green square). In the small upper box, the position of the map on the map of Mexico is observed. It was created using the GeoMapApp vs3.7.0 program and edited with Paint.net software. CTP: Compostela triple point. JB: Jalisco Block. GTP: Guadalajara triple point. The boundaries of the Jalisco block are represented by red lines (adapted from Camacho and Alvarez, 2020). NS: Nayarit Scarp. MI: Marias Island's. TB: Tamayo Bank. TT: Tamayo Trough. MP: Magdalena Platform. MF: Magdalena Fan. SBG: San Blas Gorge. The oceanic structures were adapted from DeMets and Traylen (2000) and Fletcher et al. (2007). The black dots represent the principal cities; C: Compostela. CSL: Cabo San Lucas. CH: Chamela. MZ: Manzanillo. PV: Puerto Vallarta. MZT: Mazatlán. SB: San Blas. T: Tepic. Z: Zacoalco.

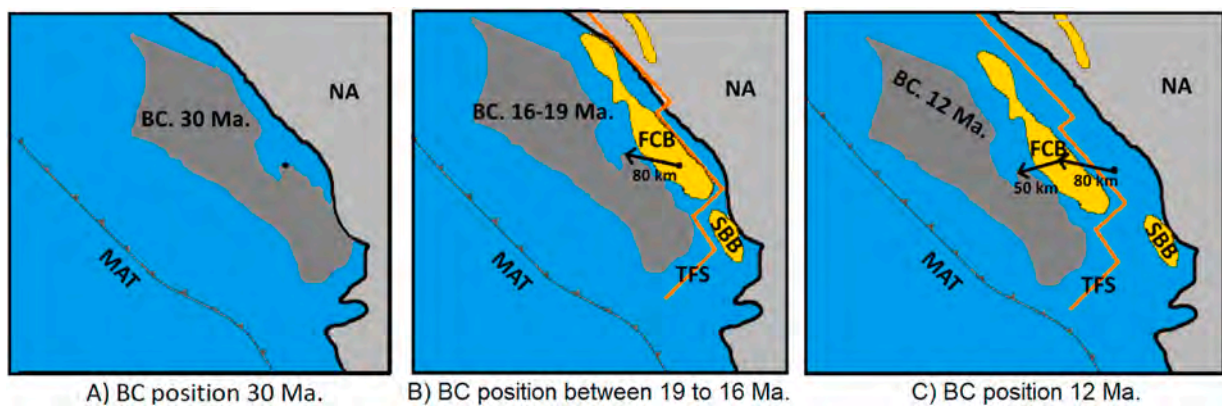


**Fig. 2.** Tectonic model of the opening of the Gulf of California, reconstruction from Ferrari et al. (2013, 2018). In dark gray, the lower portion of Baja California (BC) is observed, the orange line is the Tamayo Fault System (TFS), and the plate boundaries are generated by the separation of Baja California. In yellow, are the extensional basement areas that will become the Foca-Cerralvo Basin (FCB) and SBB.

two-stage model that would become the most influential work in the region for many years. Their model was based on the proposed interpretation of the fault system of the Tosco-Abrejos, including well logs, interpreted by Yeats and Haq (1981), and on the lack of stratigraphic units that record a substantial extension before 6 Ma. Later, the team of Fletcher et al. (2007) conducted a study to date and locate the detrital zircons of the Magdalena fan. It was previously thought that the fan material must have come from the mouth of the Gulf and was deposited there at the beginning of the rifting movement. However, the composition and dating analysis in their study shows that the source of this debris is probably from a closer source than originally thought, specifically on the Magdalena platform and to the northwest of Los Cabos

(from the Magdalena depositional fan). Thus, Fletcher et al. (2007) realized that the debris came from a nearby source, which contradicted the model proposed by Stock and Hodges (1989); they considered that for the debris to come from such a relatively close location, the movement along the Tosco-Abrejos system could not have been significant, and the occurrence must have taken place to the east of Baja California, from the beginning. Consequently, Fletcher et al. (2007) proposed a new model in which a significant portion of the lateral movement occurred inside the Gulf of California instead of throughout the Tosco-Abrejos system.

The group of Ferrari et al. (2013) proposed that the extension of Baja California began 30 Ma (Fig. 2A). It began from a position farther from

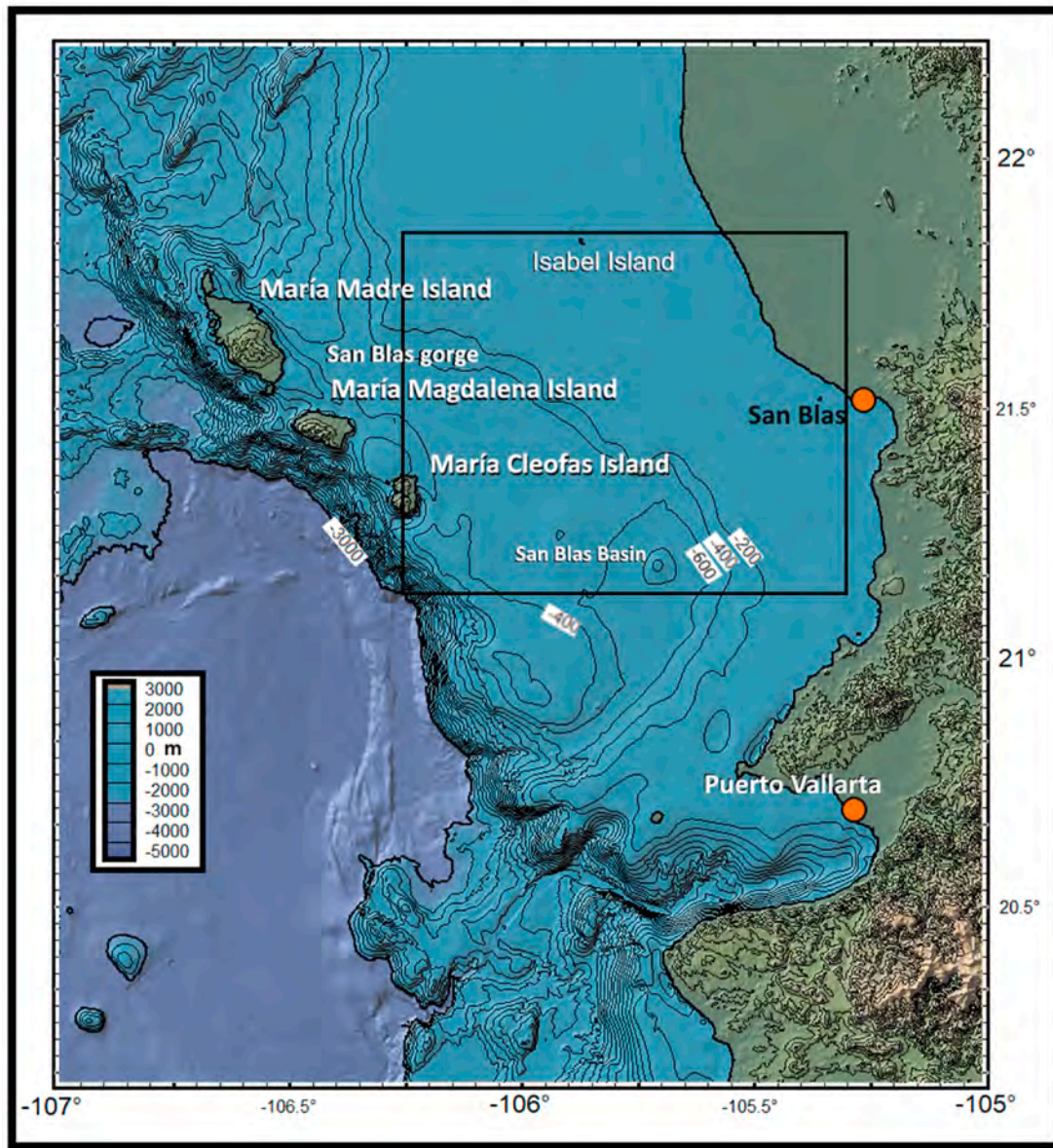


Fig. 3. Map of topography/bathymetry of the SBB. Contour interval 150 m. The color scale is in meters. In the black square the zone of the 3D gravimetric and magnetic inversions. The bathymetry data used is from SRTM15 (Tozer et al., 2019).

that shown to the south, located next to the American continent, and bordering the Jalisco Block. In that initial stage, from 30 to 18 Ma, they suggest that it moved about 85 km in the W10°N direction. Between 19 and 16 Ma (Fig. 2B), Baja California changed its direction from approximately W10°N to W10°S. During this period, Ferrari et al. (2018) expanded the proposed model by Ferrari et al. (2013) by identifying the extensional belt that includes the Baucarit basins of Sonora and their continuation in Sinaloa, as well as the Comondú basin in southern Baja California and other similar basins now submerged in the southern Gulf of California (Foca-Cerralvo -FCB- and SBB; Fig. 2B). According to the authors, these submerged basins to the south of the Gulf of California are the beginning of the formation process of the Foca-Cerralvo and SBB. In fact, for them, “the Foca-Cerralvo basin represents the western remnant of a basin axial rift, whose eastern counterpart may be the SBB”, and its position can be observed in the reconstruction of Fig. 2B. Subsequently, between 19 and 16 Ma, Baja California completed a displacement of around 50 km with movement towards W10°S, initiating the separation of the FCB and SBB basins (Fig. 2C). This left it 475 km southeast of its current position.

In 2021, Madrigal et al. (2021) interpreted a series of seismic profiles in the NE section of the Maria’s Islands section, where they determined that there is no evidence of the Rivera Plate subducting beneath the North American Plate (Fig. 1). Finally, Sánchez-Barra et al. (2022), through a set of interpreted seismic profiles, defined the basement of Mazatlán Basin. In particular, they report a map of two-way travel time (TWT) derived from these seismic profiles, in which the central section of the Mazatlán Basin is observed along the Nayarit coast, but only slightly grazes what would be the NW section of the Rivera Plate.

### 1.2. Study area

In Fig. 3, we present the topography/bathymetry of the area. It is observed that there are several, most relevant geographic features within the area, such as Banderas Canyon, the Islas Marías Rise, and the end of the Mesoamerican Trench. It is known, through the seismic interpretations of Brown (2007), Lizarralde et al. (2007), Sutherland et al. (2012), and the magnetotelluric line interpreted by Alvarez et al. (2021) that thinned crust exists. In Fig. 3, the green square shows the area

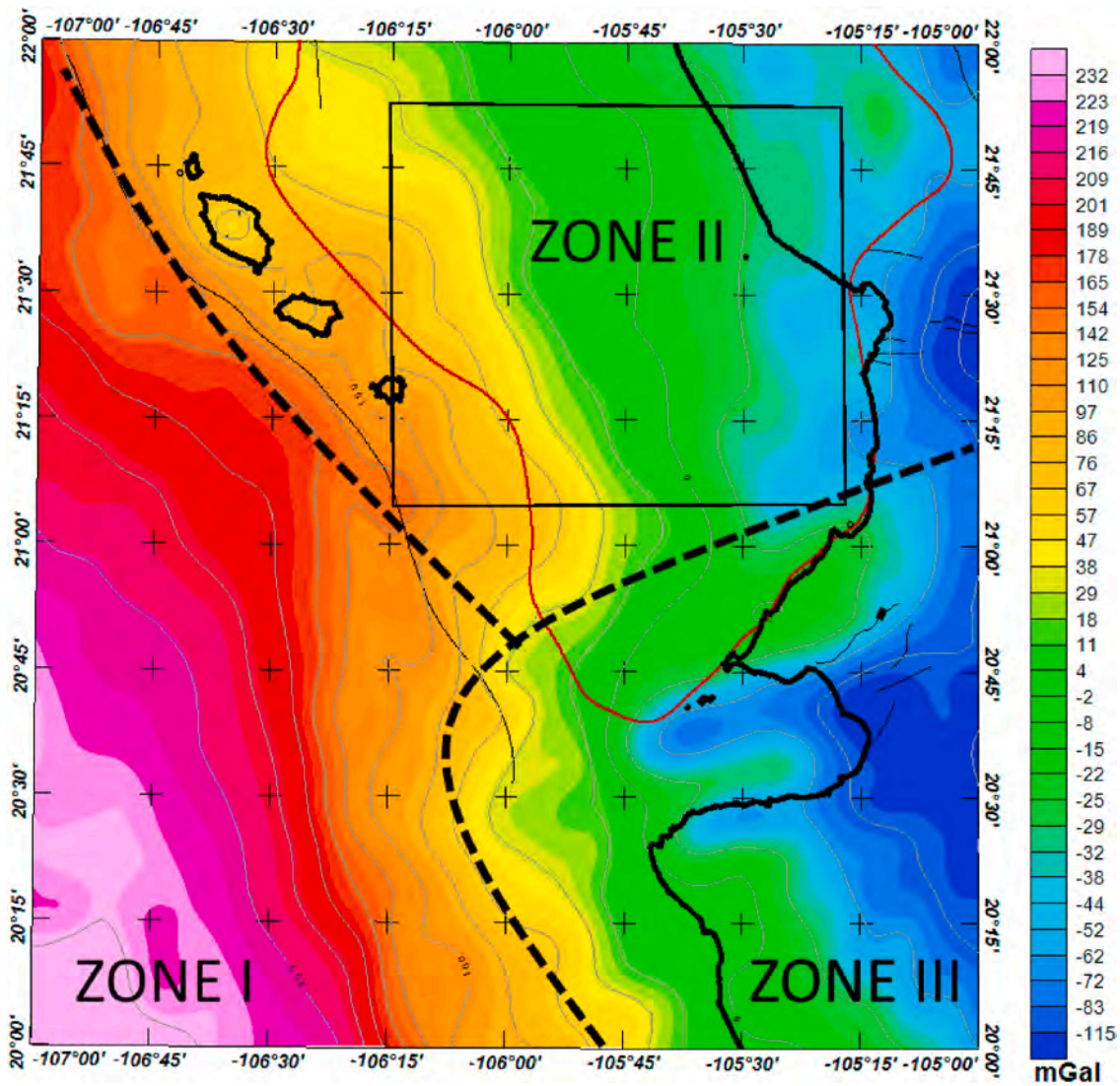


Fig. 4. Bouguer Anomaly Map (calculated from the model Eigen-6C4). The thick black line represents the coastline, while the thin gray lines represent the contours of the Bouguer anomaly. The black square is the inversion area. The brown curve represents the Mazatlán Basin as defined by Sánchez-Barra et al. (2022). The dashed lines represent the established gravity zone divisions.

commonly associated with SBB, it is noteworthy that the depth of the SBB zone does not exceed 500 m below sea level.

## 2. Data acquisition and processing

### 2.1. Topography

The topography data used for this study originates from two sources: The ETOPO1-2250 dataset, obtained from the International Centre for Global Earth Model (ICGEM; Ince et al., 2019; <http://icgem.gfz-potsdam.de/home>), features a resolution of 1 km; and the GEBCO\_2023 model, acquired from GEBCO Compilation Group (2023), offers a resolution of approximately 15 arc-seconds (about 400 m).

### 2.2. Bouguer Anomaly (BA)

#### 2.2.1. Data acquisition

The Bouguer anomaly data used for this work are from the EIGEN-6C4 satellite gravimetric model and are processed starting from observed gravity, through the methodology employed by the USGS in its latest regulation (Hildenbrand et al., 2002; Camacho and Alvarez, 2021). This methodology considers the Earth's sphericity and the

atmosphere's contribution to the correction processes. These data are obtained from the ICGEM (Ince et al., 2019).

#### 2.2.2. Data processing

In this work, we performed the calculation of the BA (Bouguer Anomaly) from the observed gravity data ( $G_{Obs}$ ), including the necessary correction according to the new gravimetric standard of the USGS (e.g., Hildenbrand et al., 2002). The calculation for BA is done using equation (1):

$$BA = G_{Obs} - G_{teo} \pm C_{alt} \mp C_{Boug2} + C_{atm} + C_{top} \quad (1)$$

To obtain the BA (Bouguer Anomaly) at each point within the working window, it is necessary to obtain each of the terms in equation (1). Therefore, we will calculate each term individually. Firstly, we calculated the theoretical gravity at each point of the dataset using equation (2) from Wollard (1979). The coefficients used in the equation are as follows:  $g_e = 978032.67715$  mGal;  $k = 0.01931851353$  y  $e^2 = 0.0066938002290$ . The coefficients "k" and "e" are dimensionless.

$$G_{teo} = g_e \frac{1 + k * (\sin \varphi)^2}{\sqrt{1 - e^2 (\sin \varphi)^2}} \quad (2)$$

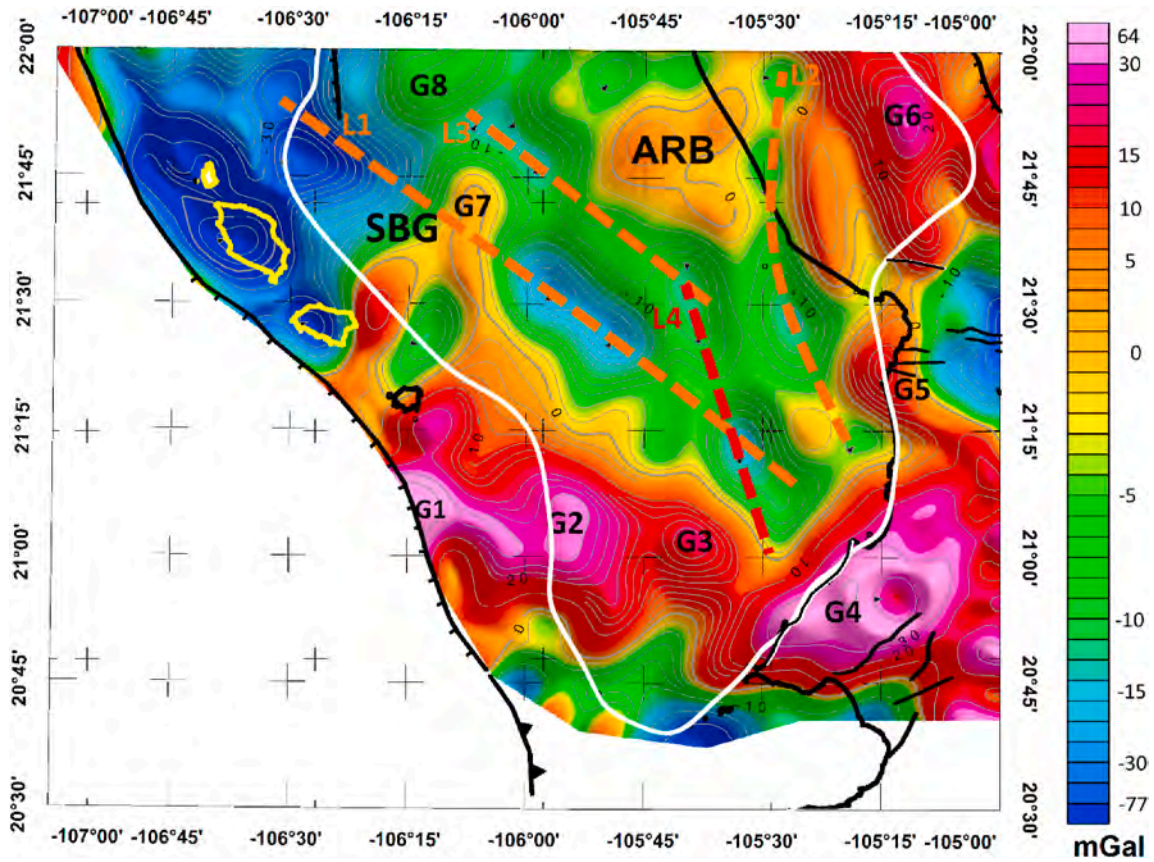


Fig. 5. BA residual map. The onshore black lines represent the main faults. ARB: Aramara Bulge. SBG: San Blas Gorge. The continuous black line and the yellow lines (Islas Marias) represent the coastline, and the gray continuous lines represent the Bouguer anomaly contours. G1-G7 represent the gravimetric anomaly points of interest and the lines L1-L3 are the gravimetric anomaly alignments of interest. The Mazatlán Basin is shown as a white line (Sánchez-Barra et al., 2022).

We corrected the value of the SRTM90 model from ellipsoidal height ( $h_{elip}$ ) to geoid height ( $H_{geo}$ ) to use gravimetric equations referenced to the geoid. This correction was done using equation (3) proposed by Götze and Li (1996). For the subsequent formulas, we will define geoidal height ( $H_{geo}$ ) as simply height ( $h$ ).

$$h_{elip} = H_{geo} + N \quad (3)$$

Through equation (4), we were calculated the height correction ( $C_h$ )

$$C_h = (0.3087691 - 0.0004398 * \sin(\varphi)^2)h + 7.2125 * 10^{-8}h^2 \quad (4)$$

Posteriorly, we calculated the atmospheric correction ( $C_{am}$ ) with equation (5) (Hildenbrand et al., 2002).

$$C_{am} = 0.874 - 9.9 * 10^{-5} * h + 3.56 * 10^{-9} * h^2 \quad (5)$$

The Bouguer correction ( $C_{Boug_{-2^\circ}}$ ), is the correction that eliminates the gravimetric attraction of the matter that exists between the reference level and the point on the topographic surface. This correction was done with equation (6).

$$C_{Boug_{-2^\circ}} = 2\pi * G * \rho * h * \left( \frac{\alpha}{2} - \eta * \left( 1 + \frac{1}{2\alpha} \right) \right) \quad (6)$$

For the topographic correction ( $C_{top}$ ) we used the Oasis Montaj software v10.1, which implemented the algorithm proposed by Kane (1962) and Nagy (1966).

With these terms resolved, we have calculated the BA through equation (1).

Subsequently, a Gaussian filter was applied to reduce noise or small-scale superficial features. This is done to enhance the structural features in the area, performing a similar task to the upward continuation of the

analytical field by 5 km. This Gaussian filter was applied using the MAGMAP Filtering module in Oasis Montaj, which utilizes equation (7). The parameters used in equation (7) are as follows:  $K_0$  represents the standard deviation of the Gaussian function in cycles per unit of land; 0 is the value for the residual component, and 1 is for the regional component (Hinze et al., 2013).

$$L(k) = 1 - e^{-\frac{k^2}{2k_0^2}} \quad (7)$$

### 2.3. Magnetic data processing

#### 2.3.1. Data acquisition

Magnetic data were obtained from the page of the United States Geological Survey (USGS; <https://mrdata.usgs.gov/magnetic/>). The data are from magnetic anomaly maps and aeromagnetic data assembled for all of North America (Mexico, United States, and Canada; Bankey et al., 2002).

#### 2.3.2. Data processing

For the magnetic data set it was necessary to reduce to the pole. For this, we used the software Oasis Montaj and applied the filtering process which uses equation (7). The program has a database to extract magnetic declination and inclination based on the year and data location, where:

$I_\alpha$  = Inclination by amplitude correction, such that  $I_\alpha > I$ .

$I$  = Geomagnetic inclination.

$D$  = Geomagnetic declination.

$$L_\theta = \frac{[\sin(I) - i * \cos(I) * \cos(D - \theta)]}{[\sin^2(I_\alpha) + \cos^2(I_\alpha) * \cos^2(D - \theta)] * [\sin^2(I) * \cos^2(D - \theta)]} \quad (8)$$

After that, a Gaussian filter was used to obtain the upward



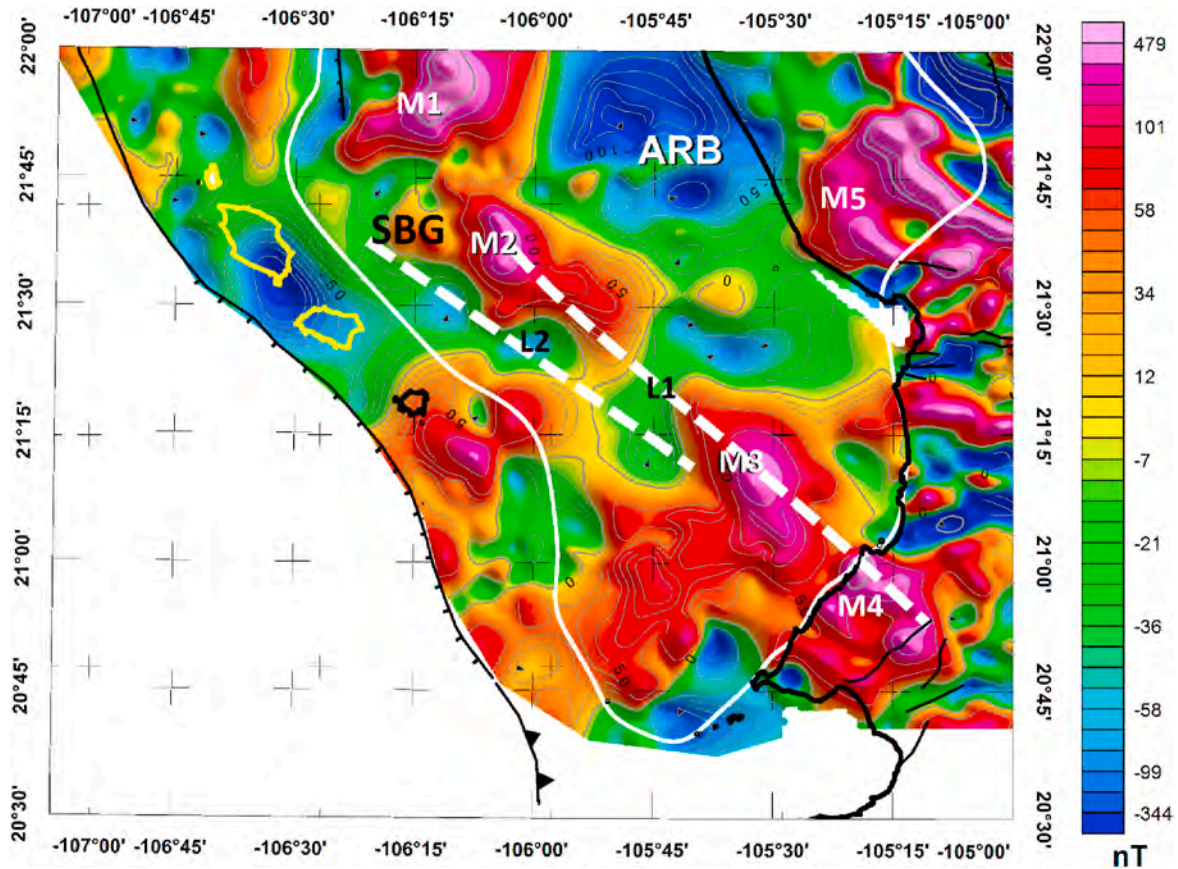


Fig. 6. Magnetic anomaly map of the SBB. The continuous black line represents the coastline, and the gray continuous lines represent the magnetic anomaly contours. The continuous white line delineates the Mazatlán Basin. ARB: Aramara Bulge. SBG: San Blas Gorge. M1-M5 represent the magnetic anomaly points of interest and the lines L1 and L2 are the magnetic anomaly alignments of interest.

continuation to 20 km (Milsom, 2003). This was necessary to homogenize the data in the map since the offshore and onshore data sets have different sampling intervals.

#### 2.4. Directional derivative processing

We use directional derivatives in the BA residual to highlight the regional structures. The directional derivative in the W-E direction, or the derivative in the X-direction, is described by equation (9). Meanwhile, the derivative in the N-S direction, or the derivative in the Y-direction, is described by equation (10) (Hince et al., 2013).

$$L(u) = (ui)^n \quad (9)$$

$$L(v) = (vi)^n \quad (10)$$

The derivative in depth, or the derivative in the Z-direction, is used to enhance the perceptibility of anomalies originating from shallow sources.

$$L(r) = (r)^n \quad (11)$$

#### 2.5. 3D inversion processing

The software employed for the 3D inversion was Oasis Montaj (OM). This software used the Cartesian Cut Cell algorithm to represent geologic volumes, and the results of the gravimetric inversion method were expressed in voxels, with their density expressed in g/cm<sup>3</sup>, and an Iterative Reweighting Inversion algorithm (IRI; Ingram et al., 2003) to match the observed results. On the other hand, the results of the magnetic inversion method were expressed in susceptibility (SI units), which

is a measure of the magnetizability of rocks. The method used for the OM was described by Macleod and Ellis (2013), with the theoretical considerations outlined by Ellis et al. (2012). This method allows for the modeling of complex geological structures with irregular geometries.

### 3. Results

#### 3.1. Bouguer Anomaly of the SBB

The Bouguer Anomaly in Fig. 4 ranges from -155 to 214 mGal. Onshore, the BA ranges from -17 to -155 mGal, while offshore, it ranges from -17 to 214 mGal. The black square is the area designated for the inversion, which will be performed later ahead. The trends of the contours of BA usually reflect the structures deep in the subsurface. In the map, we can observe three behaviors in the preferential orientations of the contours.

- i) The first one develops in a direction of approximately N45°W, running from the SW limit of the map to the Islas Marías Escarpment (IME).
- ii) The second behavior occurs in Zone II (Fig. 4) ii) developing from the Islas Marías Escarpment to the onshore region, covering what would be the SBB zone. In this area, we observe a variation in the preferential orientation of the contours, transitioning from N45°W to almost N-S, while the BA decreases from 90 mGal to -30 mGal.
- iii) The third behavior of the contours develops in Zone III, mainly the area of the Jalisco Block (Fig. 4), developing from the Islas Marías Escarpment to the onshore area, encompassing what would be the SBB zone. In this area, we observe a shift in the

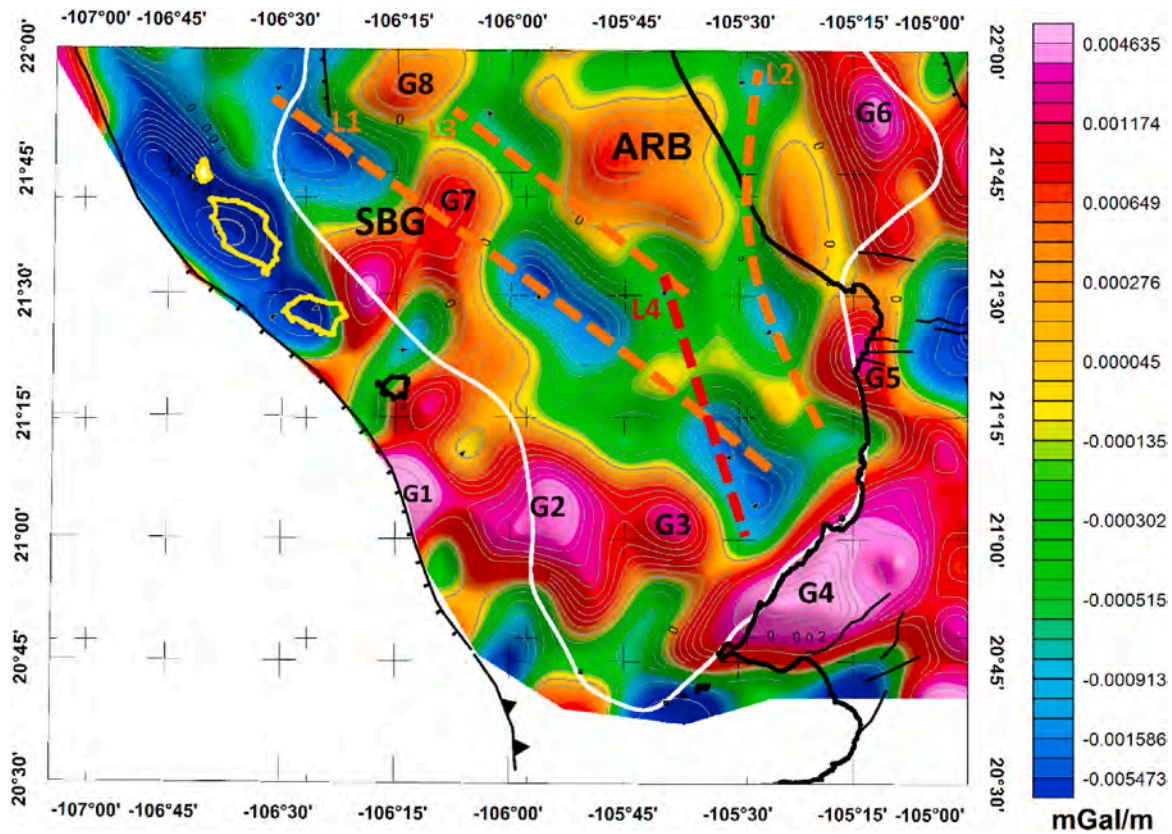


Fig. 7. Derivative in the vertical direction (Z-direction)  $BA_{Dz}$  of the Bouguer anomaly in the SBB. The continuous black line and the yellow lines (Islas Marías) represent the coastline, and the gray continuous lines represent the gravimetric anomaly contours. The continuous white line delineates the Mazatlán Basin. SBG: San Blas Gorge. ARB: Aramara Bulge. G1-G7 represent the gravimetric anomaly points of interest and the lines L1-L3 are the gravimetric anomaly alignments of interest.

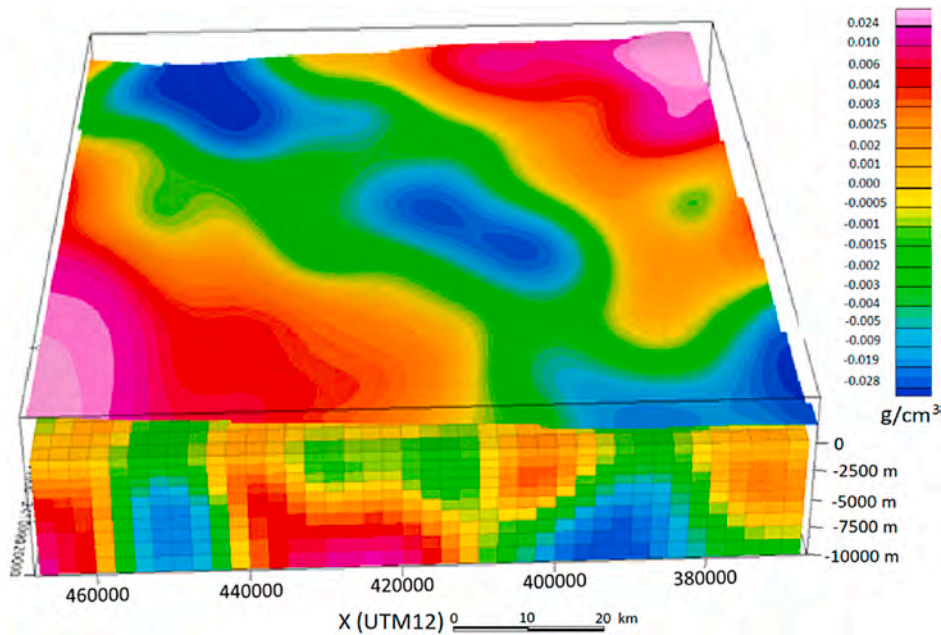


Fig. 8. 3D gravimetric inversion. In the model, a grid of BA is represented and calculated using the inversion response; this model coincides with over 96.7% of the same BA section calculated from Eigen-6C4 data (Fig. 4).

preferential orientation of the contours from N45°W to nearly N-S, with the BA decreasing from 90 mGal to -30 mGal.

### 3.2. Residual map or $BA_{tren2}$ map

For highlighting the sector of SBB, we cut the data grid restricting it to the area surrounding the MB. We used various trend removal filters on

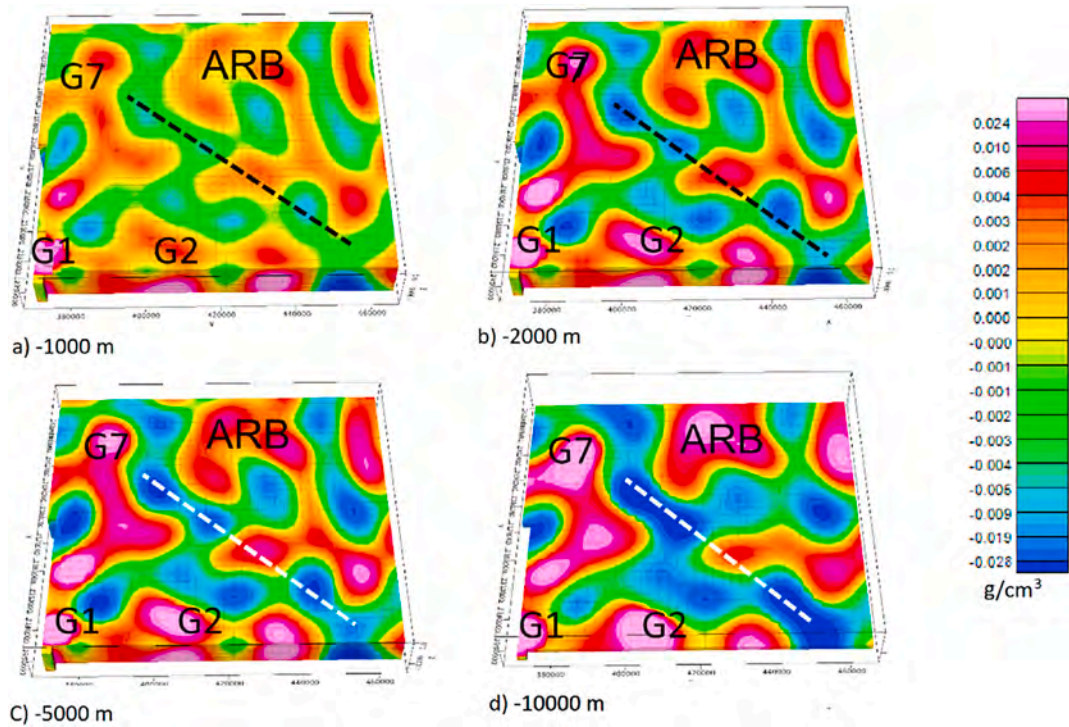


Fig. 9. Horizontal sections of the 3D gravimetric inversion. a) Section at 1000 mbsl. b) Section at 2000 mbsl. c) Section at 5000 mbsl. d) Section at 10,000 mbsl. ARB: Aramara Buge. The points are the same as the ones observed in Fig. 5. The lines coincide with the axis of the basin and with L1 in Fig. 5.

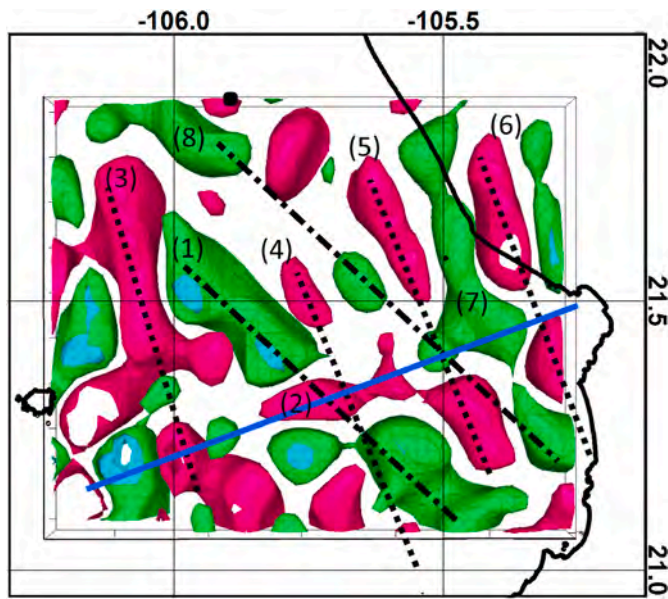


Fig. 10. Map of geo-volumes of iso-densities. In red, bodies with densities of 0.025 g/cm<sup>3</sup>, in green bodies with -0.025 g/cm<sup>3</sup>, and in blue bodies with -0.050 (concerning the reduction density of the medium 2.67 g/cm<sup>3</sup>). In black the coastline, in light gray the bathymetric contours. The light blue sections represent surfaces within the green ones.

the BA data; the case with the best fit according to the geographical location of the area, is the second-degree trend removal filter; the result shown in Fig. 5. This map displays values ranging from -77 to 64 mGal

In Fig. 5, we find structures associated with the edges of the SBB. Specifically, the S boundaries of the SBB are delineated by a series of anomaly maxima. The first point (point G1) is marked by a maximum regional anomaly, which appears to be associated with a higher-density

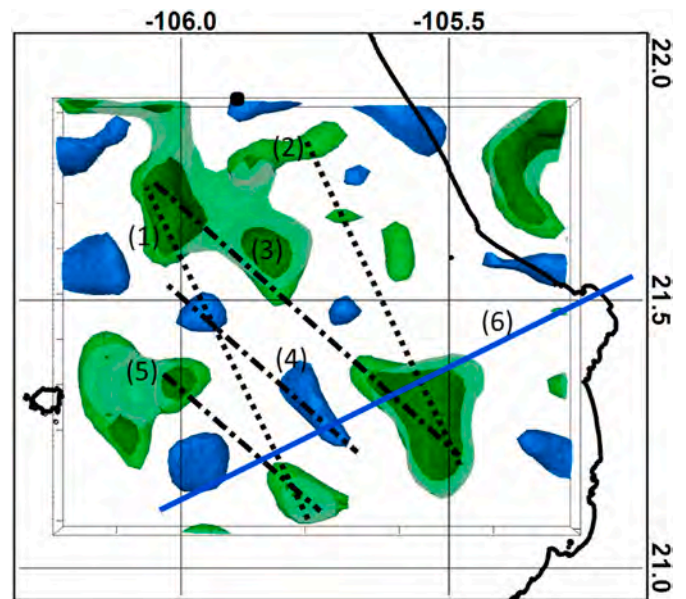
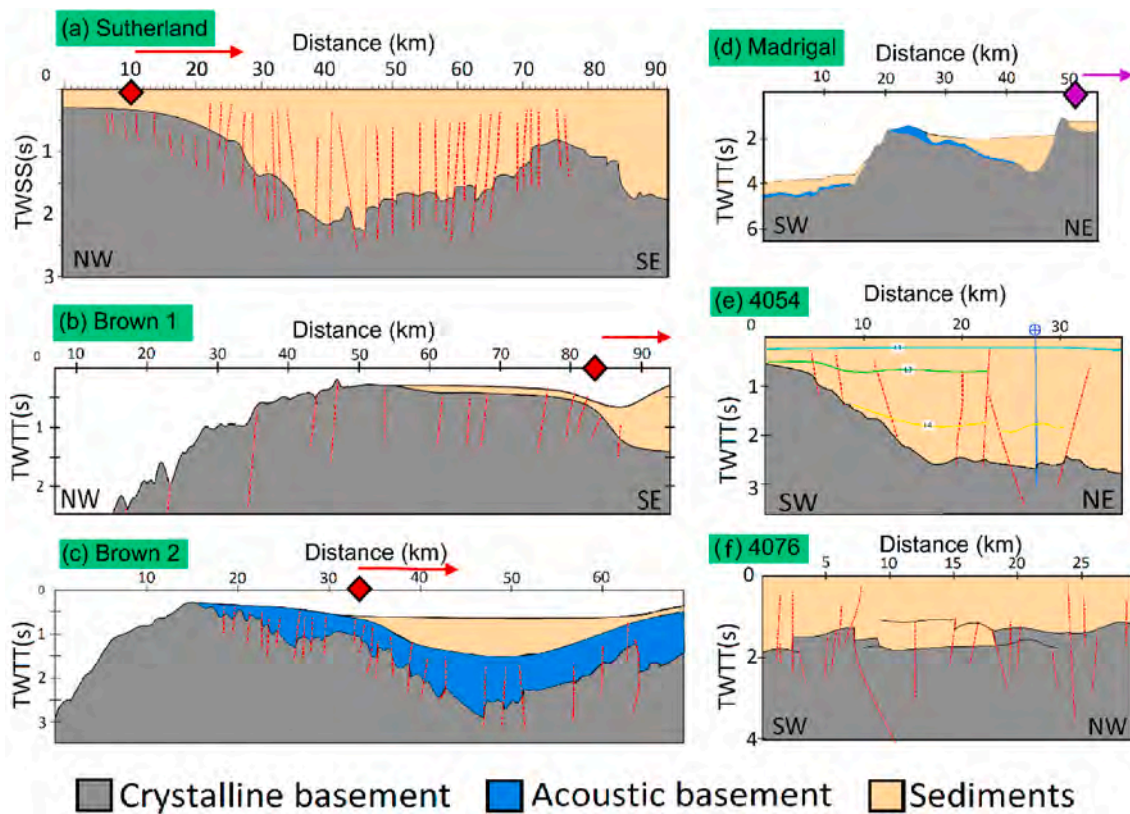


Fig. 11. Map of geo-volumes of magnetic iso-susceptibility. In blue the volumes of  $\geq 0.093$  SI of susceptibility, and in brown the volumes of  $\geq +0.17$  SI. In black line the coastline, and light gray the contours of bathymetry in the area.

structure developing at the latitude of 21°N in a W-E direction, extending from the SW sector (point G1 of the SBB to the W point G2). Notably, the second point locates a maximum regional anomaly (point G2) continuing in a point of maximum local anomaly (G3). At point G4, the absolute maximum anomaly on the map stands out, which was documented by Alvarez et al. (2021) as an anomalous batholith on the tectonic boundary between the Jalisco block and the San Blas Basin, with electrical and gravitational characteristics different from the surrounding medium, marking the SE boundary of the SBB. Thus, from G1



**Fig. 12.** Sketch of the seismic lines published in the area: line a) Sutherland published by Sutherland et al. (2012); lines b) Brown 1 and c) Brown 2 published by Brown (2007); line d) Madrigal published by Madrigal et al. (2021); and the lines e) 4054, f) 4076 and the TWTT map (two-way travel time) published by Sánchez-Barra et al. (2022). The arrows indicate the direction in which each author interprets the beginning of the SBB (in red) and the beginning of the SBG (in purple).

to G4 we have a high-density complex that limits Mazatlán Basin to the south.

Between point G3 and point G4, we find what appears to be a small canyon that connects the area with the Banderas Canyon, which could have been a remnant of the entry point of the sea when the extension of Baja California began. Continuing to the E of the map, we find point G5, where we have the boundary fracture zone of the Jalisco Block, which was determined by Camacho and Alvarez (2020) as the gravimetric expression of the Tepic-Zacoalco rift. Finally, in the NE region of the map, we can observe point G6, where there is a maximum anomaly observed on the boundary of the Mazatlán Basin proposed by Sánchez-Barra et al. (2022).

In the residual map, the feature of the Aramara Bulge (ARB) stands out, which appears to be a structural high that divides the Mazatlán Basin into the N region, and the S region, or SBB. This feature was previously reported by Alvarez et al. (2017) with relative gravity maxima anomaly values, and confirmed by Sánchez-Barra et al. (2022) through a seismic Two-Way Travel Time (TWTT) map. Thanks to this, the ARB can be understood as the NE boundary of the SBB.

On the other hand, a series of anomaly minima can be observed throughout the SBB region. Among these, two of the relative minima oriented in the NW direction (L1) stand out, which appear to form the main axis of the SBB. This alignment is disrupted by a positive anomaly that crosses in an NW direction (G7), but it appears to continue toward the northwest, along the known path of the San Blas Gorge (SBG). Furthermore, in the north-central part of the map, we observe a maximum anomaly (G8), which appears to delineate the northern boundary of the SBB. Additionally, a series of minima are observed bordering the ARB following the coast in an N-NE direction and changing direction near  $21.5^\circ$  latitude to an S-SE direction (L2). Another series of anomaly minima is observed along the southern side of the BA

in an NW direction, parallel to lineament L1 but with a lesser longitudinal development (L3). Additionally, another lineament of minimum anomalies (L4) is oriented in an approximate direction of  $N15^\circ W$ , crossing from the BA to the S part of the basin, intersecting the lineaments L1 and L3.

The SBB magnetic anomaly map is presented in Fig. 6, which displays values ranging from 184 to  $-334$  nT. The absolute minimum anomaly of the map is observed to the N of the ARB with values less than  $-300$  nT. To the N of the Mazatlán Basin region, the maximum absolute anomaly ( $479$  nT; point M1) is observed, contiguous to the absolute minimum anomaly of the map. Furthermore, a series of anomaly maxima are observed, which appear to be aligned in an  $N45^\circ W$  direction (L1) and develop through the previously exposed zone as the possible central axis of SBB, from point M2 to point M4. This is where the maximum regional anomaly is located, associated with the Puerto Vallarta Batholith reported by Alvarez et al. (2021). At point M5, a maximum anomaly is reported with a value very close to the absolute maximum, which develops onshore and appears to form a magnetic pair with the absolute minimum of the map.

### 3.3. Directional derivative maps

We used different directional filters to emphasize the continuity of structures in defined directions. In the case of Fig. 7, we used the derivative in Z of the Bouguer anomaly, which helps highlight the depth continuity of the structures (Hinze et al., 2013).

In this map (Fig. 7), we can observe a strong correlation with the residual map from Fig. 5, which displays nearly identical features. As a result, we labeled the same points and lineaments as in the residual map (Fig. 5) to emphasize consistency. However, there are some variations in terms of the relative magnitude with which certain structures stand out,

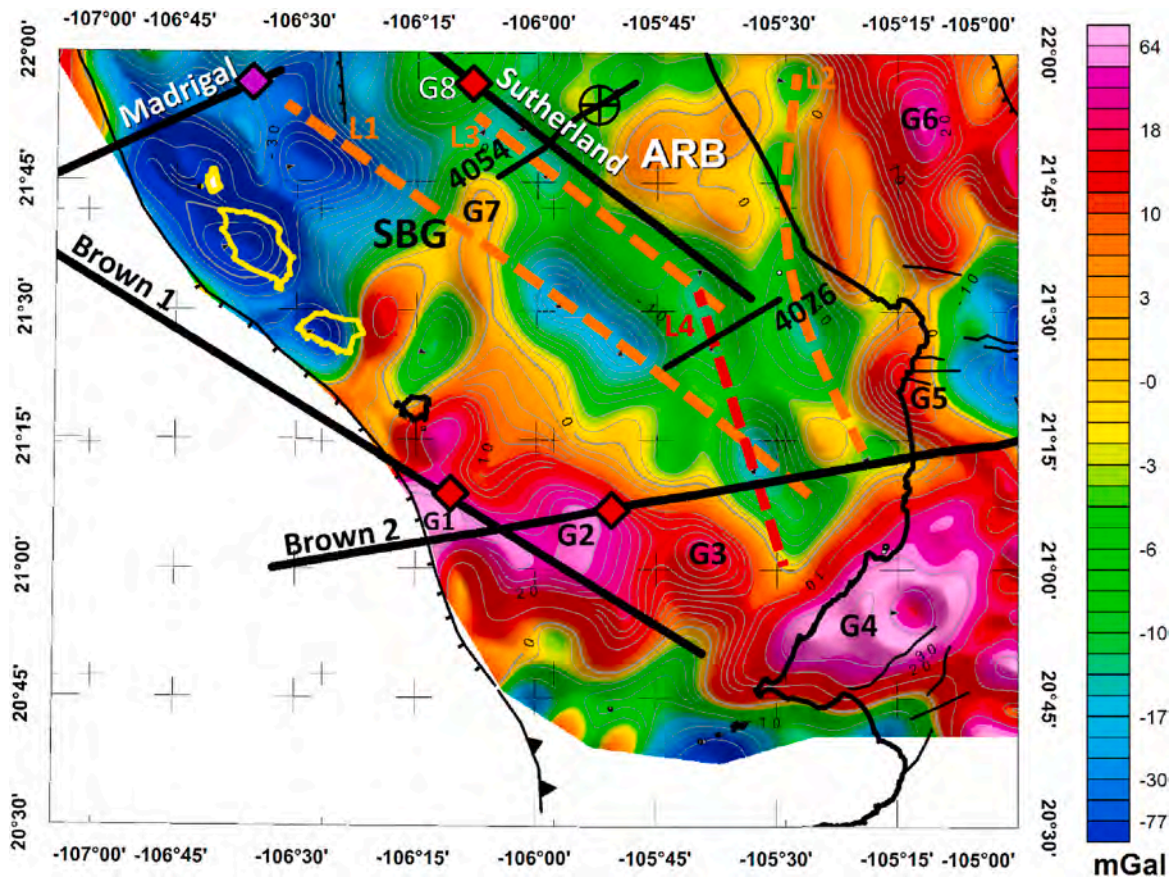


Fig. 13. BA map with 2nd degree trend removal (residual) and seismic lines interpreted. The black lines show the principal published seismic lines in the region: Line Brown1 and Line Brown 2 for the lines published by Brown, 2007; Line Sutherland for the line published by Sutherland et al., 2012; Line Madrigal for the line published by Madrigal et al., 2021; and lines 4054 and 4076 for the lines published by Sánchez-Barra et al., 2022. The red diamonds show the position of the beginning of the SBG according to the interpretation of Madrigal et al. (2021). SBG: San Blas Gorge. ARB: Aramara Bulge. G1-G7 represent the gravimetric anomaly points of interest and the lines L1-L4 are the gravimetric anomaly alignments of interest.

especially at the boundaries of the NW section of the SBB (point G7), and ARB as the NW boundary of the SBB.

Additionally, to the NW of L1 and point G7, a separate minimum anomaly develops, distinct from the minimum anomaly in the area of the Marias Islands. We observed another point (G8) in this map that becomes relevant as the NW boundary of L3 and the SBB.

The L1 lineament highlights a series of anomaly minima that are the most prominent within the area, suggesting the primary axis of the SBB. The L3 lineament features a series of minima that run parallel to the presumed primary axis (L1). Furthermore, a pair of minima seem to connect in an N15°W direction (L4), linking the SE points of the L1 and L3 lineaments. The L2 lineament stands out with a zone of anomaly minima bordering the W of the ARB and traversing the coastline approximately in a northward direction. Points G1, G2, and G4 are identified as locations with maxima anomalies, associated with the southern and southeastern boundaries of the SBB.

### 3.4. 3D inversion of gravimetric data

A 3D inversion transforms gravity data in mGal, into density data in  $\text{g}/\text{cm}^3$ ; the density distribution helps visualize mass deficiency or excess in given areas that assist in their association with processes in the region.

Gravimetric inversion was conducted following the methodology proposed by McLeod and Ellis (2013). The implementation of this method was executed using the Oasis Montaj software, with due consideration of the theoretical foundations laid out by Ellis et al. (2012). Subsequently, the software employed the Cartesian Cut Cell algorithm to model geological volumes for the inversion calculation.

Furthermore, the software employed the Iterative Reweighting Inversion algorithm (IRI; Ingram et al., 2023) to juxtapose the results with the observed data, aiming to ensure a response characterized by an error no greater than 5% of the standard deviation. An example of this method can be observed in the work of Alvarez and Camacho (2023a) and Alvarez and Camacho (2023b), where the same methodology is employed to correlate volumes of lower density with the plumbing system of Hunga Tonga Hunga Ha'apai Volcano and the plumbing system of the Nevado Volcano, respectively.

The inversion area is shown in Figs. 3 and 4. The inverted volume can be seen in Fig. 8, where on top is the grid generated by the calculated gravitational response, which has a 97.6% match with the same section of the data calculated through  $G_{obs}$ . The cubic units of the inversion model are known as voxels. The inversion area measures  $50 \text{ km} \times 50 \text{ km} \times 15 \text{ km}$  in depth.

Fig. 9, horizontal sections sampled at various depths. The figure shows the pair of minima anomalies previously associated with the main axis of the SBB. In the different cross-sections, we can see how the anomaly develops penetrating deeper into the model. Points 1 and 2 (taken from Fig. 5), which were previously associated with basement points where the SBB begins, as described by Brown (2007), are now seen as high-density anomalies that increase with depth.

Finally, we generate volumetric bodies of equal density (geo-volumes) to highlight areas of higher and lower density within the model. The results are shown in Fig. 10. The generated geo-volumes exhibit different densities relative to the reference density of  $2.67 \text{ g}/\text{cm}^3$ : bodies in red indicate a variation of  $+0.025 \text{ g}/\text{cm}^3$ , bodies in green show a variation of  $-0.025 \text{ g}/\text{cm}^3$ , and bodies in blue (embedded within the

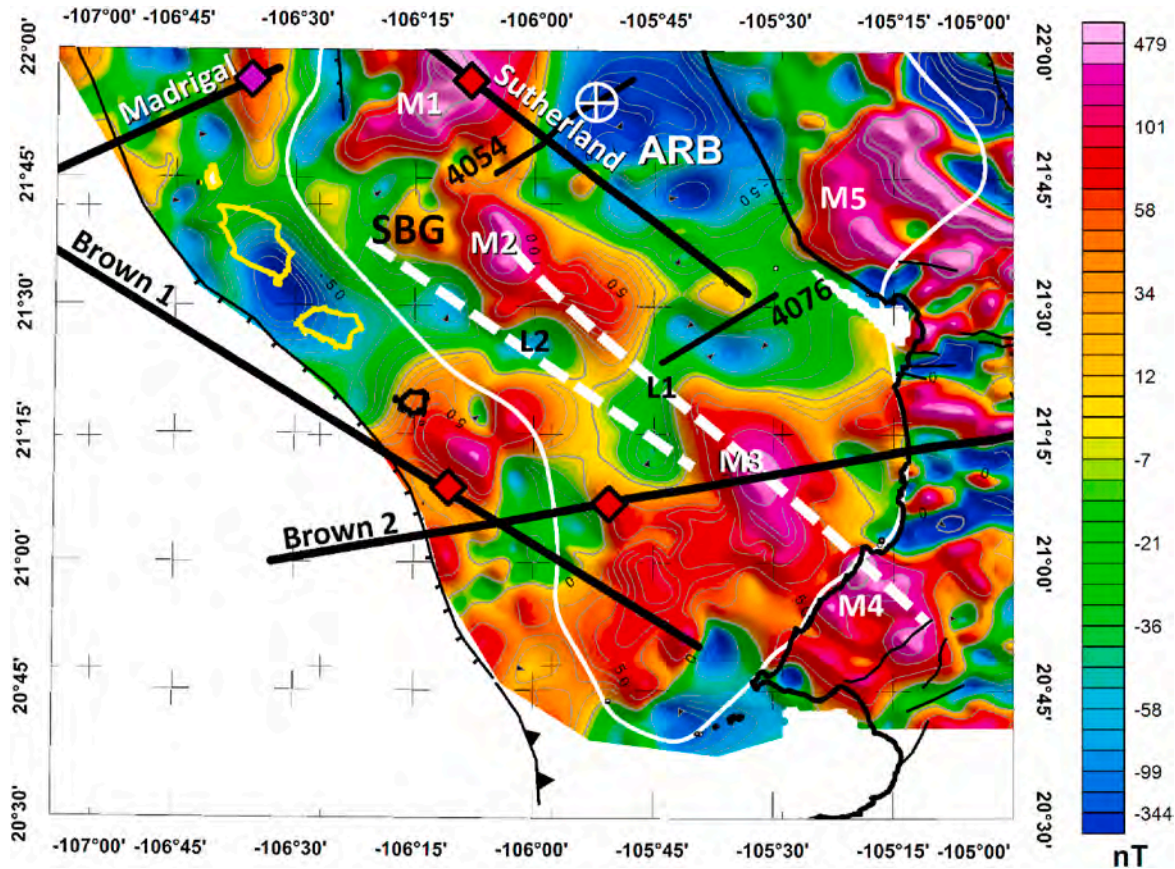


Fig. 14. Magnetic anomaly map of the SBB reduced to pole. The continuous black line represents the coastline, and the gray continuous lines represent the magnetic anomaly contours. The continuous white line delineates the Mazatlán Basin. The black lines show the principal published seismic lines in the region. The red diamonds show the position of the beginning of SBB according to the seismic interpretation by the authors, and the purple diamond with the initiation of the SBG. HUICHOL-1 is well in a white circle. SBG: San Blas Gorge. ARB: Aramara Bulge. M1-M5 represent the magnetic anomaly points of interest and the lines L1 and L2 are the magnetic anomaly alignments of interest.

green bodies) exhibit a variation of  $-0.050 \text{ g/cm}^3$ .

In Fig. 10, it is observed that the main density values within the area, assumed to be the central axis of the basin, are oriented towards  $N45^\circ W$  (indicated by the dashed and dashed black line 1 in Fig. 10). The development of this low-density body is interrupted by a body of positive densities with a perpendicular orientation (represented by the blue line 2 in Fig. 10), which extends towards the coastline. In the western section of the map, we encounter the most extensive and densest anomaly on the map, characterized by an  $N15^\circ W$  direction (marked by dashed line 3 in Fig. 10). Additionally, three bodies of high density aligned parallel to the previous one traverse the entire extent of the basin (lines 4, 5, and 6; Fig. 10) and seem to be intersected by the previously mentioned series of anomalies, connected by a blue line (line 2; Fig. 10). Of these bodies, the longest one with minimal density on the map is highlighted, also oriented approximately in the  $N15^\circ W$  direction (line 7; Fig. 10). Finally, it is worth noting a series of bodies with minimal density oriented towards  $N45^\circ W$  (line 8; Fig. 10). We conclude that these bodies align in three main directions: dashed lines (1 and 8), dashed lines (3, 4, 5, 6, and 7), and a blue line (2).

### 3.5. 3D inversion of magnetic data

For the magnetic data, we followed the same procedure as in the magnetic inversion. The 3D magnetic inversion data is presented in Fig. 11. From the magnetic inverted volume, we extracted surfaces of equal magnetic susceptibility, containing volumes of susceptibility higher or lower compared with the average susceptibility value of the zone (0.1 SI). In blue the volumes of  $\geq 0.093$  SI of susceptibility, and in

brown the volumes of  $\geq +0.17$ . In Fig. 11, a greater dominance of positive anomalies is observed within the map, although the magnetic anomaly patterns are less well-defined than in the case of the gravity anomaly. Two aligned patterns are observed at  $N15^\circ W$  (lines 1 and 2; Fig. 11), developing across the entire basin area between two anomalies. However, it should be noted that while the trend in the first pattern's line is clear, the trend in the second pattern's line is not as clear. In an  $N45^\circ W$  direction, the development of the three main positive anomalies on the map (line 3; Fig. 11) can be observed, which crosses parallel and very close to the SBG. This suggests a boundary and coincides with alignment 8 in Fig. 10. Towards the S of the SBG, a series of aligned minima is observed (line 4; Fig. 11) parallel to line 3, this reinforces the concept of a basin axis that extends along the SBG. Farther S of this position there is a pair of anomaly minima aligned in a direction parallel to  $N45^\circ W$  (line 5; Fig. 11). In the blue line (line 6; Fig. 11), we infer that a certain pattern associated with this direction is evident in the positive anomaly farther to the SE of the map, reaching the negative anomaly to the SW.

## 4. Discussion

### 4.1. Basin boundaries

Although the area of the Mazatlán Basin has recently been delimited (Sánchez-Barra et al., 2022), to the S region to which the SBB belongs, it does not have well-defined borders in the literature (e.g.: Brown, 2007; Sutherland et al., 2012; Ferrari et al., 2018; Sánchez-Barra et al., 2022). It is located somewhere between Marías islands and the continental

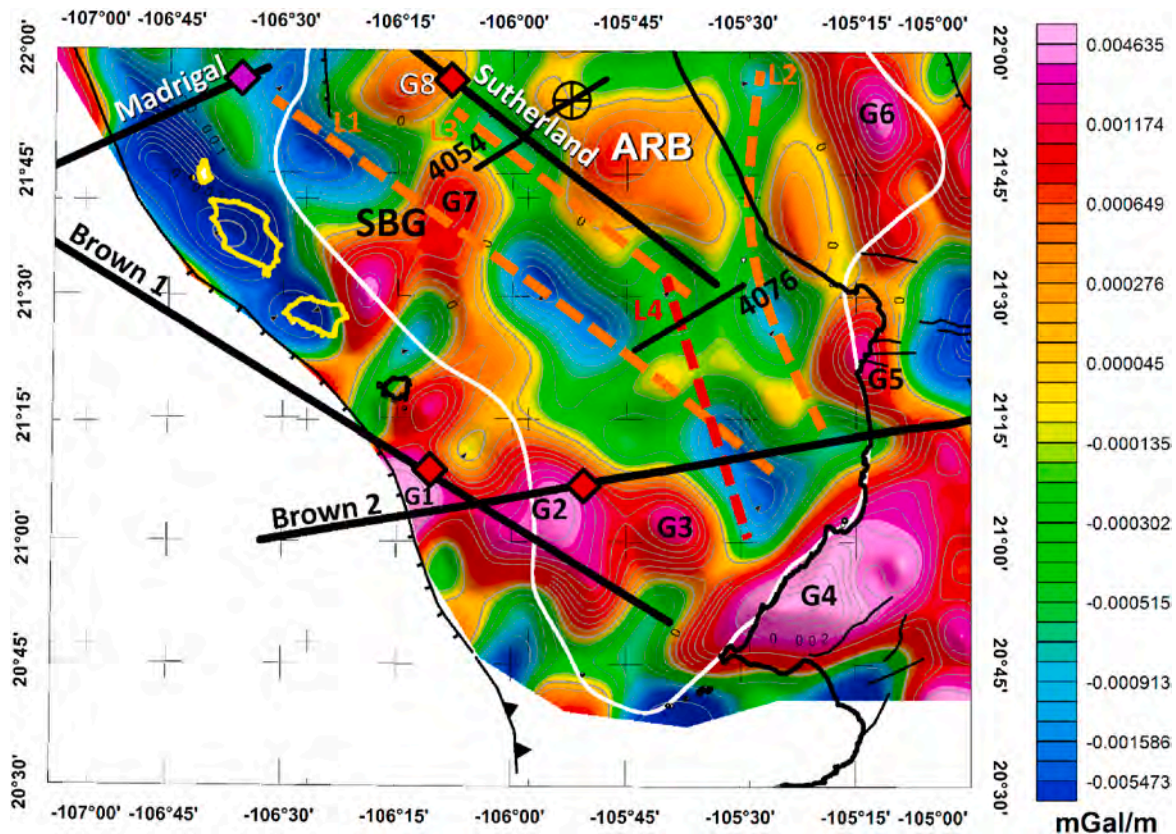


Fig. 15. Z-derivate of the Bouguer anomaly (BA\_Dz) in the SBB with the seismic lines. The points and lineaments are the same as those presented in Fig. 13.

coastline, without properly defining its extension, form, or dimensions. However, we aim to delineate the boundaries of the basin through the analysis of gravity and magnetic data, and the utilization of several results in publications from which specific information can be extracted regarding the interpreted boundaries of the SBB. These publications include Brown (2007), Sutherland et al. (2012), and Madrigal et al. (2021), as well as a TWTT map of the central section of the Mazatlán Basin published by Sánchez-Barra et al. (2022). Their main features can be seen in Fig. 12.

In Fig. 13 we have georeferenced the seismic lines from the publications, including Brown (2007), Sutherland et al. (2012), and Madrigal et al. (2021). Additionally, we have included a red diamond at the position indicated by each author as the starting point of the SBB, and a purple diamond as the starting point of the SBG (Madrigal et al., 2021). This way, we can make a direct comparison between the residual map and the seismic data interpreted by the authors.

In Fig. 13, it is observed that the W, the S, the SE, and the E of the SBB are delineated by a series of anomaly maxima. The first point (point G1) is marked by a maximum of the regional anomaly, which coincides with the position interpreted by Brown (2007) as the initiation of the SBB (red diamond line Brown 1; Fig. 5). The second point is marked by a maximum regional anomaly (point G2) also associated with the beginning of the SBB interpreted by Brown (2007) and indicated in the seismic line (Brown 2) with the red diamond (Fig. 13). Among the largest anomaly maxima on the map, there is an area where the direction of the anomaly contour changes radically (from NW to NE); after this point (G3) seems to be associated with a small canyon that connects the area with the Banderas Canyon, which could have been the entry point of the sea when the extension of Baja California began. At point G4, the absolute maximum anomaly on the map stands out (point G4, which is reported by Alvarez et al. (2021) as the Puerto Vallarta batholith, marking the SE boundary of the SBB. Continuing to the N, we find point G5. This point (G5) marks the boundary fracture zone of the Jalisco

Block, which has been determined by Camacho and Alvarez (2020) as the gravimetric expression of the Tepic-Zacoalco rift. Finally, at point G6, there is a maximum anomaly observed on the boundary of the Mazatlán Basin proposed by Sánchez-Barra et al. (2022).

In the map of Fig. 13, the feature of the BA stands out, which appears to be a structural high that divides the northern region of the Mazatlán Basin from the southern region (SBB), with relative maxima anomaly values. This feature was previously reported by Alvarez et al. (2017) and confirmed by Sánchez-Barra et al. (2022) through a seismic TWTT map (Fig. 12). Therefore, the ARB is to be understood as the NE boundary of the SBB.

On the other hand, a series of anomaly minima can be observed across the SBB region. Among these, two of the relative minima oriented in the N45°W direction (L1) stand out, which appear to form the main axis of the SBB. This alignment is disrupted by a positive anomaly that crosses in an NE direction (G7; Fig. 13), but its alignment of minima seems to continue towards the NE, reaching the area of the seismic data from Madrigal et al. (2021) along the known path of the SBG.

Additionally, a series of minima are reported to traverse the coast in an N-S direction to the E of the ARB (L2). Another series of anomaly minima (L3) is reported to border the S side of the ARB in the NW direction, which coincides with the seismic profile of Sutherland et al. (2012) and exhibits a morphology similar to that of the SBB found in that seismic profile (Fig. 12 y Fig. 13). Furthermore, the seismic line interpreted by Brown (2007; Brown 2) shows a morphological consistency with the residual map, where the anomaly minimum follows the same location as depicted in the seismic data, reflecting the depocenter of the SBB (Figs. 12 and 13).

The seismic profile 4076 reported by Sánchez-Barra et al. (2022), shows that high-amplitude horizons appear chaotic and occur at various depths, which coincides with the somewhat chaotic pattern displayed by the residual map along the profile, reflecting a series of relatively small depocenters in the area. Towards the SW part of the profile, it can be

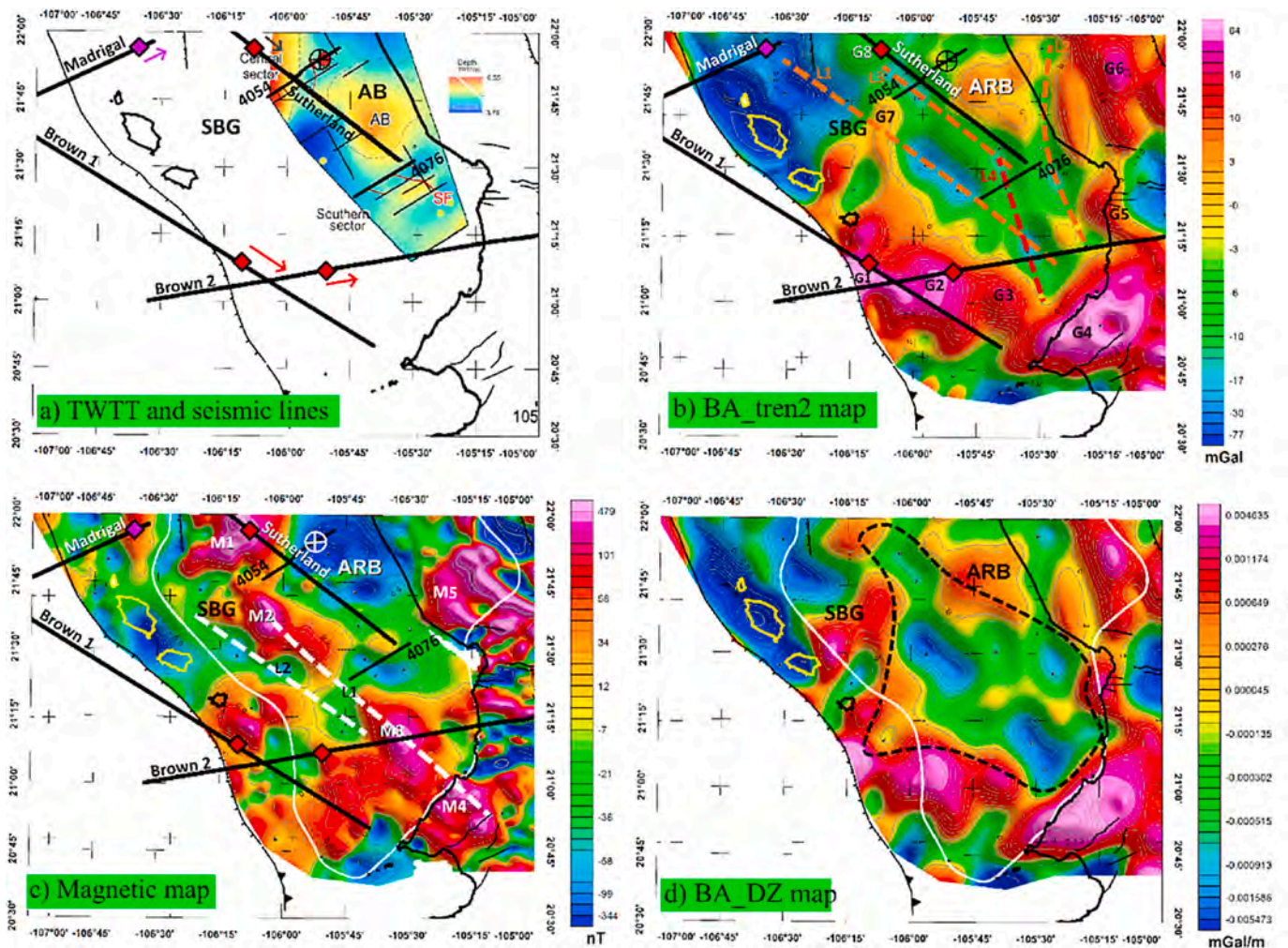


Fig. 16. Comparison of maps. a) TWTT map and seismic line positions. b) residual (Fig. 13). c) Magnetic map (Fig. 14). d) BA\_Dz with the possible boundaries of the SBB (Fig. 7). The arrows indicate the direction in which each author interprets the beginning of the SBB (in red) and the beginning of the SBG (in purple).

observed that the diffused section in the seismic data, attributed to interpreted gas, borders what appears to be the main axis of the SBB (L1 of Fig. 13; 4076 of Fig. 12).

Seismic profile 4054, starts with a decrease in gravity in the SW to NE direction, which is directly related to the seismic profile's descent into the acoustic basement. However, it begins to ascend around the midpoint of the profile. This behavior seems to be related to the igneous intrusions detected in the profile, from where the basement becomes diffused (Figs. 12 and 13).

The SBB magnetic anomaly map is presented with the seismic lines in Fig. 14. It is observed that the minima anomaly values are located over the area of the HUICHOL-1 well, in the seismic profile 4054 reported by Sánchez-Barra et al. (2022). The descending pattern of the anomaly aligns with the expected deepening of the basin towards the NE. However, the values are more negative than anticipated for an area of average depth, as indicated in the TWTT map by Sánchez-Barra et al. (2022), therefore it does not appear to be entirely associated with a basement feature.

The maximum offshore relative anomaly on the map (point M1; Fig. 14) is situated over the seismic profile of Sutherland et al. (2012). This anomaly begins to decrease at the point interpreted by the author as the start of the SBB. However, the behavior along the profile falls within relatively intermediate anomaly values, with some local maximum of anomaly that doesn't completely match the shape of the seismic profile.

On the SBB section, a series of anomaly maxima (points M2, M3, and M4; Fig. 14) stand out, aligned in a NW direction (L1). Among these

maxima: the one at point M1 is located over the gravimetric bulge highlighted in the residual map (Fig. 13; point 7) and the BA\_Dz map (point G8; Fig. 15) and seems to extend towards the SE over SBG, what was speculated as the main axis of the SBB in the residual map, up to point M3 and point M4. The anomaly at point M3 is directly situated over the SE gravitational minimum of the SBB. Point M4 is related to the Puerto Vallarta Batholith described by Alvarez et al. (2021).

In the onshore region, the absolute maximum anomaly of the map is observed. At this point (M5), appears to determine the E edge of the Mazatlán Basin as described by Sánchez-Barra et al. (2022). Furthermore, it can be observed that there is a minimum anomaly over the BA that connects with the absolute minimum anomaly of the map and is located at the abrupt change of concavity on the boundary of the Mazatlán Basin.

In the case of BA\_Dz (Fig. 15), we can observe a strong correlation between the residual map from Fig. 5 and the map of BA\_Dz from Fig. 13, which display nearly identical features. Some of the most prominent characteristics include a clearer description of continuities and discontinuities within the map. The ARB area is again delineated as a structural high and point G7 is marked as a structural high that disrupts the continuity between the SBG (L1) and the anomalies associated with the central axis of the SBB. To the NW of L1, between the point interpreted by Madrigal et al. (2021) and point G7, a separate minimum anomaly develops, distinct from the minimum anomaly in the Marias Islands.

We observe that point G8 (Fig. 13) coincides with the point of maximum magnetic anomaly (M1; Fig. 14) and with the interpretation



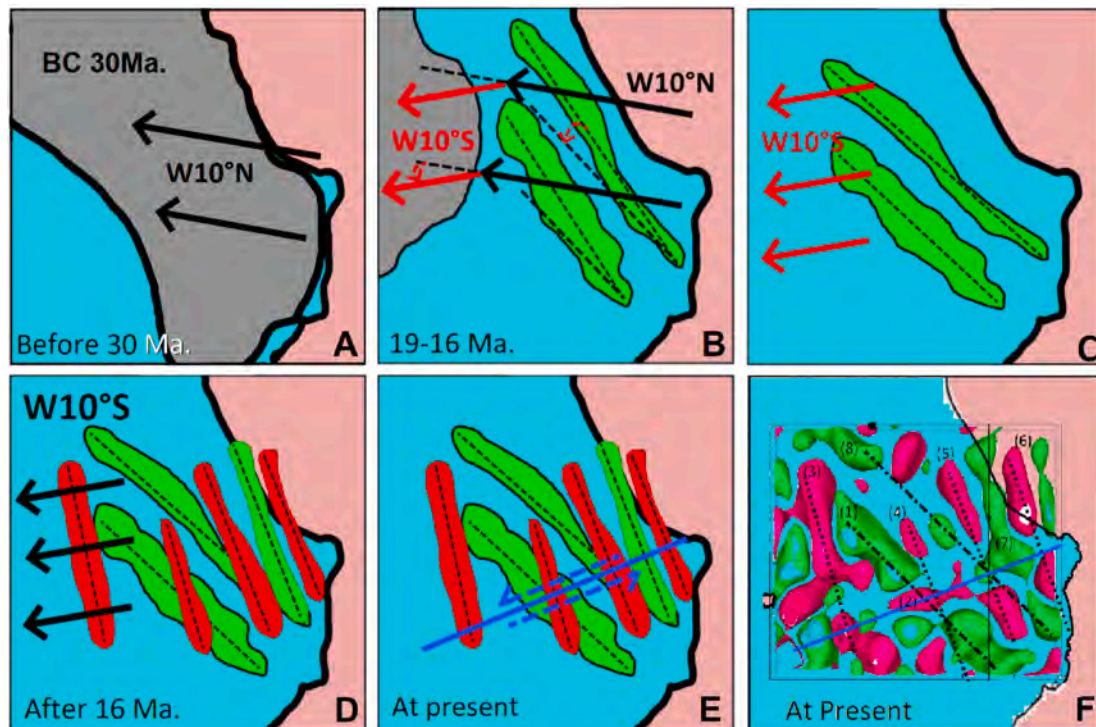


**Fig. 17.** Tectonic development of the SBB area between 30 Ma and the present. In panel A, we observe the position of the North American plate when the separation movement of BC began about 30 million years ago. Panel B refers to the process of change in the movement direction, occurring between 19 and 16 million years ago, over areas of extension and cortical thinning, causing its rotation. Panel C indicates the consolidation of the movement and the final rotated position of bodies associated with crustal thinning zones. Panel D shows the appearance of zones of high-density material associated with intrusions formed by the continuous extension regime. In panel E appears a fault system over the zone, which cuts through it. Panel F shows the geo-volume's current configuration, obtained from the 3D inversions.

of Sutherland et al. (2012) as the start of the SBB. Meanwhile, the BA area is traversed on the SW flank by the seismic data from Sutherland et al. (2012), which aligns with the morphology described by the seismic line. In this interpretation, at the beginning of the NW portion of the seismic trace, there is a relatively shallow basin, followed by a structural high related to the BA, and subsequently, a deeper development towards the SE where the seismic line does not reach the S boundary of the SBB (Fig. 12).

The seismic line 4076 traverses an area where the depth undergoes abrupt changes but exhibits a faulted basement with a diffuse horizon. The seismic trace 4054 shows a basement that descends from W to E, similar to what happens in the BA\_Dz, until the area just before the HUICHOL-1 well, where it increases slightly. This behavior closely resembles what was found in the TWTT map by Sánchez-Barra et al. (2022) (Fig. 12).

Fig. 16, shows a comparison of the TWTT map by Sánchez-Barra et al. (2022), residual, the magnetic map, and BA\_Dz. In Fig. 16a, we can observe the TWTT map. It delineates what would be the northern boundary of the SBB between the ARB and the high basement in the central sector of the Mazatlán Basin. This boundary seems to be correlated with the gravimetric bulge found in the residual and BA\_Dz maps (point G7; Figs. 13, 15 and 16b). Additionally, there is a minimum in the acoustic basement that serves as a connecting throat between the central section of the Mazatlán Basin and the SBB. Furthermore, in this TWTT map (Fig. 16a), it is evident that the depocenter of the basement is located in the southwestern section, where the minimum gravity anomalies are located in the maps of BA\_Dz\_trend2 (L1; Fig. 16b) y BA\_Dz (Fig. 16d) and in the gravimetric inversion (2; Fig. 10) that has been presented as the main axis of the SBB.

The magnetic map (Fig. 16c), highlights the absolute minimum anomaly of the map, which extends over the HUICHOL-1 well, and a minimum regional anomaly that extends over the ARB tableland. These

magnetic anomaly minima do not appear to be directly associated with the shape of the basement but seem to be associated with a region of high geothermal gradient, which would negatively influence the magnetism of the surrounding rocks.

Additionally, the maxima magnetic anomalies observed on the main axis of the SBB (L1, M2, and M3; Fig. 16c) appear to have similar origins. The NW maximum anomaly (point M2; Fig. 16c) seems to be associated with a gravity bulge that interrupts the connection between SBG and the SBB (point G7 of Fig. 16b). This suggests that it could be a volcanic process that may have deposited thin material onto the main axis of the Basin, thus explaining why the high magnetism appears to follow the depocenter of the basin, precisely where gravity has low values.

Similarly, in the SE magnetic anomaly of the main axis of the SBB (M3; Fig. 16c), the magnetic anomaly is recorded from the NW, just before the decrease in the gravity anomaly (L1 in Fig. 16b and d). Then it overlaps the shape of the gravity anomaly minimum combined with the relative maximum of magnetic anomaly located to the NW. This suggests that it could be a volcanic process that dispersed material into the basin.

Summarizing the geophysical evidence in the area, we can correlate the different gravimetric and magnetic anomalies with the boundaries of the SBB, connecting them in Fig. 16d through a segmented line.

In the northernmost part, we find the point identified by Sutherland et al. (2012) as the starting point of the SBB. To the W of the SBB, we observe a maximum of the anomaly developing in an almost N-S direction, connecting with the point (G1) interpreted by Brown (2007; seismic line Brown 1) as the beginning of the SBB. This anomaly further connects with point G2 on seismic line "Brown 2," which the author interprets as the start of the SBB.

At point G4, we encounter the absolute maximum anomaly on the map, which aligns with the Puerto Vallarta Batholith, defining the southeastern boundary of the basin.

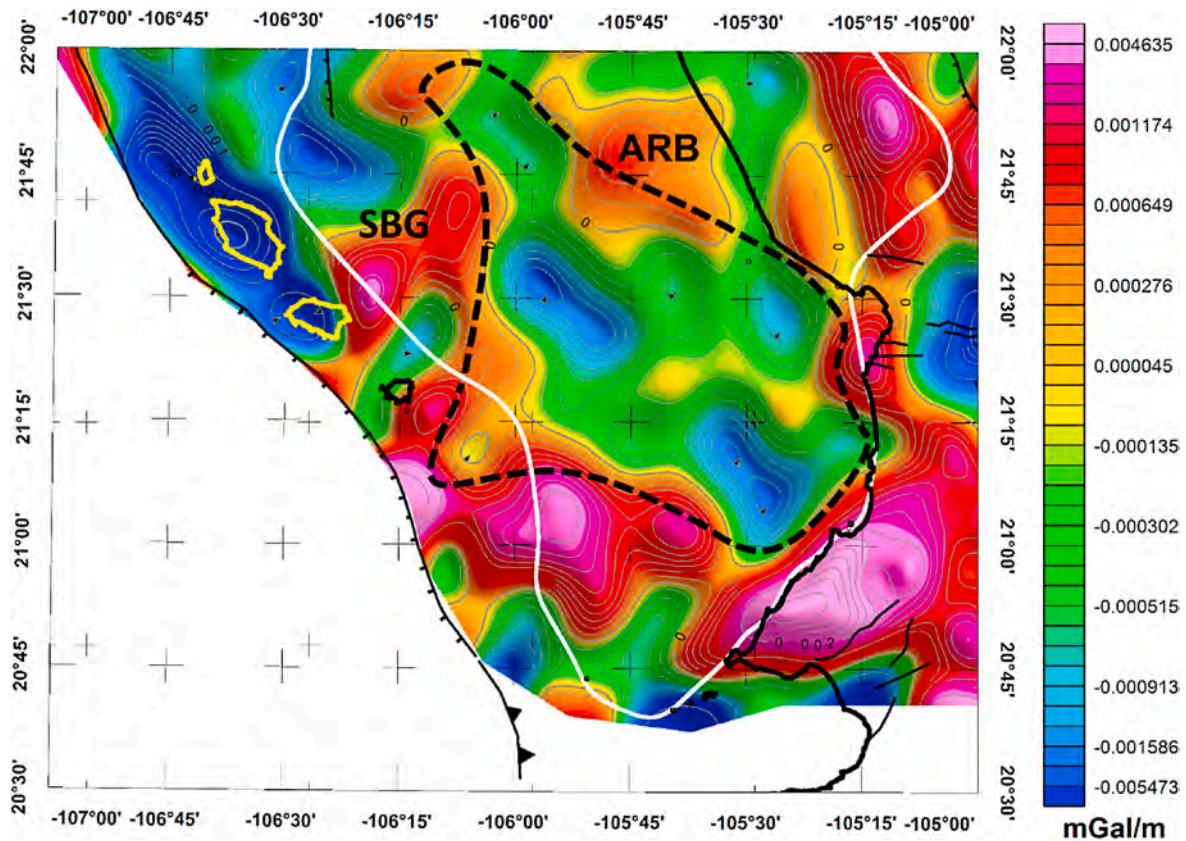


Fig. 18. Map of BA<sub>Dz</sub>. In gray lines, the anomaly contours. In thin black lines the most representative onshore faults in the area. The continuous black line represents the coastline, and the gray continuous lines represent the Bouguer anomaly contours. The continuous white line delineates the Mazatlán Basin. SBG: San Blas Gorge. ARB: Aramara Bulge. The segmented black line locates the proposed SBB boundaries.

Moving towards point M5, we observe a maximum anomaly that intersects with a minimum anomaly described by Camacho and Alvarez (2020), which is associated with the boundary of the Jalisco Block along the Tepic-Zacoalco Rift and, therefore, the connecting zone with the SBB. Finally, we see that these anomalies continue to the north through a couple of smaller gravimetric anomalies, which connect with the Aramara Bulge (ARB) described by Alvarez et al. (2017), following a relatively small throat, which is consistent with the shape shown on the TWTT map. Additionally, these anomalies correlate with a magnetic structure observed at point M5 on the magnetic map (Fig. 16c).

#### 4.2. 3D inversions summary

From the 3D gravimetric and magnetic inversion models, we can infer that there are three main directions of alignment of the anomaly bodies; we submit that these directions are possibly associated with the tectonic processes that occurred in the area.

The first of these patterns, represented by the blue line in Figs. 10 and 11, appears to intersect the other two anomaly patterns. This suggests that it may be a fault that intersects those patterns. We observe that this alignment is evident in the density inversion and magnetic susceptibility results, further supporting the idea of a boundary along that area.

The second pattern of maximum density anomaly bodies, oriented at N15°W and outlined by the dashed line (lines 3, 4, 5, and 6; Fig. 10), may be associated with an intrusion process resulting from crustal fractures caused by extensional movements between 18 and 12 million years ago. This aligns with the direction of movement of the Baja California microplate during that period and age, as suggested by some of the batholiths found along the coastline, as documented by Duque-Trujillo et al. (2015) and Ferrari et al. (2018). The minimum density anomaly body with the same orientation (line 7; Fig. 10) could be linked

to a crustal extension and thinning process that occurred during the period from 18 to 12 million years ago, although it did not lead to the development of material intrusions.

The third pattern is represented by the bodies associated with the density anomaly minima. Lineaments that present an orientation of N45°W approximately, located over the SBG (line 1; Fig. 10) and in the area of greatest basin depth (line 8; Fig. 10; according to the seismic line of Sutherland et al., 2012). This pattern may be indicative of zones of crustal thinning by extension at the time of SBB formation, which likely began between 19 and 16 Ma, as pointed out by Ferrari et al. (2018). If the SBB was formed during that period, it would be exposed to a change in orientation when the movement of Baja California passed from W10°N to W10°S, at approximately 18 Ma. For this reason, it is reasonable to assume that the orientation of the SBB was shifted to the SW from its initial orientation due to the movement of BC. If we take the current position of the SBB and rotate it in the opposite direction to the movement described 20–25° counterclockwise, we observe that parallelism arises with the lineaments found in bodies oriented N15°W. This suggests that the SBB formed in the transition period of BC's movement from W10°N to W10°S, and that, as Baja California reoriented from the W10°S direction 18 Ma to the present one, it also reoriented the direction of the SBB to its current position.

The development of the SBB according to the inferred BC movement is explained in Fig. 17, through the trends and bodies found in the gravimetric inversion. The position of the coastline and the beginning of the W10°S movement at 30 Ma of BC is shown in Fig. 17A. Fig. 17B shows the lower-density bodies in their possible position of creation between 19 Ma and 16 Ma, just before the change in direction of BC's movement; when the direction of BC's movement changes, it tends to deform the crustal area between BC and the continent, generating a change in orientation of the bodies' axis. In Fig. 17C, the movement of

BC changes towards W10°S, and its motion takes it beyond the exposed window, establishing a stress regime in the direction of W10°S. In Fig. 17D, it is observed how this tectonic force stretches and thins the crust, allowing the zone of intrusion of material and crustal thinning represented by the red (intrusions) and green (thinning) bodies. In Fig. 17E, emerges the fault system that generates the rupture pattern observed in the 3D inversion. Fig. 17F shows the gravimetric inversion area, with the lineaments and bodies in their current position.

## 5. Conclusions

The Bouguer anomaly in the SBB area decreases in a direction that coincides with the orientation of the intrusive bodies (Figs. 4 and 10). In addition, the large number of landforms present in the area mask the characteristic features of the SBB, which requires detailed filtering processes of the gravimetric data to be exposed, such as those applied in this study.

The directional derivative filters demonstrate a correlation with seismic surveys, which proves to be valuable for identifying target areas. This complements the results obtained from other geophysical methods such as TWTT in seismic lines.

From 3D inversions, it is inferred that the most important tectonic processes in the SBB area go mainly in two directions. This tends to reaffirm the argument of Sutherland et al. (2012), in which the SBB had to be older than 12 Ma and could be related to the period between 30 and 18 Ma suggested by Ferrari et al. (2013) and ratified by Ferrari et al. (2018) since it has a concordant development in the orientations of the bodies found. Consequently, the SBB formation model proposed herein is consistent with such observations.

Fig. 17 shows the development model of the SBB, through the 3D gravimetric inversion model located in the area, for the last 30 Ma.

The interpretation of the previously exposed geophysical evidence and finally the interpreted seismic lines suggest that the boundaries of the SBB are those presented in Fig. 18, in which an overlaid polygon is observed, which represents the proposed delimitation obtained for the geometry of the SBB.

## CRedit authorship contribution statement

**M. Camacho-Ascanio:** Writing – original draft, Visualization, Validation, Software, Resources, Methodology, Investigation, Funding acquisition, Formal analysis, Data curation, Conceptualization. **R. Alvarez:** Writing – review & editing, Supervision, Project administration, Conceptualization.

## Declaration of competing interest

The authors declare that they have no known competing financial interests or personal relationships that could have appeared to influence the work reported in this paper.

## Data availability

Data will be made available on request.

## Acknowledgments

During the development of this work, Miguel Camacho received support from the Consejo Nacional de Ciencia y Tecnología (CON-AHCYT, México). This study was supported by: Instituto de Investigaciones en Matemáticas Aplicadas y en Sistemas, Universidad Nacional Autónoma de México, Posgrado en Ciencias de la Tierra, and Instituto de Geofísica, Universidad Autónoma de México. We acknowledge material support from these institutions.

## References

- Alvarez, R., Corbo Camargo, F., Yutsis, V.v., Arzate, J.A., 2017. A volcanic center in Mexico's Pacific continental shelf. Geological Society, London, Special Publications 446 (1), 281–293. <https://doi.org/10.1144/SP446.12>.
- Alvarez, R., Corbo-Camargo, F., Yutsis, V., 2021. The great tectonic discontinuity of Bahía de Banderas, Mexico. Tectonophysics 803. <https://doi.org/10.1016/j.tecto.2021.228762>.
- Alvarez, R., Camacho, M., 2023a. Plumbing system of Hunga Tonga Hunga ha'apai Volcano. J. Earth Sci. 34, 706–716. <https://doi.org/10.1007/s12583-022-1792-0>.
- Alvarez, R., Camacho, M., 2023b. Applying high-resolution gravity analysis to volcanic plumbing systems: the case of Nevado de Toluca volcano, Mexico. Transactions on Engineering and Computing Sciences 11 (4), 184–207. <https://doi.org/10.14738/tecs.114.15392>.
- Bankey, V., Hernandez, I., Pilkington, M., Shearer, S., Cuevas, A., Hill, P., Roberts, C., Snyder, S., Daniels, D., Kucks, R., Roest, W., Sweeney, R., 2002. Carte des Anomalies Magnétiques de l'Amérique du Nord Magnetic Anomaly Map of North America Mapa de la Anomalia Magnética de Norteamérica Processing, Compilation, and Geologic Mapping Applications of the New Digital Magnetic Anomaly Database and Map of North America By North American Magnetic Anomaly Group (NAMAG). <https://pubs.usgs.gov/of/2002/ofr-02-414/>.
- Brown, H., 2007. Crustal Rupture, Creation, and Subduction in the Gulf of California and the Role of Gas Hydrate in the Submarine Storegga Slide, Offshore Norway [Ph.D. Thesis. Laramie, University of Wyoming, p. 165.
- Camacho, M., Alvarez, R., 2020. Gravimetric analysis of the rifts and volcanic fields of the Jalisco block, Mexico. Tectonophysics 791 (July), 228577. <https://doi.org/10.1016/j.tecto.2020.228577>.
- Camacho, M., Alvarez, R., 2021. Geophysical modeling with satellite gravity data: eigen-6C4 vs. GGM Plus. Engineering 13 (12), 690–706. <https://doi.org/10.4236/eng.2021.1312050>.
- DeMets, C., Traylen, S., 2000. Motion of the Rivera plate since 10 Ma relative to the Pacific and North American plates and the mantle. Tectonophysics 318 (1–4), 119–159. [https://doi.org/10.1016/S0040-1951\(99\)00309-1](https://doi.org/10.1016/S0040-1951(99)00309-1).
- Duque-Trujillo, J., Ferrari, L., Orozco-Esquivel, T., López-Martínez, M., Lonsdale, P., Bryan, S.E., Kluesner, J., Piñero-Lajas, D., Solari, L., 2015. Timing of rifting in the southern Gulf of California and its conjugate margins: insights from the plutonic record. Bull. Geol. Soc. Am. 127 (5–6), 702–736. <https://doi.org/10.1130/B31008.1>.
- Ellis, R.G., de Wet, B., Macleod, I.N., 2012. Inversion of magnetic data from remanent and induced sources. ASEG Extended Abstracts 2012 (1), 1–4. <https://doi.org/10.1071/ASEG2012ab117>.
- Ferrari, L., López-Martínez, M., Orozco-Esquivel, T., Bryan, S.E., Duque-Trujillo, J., Lonsdale, P., Solari, L., 2013. Late Oligocene to middle Miocene rifting and syn extensional magmatism in the southwestern Sierra Madre Occidental, Mexico: the beginning of the Gulf of California rift. Geosphere 9 (5), 1161–1200. <https://doi.org/10.1130/GES00925.1>.
- Ferrari, L., Orozco-Esquivel, T., Bryan, S.E., López-Martínez, M., Silva-Fragoso, A., 2018. Cenozoic magmatism and extension in western Mexico: linking the Sierra Madre Occidental silicic large igneous province and the Comondú Group with the Gulf of California rift. Earth Sci. Rev. 183, 115–152. <https://doi.org/10.1016/j.earscirev.2017.04.006>. May 2017.
- Fletcher, J.M., Grove, M., Kimbrough, D., Lovera, O., Gehrels, G.E., 2007. Ridge-trench interactions and the Neogene tectonic evolution of the Magdalena shelf and the southern Gulf of California: insights from detrital zircon U-Pb ages from the Magdalena fan and adjacent areas. Bull. Geol. Soc. Am. 119 (11–12), 1313–1336. <https://doi.org/10.1130/B26067.1>.
- Gastil, G., Krummenacher, D., Minch, J., 1979. The record of Cenozoic volcanism around the Gulf of California. Bull. Geol. Soc. Am. 90 (9), 839–857. [https://doi.org/10.1130/0016-7606\(1979\)90<839:TROCVA>2.0.CO;2](https://doi.org/10.1130/0016-7606(1979)90<839:TROCVA>2.0.CO;2).
- GEBCO Compilation Group, 2023. The GEBCO\_2023 Grid - a continuous terrain model of the global oceans and land. [https://www.gebco.net/data\\_and\\_products/gridded\\_bathymetry\\_data/](https://www.gebco.net/data_and_products/gridded_bathymetry_data/).
- Götze, H.J., Li, X., 1996. Topography and geoid effects on gravity anomalies in mountainous areas as inferred from the gravity field of the Central Andes. Phys. Chem. Earth 21 (4), 295–297. [https://doi.org/10.1016/S0079-1946\(97\)00051-7](https://doi.org/10.1016/S0079-1946(97)00051-7).
- Hildenbrand, T.G., Briesacher, A., Flanagan, G., Hinze, W.J., 2002. Rationale and Operational Plan to Upgrade the U.S. Gravity Database, vols. 1–12. USGS Open File Report.
- Hinze, W.J., von Frese, R.R.B., Saad, A.H., 2013. Gravity and Magnetic Exploration. Cambridge University Press. <https://doi.org/10.1017/CBO9780511843129>.
- Ince, E.S., Barthelmes, F., Reißland, S., Elger, K., Förste, C., Flechtner, F., Schuh, H., 2019. Icgem – 15 years of successful collection and distribution of global gravitational models, associated services and future plans. Earth Syst. Sci. Data 11, 647–674. <https://doi.org/10.5194/essd-11-647-2019>.
- Ingram, D.M., Causon, D.M., Mingham, C.G., 2003. Developments in Cartesian cut cell methods. Math. Comput. Simulat. 61 (3–6), 561–572. [https://doi.org/10.1016/S0378-4754\(02\)00107-6](https://doi.org/10.1016/S0378-4754(02)00107-6).
- Kane, M.F., 1962. A comprehensive system of terrain corrections using a digital computer. Geophysics 27 (4), 455–462. <https://doi.org/10.1190/1.1439044>.
- Karig, D.E., Jency, W., 1972. The proto-Gulf of California. Earth Planet Sci. Lett. 17 (1), 169–174. [https://doi.org/10.1016/0012-821X\(72\)90272-5](https://doi.org/10.1016/0012-821X(72)90272-5).
- Lizarralde, D., Axen, G.J., Brown, H.E., Fletcher, J.M., González-Fernández, A., Harding, A.J., Holbrook, W.S., Kent, G.M., Paramo, P., Sutherland, F., Umhoefer, P. J., 2007. Variation in styles of rifting in the Gulf of California. Nature 448 (7152), 466–469. <https://doi.org/10.1038/nature06035>.

- Macleod, I.N., Ellis, R.G., 2013. Magnetic vector inversion, a simple approach to the challenge of varying direction of rock magnetization. *Australian Society of Exploration Geophysicists, Extended Abstracts 2013*, 1–4. Melbourne.
- Madrigal, L.A., Núñez, D., Escalona-Alcázar, F. de J., Núñez-Cornú, F.J., 2021. Crustal structure across the northern region of the Islas Marías archipelago. *Front. Earth Sci.* 9 <https://doi.org/10.3389/feart.2021.682206>.
- Milsom, J., 2003. Magnetic Methods. In *FIELD GEOPHYSICS. THE GEOLOGICAL FIELD GUIDE SERIES. Issue C*.
- Moore, D.G., 1973. Plate-edge deformation and crustal growth, gulf of California structural province. *Bull. Geol. Soc. Am.* 84 (6), 1883–1906. [https://doi.org/10.1130/0016-7606\(1973\)84<1883:PDACGG>2.0.CO;2](https://doi.org/10.1130/0016-7606(1973)84<1883:PDACGG>2.0.CO;2).
- Nagy, D., 1966. The gravitational attraction of a right rectangular prism. *Geophysics* 31 (2), 362–371. <https://doi.org/10.1190/1.1439779>.
- Ortega-Gutiérrez, F., Elías-Herrera, M., Morán-Zenteno, D.J., Solari, L., Luna-González, L., Schaaf, P., 2014. A review of batholiths and other plutonic intrusions of Mexico. *Gondwana Res.* 26 (3–4), 834–868. <https://doi.org/10.1016/j.gr.2014.05.002>.
- Sánchez-Barra, A.C., González-Escobar, M., Ferrari, L., 2022. Subsurface structure of the Mazatlán basin, southeastern Gulf of California, Mexico, from seismic reflection and well data. *Tectonophysics* 838. <https://doi.org/10.1016/j.tecto.2022.229505>.
- Sutherland, F.H., Kent, G.M., Harding, A.J., Umhoefer, P.J., Driscoll, N.W., Lizarralde, D., Fletcher, J.M., Axen, G.J., Holbrook, W.S., González-Fernández, A., Lonsdale, P., 2012. Middle Miocene to early Pliocene oblique extension in the southern Gulf of California. *Geosphere* 8 (4), 752–770. <https://doi.org/10.1130/GES00770.1>.
- Stock, J.M., Hodges, K., 1989. Pre-pliocene extension around the gulf of California and the transfer of Baja California to the pacific plate. *Tectonics*. <https://doi.org/10.1029/TC008i001p00099>, June 2014.
- Tozer, B., Sandwell, D.T., Smith, F., Olson, C., Beale, J.R., Wessel, P., 2019. Global bathymetry and topography at 15 arc sec: SRTM15+. *Earth Space Sci.* 6 (10), 1847–1864. <https://doi.org/10.1029/2019EA000658>.
- Yeats, R.S., Haq, B.U., 1981. Deep-Sea drilling off the California's: implications of leg 63. *Initial Rep. Deep Sea Drill. Proj.* 63 <https://doi.org/10.2973/dsdp.proc.63.141.1981>. September.

Capítulo 3: *Gravimetric analysis of the rifts and volcanic fields of the Jalisco block, Mexico.*



# Gravimetric analysis of the rifts and volcanic fields of the Jalisco block, Mexico

Miguel Camacho<sup>a</sup>, Román Alvarez<sup>b,\*</sup>

<sup>a</sup> Posgrado en Ciencias de la Tierra, Ciudad Universitaria, Universidad Nacional Autónoma de México, Mexico City 04510, Mexico

<sup>b</sup> Instituto de Investigaciones en Matemáticas Aplicadas y en Sistemas (IIMAS), Universidad Nacional Autónoma de México, Mexico City 04510, Mexico

## ARTICLE INFO

### Keywords:

EIGEN-6C4 satellite data  
Jalisco Block  
Guadalajara Triple Point  
Colima rift  
Bahía de Banderas  
Bouguer anomalies

## ABSTRACT

The gravity map of the complete Jalisco Block (JB) is obtained from satellite-derived measurements at a resolution of ~1 km separation, including the offshore region up to the Middle America Trench (MAT). Tepic-Zacoalco (TZ) and Colima delimiting rifts of the JB are identified as gravimetric minima. The NW limit of the block appears also as a rifted zone, with a gravity minimum connecting Bahía de Banderas with the TZ rift, defining a new triple point: the Compostela Triple Point (rift-rift-rift) that together with the Guadalajara Triple Point determine the north boundary of the Jalisco Block. The largest negative gravity anomalies are observed associated with the Central Jalisco Volcanic Lineament (CJVL) and Bahía de Banderas; they appear to be connected since they are only separated by a small positive anomaly east of Bahía de Banderas. The CJVL is parallel to the Middle America Trench, exhibiting a discontinuous alignment of Quaternary volcanism from the Colima Volcanic Complex to the northwestern rifted limit of the Jalisco Block. Ameca and Santiago rivers flow parallel to each other in a northwesterly direction for 100 km, then Santiago river changes course to continue 64 km in a north-northwesterly direction up to Aguamilpa dam. Ameca river should follow the same direction; instead, it abruptly changes its course to a southwesterly direction to discharge in Bahía de Banderas. The drastic course deviation is attributed to the intersection of Ameca river causeway with the Bahía de Banderas-Compostela rift, proposed in this study to be the northwestern limit of the Jalisco Block.

## 1. Introduction

Rifting and lithospheric extension are often associated with the separation of large land masses (Hopper and Buck, 1996; Rosenbaum et al., 2008; Thybo and Artemieva, 2013). A separation process of this type has been occurring in western Mexico since ~12 Ma; Baja California peninsula has been drifting northwesterly since its capture by the Pacific plate (Lonsdale, 1989; Fletcher et al., 2007; Ferrari et al., 2013). The continental region left behind by the retreating peninsula is known as the Jalisco Block.

The limits of the Jalisco Block (JB) were originally established by Allan (1986) and are schematically shown in Fig. 1a. Baja California was close to the JB before rifting induced the separation between the peninsula and mainland Mexico, which according to Ferrari et al. (2013) could have begun as early as the Late Oligocene; those initially neighboring regions are now identified as Los Cabos Block and Jalisco Block (Böhnel and Negendank, 1988; Böhnel et al., 1992; Ortega-Rivera, 2003; Duque-Trujillo et al., 2015). In the separation process, the crust NW of the JB (Bahía de Banderas) was extended and thinned

(Lizarralde et al., 2007; Sutherland et al., 2012) creating a passive margin, whilst SE of Bahía de Banderas an active margin exists. In addition, there is a major transition N of the JB, where the Mesozoic plutonic rocks of the Puerto Vallarta batholith change to Oligocene-Miocene volcanics of the Sierra Madre Occidental (Fletcher et al., 2007).

For around three decades, the NW limit of the JB has been debated. If it is located where Johnson and Harrison (1990) and Alvarez (2002) have proposed, then the neighboring San Blas basin must be identified as a continental sliver, different from the JB. Here, we analyze this boundary by means of a gravity analysis that includes not only the NW region, but the overall land limits of the JB. The gravity analysis has unprecedented accuracy and resolution, allowing for establishing anomaly trends and characteristics that previous studies were unable to discern. As we will show, these results support the existence of a rifted region as the NW limit of the JB, adding the observation that where this limit intersects the N limit of the JB (Tepic-Zacoalco rift) there is a newfound triple point (Compostela Triple Point).

\* Corresponding author.

E-mail address: [roman.alvarez@iimas.unam.mx](mailto:roman.alvarez@iimas.unam.mx) (R. Alvarez).

<https://doi.org/10.1016/j.tecto.2020.228577>

Received 18 February 2020; Received in revised form 20 July 2020; Accepted 28 July 2020

Available online 01 August 2020

0040-1951/ © 2020 Published by Elsevier B.V.

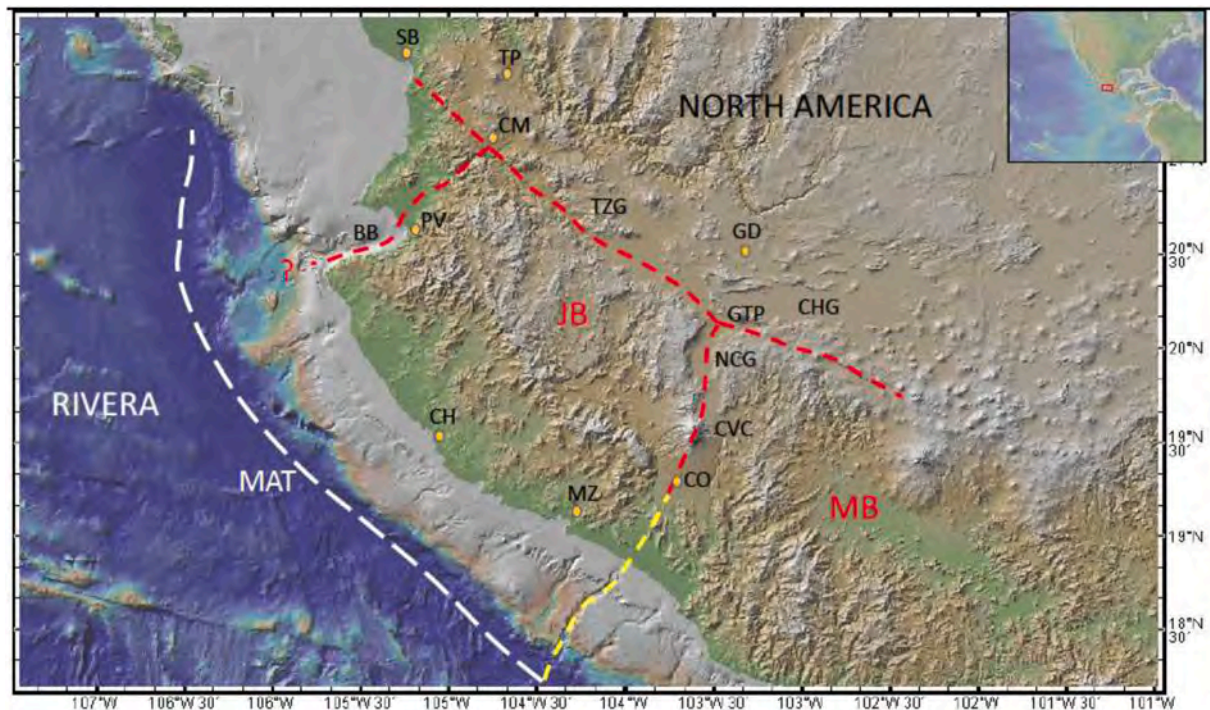


Fig. 1. a) Established and proposed limits of the Jalisco Block (JB). This gravimetric study involves the whole of the Jalisco Block (JB), including the offshore region to the MAT, at a resolution of  $\sim 1$  km. The yellow line at the SE portion of the block is the limit proposed by Alvarez and Yutsis (2015a). Bathymetry (blue to light brown) and topography (light green to brown) are from Ryan et al. (2009). MAT, Middle America Trench. MB, Michoacán Block. CVC, Colima Volcanic Complex. GTP, Guadalajara Triple Point. BB, Bahía de Banderas, NCG, Northern Colima Graben. CHG, Chapala Graben. TZG, Tepic-Zacoalco Graben. Orange dots correspond to cities: SB, San Blas. TP, Tepic. CM, Compostela. GD, Guadalajara. CH, Chamela. CO, Colima. MZ, Manzanillo. b) Main tectonic elements of the Jalisco Block, showing its rifted limits and the major topographic domains (static and uplifted). MAT, Middle America Trench. Orange traces correspond to geologic faults. Triangles represent volcanic fields. CVC, Colima Volcanic Complex. Central Jalisco Volcanic Lineament (CJVL, black dashed line) including San Sebastián Volcanic Field (SSVF), Mascota Volcanic Field (MVF), Ayutla Volcanic Field, (AVF). Other volcanic outcrops are: SJ, San Juan. SGG, Sanguaney. CB, Ceboruco. LVVF, Los Volcanes Volcanic Field. Dots correspond to cities: SB, San Blas. TP, Tepic. CM, Compostela. GD, Guadalajara. CH, Chamela. CO, Colima. MZ, Manzanillo. BN, Barra de Navidad. GTP, Guadalajara Triple Point. LCH, Chapala Lake. (For interpretation of the references to colour in this figure legend, the reader is referred to the web version of this article.)

## 2. The Jalisco Block

The boundaries of the Jalisco Block were originally defined by Allan (1986) as three large graben systems: the Chapala graben, the Tepic-Chapala rift and the south trending Colima rift, which together outline the Tepic-Colima Structural Block presently known as the Jalisco Block. This author considered the Tepic-Chapala graben extending north-westerly from the triple junction south of Guadalajara city to the coast of Nayarit, and the Colima rift extending from the triple point southwardly to the Colima coast; Fig. 1a shows these limits. Definitions of the JB limits have been discussed by various authors (e.g., Rosas-Elguera et al., 1996); offshore limits have also been proposed (e.g., Bourgois et al., 1988).

The geodynamics of the Rivera, Cocos, and North America plates determines the tectonics of the Jalisco Block (DeMets and Stein, 1990; Barrier et al., 1990; Stock and Hodges, 1989; Bandy et al., 1995; Pardo and Suárez, 1995; Ferrari and Rosas-Elguera, 2000; Ferrari et al., 2012). From the plate interactions, the block developed extensional tectonics on the NE portion (Colima rift) as well as on the N portion (Tepic-Zacoalco rift). On the SE portion the block shows compressional tectonism originating in the subduction of the Rivera and Cocos plates under the North America plate (Stock, 1993; León-Soto et al., 2009; Khutorskoy et al., 1994; Alvarez and Yutsis, 2015a).

Owing to the size of the Jalisco Block previous gravimetric determinations have been restricted mostly to studies along two-dimensional profiles, or local portions of the block (Allan, 1985; Serpa et al., 1992; Bandy et al., 1993; Urrutia-Fucugauchi and Molina-Garza, 1992; Medina et al., 1996; Bandy et al., 1999; Urrutia-Fucugauchi et al., 1999;

Serrato-Díaz et al., 2004; Alvarez and Yutsis, 2015b). This is the first attempt at describing the characteristics of the full block up to the Middle America Trench (MAT) from the viewpoint of its gravity properties, with a resolution of  $\sim 1$  km, which is made possible by the availability of a new set of gravity data derived from the satellite observations of the EIGEN-6C4 gravity model, to be discussed below. There is one previous exercise in which the Bouguer anomaly of the complete Jalisco Block was included in a map of the Trans-Mexican Volcanic Belt (Urrutia-Fucugauchi and Flores-Ruiz, 1996); however, their work focused on crustal thickness under central Mexico and its resolution was of 11.11 km, contrasting with the resolution of 1 km in the present study.

With the present approach we not only can evaluate the surface characteristics of the major components of the block, such as the limiting rifts and the Colima Volcanic Complex, but also can determine some of its characteristics, such as alignment of gravity anomalies, and the presence and extent of massive bodies associated with the Puerto Vallarta or Manzanillo batholiths (Böhnel and Negendank, 1988; Schaaf et al., 1993). The offshore region reaching beyond the MAT is also included in this dataset, allowing for the connection between features that encompass both regions.

This integral, gravimetric view of the Jalisco Block allows for identifying previously unknown links and trends of the anomalies that may help explain why the Jalisco Block constitutes a tectonic unit. The map in Fig. 1b shows the main elements of the tectonic block, including the rifted limits and the uplifted and static domains defined by Alvarez et al. (2006); the former consists of highlands above 1800 m altitude, whereas the latter consists mainly of coastal plains. The limit between

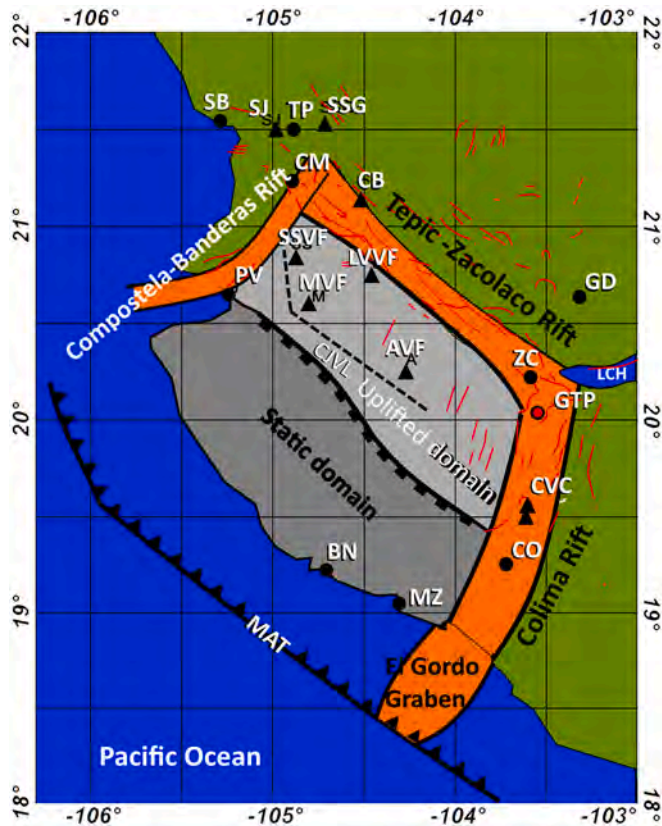


Fig. 1. (continued)

the two domains follows a trench-parallel orientation. There is a fair correlation between this limit and the volcanic activity observed along the Central Jalisco Volcanic Lineament (CJVL), suggesting a connection of the uplifted domain and the CJVL with the plate rollback. The effects of tectonic forces, surface processes, and mantle flow on the alteration of surface topography reported by Cassel et al. (2018) show that in the hinterland of the North American Cordillera subsidence from suction at the slab hinge, as well as surface uplift from isostatic effects of heating and delamination create a tectonic scenario that we consider quite similar to that of the Jalisco Block. If this proves to be true, the implication is that the plate rollback that has been inferred at the NW and NE ends of the block (Yang et al., 2009; León-Soto et al., 2009; Corbo et al., 2013) probably involves the full, trench-parallel width of the Jalisco Block, as depicted in Fig. 1b.

In the present version, the NW rift (Fig. 1b) terminates at the W end of Bahía de Banderas. From that point to the Middle America Trench (MAT) there are intricate patterns of the bathymetry and the Bouguer anomaly introduced by the NW to N bending of the MAT near its terminus. This region needs detailed local modeling and interpretation, in order to determine if the rift actually extends to the MAT, and if it does in what direction. Owing to its complexity and its great interest for the tectonics of the Jalisco Block, a detailed study of this region cannot be dealt with in the present work.

### 3. Data acquisition and processing

Obtaining the Bouguer anomaly from gravity data is a well-known procedure; however, recent additions to data processing improve data precision, yielding higher resolutions. In our calculations we include several of these improvements. In particular, we perform ellipsoidal corrections using a higher resolution of the ellipsoid, which are not common in many gravimetric calculations, as neither are the aggregate of second-degree terms to the traditional textbook equations, taking

into account the earth's curvature and a term for the correction of distortion by spherical layers. The atmospheric correction, included in these calculations, is neither common in traditional Bouguer anomaly estimations, but is particularly necessary for satellite data. Using the most recent satellite database (EIGEN-6C4) allowed us to observe and define structural features which had not been resolved by traditional gravimetry or previous satellite data models in the area. These differences with traditional calculations persuaded us to present the detailed procedure to obtain the Bouguer anomaly, involving land and oceanic areas in the same dataset. This treatment gives our work greater precision with unprecedented resolution; the present data treatment can be of interest in gravity studies elsewhere.

#### 3.1. Bouguer anomaly

We use the observed gravity model of EIGEN-6C4 of the International Centre for Global Earth Models (ICGEM), (Barthelmes and Köhler, 2016), with a node separation of ~1 km. For the topography we used the Digital Elevation Model (DEM) of ASTER (<https://gdex.cr.usgs.gov/gdex/>) with a 30 m resolution and the bathymetry of SRTM30 with 200 m resolution obtained from ([http://topex.ucsd.edu/cgi-bin/get\\_srtm30.cgi](http://topex.ucsd.edu/cgi-bin/get_srtm30.cgi)). The gravity data were processed according to the new standard of the United States Geological Survey (USGS) described by Hildenbrand et al. (2002). The data from ICGEM are given as Observed Gravity Data (G\_Obs); consequently, we calculated the Topographic Correction (TC), the Theoretical Gravity (G\_Theo), the Free Air Correction (C\_FA), the Atmospheric Correction (C\_Atm), the Free Air Anomaly (FA), the Bouguer Correction (BC), and finally the Bouguer Anomaly (BA), all of them calculated to the second order.

We combined the topographic and bathymetric data (ASTER and SRTM30) in a single database. We performed the necessary corrections to go from the raw data to the first degree Bouguer anomalies reduced to the GRS80 ellipsoid, with a reduction density of 2.67 g/cm<sup>3</sup>. The EIGEN-6C4 data were downloaded without filters, with expansion to the 2190 harmonic, and a resolution of 0.09° (approximately 1 km) between nodes. The topography data with 30 m resolution were downloaded from longitude -107.5 to -103.0° and from latitude 17.0 to 22.0°; that is, with approximately one additional degree on the sides of the study area. The same area was covered for the bathymetry from SRTM30. From the ICGEM web page we also downloaded the EMG96 database for the geoid in the same window as the topography data.

The theoretical gravity was calculated using eq. (1) based on the geo-reference system GRS80 (Moritz, 2000; Hildenbrand et al., 2002).

$$G_{theo} = G_e \frac{(1 + k * (\sin \varphi)^2)}{\sqrt{1 - e^2 * (\sin \varphi)^2}} \quad (1)$$

where:  $\varphi$  = latitude

$$G_e = 978032.67715 \text{ (mGal)}$$

$$k = 0.001931851353$$

$$e^2 = 0.0066943800229$$

The Free Air correction to the second order was calculated with eq. (2), where h (in m) is the difference from the station to the ellipsoid (Li and Gotze, 2001; Hildenbrand et al., 2002). We assumed h = 0 in the data over the sea, since they are reported with respect to the surface of the ocean (Smith and Sandwell, 1997)

$$C_{FA} = (0.3087691 - 0.0004398 * \sin^2(\varphi)) * h + 7.2125 * 10^{-8} * h^2 \text{ [mGal]} \quad (2)$$

h in m.

The atmospheric correction was performed with eq. (3), where h (in m) is the station height with respect to the ellipsoid (Hildenbrand et al., 2002), to correct for the air mass above the station

$$C_{Atm} = 0.874 - 9.9 * 10^{-5}h + 3.56 * 10^{-9}h^2 \text{ [mGal]} \quad (3)$$



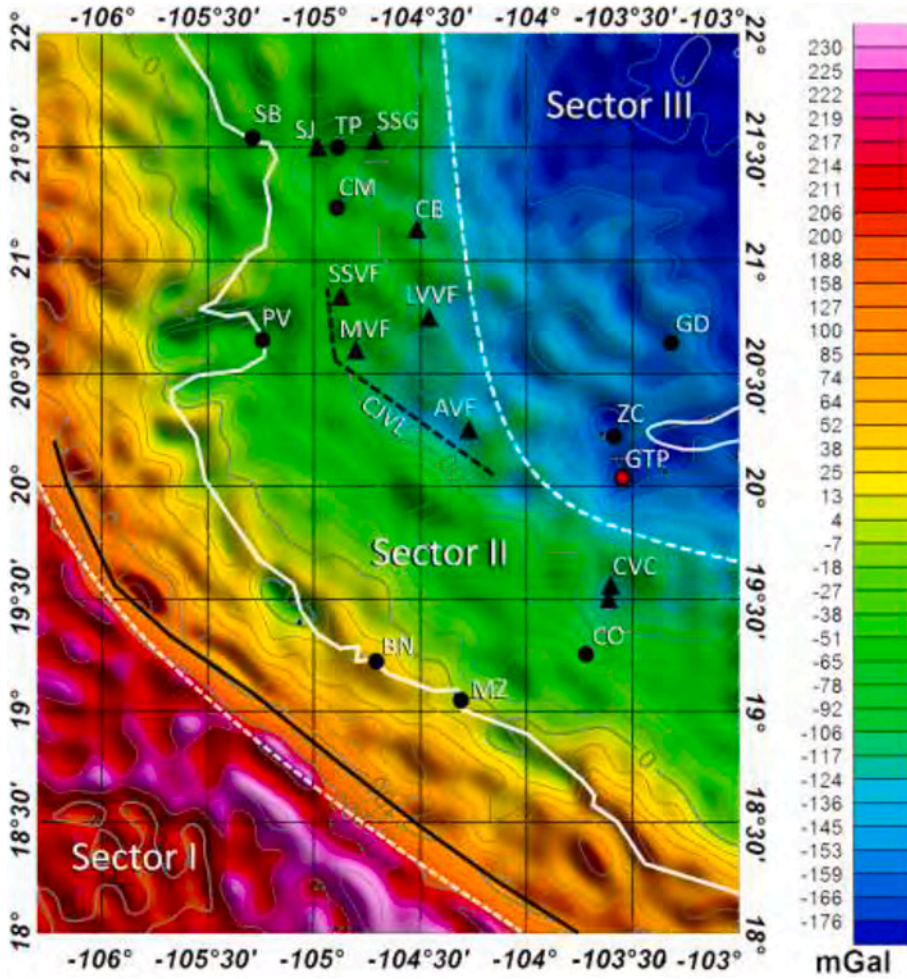


Fig. 2. Bouguer anomaly map (BA) of the study area and its contours (light gray). Three sectors are defined according to anomaly intervals: Sector I, from 158 to 230 mGal, Sector II, from 157 to  $-100$  mGal, and Sector III, from  $-100$  to  $-175$  mGal; the dashed lines are the limits between sectors. The continuous black line close to the boundary between Sector I and Sector II corresponds to the trace of the Middle America Trench (MAT). Triangles represent volcanic fields. Main volcanic fields are: Colima Volcanic Complex (CVC). Central Jalisco Volcanic Lineament (thick dashed line) composed by San Sebastián Volcanic Field (SSVF), Mascota Volcanic Field (MVF), Ayutla Volcanic Field (AVF). Other volcanic outcrops are: SJ, San Juan. SGG, Sanganguey. CB, Ceboruco. LVVF, Los Volcanes Volcanic Field. Cities are: TP, Tepic. SB, San Blas. CM, Compostela. GD, Guadalajara. ZC, Zacoalco. CO, Colima. MZ, Manzanillo. BN, Barra de Navidad. Other labels: MB, Michoacán Block. GTP, Guadalajara Triple Point.

The Bouguer correction to the second order was performed using eq. (4) which is standardly used by the USGS for a spherical layered earth (LaFehr, 1991; Hildenbrand et al., 2002).

$$C_{B_{esf}} = 2\pi G * \rho t * (\mu h - \lambda R) = -0.004192 * \rho t * (\mu h - \lambda R) [mGal] \quad (4)$$

However, since here we have stations under the sea level (i.e. at the bottom of the ocean) we need to correct the equation for the water density layer ( $\rho_a$ ). Thus, eq. (5) is applied for stations at the sea bottom

$$C_{B_{esf}} = 2\pi G * (\rho t - \rho_a) * (\mu h - \lambda R) = 0.004192 * (\rho t - \rho_a) * (\mu h - \lambda R) * h [mGal] \quad (5)$$

Where:  $C_{B_{esf}}$  = Bouguer correction in mGal  $G$  = Gravitational Earth's constant  $\rho t$  = Earth's mean density ( $2.67 \frac{g}{cm^3}$ )  $\rho_a$  = Mean sea water density ( $1.025 \frac{g}{cm^3}$ )  $\mu$   $\lambda$  = Coefficients (dimensionless) defined by LaFehr (1991).  $h$  = Ellipsoidal elevation of the station.

The Free Air anomaly is calculated (Telford et al., 1990) from eq. (6)

$$FA = G_{obs} - G_{theo} + C_{FA} + C_{atm} \quad (6)$$

The Bouguer Anomaly (BA), obtained adding the second order anomalies  $C_{B_{esf}}$ ,  $TC$  and  $FA$ .

according to eq. (7), which is the equation for a spherical layered earth (Hildenbrand et al., 2002).

$$AB = G_{obs} - G_{theo} \pm C_{FA} \pm BC + TC + C_{Atm} = AL \pm CB + TC \quad (7)$$

The Bouguer Anomaly map was finally assembled with the gridded data obtained from eq. (7) and is shown in Fig. 2.

### 3.2. Anomaly division in sectors

The Bouguer anomaly map in Fig. 2 can be divided in sectors according to anomaly intervals. Sector I corresponds mainly to the oceanic plate extent, mostly Rivera plate, although the SE portion of the map corresponds to the Cocos plate. This sector is characterized by a low gradient (0.06 mGal/km), which is expected, since the oceanic plate maintains a uniform surficial level throughout the area. Anomaly contours maintain a N60°W orientation, suggesting that the anomaly source is a rather homogeneous structure.

Sector II exhibits a larger gradient (0.20 mGal/km) in the NE direction. South of 20° 30'N anomaly contours also show a N60°W direction, appearing clearly associated with plate subduction, whereas to the North they change to a nearly N orientation. A local minimum of  $-116$  mGal is observed at 19° 30'N and 103° 30'W, coinciding with a previously reported gravity minimum associated with the Colima Volcanic Complex (CVC) (Alvarez and Yutsis, 2015b). Another local minimum of  $-50$  mGal is located at 19° 41'N and 103° 40'W associated with the Colima graben, and another one of  $-90$  mGal at 20° 40'N and 105° 34'W located in the plate roll-back region of Bahía de Banderas identified by Yang et al. (2009) and confirmed by Corbo et al. (2013) extending to Valle de Banderas graben (Arzate et al., 2006).

Sector III has an anomaly gradient of 0.08 mGal/km; it contains a V-shaped composite minimum, consisting of three gravity lows at (20° 00'N, 103° 30'W) in the vicinity of the Guadalajara Triple Point (GTP). In the N portion of this sector we obtain the lowest anomaly values, probably associated with the presence of the Sierra Madre Occidental, a large silicic igneous province in northwestern Mexico (Ferrari et al., 2018).

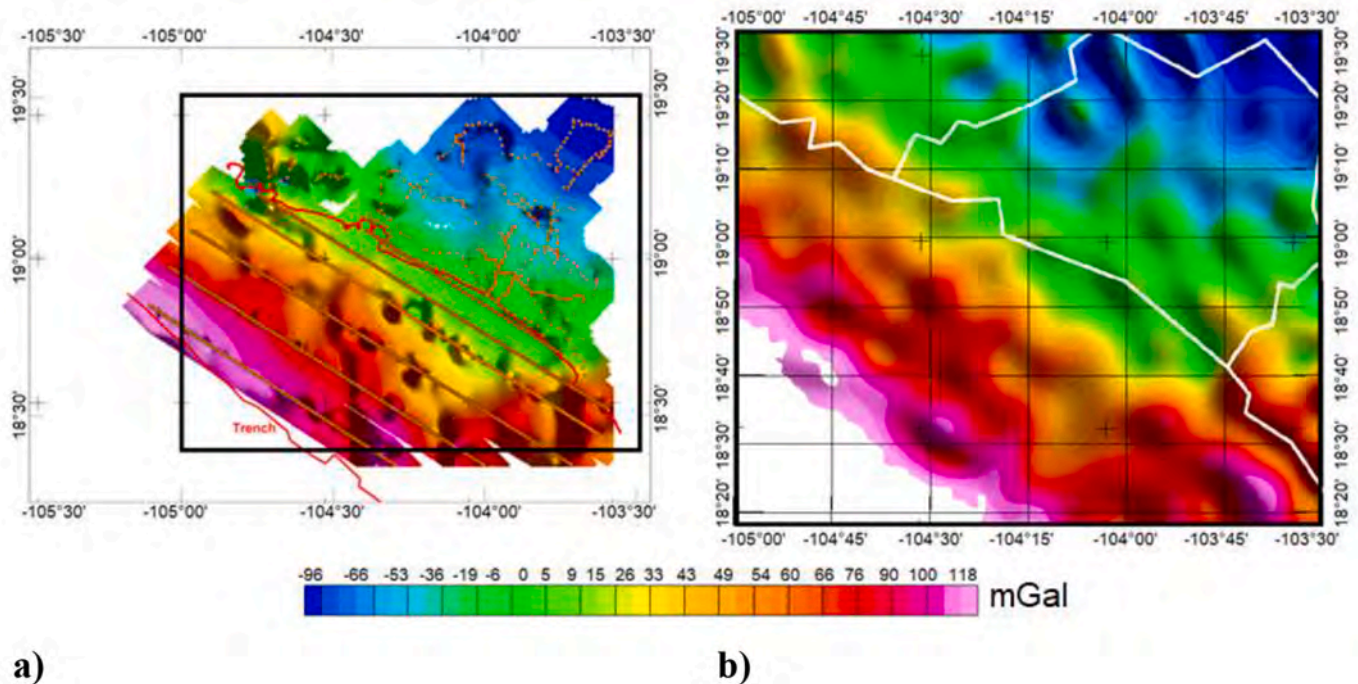


**Fig. 3.** Bouguer anomaly comparison between surface measurements and satellite derived field values. Total Bouguer anomaly in **a)** was obtained from in-land and offshore gravity stations (dots and lines) from Alvarez and Yutsis (2015a), whereas in **b)** the original data comes from the EIGEN-6C4 model (Fig. 2). The great similitude between them can be easily appreciated. The scale applies to both maps.

### 3.3. Anomaly validation

The question naturally arises of how the satellite derived data compares with traditional measurements onshore, or with ship transects offshore. To answer the question, we perform a comparison with a previously published Bouguer anomaly of the region. It involves the map reported by Alvarez and Yutsis (2015a), which is shown in Fig. 3a, involving the inland and offshore regions in the vicinity of the Rivera-Cocos plate boundary, showing a range of values between  $-90$  to  $+140$  mGal. In Fig. 3b we show the same portion of the map, extracted from the data in Fig. 2, with a range of anomaly values between  $-103.7$  and  $141.0$  mGal that closely matches the characteristics of the anomaly in Fig. 3a, not only offering full coverage of the land area but also a more detailed anomaly resolution. This comparison shows that the EIGEN-6C4 model adequately reproduces Bouguer anomalies in the onshore and offshore regions.

## 4. Anomaly analyses

To further enhance the onshore characteristics of the Jalisco Block the total Bouguer anomaly map in Fig. 2 is transformed into a residual Bouguer anomaly map by means of additional signal filtration. We selected a second-degree polynomial to be the regional surface to be subtracted from the complete Bouguer anomaly. A second-degree surface is adequate, since it involves small curvatures yielding smoother corrections. The result is shown in Fig. 4a where various anomaly features are now more clearly appreciated. Several alignments are highlighted with dashed lines labeled a through i. Fig. 4b shows the topography map, included to readily compare with the gravity and magnetic maps of the region. The magnetic map appears in Fig. 4c; it is reduced to the pole and upward continued 6 km.

We aim to define the onshore gravity characteristics of the Jalisco Block. Since the largest anomaly values occur offshore (Fig. 2) we opted for screening them out, to generate a map containing only the onshore Bouguer anomaly. This decreases the anomaly dynamic range (i.e.,  $BA_{\max}/BA_{\min}$ ) in that area, allowing for a better discrimination of its

subtler characteristics. The result is the Bouguer anomaly map in Fig. 5, where the anomaly fluctuates between  $+35$  and  $-190$  mGal; in comparison, the fluctuation in Fig. 2 goes from  $+235$  to  $-185$  mGal.

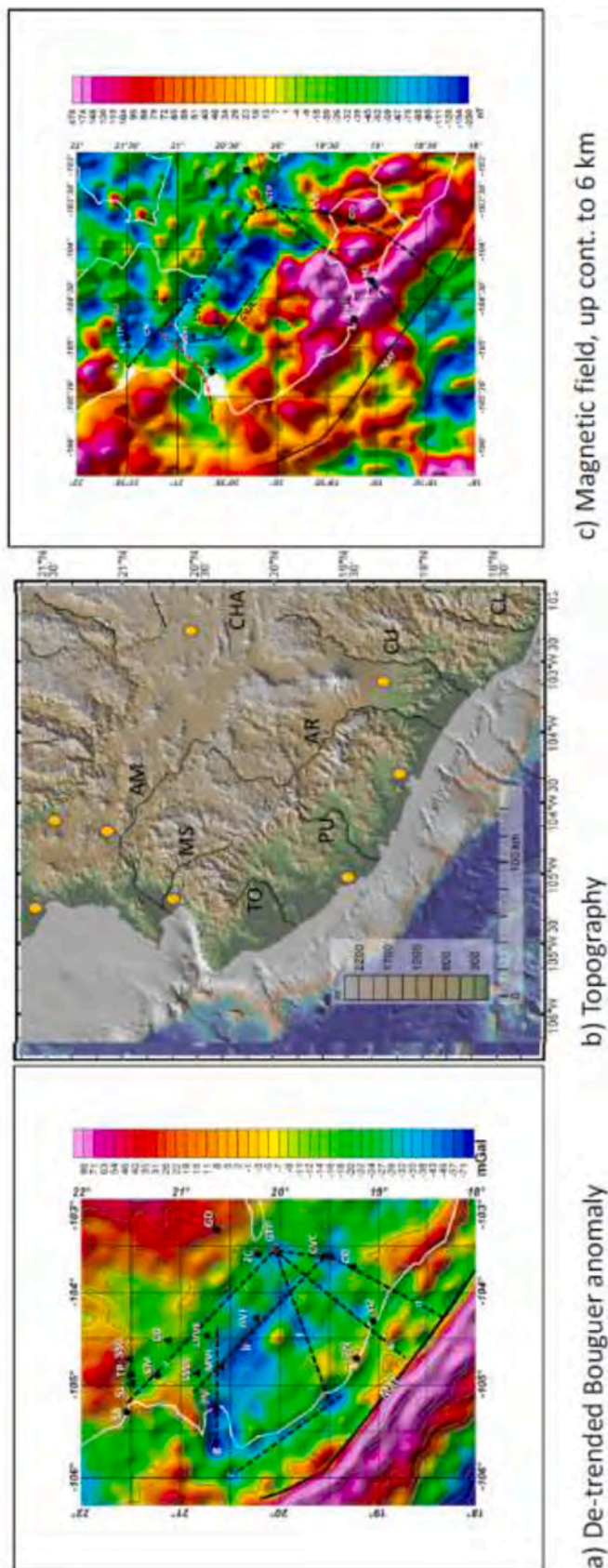
The more obvious changes between both maps can be observed in the region along the coastline, which in Fig. 2 is a low-relief surface, whereas in Fig. 5 it shows three positive anomalies, the largest one immediately SW of the CVJL, as well as the negative anomaly NE of Manzanillo (MZ).

Fig. (4c) shows the magnetic map (NAMAG, 2002) of the JB from which we will obtain the magnetic profiles to be reported in Section 5. We present the magnetic data as a complement to the gravity information; for the size of the Jalisco Block we estimated that an upward continuation of 6 km would get rid of the near surface magnetic noise while maintaining an adequate resolution of the magnetic sources.

### 4.1. Central Jalisco Volcanic Lineament

A prominent negative anomaly around  $(20^{\circ} 15'N, 104^{\circ} 30'W)$  corresponds with the Central Volcanic Jalisco Lineament (CJVL) composed of Mascota (MVF), Atenguillo, and Ayutla (AVF) volcanic fields (Richter and Carmichael, 1992; Richter and Rosas-Elguera, 2001; Bandy et al., 2001; Suhardja et al., 2015) (Figs. 4a and 5; Line b). San Sebastián Volcanic Field (SSVF), and Los Volcanes Volcanic Field (LVVF) are usually incorporated in the CJVL; however, these volcanic fields are obviously not aligned with it. The main orientation of the Bouguer anomaly of the CJVL is trench parallel ( $N45^{\circ}W$ ), although small, perpendicular elongations are observed at the center and SE portions of the alignment, suggesting anomaly propagation in that direction at those locations. To the SE, aligned with the CJVL anomaly, there are two gravity lows, one located at  $(19^{\circ} 55'N, 104^{\circ} 14'W)$  (Fig. 5) corresponding to a local topographic low (valley) of 900 m elevation, flanked to the NE by the Armería river (Fig. 4b).

The other minimum is associated with the Colima Volcanic Complex (CVC) at  $(19^{\circ} 25'N, 103^{\circ} 40'W)$ . From the CVC to the Mascota Volcanic Field they constitute a non-continuous, 200-km volcanic alignment (Line b) along the SW border of the region denoted as the uplifted



**Fig. 4.** Gravity, topography and magnetics of the Jalisco Block. a) Bouguer anomaly of the Jalisco Block, de-trended with a 2d-degree polynomial, with anomaly values between  $-75.0$  to  $+90.0$  mGal. The Dashed lines (a through i) help identify anomaly trends. Other abbreviations as in Fig. 2. MAT, Middle America Trench. b) Digital elevation model of the study area (Ryan et al., 2009); the black traces correspond to main rivers: AM, Ameca. MS, Mascota. TO, Tomatlán. PU, Purificación. AR, Armería. CU, Coahuayana. CL, Coalcomán. CHA, Chapala lake. Orange dots correspond to cities; names appear in Fig. 1 c) Magnetic field (nT) corresponding to the study area, reduced to the pole and with upward continuation to 6 km, obtained from NAMAG (2002). The dashed lines represent the location of the rifted margins, except the dashed line going through Manzanillo (MZ). Abbreviations as in Fig. 2.

domain of the Jalisco Block (Alvarez et al., 2006), containing Quaternary volcanic structures along its length. Another trench-parallel set of aligned minima of lesser amplitudes starts at the GTP running along the Tepic-Zacoalco rift (Line a).

#### 4.2. Bahía de Banderas

Another local minimum at  $(20^{\circ} 40'N, 105^{\circ} 30'W)$  is oriented in the E-W direction (Fig. 5) and occupies the whole of Bahía de Banderas (BB). It shows a complex structure with three minima and a maximum located at the south-central portion of the bay (Line g). Yang et al. (2009) and Corbo et al. (2013) have shown that in this region the subducting plate undergoes an almost vertical roll-back. The size, position, and anomaly magnitude are similar to that of the CJVL, and in spite of its different orientation it could be considered directly linked to that of the CJVL; both are only separated by a small gap. The  $-43$  mGal contour surrounds both anomalies, BB and CJVL; together they constitute the gravity anomaly of largest extent in the JB. Based on preliminary analyses of magneto-telluric and gravity models to be reported elsewhere we believe that these two anomalies are related to plate rollback; however additional work is necessary to elucidate the relationship between these two gravity anomalies.

#### 4.3. Colima Volcanic Complex

A gravity minimum is associated with the Colima Volcanic Complex (CVC) at  $(19^{\circ} 25'N, 103^{\circ} 40'W)$ , confirming the gravity minimum previously reported by Alvarez and Yutsis (2015b) from land gravity determinations. Fig. 5 shows that associated with it there are two smaller, but well-defined minima to the E  $(19^{\circ} 20', 103^{\circ} 20'W)$  and W  $(19^{\circ} 35'N, 103^{\circ} 50'W)$  of the main anomaly; the trend of these three anomalies is  $N80^{\circ}W$ . The W minimum is of lesser amplitude than the E one and is part of a group of gravity minima that starts at the Guadalajara Triple Point (GTP) and continues in a  $S40^{\circ}W$  trend to Manzanillo Harbor (Fig. 5, Line e).

The CVC gravity low is linked to an elongated gravity low that follows a  $S15^{\circ}W$  direction (Fig. 5, Line d), crossing the Central and Southern Colima Graben sections (Serpa et al., 1992), reaching down to the trench along a trajectory that closely coincides with the Rivera-Cocos boundary (see Fig. 1) defined by Alvarez and Yutsis (2015a). Luhr and Carmichael (1980) noted that the southward migrating volcanism from Cántaro to Volcán de Fuego chain, is also reflected by a southward-younging progression at Cántaro itself, giving rise to the two volcanic edifices of Cántaro volcano. The Potassium-Argon ages of Cántaro were established by Siebert et al. (2003) from 1.7 to 1.0 Ma, framing the continuous volcanic activity of the Colima Volcanic Complex between 1.7 Ma and the Present, including that of today's Colima Fuego Volcano. Alvarez and Yutsis (2015b) reported the existence of an additional extension to the S of the chamber of the Colima Fuego Volcano, in line with the southward volcanic migration. The data presented here allows us to associate these volcanic manifestations to the  $S15^{\circ}W$  gravity-low trend (Fig. 5, Line d), which follows the full length of the Colima rift.

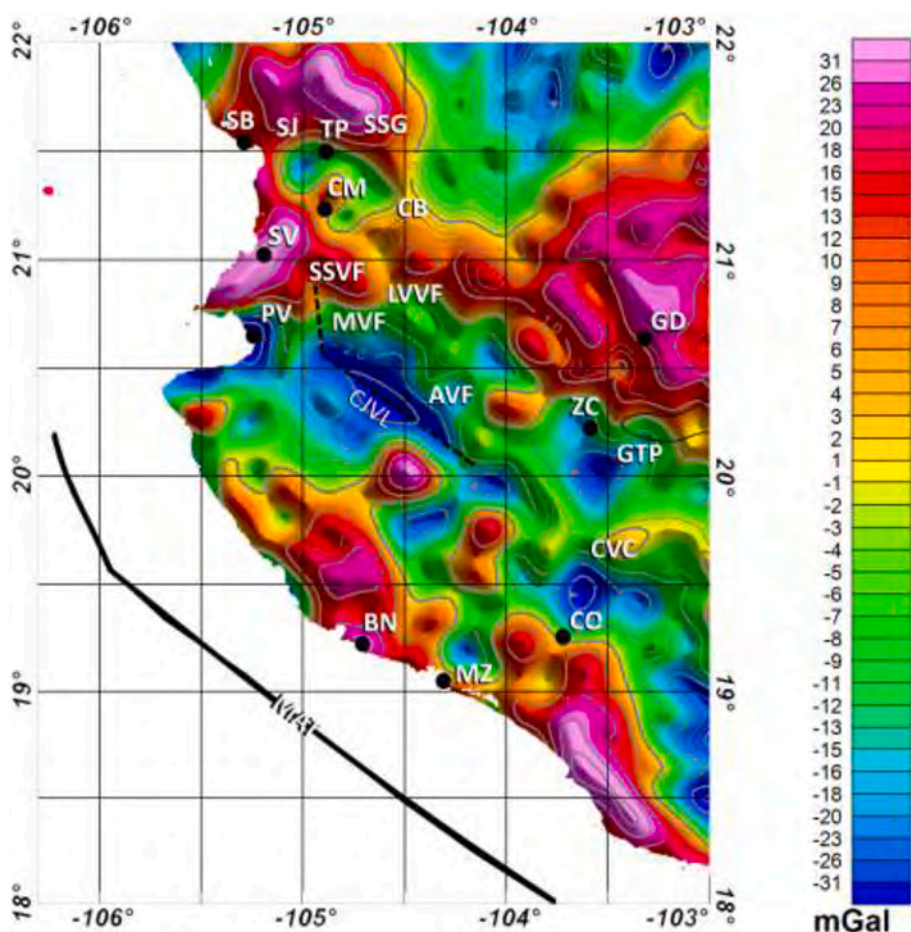


Fig. 5. Onshore Bouguer anomaly of the Jalisco Block, de-trended with a 2d-degree polynomial. It provides a complementary view to map in Fig. 4a of the set of anomalies, since the offshore region is excluded, along with the associated alignments; the anomaly ranges between  $-32.0$  to  $+35.0$  mGal and onshore negative anomalies are enhanced. The dashed lines (a through i) help identify anomaly trends. Sierra de Vallejo (SV). Other abbreviations as in Fig. 2.

#### 4.4. Guadalajara Triple Point

The Guadalajara Triple Point displays a Y-shaped anomaly, more clearly defined in Fig. 5, with two smaller lobes on the two branches of the Y. Location ( $20^{\circ} 06.9'N$ ,  $103^{\circ} 29.6'W$ ) can be considered the geographic location of the associated GTP, which is often located rather vaguely (e.g., 55 km south of Guadalajara City) (Barrier et al., 1990; Garduño and Tibaldi, 1991; Michaud et al., 1994). This location not only corresponds to the gravity minimum it also corresponds to the topographic minimum in the area (1258 m amsl). The distance between the two gravity minima, CVC and GTP, is 60 km along direction  $S8.5^{\circ}W$  and is occupied by the Northern Colima Graben (Allan, 1986). The age of the active system of the Guadalajara Triple Point is normally considered Pliocene-Pleistocene (Luhr et al., 1985; Allan, 1986; Barrier et al., 1990).

## 5. Results

### 5.1. Rift profiling

We try to characterize the rifted margins of the JB by simultaneously mapping their gravity, magnetic, and topographic characteristics along the full extent of the rifts by means of profiles perpendicular to their trajectories. We start with the Tepic-Zacoalco and the Colima rifts and subsequently analyze the NW boundary of the JB. The profiles' extent and position of T-Z and Colima rifts are shown in Fig. 6. Fig. 4c shows the magnetic map of the JB from which we obtained the corresponding profiles. In the following sections we present the magnetic data as a complement to the gravity information; for the size of the Jalisco Block we estimated that an upward continuation of 6 km would

get rid of the near surface magnetic noise while maintaining an adequate resolution of the magnetic sources. We present directional derivatives (DhX, DhY, and DZ2) of the Bouguer anomaly map. The NW margin of the Jalisco Block will be treated independently.

#### 5.1.1. Horizontal (X) derivative

In the previous section we described the gravity anomalies de-trended with a second-degree polynomial (Fig. 5). In this section we apply directional derivatives to those anomaly maps to analytically enhance the presence of alignments.

Fig. 7a shows the horizontal (X) derivative over the onshore portion. This derivative enhances discontinuities in the x-direction; rock density being the physical property associated with the gravity field, it translates into density variations in this direction. Regions coded red in this map show high-density contrasts, whilst those coded blue show regions of low-density contrast. For instance, the Central Jalisco Volcanic Lineament (LVCJ) shows a high-density contrast at the boundary between the volcanic lineament and the neighboring non-volcanic formations.

The limits of the Jalisco Block are identified in this map with dashed lines. In Bahía de Banderas, N of  $20^{\circ} 30'N$ , a group of gravity lows conforms a  $N45^{\circ}E$  trend, along the Valle de Banderas region, ending beyond the Tepic-Zacoalco rift. In Fig. 7a this alignment clearly shows a  $N45^{\circ}E$  trend (red, dashed line). This lineament is of particular importance since it helps define the rifted NW boundary of the JB, as proposed by Johnson and Harrison (1990) and Alvarez (2002). Furthermore, it defines a rift-rift-rift junction, which we identify as a triple point, to be called the Compostela Triple Point (CTP) that together with the Guadalajara Triple Point define the N limit of the JB. We will return to this observation when constructing various profiles along the rifted

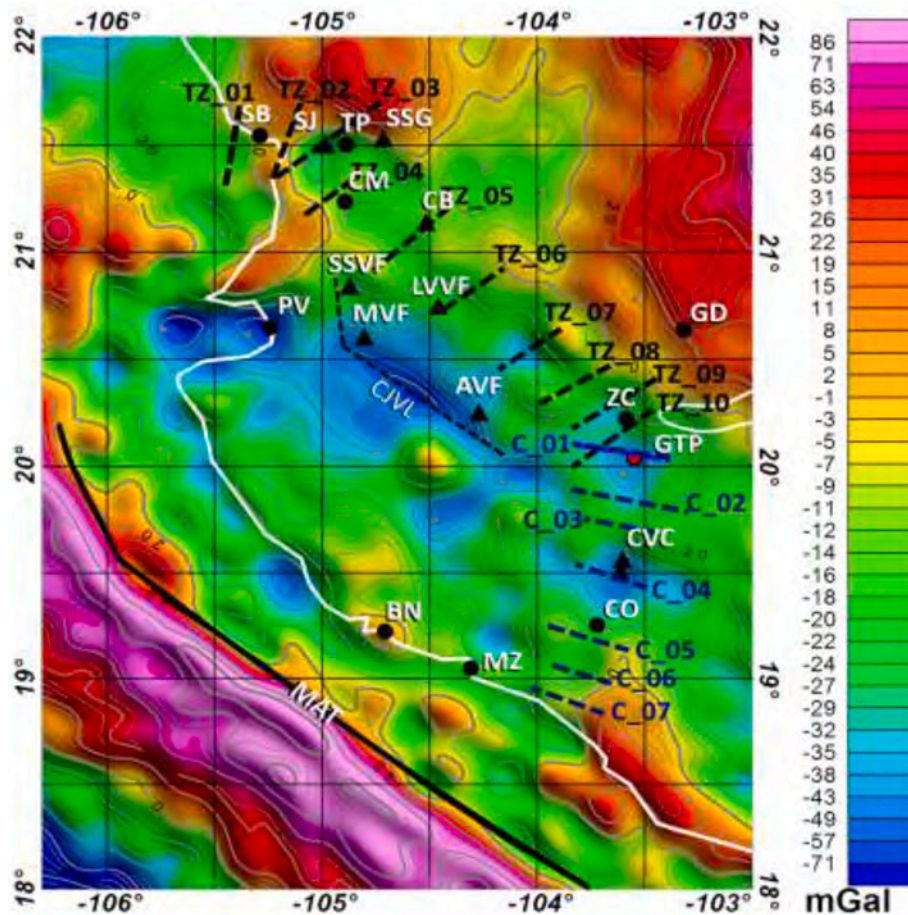


Fig. 6. Bouguer anomaly map with a second-degree trend removed. Profiles preceded by TZ correspond to Tepic-Zacoalco rift, whilst those preceded by C correspond to the Colima rift. MAT, Middle America Trench. Other abbreviations as in Fig. 2.

regions of the JB.

On the SE portion of Fig. 7a the anomaly bifurcation (Fig. 5, Lines d, e) starting at GTP extend into the offshore region, crossing the Middle America Trench, including El Gordo graben region, confirming previous observations that suggest a connection between these structures (Bourgeois et al., 1988; Khutorskoy et al., 1994; Bandy et al., 2005).

### 5.1.2. Vertical (Y) derivative

Fig. 7b shows the vertical derivative of the Bouguer anomaly; it confirms the trends observed in Fig. 7a, particularly the alignment of minima trending NE interpreted as the NW limit of the JB. Outlined with dashed lines are the Tepic-Zacoalco rift, the Bahía de Banderas-Compostela trend, and the Colima Neo-graben. There are subtle differences between the DhX and DhY derivatives.

### 5.1.3. Depth (Z) derivatives

The first and second depth derivatives (DZ1 and DZ2) of the gravity field inform about the depth structural continuity; in particular, DZ2 tends to enhance local density increments or deficits. Here we restrict this analysis to DZ2, whilst the first derivative will be presented in relation to several profiles discussed below. Fig. 7c shows the onshore portion of the map; as in the previous cases, the dashed lines represent the limits of the JB and the rift bifurcation at the SE portion. Within these limits we identify a periodic alternation of maxima and minima of the values of DZ2, with a clear NW trend and a wavelength of  $\sim 30$  km in the NE direction, with the same orientation as that of the corresponding section of the Middle America Trench. This periodic pattern ends at the NW limit of the JB. The figure shows that such a periodicity

is only observed within the limits of the JB; the pattern is lost outside this region.

In particular, we note the Central Volcanic Jalisco Lineament and the Tepic-Zacoalco rift, both correspond to minima of this variable. Although directional derivatives DhX and DhY tend also to show the limits of the JB, it is the second-degree depth derivative (DZ2) the one that more clearly delimits its extent; furthermore, the fact that it involves only the changes in depth, highlights the horizontal periodicity reported above. As in the previous derivatives, the intersection of the Compostela-Banderas rift with the Tepic-Zacoalco rift defines the location of the Compostela Triple Point.

## 5.2. Rift profiles

We can now proceed to characterize the rifted margins of the JB by simultaneously plotting their gravity, magnetic, topographic, and horizontal (DhX), vertical (DhY), and depth (DZ1 and DZ2) directional derivatives of the Bouguer anomaly, along the full extent of the rifts, with profiles perpendicular to the trajectory of Tepic-Zacoalco and Colima rifts. We illustrate this exercise with some of the profiles. Subsequently we apply the same analysis to the NW boundary of the JB. Fig. 6 shows the location of the profiles and Fig. 4c the magnetic map from which the magnetic profiles were extracted.

### 5.2.1. North and east rifts

In the T-Z and Colima rifts (Figs. 9 and 10) we appreciate that parameters AB, DZ1, and De-Trend reach minima at, or close to, the corresponding rift location. The magnetic profiles also reach minima in

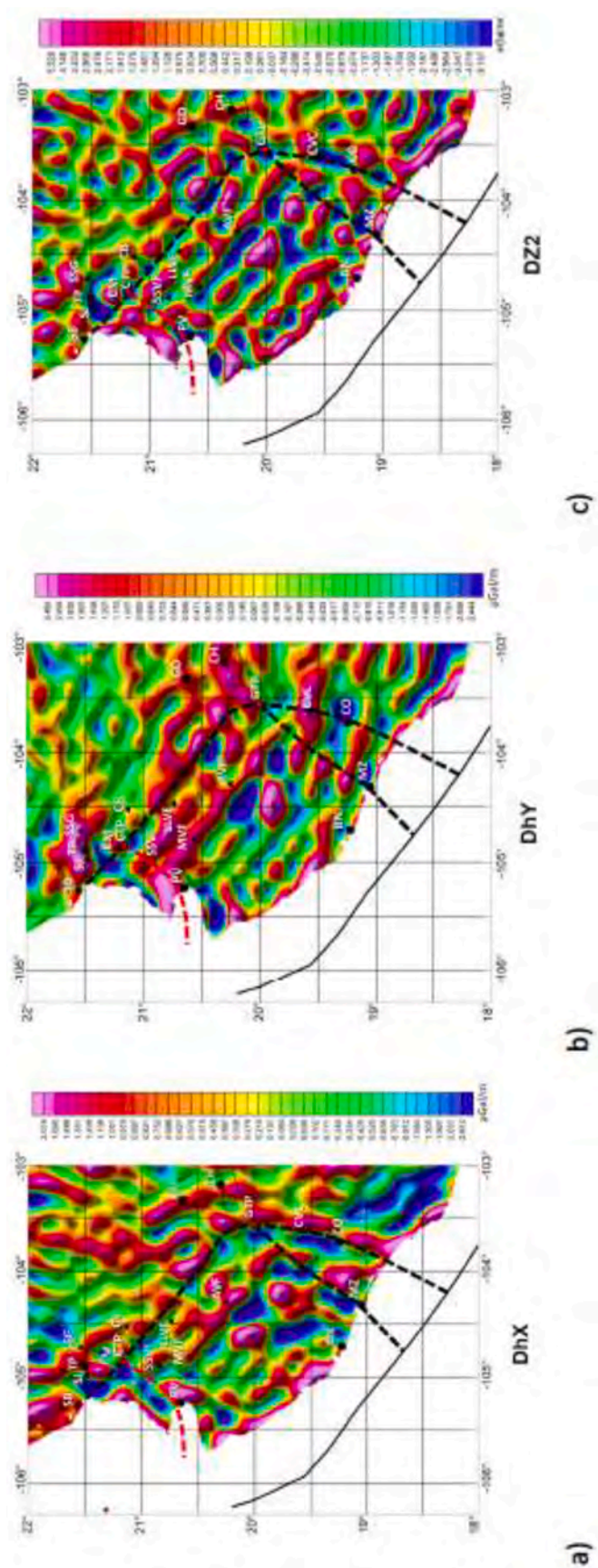


**Fig. 7.** a) Onshore map of the horizontal derivative  $DhX$  of the de-trended gravity map shown in Fig. 5. The red, dashed line starting at Bahía de Banderas enhances the rift trend between Bahía de Banderas and Compostela Triple Point (CTP), located at the intersection with the T-Z rift. b) Onshore portion of the vertical derivative  $DhY$  from the map in Fig. 5. As in Fig. 7a, the red, dashed line starting in Bahía de Banderas enhances the rift trend between Bahía de Banderas and Compostela Triple Point (CTP). c) Second-degree depth derivative ( $DZ2$ ) of the gravity field in the onshore portion. MAT, Middle America Trench. Abbreviations as in Fig. 2. (For interpretation of the references to colour in this figure legend, the reader is referred to the web version of this article.)

some cases; however, it does not necessarily reach minima at the rifted margins, the reason being that materials with magnetic susceptibility distributions different from those in which the graben developed, such as volcanic structures and lava flows, may be present distorting the local magnetic response. Topographic profiles also reach minima at some of those places (e.g. TZ\_08, TZ\_09, C\_01, C\_02, C\_05); however, in others it shows the opposite behavior, as in the case of Colima volcano (C.04). Gravity lows have been located in limited, rifted locations of the boundaries of the JB (Allan, 1985; Campos-Enríquez and Alatorre-Zamora, 1998; Alvarez and Yutsis, 2015a). Based on geological considerations the JB limits have been proposed by several authors (Allan, 1986; Rosas-Elguera et al., 1996; Ferrari and Rosas-Elguera, 2000). The present results establish the N and E boundaries of the Jalisco Block as gravity lows. The conclusion is that gravity-associated parameters properly locate the rifts' positions in these rift-perpendicular profiles, allowing for their local identification and mapping.

### 5.2.2. The NW rift

We now apply this analysis to the region of the Jalisco Block that has been proposed as its NW boundary (Johnson and Harrison, 1990; Alvarez, 2002). Fig. 10a shows three profiles (MGG6, MGG7, and MGG8) that cover the region from Bahía de Banderas to Compostela where rifting has been proposed. We shall call it the Banderas-Compostela rift.

#### Tepec-Zacoalco rift

Analyzing profile MGG8, which crosses Valle de Banderas we can see that not only AB, DZ1, and De-Trend reach minima at the SE boundary of the valley but Topo and DZ2 also do, whilst the minimum of  $DhX$  is displaced to the NW. Continuing with profile MGG7 we note that the topographic profile changes abruptly at the middle of the profile; DZ1, DZ2, and Mag reach minima close to the center of the profile, at the place where topography changes drastically.  $DhX$  is again displaced to the NW with respect to the corresponding minima. De-Trend and AB closely track each other, showing decreasing values from NW to SE.

Topography along Profile MGG6 does not show the usual depression associated with rifting; however, parameters DZ1, DZ2, and De-Trend show minima towards the center of the profile, where AB shows a slight inflection. The minima of Mag and  $DhX$  are slightly displaced towards the NW following the previously observed pattern for those parameters. We conclude that along the NW portion of the JB the response of these parameters along Valle de Banderas exhibit mature rifting, that is, a well-developed semi-graben structure (Arzate et al., 2006), whilst profiles MGG6 and MGG7 appear to show rifting in the process of developing at those locations. From the Bouguer anomaly map in Fig. 10a we note that profile MGG8 is the only one fully intersecting a gravity minimum, whilst profiles MGG7 and MGG6 intersect regions involving mostly positive anomalies. This reflects in AB not showing minima at the expected central positions. Nonetheless, De-Trend, DZ1, DZ2 show minima at those positions and Mag and  $DhX$  also do, slightly displaced towards the NW.

## Tepic-Zacoalco rift

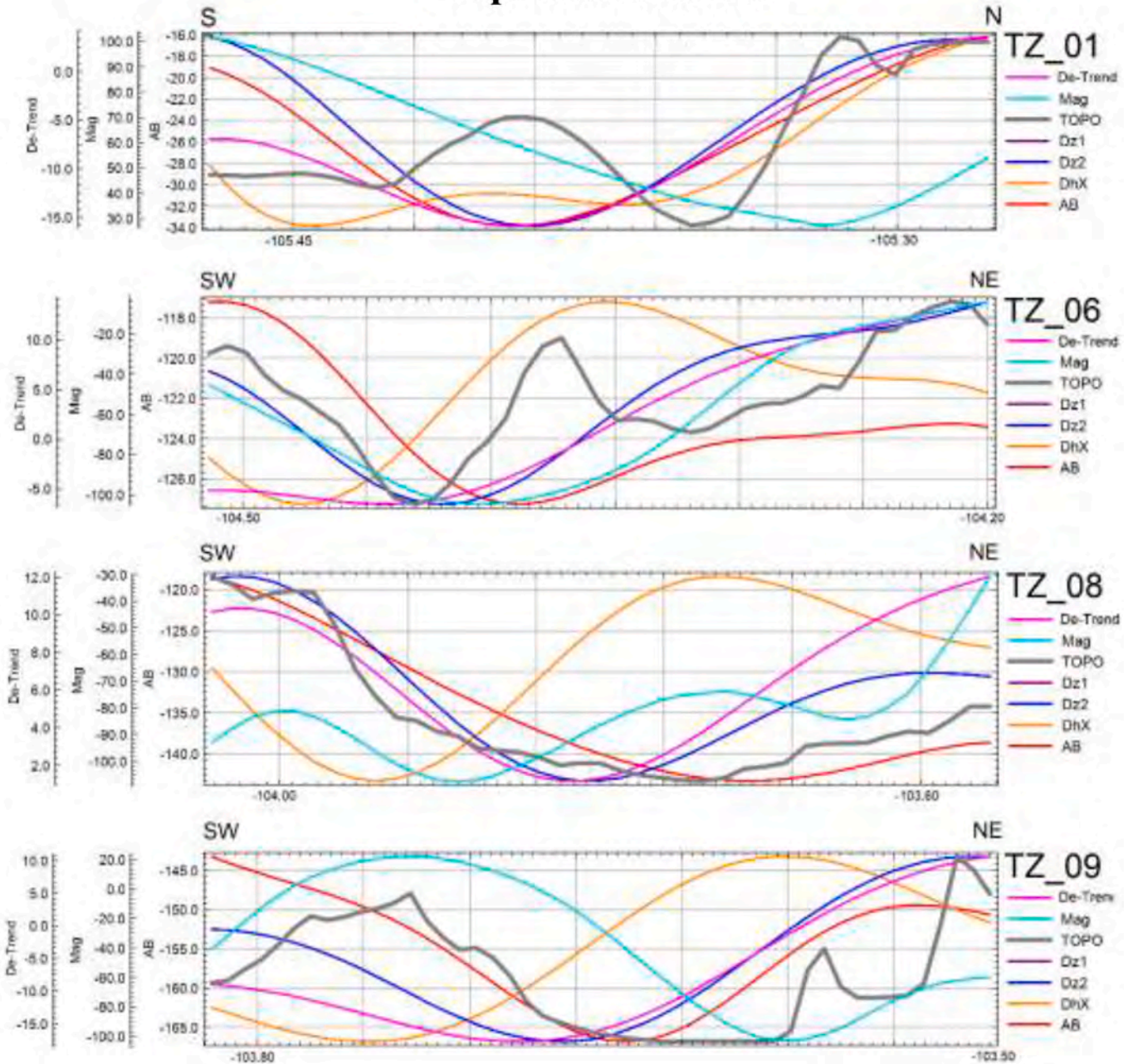


Fig. 8. Selected profiles along the Tepic-Zacoalco rift. See Fig. 6 for location. Each profile shows topography (Topo, outstanding black line), de-trended Bouguer anomaly (De-Trend), magnetic field (Mag), directional derivatives (DZ1, DZ2, DhX), and Bouguer anomaly (AB).

### 5.3. Ameca and Santiago rivers

Ameca and Santiago rivers flow parallel to each other in a N45W direction for approximately 100 km, starting 13 km SE of Ameca and ending 11 km W of Ceboruco volcano (Fig. 11); their average separation in that transect is 50 km. It is important to note that the region between the two rivers constitutes a corridor that contains recent volcanic manifestations in the area, notably Tequila and Ceboruco volcanoes. Thus, the volcanic region bounding the Jalisco Block to the N occurs between two parallel, topographic depressions along which Santiago and Ameca rivers flow.

The change of flow direction of Santiago river from the N45W to N25W direction, starts at the location where the parallel flow of the rivers ends. This new trend changes again when Santiago river sharply

turns in the W45S direction at Aguamilpa dam to finally discharge in the ocean. The N25W section of the Santiago river corresponds to a region that has been described by Ferrari and Rosas-Elguera (2000) as the Pochotitlán fault system, located in the Gulf extensional province, a tectonic unit different from the Jalisco Block, consisting of a series of lystric faults and a vertical displacement of less than 2000 m, related to the opening of the Proto-Gulf (Karig and Jensky, 1972; Ferrari et al., 2013; Ferrari et al., 2018).

We submit that Ameca river should also continue in a trajectory parallel to Santiago river in the N25W direction; instead it experiences a sharp turn close to Compostela in the W45S direction, discharging into Bahía de Banderas. The red, dashed lines trending N25W in Fig. 11 delimit the portion of the volcanic region that includes San Juan, Sanganguey, and Las Navajas volcanoes, characterized by an average

## Colima Rift

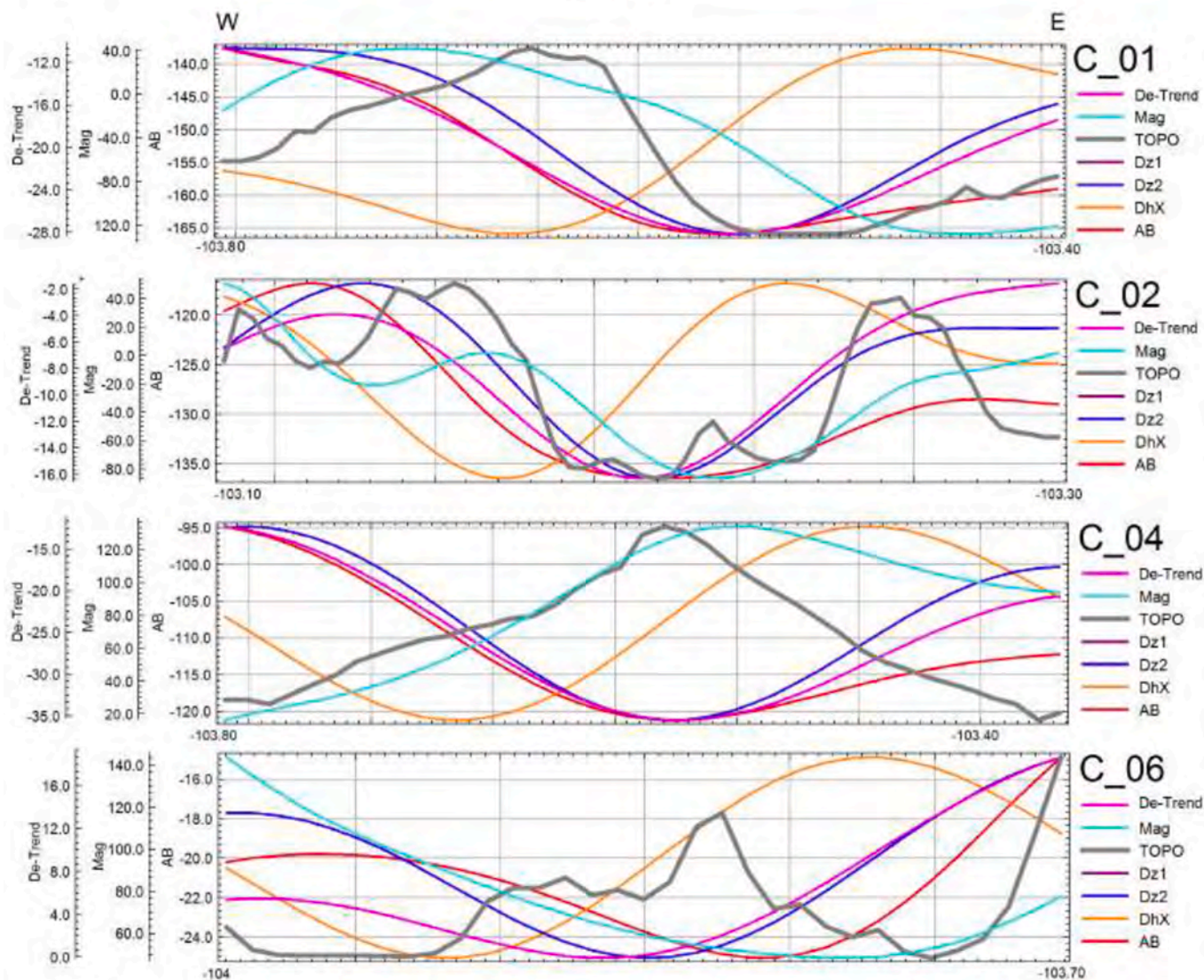


Fig. 9. Four most representative profiles across the Colima rift. The topography profile is the outstanding black line. See Fig. 6 for location.

altitude of 1000–1200 m. The region is flanked to the SW by the graben structure trending NNW that is the continuation of the Ameca river causeway, where Compostela is located, and to the NE by the Pochotitlán fault system.

The figure shows that N of Compostela these lineaments indeed follow a trajectory parallel to the Pochotitlán fault system along 64 km, and together enclose the volcanic region, as in the case of the N45W transects. Furthermore, the separation between these lines (50 km) is the same as the corresponding separation in the N45W transect. These observations support the idea that Ameca river should continue in the N25W direction, following a trajectory that parallels that of Santiago river.

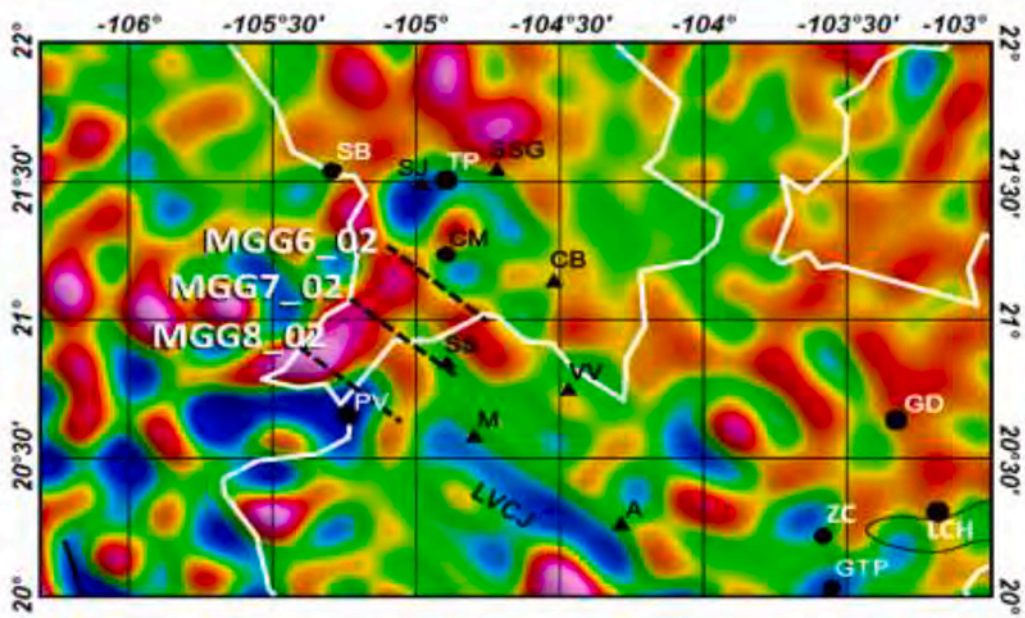
We attribute the sharp change in trajectory of the Ameca river to the intersection of its causeway by the rift structure of the NW boundary of the Jalisco Block, herein identified as the Banderas-Compostela rift (BCR). To the NW of this rift follows the Gulf extensional province. Ameca river changes direction to W45S at the intersection with the Banderas-Compostela rift, and Santiago river changes to N25W flow direction at the opposite limit. The location and direction of both rivers is trench-parallel up to Compostela; the volcanic region between them is also trench-parallel. It appears that their orientations are controlled

by the subduction of the section of the Rivera plate between Bahía de Banderas and Manzanillo.

### 5.4. Compostela Triple Point

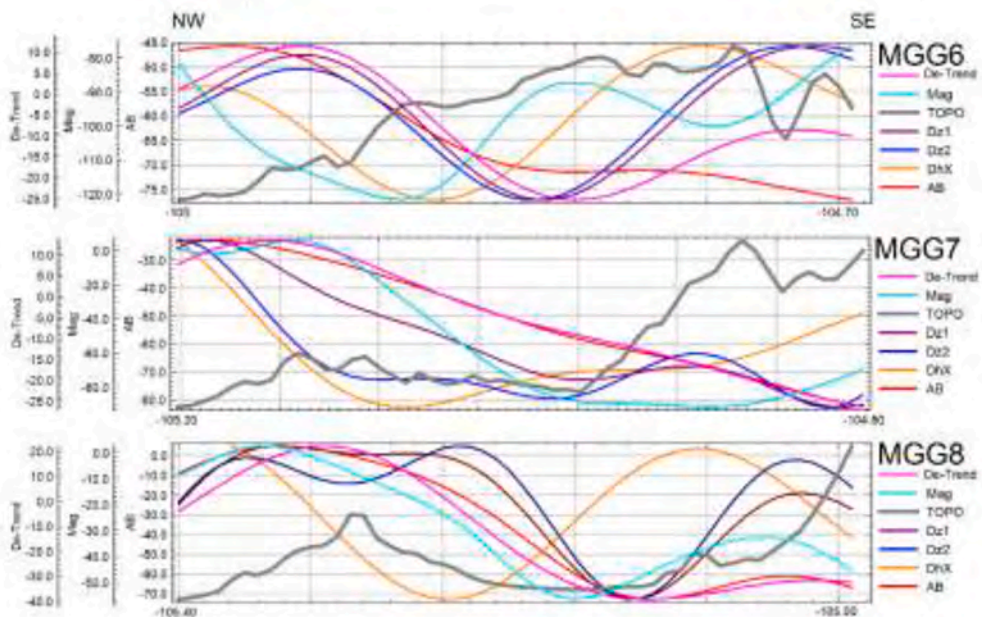
We propose the existence of the Compostela Triple Point (CTP) (rift-rift-rift) over the Tepic-Zacoalco rift near Compostela, Jalisco, at the intersection with the Banderas-Compostela rift (104.75°W, 21.04°N, Fig. 7a). The two triple points (GTP and CTP) define the N boundary of the JB. The onset of the TZR is established between the late Miocene and the Pliocene, around 10 Ma (Lühr et al., 1985; Allan, 1986). It is attributed to the magmatism resulting from the subduction of the Rivera plate under the Jalisco Block. Regarding the initiation of the Banderas-Compostela rift, the report from Jensky (1974) can help define an approximate date; he found the rocks in Sierra de Vallejo region extended in the E-W direction, concurrently with the intrusion of over 20 dikes oriented N8°E and dated between 13.3 and 10.1 Ma. He interpreted Bahía de Banderas as the trough that divides the intruded, tectonically extended region of the Sierra de Vallejo (Fig. 5) from the stable rocks of the Jalisco Block. This allows us to estimate that rifting also started in the 13–10 Ma interval in the Banderas-Compostela rift,





a)

### Banderas-Compostela rift



b)

**Fig. 10.** a) Location of three profiles along the Banderas-Compostela rift, in the NW portion of the Jalisco Block; the base map is the same as in Fig. 6, at a larger scale. b) the profiles include the same parameters as those in Figs. 8 and 9; together they define the landward perimeter of the JB.

although its development appears to have been slower than the Tepic-Zacolaco and Colima rifts. The third branch of the rift, from Compostela Triple Point to the NW, delimits the volcanic region in the extended

Gulf province. Thus, the late Miocene period exhibited a great tectonic activity in this region, originating the Tepic-Zacolaco rift and the Banderas-Compostela rift.

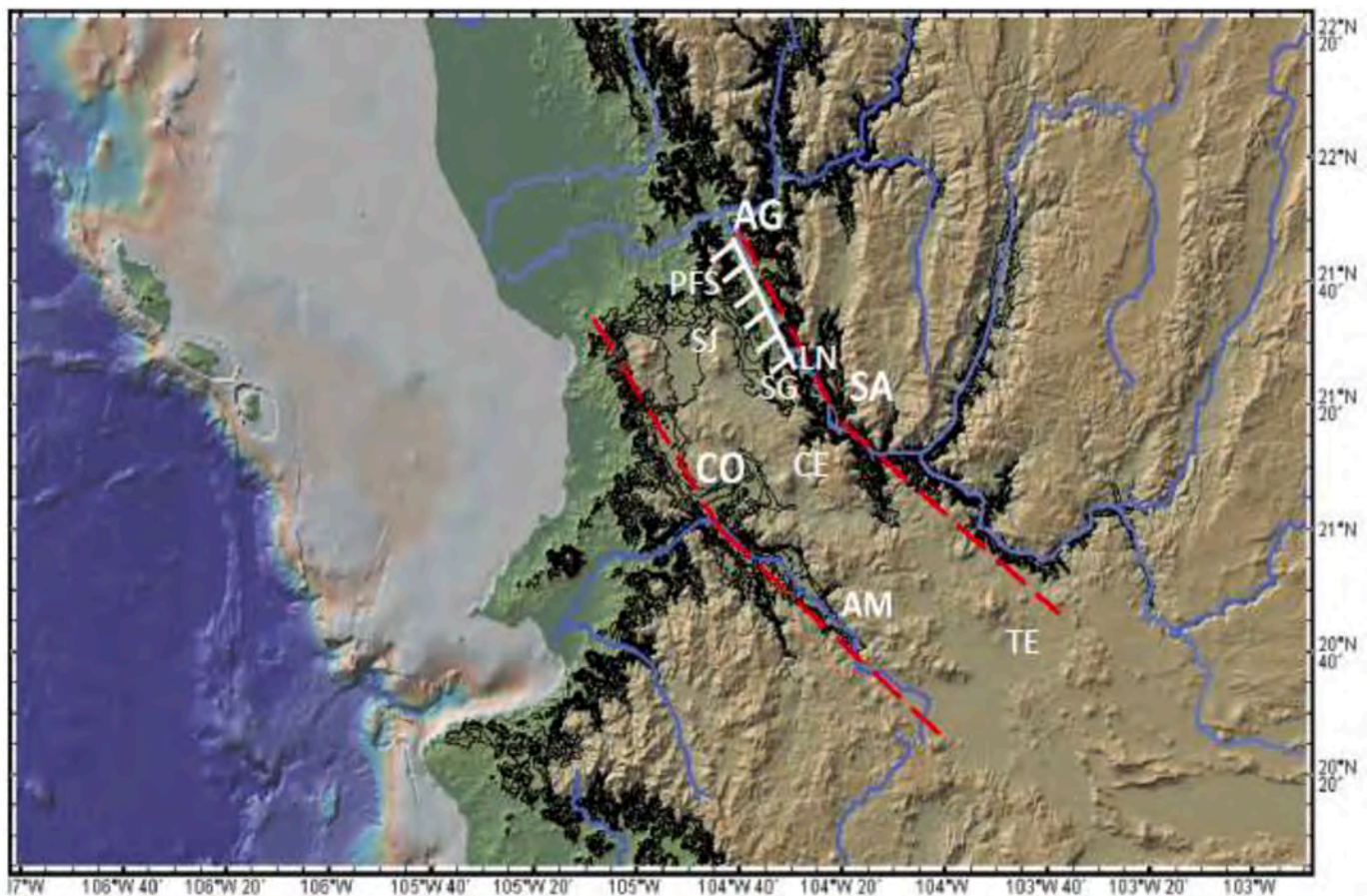


**Fig. 11.** Ameca (AM) and Santiago (SA) rivers and some tributaries in the NW portion of the Jalisco Block. All rivers are in blue. PFS, Pochotitlan Fault System, showing downthrown side. Volcanoes: TE, Tequila. CE, Ceboruco. SG, Sanguanguey. LN, Las Navajas. SJ, San Juan. The dark regions are elevation contours at 100 m interval from 700 to 1000 m. The trends discussed in the text are highlighted in red, dashed lines. CO, Compostela. AG, Aguamilpa dam. (For interpretation of the references to colour in this figure legend, the reader is referred to the web version of this article.)

The existence of the CTP establishes the NW limit of the JB, just as the GTP delimits it to NE, separating the JB from the Michoacán Block; without it, the extent of the JB remained speculative. It is a direct result of identifying the Banderas-Compostela rift, which defines the limit of the JB along its extent. Comparing the gravity responses of the two triple points we find that GTP shows a larger, better defined negative anomaly, a consequence of fuller graben development. The CTP also delimits the locations where the Extensional Gulf Province starts, implicating the existence of a continental sliver extending to the N of Bahía de Banderas, the Tres Marias Sliver, independent from the Jalisco Block, bounded by Tres Marias islands, and the coast of Nayarit up to latitude 22 degrees.

## 6. Discussion

The Tepic-Zacoalco rift is characterized by a series of gravity minima along its length as shown above; this lineament is identified as Line **a** in Fig. 5. In this work we find that the gravity minima associated with the CJVL (Line **b**) are considerably larger in amplitude than those of the Tepic-Zacoalco rift, locating in that region a recent volcanic front. Line **b** joins Quaternary volcanic activity centers along 200 km; furthermore, the Colima Volcanic Complex, usually not associated with other volcanic centers in the region, aligns with the CJVL, suggesting that volcanism in this region may be associated with the subducting plate having similar conditions along this front, favoring the accumulation of magma. Line **b** is parallel to Line **a**, and both are parallel to the Middle America Trench in this region, indicating these anomalies are related to the subduction of the oceanic plate. This result tends to

confirm that magmatism in this region has migrated trench ward during the past 10 Ma (Gómez-Tuena et al., 2007; Ferrari et al., 2012) and that the current front of the magmatic arc is ~60 km south of the Tepic-Zacoalco Rift.

A general observation regarding the overall gravimetric response of the Jalisco Block, can be summarized as a set of gravity lows comprising nearly 50% of the area of the JB (Fig. 5). We tentatively attribute this gravimetric response to the effect of plate rollback, which seems to occur in an extensive, trench-parallel front. We recall that plate rollback has been identified at the NW and E boundaries of the JB (Yang et al., 2009; León-Soto et al., 2009; Corbo et al., 2013). Since the gravity anomalies of the CJVL are located along the SW portion of the uplifted domain of the JB (Alvarez et al., 2006), a region that rises abruptly from the coastal plains to ~1800 m altitude along ~200 km; we speculate that they are related to the magmatic process that generated the uplifted domain.

A direct link is revealed between the BB gravity anomaly and the CJVL anomaly, in spite of their different trending directions, which meet at a 135° angle; these anomalies are only separated by a thin, positive gravity anomaly SE of Puerto Vallarta (PV) in the map of Fig. 6. Together they constitute the largest, negative gravity anomaly in the Jalisco Block, corresponding to a major tectonic alteration of the crust in this region. The region of BB presents a larger degree of erosion represented by the deep canyon along the southern littoral of the bay, exhibiting a half-graben structure (Alvarez, 2007; Alvarez et al., 2010) with some hydrothermal activity in the NW portion of the bay (Núñez-Cornú et al., 2000), whereas the region of the CJVL contains various graben structures and numerous Quaternary volcanic manifestations.

Up to this point, it was an unsuspected connection between the two anomalies; unveiling this connection has been made possible by the dense mesh of the EIGEN-6C4 data set.

The volcanic trench ward migration from T-Z rift to the CJVL may be compared to the trench ward migration that has also been documented in the Colima Volcanic Complex (Luhr and Carmichael, 1980; Alvarez and Yutsis, 2015b). Migration in the CVC has left a continuous volcanic trace (i.e., El Cántaro Norte, El Cántaro Sur, Nevado de Colima, and Volcán de Fuego), whilst migration of magmatism from the Tepic-Zacoalco rift to the CJVL does not appear to exhibit a similar pattern. Volcanic activity is now shared between two regions parallel to the trench, but separated by 60 km. In fact, a northwest trend of younger rocks ranging from 3 Ma near Ayutla to Holocene ages in the Mascota fields is documented (Bandy et al., 2001). This interesting subject should be addressed in a detailed study of the region between the T-Z rift and the CJVL.

## 7. Conclusions

The integral analysis of the Jalisco Block from a gravimetric viewpoint allowed for the definition of structures and tendencies not previously reported. The Tepic-Zacoalco and the Northern Colima rifts meet at and define the Guadalajara Triple Point. Here we identified two additional structural trends, represented by aligned sequences of gravity minima, that start at the GTP and continue southwestwardly at S15°W and S35°W directions; the former ending at Manzanillo Harbor and the latter ending offshore, close to the Pacific coast. Together with the Northern Colima Rift they conform a fan-like distribution of gravity trends, with the GTP as the common point.

The extent and amplitude of the gravity anomalies associated with the Central Jalisco Volcanic Lineament are likely associated with the trench ward migration of the volcanic front. We found that all the volcanic fields in the Jalisco Block (Colima Volcanic Complex, Mascota, Atenguillo, Tapalpa, etc.) are associated with gravity lows. Furthermore, the similarity and proximity of the W section of the CJVL with the gravity anomaly of Bahía de Banderas suggests that both anomalies are linked by a tectonic process induced by the subduction of the Rivera plate. Two magnetotelluric lines that cross the CJVL show electrically conductive sections from the surface to depths of 10 km in this region, contrasting with adjacent resistive strata (Corbo et al., 2013), indicating that conductive fluids and/or magmas have intruded this region, inducing the observed negative gravity anomalies.

The Jalisco Block boundaries are confirmed as the Tepic-Zacoalco and the Colima rifts and gravimetric trends presented confirm the location of the NW boundary of the Jalisco Block along the Banderas-Compostela rift.

## Declaration of Competing Interest

The authors declare that they have no known competing financial interests or personal relationships that could have appeared to influence the work reported in this paper.

## Acknowledgements

We acknowledge support for one of us (MC) from Consejo Nacional de Ciencia y Tecnología, México (CONACYT), and to Instituto de Investigaciones en Matemáticas Aplicadas y en Sistemas (IIMAS) of Universidad Nacional Autónoma de México (UNAM) for material support of this research. We acknowledge the thorough revision of the manuscript by two anonymous reviewers; their remarks greatly improved the quality of the manuscript.

## References

- Allan, J.F., 1985. Sediment depth in the northern Colima graben from 3-D interpretation of gravity. *Geofis. Int.* 56, 992–1002.
- Allan, J.F., 1986. Geology of the Northern Colima and Zacoalco Grabens, Southwest Mexico: Late Cenozoic Rifting in the Mexican Volcanic Belt. *Geol. Soc. Am. Bull.* 97, 473–485. [https://doi.org/10.1130/0017606\(1986\)97<473:gotnca>2.0.co;2](https://doi.org/10.1130/0017606(1986)97<473:gotnca>2.0.co;2).
- Alvarez, R., 2002. Banderas Rift Zone: A plausible NW limit of the Jalisco Block. *Geophys. Res. Lett.* 29 (20), 1994–1997. <https://doi.org/10.1029/2002GL016089>.
- Alvarez, R., 2007. Submarine topography and faulting in Bahía de Banderas, Mexico. *Geofis. Int.* 46 (2), 93–116.
- Alvarez, R., Yutsis, V., 2015a. The Elusive Rivera-Cocos Plate Boundary: Not Diffuse. In: Wright, T.J., Ayele, A., Ferguson, D.J., Kidane, T., Vye-Brown, C. (Eds.), *Magmatic Rifting and Active Volcanism*. vol. 420 Geological Society, London Special Publications.
- Alvarez, R., Yutsis, V., 2015b. Southward migration of magmatic activity in the Colima Volcanic Complex, Mexico: An ongoing process. *Int. J. Geosci.* 6, 1077–1099. <https://doi.org/10.4236/ijg.2015.69085>.
- Alvarez, R., López-Loera, H., Arzate, J., 2006. Evidence of the existence of an uplifted and a static domain in the Jalisco Block. In: *Backbone of the Americas: Patagonia to Alaska, Mendoza, Argentina: Geological Society of America, Abstracts with Programs, Specialty Meetings No. 2*, pp. 108.
- Alvarez, R., López-Loera, H., Arzate, J., 2010. Modeling the marine magnetic field of Bahía de Banderas, Mexico, confirms the half-graben structure of the bay. *Tectonophysics* 489 (1–4), 14–28. <https://doi.org/10.1016/j.tecto.2010.03.012>.
- Arzate, J.A., Alvarez, R., Yutsis, V., Pacheco, J., López-Loera, H., 2006. Geophysical modeling of valle de Banderas graben and its structural relation to Bahía de Banderas, Mexico. *Rev. Mexican. Cien. Geol.* 23 (2), 184–198.
- Bandy, W.L., Mortera-Gutierrez, C.A., Urrutia-Fucugauchi, J., 1993. Gravity field of the southern Colima graben, Mexico. *Geofis. Int.* 32, 561–567.
- Bandy, W.L., Mortera-Gutierrez, C.A., Urrutia-Fucugauchi, J., Hilde, T.W.C., 1995. The subducted Rivera-Cocos plate boundary: Where is it, what is it, and what is its relation to the Colima rift? *Geophys. Res. Lett.* 22, 3075–3078.
- Bandy, W., Kostoglodov, V., Hurtado-Díaz, A., Mena, M., 1999. Structure of the southern Jalisco subduction zone, Mexico, as inferred from gravity and seismicity. *Geofis. Int.* (38–3), 127–136.
- Bandy, W.L., Urrutia-Fucugauchi, J., McDowell, F.W., Morton-Bermea, O., 2001. K-Ar ages of four mafic lavas from the Central Jalisco Volcanic Lineament: Supporting evidence for a NW migration of volcanism within the Jalisco block, western Mexico. *Geofis. Int.* 40, 259–269.
- Bandy, W.L., Michaud, F., Bourgois, J., et al., 2005. Subsidence and strike-slip tectonism of the upper continental slope off Manzanillo, Mexico. *Tectonophysics* 398, 115–140.
- Barrier, E., Bourgois, J., Michaud, F., 1990. Le système de rifts actifs du point triple de Jalisco: vers un proto-golfe de Jalisco. *C.R. Acad. Sci. Paris*, t. 310, 1513–1515.
- Barthelmes, F., Köhler, W., 2016. International Centre for Global Earth Models (ICGEM), in: Drewes, H., Kuglitsch, F., Adám, J. et al., *The Geodesists Handbook 2016*. J. Geod. 90 (10), 907–1205. <https://doi.org/10.1007/s00190-016-0948-z>.
- Böhnel, H., Negendank, J.F.W., 1988. Paleomagnetism of the Puerto Vallarta intrusive complex and the accretion of the Guerrero terrain, Mexico. *Phys. Earth Planet. Int.* 52, 330–338.
- Böhnel, H., Morán-Zenteno, D., Schaff, P., Urrutia-Fucugauchi, J., 1992. Paleomagnetic and isotope data from southern Mexico and the controversy over the pre-Neogene position of Baja California. *Geofis. Int.* 31–3, 253–261.
- Bourgois, J., Renard, V., Aubouin, J., et al., 1988. Active fragmentation of the North American plate: Offshore boundary of the Jalisco block off Manzanillo. *C.R. Acad. Sci. Paris* 307 (Ser. II), 1121–1130.
- Campos-Enríquez, J.O., Alatorre-Zamora, M.A., 1998. Shallow structure of the junction of the graben of Chapala, Tepic-Zacoalco and Colima, Mexico. *Geofis. Int.* 37–4, 263–282.
- Cassel, E.J., Smith, M.E., Jicha, B.R., 2018. The impact of slab rollback on Earth's surface: Uplift and extension in the hinterland of the North American Cordillera. *Geophys. Res. Lett.* 45, 10,996–11,004. <https://doi.org/10.1029/2018GL079887>.
- Corbo, F., Arzate, J.A., Alvarez, R., Aranda, J.J., Yutsis, V., 2013. Subduction of the Rivera Plate beneath the Jalisco Block as imaged by magnetotelluric data. *Rev. Mexican. Cienc. Geol.* 30, 268–281.
- DeMets, C., Stein, S., 1990. Present-day kinematics of the Rivera plate and implications for tectonics in southwestern Mexico. *J. Geophys. Res.* 95, 21,931–21,948.
- Duque-Trujillo, J., Ferrari, L., Orozco-Esquivel, T., López-Martínez, M., Lonsdale, P., Bryan, S.E., Kluesner, J., Piñero-Lajas, D., Solari, L., 2015. Timing of rifting in the Southern Gulf of California and its conjugate margins: Insights from the plutonic record. *Geol. Soc. Am. Bull.* 127 (5/6), 702–736. <https://doi.org/10.1130/B31008.1>.
- Ferrari, L., & Rosas-Elguera, J., (2000). Late Miocene to Quaternary extension at the northern boundary of the Jalisco block, western Mexico: The Tepic-Zacoalco rift revisited. In: Delgado-Granados, H., Aguirre-Díaz, G., and Stock, J. M., eds., *Cenozoic Tectonics and Volcanism of Mexico: Boulder, Colorado, Geological Society of America, Special Paper* 334.
- Ferrari, L., Orozco-Esquivel, M.T., Manea, V., Manea, M., 2012. The dynamic history of the Trans-Mexican Volcanic Belt and the Mexico subduction zone. *Tectonophysics* 522–523, 122–149. <https://doi.org/10.1016/j.tecto.2011.09.018>.
- Ferrari, L., López-Martínez, M., Orozco-Esquivel, M.T., Bryan, S.E., Duque-Trujillo, J., Lonsdale, P., Solari, L., 2013. Late Oligocene to middle Miocene rifting and syn-extensional magmatism in the southwestern Sierra Madre Occidental, Mexico: The beginning of the Gulf of California rift. *Geosphere* 9 (5), 1161–1200.
- Ferrari, L., Orozco-Esquivel, T., Bryan, S.E., López-Martínez, M., Silva-Fragoso, A., 2018. Cenozoic magmatism and extension in western Mexico: Linking the Sierra Madre

- Occidental silicic large igneous province and the Comondú Group with the Gulf of California rift. *Earth Sci. Rev.* 183, 115–152. <https://doi.org/10.1016/j.earscirev.2017.04.006>.
- Fletcher, J.M., Grove, M., Kimbrough, D., Lovera, O., Gehrels, G.E., 2007. Ridge-trench interactions and the Neogene tectonic evolution of the Magdalena shelf and southern Gulf of California: Insights from detrital Zircon U-Pb ages from the Magdalena fan and adjacent areas. *GSA Bull.* 119 (11–12), 1313–1336. <https://doi.org/10.1130/B26067.1>.
- Garduño, V.H., Tibaldi, A., 1991. Kinematic evolution of the continental active triple junction of the western Mexican volcanic belt. *C.R. Acad. Sci. Paris t 312 (Ser. II)*, 135–142.
- Gómez-Tuena, A., Langmuir, C.H., Goldstein, S.L., Straub, S.M., Ortega-Gutiérrez, F., 2007. Geochemical evidence for slab melting in the Transmexican Volcanic Belt. *J. Petrol.* 48, 537–562. <https://doi.org/10.1093/ptrology/egl071>.
- Hildenbrand, T.G., Briesacher, A., Flanagan, G., Hinze, W.J., Hittelman, A.M., Keller, G.R., Kucks, R.P., Plouff, D., Roest, W., Seeley, J., Smith, D.A., Webring, M., 2002. Rationale and operational plan to upgrade the U.S. Gravity Database. In: U.S. Geological Survey OpenFile Report 02-463, pp. 12.
- Hopper, J.R., Buck, W.R., 1996. The effect of lower crustal flow on continental extension and passive margin formation. *J. Geophys. Res.* 101 (B9), 20,175–20,194.
- Jensky, W.A., 1974. Reconnaissance Geology and Geochronology of the Bahía de Banderas Area, Nayari and Jalisco, Mexico. MA thesis. California State University, San Diego, pp. 80.
- Johnson, C.A., Harrison, C.G.A., 1990. Neotectonics in central Mexico. *Phys. Earth Planet. Int.* 64, 187–210.
- Karig, D., Jensky, W., 1972. The Proto-Gulf of California. *Earth Planet. Sci. Lett.* 17, 169–174. [https://doi.org/10.1016/0012-821X\(72\)902-572](https://doi.org/10.1016/0012-821X(72)902-572).
- Khutorskoy, M.D., Delgado-Argote, L.A., Fernández, R., Kononov, V.I., Polyak, B.G., 1994. Tectonics of the offshore Manzanillo and Tecpan basins, Mexican Pacific, from heat flow, bathymetric and seismic data. *Geofis. Int.* 33, 161–185.
- Lafehr, T.R., 1991. An exact solution for the gravity curvature (Bullard B) correction. *Geophysics* 56, 1179–1184.
- León-Soto, G., Ni, J.F., Grand, S.P., Sandvol, E., Valenzuela, R.W., Guzmán-Speziale, M., González-Gómez, J.M., Domínguez-Reyes, T., 2009. Mantle flow in the Rivera-Cocos subduction zone. *Geophys. J. Int.* 179, 1004–1012.
- Li, X., Gotze, H.-J., 2001. Ellipsoid, geoid, gravity, geodesy and geophysics tutorial. *Geophysics* 66, 1660–1668.
- Lizarralde, D., Axen, G., et al., 2007. Variable styles of rifting in the Gulf of California. *Nature* 448, 466–469.
- Lonsdale, P., 1989. Geology and tectonic history of the Gulf of California. In: Winterer, E.L., Hussong, D.M., Decker, R.W. (Eds.), *The Geology of North America, The Eastern Pacific Ocean and Hawaii*. Geological Society of America, Boulder, CO, pp. 499–521.
- Luhr, J.F., Carmichael, I.S.E., 1980. The Colima Volcanic Complex, Mexico. *Contrib. Mineral. Petrol.* 71, 343–372.
- Luhr, J., Nelson, S., Allan, J., Carmichael, I.S.E., 1985. Active rifting in southwestern Mexico: Manifestations of an eastward spreading ridge jump. *Geology* 13 (1), 54–57. [https://doi.org/10.1130/0091-7613\(1985\)13<54:ARISMM>2.0.CO;2](https://doi.org/10.1130/0091-7613(1985)13<54:ARISMM>2.0.CO;2).
- Medina, F., Espindola, J.M., De la Fuente, M., Mena, M., 1996. A gravity model of the Colima, Mexico region. *Geofis. Int.* 35, 409–414.
- Michaud, F., Bourgois, J., Parrot, J.-F., Taud, H., Kasser, M., 1994. Tectonic development of the Jalisco triple junction (western Mexico) from SPOT- DEM data processing. *C.R. Acad. Sci. Paris t. 318 (Ser. II)*, 1117–1124.
- Moritz, H., 2000. Geodetic reference system 1980. *J. Geod.* 74, 128–133. <https://doi.org/10.1007/s001900050278>.
- NAMAG, 2002. North American Magnetic Anomaly Group. Magnetic Anomaly Map of North America. In: US Department of the Interior and US Geological Survey. Scale 1:10000000.
- Núñez-Cornú, F.J., Prol-Ledesma, R.M., Cupul-Magaña, A., Suárez-Plascencia, C., 2000. Near shore submarine hydrothermal activity in Bahía de Banderas, western Mexico. *Geofis. Int.* 39 (2), 171–178.
- Ortega-Rivera, A., 2003. Geochronological constraints on the tectonic history of the Peninsular Ranges batholith of Alta and Baja California: Tectonic implications for western Mexico. *Geol. Soc. Am. Special Paper* 374, 297–336.
- Pardo, M., Suárez, G., 1995. Steep subduction geometry of the Rivera plate beneath the Jalisco block in western Mexico. *Geophys. Res. Lett.* 20, 2391–2394.
- Righter, K., Carmichael, I.S., 1992. Hawaiites and related lavas in the Atenguillo graben, western Mexican Volcanic Belt. *Geol. Soc. Am. Bull.* 104, 1592–1607.
- Righter, K., Rosas-Elguera, J., 2001. Alkaline lavas in the volcanic front of the western Mexican Volcanic Belt: Geology and petrology of the Ayutla and Tapalpa volcanic fields. *J. Petrol.* 42 (12), 2333–2361.
- Rosas-Elguera, J., Ferrari, L., Garduño-Monroy, V.H., Urrutia-Fucugauchi, J., 1996. Continental boundaries of the Jalisco block and their influence in the Pliocene-Quaternary kinematics of western Mexico. *Geology* 24, 921–924.
- Rosenbaum, G., Weinberg, R.F., Regenauer-Lieb, K., 2008. The geodynamics of lithospheric extension. *Tectonophysics* 458, 1–8. <https://doi.org/10.1016/j.tecto.2008.07.016>.
- Ryan, W.B.F., Carbotte, S.M., et al., 2009. Global multi-resolution topography synthesis. *Geochem. Geophys. Geosyst.* 10, Q03014. <https://doi.org/10.1029/2008GC002332>.
- Schaaf, P., H. Köhler, D. Muller-Sohnius and Von Drach, V. (1993), The Puerto Vallarta Batholith-its anatomy displayed by isotopic fine structure. In: Proceedings of the First Circum-Pacific and Circum-Atlantic Terrane Conference, edited by F. Ortega-Gutiérrez, P.J. Coney, E. Centeno-García and A. Gómez-Caballero, Instituto de Geología, Universidad Nacional Autónoma de México, November, 1993, Guanajuato, México, pp. 133–135.
- Serpa, L., Smith, S., Katz, C., Skidmore, C., Sloan, R., Pavlis, T., 1992. A geophysical investigation of the southern Jalisco block in the State of Colima, Mexico. *Geofis. Int.* 31, 475–492.
- Serrato-Díaz, G.S., Bandy, W.L., Mortera-Gutiérrez, C.A., 2004. Active rifting and crustal thinning along the Rivera-Cocos plate boundary as inferred from mantle Bouguer gravity anomalies. *Geofis. Int.* 43, 361–381.
- Siebert, L., Calvin, C.L., Kimberly, P., Luhr, J.F., Kysar, G., 2003. Volcanoes of México (CD-ROM). In: Smithsonian Institution. Global Volcanism Program. Digital Information Series, GVP-6.
- Smith, W.H.F., Sandwell, D.T., 1997. Global sea floor topography from satellite altimetry and ship depth soundings. *Science* 277, 1956–1962.
- Stock, J.M., 1993. Plate tectonics and the evolution of the Jalisco block, Mexico. *GEOS Bull. Unión Geofis. Mexican.* 13-3, 3–9 (In Spanish).
- Stock, J.M., Hodges, K.V., 1989. Pre-Pliocene Extension around the Gulf of California and the transfer of Baja California to the Pacific Plate. *Tectonics* 8 (1), 99–115. <https://doi.org/10.1029/TC008i001p00099>.
- Suhardja, S.K., Grand, S.P., Wilson, D., Guzman-Speziale, M., Gomez- Gonzalez, J.M., Domínguez-Reyes, T., Ni, J., 2015. Crust and subduction zone structure of Southwestern Mexico. *J. Geophys. Res. Solid Earth* 120, 1020–1035. <https://doi.org/10.1002/2014JB011573>.
- Sutherland, F.H., Kent, G.M., Harding, A.J., Umhoefer, P.J., Driscoll, N.W., Lizarralde, D., Fletcher, J.M., Axen, G.J., Holbrook, W.S., González-Fernández, A., y Lonsdale, P., 2012. Middle Miocene to early Pliocene oblique extension in the southern Gulf of California. *Geosphere* 8 (4), 752–770. <https://doi.org/10.1130/GES00770.1>.
- Telford, W., Geldart, L.P., Sheriff, R.E., 1990. *Applied Geophysics* (2d. Ed). Cambridge University Press, Cambridge. <https://doi.org/10.1017/CBO9781139167932>. ISBN:9781139167932.
- Thybo, H., Artemieva, I.M., 2013. Moho and magmatic underplating in continental lithosphere. *Tectonophysics* 609, 605–619. <https://doi.org/10.1016/j.tecto.2013.05.032>.
- Urrutia-Fucugauchi, J., Flores-Ruiz, J.H., 1996. Bouguer gravity anomalies and regional crustal structure in central Mexico. *Int. Geol. Rev.* 38, 176–194.
- Urrutia-Fucugauchi, J., Molina-Garza, R., 1992. Gravity modeling of regional crustal and upper mantle structure of the Guerrero terrane-1. Colima graben and southern Sierra Madre Occidental, western Mexico. *Geofis. Int.* 31, 493–507.
- Urrutia-Fucugauchi, J., Flores-Ruiz, J.H., Bandy, W.L., Mortera-Gutiérrez, C.A., 1999. Crustal structure of the Colima rift, western Mexico: Gravity models revisited. *Geofis. Int.* 38 (4), 205–216.
- Yang, T., Grand, S.P., Wilson, D., Guzmán-Speziale, M., Gómez-González, J.M., Domínguez-Reyes, T., Ni, J., 2009. Seismic structure beneath the Rivera subduction zone from finite-frequency seismic tomography. *J. Geophys. Res.* 114, B01302.

*Capítulo 4: Applying High-Resolution Gravity Analysis to Volcanic Plumbing Systems: The Case of Nevado De Toluca Volcano, Mexico.*



## Applying High-Resolution Gravity Analysis to Volcanic Plumbing Systems: The Case of Nevado De Toluca Volcano, Mexico

**R. Alvarez**

Instituto de Investigaciones en  
Matemáticas Aplicadas y en Sistemas (IIMAS),  
Universidad Nacional Autónoma de México

**M. Camacho**

Posgrado en Ciencias de la Tierra,  
Universidad Nacional Autónoma de México

### ABSTRACT

The plumbing systems of volcanoes are the reservoirs and conduits in which magma is stored and transported in a volcanic structure; their geometries and volumes help place physical limits to the location and size of shallow magma deposits and associated volcanic products. Density variations in the volcanic interior are reflected in the surface gravity field. Performing 3D inversions of the Bouguer anomaly allows the modeling of density distributions, thereby inferring the plumbing system. The process is here exemplified by Nevado de Toluca volcano; it has been active over the past 2.6 My through emissions of andesitic lava flows and pyroclastic deposits. The crater was destroyed at least two times, and the latest activity was recorded at 3.3 ka. Using a high-resolution, satellite gravity data set, and a corresponding magnetic field set, also collected via satellite, we performed 3D inversions on the Bouguer anomaly and the magnetic measurements enclosing this volcanic structure, with resolutions of 500 and 1000 m; the results were obtained in the form of density and magnetic susceptibility volumes, with depths reaching 5 km from the surface. The resolution of the gravity data set unveiled hitherto unknown characteristics of the upper sections of the volcano's plumbing system consisting of a magma chamber and at least two conduits reaching the surface; a cross-section through the summit shows the dacitic dome known as El Ombligo, between those conduits. Preliminary estimates of the depth and volume of the magmatic chamber are 5-6 km below the summit and  $\sim 16 \text{ km}^3$ , respectively. The low-density regions are also associated with the neighboring San Antonio volcano and the Tenango lava flows. Since the high-resolution, satellite gravity data used here were gathered all over continents and numerous islands between  $\pm 60^\circ$  latitudes, this procedure can be applied to almost any volcanic structure within this latitudinal range.

**Keywords:** Nevado de Toluca, Satellite gravity data, 3D inversions, Volcanic plumbing systems, Trans Mexican Volcanic Belt.

## INTRODUCTION

Plumbing systems are identified as the conduits that transport and store magma from the source to the surface (Murcia et al., 2019); they consist of the network that transports magma from its sources in the asthenosphere and the lithosphere, feeding magma chambers through dikes and sills. Our objective is to locate such conduits and chambers by means of high-resolution ( $\sim 220$  m) gravimetric measurements and 3D inversions.

Gravimetric and magnetic determinations and models were used to associate density and magnetic susceptibility anomalies with the structural traits of the volcanic region. Gravimetric studies help determine the characteristics of volcanic fields (Kauahikaua et al., 2000; Camacho et al., 2018; Camacho and Alvarez, 2020; Guevara et al. 2021); and may help identify their plumbing systems (e.g., Alvarez and Yutsis, 2015; Camacho et al. 2018). Magnetic determinations often complement gravity studies (e.g., Guevara et al. 2021). With the models calculated here, we focused on the processes occurring in the upper 5-6 km of the lithosphere. To illustrate the procedure, we performed 3D inversions of gravity and magnetic data on the Nevado de Toluca volcano in central Mexico. The Trans Mexican Volcanic Belt (TMVB) extends in an E-W direction over 1000 km along the central portion of Mexico and includes numerous volcanic edifices of diverse ages, some of which are in various stages of activity (Ferrari et al., 2012). One of these volcanoes is Nevado de Toluca (NT, 4680 m). The active Popocatepetl volcano and NT are situated at equal distances from Mexico City ( $\sim 70$  km). Toluca City is located  $\sim 26$  km NE from NT. This is a densely populated region which is one of the large industrial centers of Mexico. Some of its current volcanic hazards were evaluated by Aceves-Quezada et al. (2007).

Nevado de Toluca is located at  $99^{\circ} 45'W$ ,  $19^{\circ} 06'N$ ; DeCserna and Fries (1981) obtained an age determination of 1.6 Ma through K-Ar dating for its initial stages of activity. However, Martinez-Serrano et al. (2004) reported that activity started 2.6 Ma with the emission of andesitic lavas, which was modified in the last 40 Ky into emissions of lava flows and pyroclastic deposits with predominantly orthopyroxene-hornblende dacitic compositions, concluding that the construction of the NT volcano occurred at the intersection of three fault systems: the Taxco-Querétaro (NNW-SSE), San Antonio (NE-SW), and Tenango (E-W) fault systems. The authors observed that the Plio-Quaternary E-W trending system actively controlled the ascent and storage of magmas during the recent volcanic activity. Regional fault systems are described in more detail in Norini et al., (2006). Many smaller volcanic structures surround the main edifice (e.g., La Guadalupana, Volcán Gordo, San Antonio volcanoes, as well as the neighboring Tenango volcanic field (Bloomfield, 1974, 1975; Martinez-Serrano et al., 2004) cinder cones and extensive basaltic eruptions conform the landscape.

Cantagrel et al. (1981) reported that NT was built in two very dissimilar phases; the first one lasted over 1 My and the second one developed over the last 100 Ky. However, based on field data and  $^{40}\text{Ar}/^{39}\text{Ar}$  dating, Torres-Orozco et al. (2017) concluded that volcanism at NT was initiated during the mid-Pleistocene ( $\sim 1.5$  Ma). The authors recognized an early history of effusive volcanism with centralized vents, which has been continuous since they found no gaps in the volcano's activity. These authors also recognized that the volcano's original morphology has been severely modified by subsequent explosive eruptions and flank collapses. The original edifice of NT has apparently been destroyed twice, as suggested by debris avalanches, lahars,

and fluvial deposits observed on its south flank (Macías et al., 1997; Capra and Macías, 2000), indicating that the region is prone to explosive activity which could induce major damage in this urban and industrialized area.

Bloomfield and Valastro (1974, 1977) reported two Plinian eruptions at 24.5 and 11.6 Ka; García-Palomo et al. (2002) reported four Plinian eruptions at ~36, ~24.5, 12.1, and 10.5 Ka, dated from the corresponding debris flow avalanches. Aceves-Quezada et al. (2007) reported activity on 14 dates from 1.4 Ma to 3.3 Ka, including andesitic lava flows, debris flows and avalanches, lahars, pumice, and ash flows. Arce et al. (2003) described a Plinian eruption at 10.5 Ka.

The Plinian products and erupted bulk-rock compositions of NT show that the eruptions originated in an upper crustal reservoir (Arce et al., 2013a and b). Weber et al., (2020) concluded that a hybridization processes of deep basaltic-andesite recharge magma and an upper crustal silicic mush was reflected in the compositional zoning of all mineral phases; they concluded that NT is fed from two spatially separated magma sources residing either in the upper mantle or the lower crust.

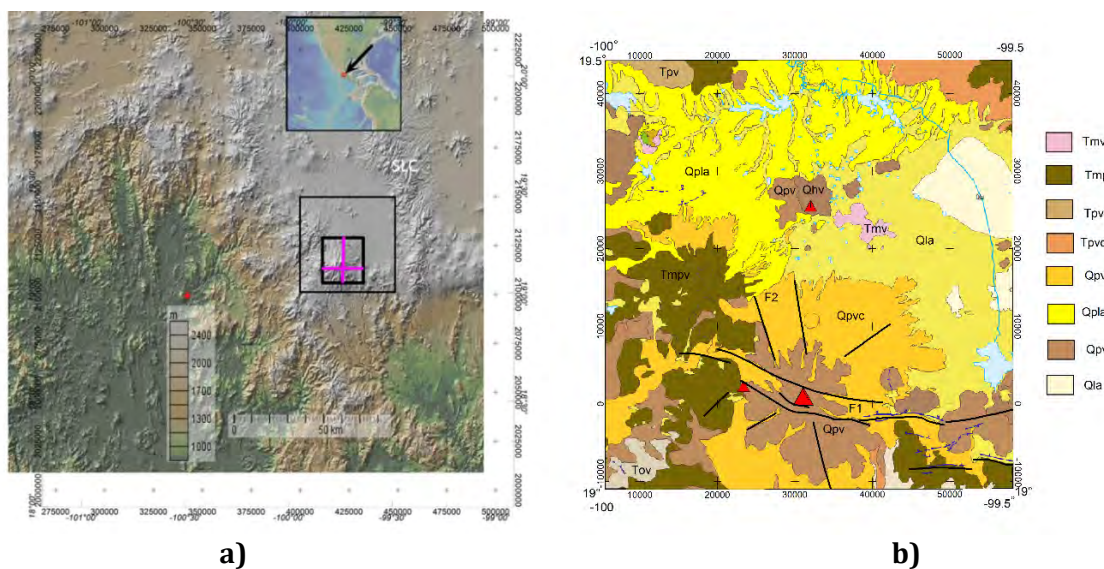


**Figure: 1**

**Legend:** Tmv basaltic lavas; Tmpv andesite-basaltic lava flows; Tpv basalt and andesite; Tpvc volcanic rocks and alluvial deposits; Qpvc lahars and volcanoclastic deposits; Qpla lacustrine sediments; Qpv basaltic lava flows; Qla lacustrine deposits and volcanic ash.

**Fig. 1** a) Topography of the Nevado de Toluca area and location of two 3D inversions: the larger, black rectangle corresponds to the 1000 m resolution inversion, and the smaller black rectangle to the 500 m resolution. Also shown, are the locations of two cross-sections-oriented N-S and E-W (magenta) and obtained from the inverted voxel. b) Geologic map of Nevado de Toluca volcano corresponding to the area covered by the large rectangle. The larger red triangle shows the location Nevado de Toluca. The small red triangle W of NT corresponds to El Gordo volcano, whilst the one to the N corresponds to El Molcajete volcano. Lines in black represent geologic



faults: F1 (Tenango-San Antonio Fault System) and F2 (Taxco-Querétaro Fault System). Figure 1a made with GeoMapApp ([www.geomapapp.org](http://www.geomapapp.org)) / CC BY/ (Ryan et al., 2009). Figure 1b adapted from the Geologic Chart of the State of Mexico, [https://ifomegem.edomex.gob.mx/carta\\_geologica](https://ifomegem.edomex.gob.mx/carta_geologica).

Characterization of volcanic structures in terms of gravity varies depending on several factors. The resolution of the gravity used in the study is of fundamental importance; large scale studies involving hundreds of kilometers traditionally have used low-resolution data sets. The studies in the islands of Hawaii are an example (Kauahikaua et al., 2000), and in the Canary Islands (Camacho et al., 2018); in both instances positive anomalies were associated with portions of the volcanic region. In the case of Hawaii, positive anomalies are associated with dense cores, interpreted as magma storage regions, whilst in the case of Lanzarote, in the Canary Islands, three high-density regions are associated with three main volcanic complexes. In both cases, ground gravity surveys were used.

In inactive volcanic systems, whose activity ceased several Myr ago, the magma chambers, the intrusives, and the lava conduits have by now crystallized and cooled off, giving rise to anomalies with high density values, associated with positive Bouguer anomalies, and high susceptibility values. On the contrary, young, dynamic volcanoes fed by magma chambers with active mush and partial melts discharged through the conduits associated with their plumbing systems, usually present negative Bouguer anomalies, corresponding to the concentration of low-density materials, and lesser magnetic susceptibility values. Cases may occur in which both situations may appear, as in the case of Colima volcano (Guevara et al., 2021) or Kilauea volcano in Hawaii (Kauahikaua et al., 2000), in which old eruption paths have been abandoned and substituted by young, active plumbing systems.

## METHODOLOGY

We obtain the gravity data from the GGMplus data set, discuss data resolution, and obtain the Bouguer anomaly in the study area. Two 3D inversions were produced with resolutions of 1000 and 500 m. The former corresponds to the larger rectangle shown in Figures 1a and 2, and the second (500 m resolution) encompasses the NT structure.

### Data Processing

The GGMplus gravimetric data set was used for the 3D inversion (Hirt et al., 2013). This model presents the gravimetric data in two formats: as a FA anomaly and the gravity observed on the surface ( $G_{Obs}$ ). The advantages of using the GGMplus model versus other high-resolution models is discussed in Camacho and Alvarez (2021). In this work, we calculated BA from  $G_{Obs}$  and this correction was included according to the new gravimetric standard of the USGS (e.g., Hildenbrand et al., 2002).

The theoretical gravity was obtained for each point of the data set (equation 1) (Wollard, 1979) calculate the BA, where the coefficients were:  $g_e=978032.67715$  mGal,  $k=0.01931851353$ , and  $e^2=0.0066938002290$ . Coefficients  $k$  and  $e$  are dimensionless.

$$G_{teo} = g_e \frac{1 + k * (\sin \varphi)^2}{\sqrt{1 - e^2 (\sin \varphi)^2}} \quad (1)$$

The elevation at each point must be known; to accomplish this, we used the topographic model SRTM90 with a 7.5 arc-sec resolution which was the same as in the GGMplus model (Jarvis et al., 2008; <https://srtm.csi.cgiar.org/srtmdata>). Subsequently, the values of the ellipsoidal height ( $h_{ellip}$ ) and the geoid height were placed at geoidal height ( $H_{geo}$ ) through equation (2) (Li and Götze, 1996). For the following formulas the geoidal height ( $H_{geo}$ ) will be defined as height (h).

$$h_{ellip} = H_{geo} + N \quad (2)$$

Where N is the geoid height, which can be readily observed in the page of ICGEM (Barthelmes & Kohler, 2016).

Knowing the height from the DEM at each point, we obtained the height correction ( $C_h$ ) through equation (3).

$$C_h = ((0.3087691 - 0.0004398 * \sin(\varphi)^2)h + 7.2125 * 10^{-8}h^2) \left[ \frac{mGal}{m} \right] \quad (3)$$

We then calculated the atmospheric correction ( $C_{atm}$ ) considering the gravimetric attraction produced by the mass of air over the point determined with equation 4 (Hildenbrand et al., 2002).

$$C_{atm} = 0.874 - 9.9 * 10^{-5} * h + 3.56 * 10 * 10^{-9} * h^2 \quad (4)$$

The Bouguer correction ( $C_{Boug_{2^\circ}}$ ) is the correction that eliminates the gravimetric attraction of the masses existing between the reference level and the point on a topographic surface (equation 5).

$$C_{Boug_{2^\circ}} = 2\pi * G * \rho * h * \left( \frac{\alpha}{2} - \eta * \left( 1 + \frac{1}{2\alpha} \right) \right) \left[ \frac{mGal}{m} \right] \quad (5)$$

Where  $\alpha$  and  $\eta$  are coefficients defined by Lafehr (1991), G is the gravimetric constant, and  $\rho$  the density of the medium.

For the topographic correction ( $C_{topo}$ ), we used the method implemented in the Oasis Montaj program of Geosoft, which uses the algorithm proposed by Kane (1962) and supplemented by Nagy (1966). AB was then calculated with equation (6).

$$AB = G_{Obs} - G_{teo} \pm C_{alt} \mp C_{Boug_{2^\circ}} + C_{atm} + C_{topo} \quad (6)$$

The results produced the Bouguer anomaly map shown in Figure 2. The region was much larger than the area covered by the NT volcano to allow for additional modeling in various expanses of this region.

### **Data Resolution**

The resolutions of the gravity and magnetic data sets are relevant when comparing the inversion results. Ideally, one would like to achieve the same high resolution in both data sets. However, aeromagnetic data with adequate resolutions are sometimes missing from study areas, as in the case of the NT region. The options were: i) not to invert the magnetic data or, ii) use a magnetic data set with a smaller resolution if available. In this case we opted for the latter, using the EMAG2V3 satellite data set and adding information to the results' interpretation. In every instance, we used the topographic model SRTM90 with a 7.5 arc-sec resolution, which was the same as in the GGMplus model.

The EMAG2V3 is a global Earth Magnetic Anomaly Grid compiled from satellite, ship, and airborne magnetic measurements with a resolution of 2 arc-min (~3700 m) and an altitude of 4 km above the geoid (Meyer et al., 2017; Figure 3). The GGMplus gravimetric data set (Figure 2) with a resolution of 7.5 arc-sec (~220 m) was used here (Hirt et al., 2013); this model is available from <http://ddfe.curtin.edu.au/gravitymodels/GGMplus/>. Although the resolutions between the gravity and magnetic data sets were different, the results were complementary and useful for confirming tendencies in either data set, as will be disclosed later in the text.

The two available satellite gravity data sets of higher resolution were compared in a companion study (Camacho and Alvarez, 2021), and it was concluded that the GGMplus data set presently provides the highest resolution. They compared their frequency histograms, Free Air anomalies, power spectra, and simple Bouguer anomalies. The nature of the digital elevation models used for data reduction was also addressed. From a volcanic viewpoint, where the acquisition of gravity ground data is particularly difficult, and in the case of active structures, a task of high risk, having a satellite data set of the area represents a major advantage. Indeed, satellite determinations are distributed uniformly, whilst ground measurements are seldom obtained evenly on volcanoes. In addition, most satellite data sets are freely obtained through servers, and finally, satellite data sets also have a global coverage that makes their application suitable for any volcanic region in the world within the latitudinal limits of the satellite.

we want to stress the fact that the data resolution and the resolution of an inverted model are different. The latter refers to the size of the voxel units used to perform the inversion; further discussion of this topic is made in the 3D inversion section.

### **Bouguer Anomaly**

We used a satellite-derived Bouguer anomaly data set, covering several times the area occupied by the NT structure, which corresponds to the GGMplus data set (Hirt et al., 2013). The idea of processing high-resolution data for the larger area, is to be prepared for the expansion of this analysis to neighboring regions. Gravimetry data were prepared for inversion through a Gaussian filter that separates the residual, in order to highlight the level structures associated with volcanic edifices.

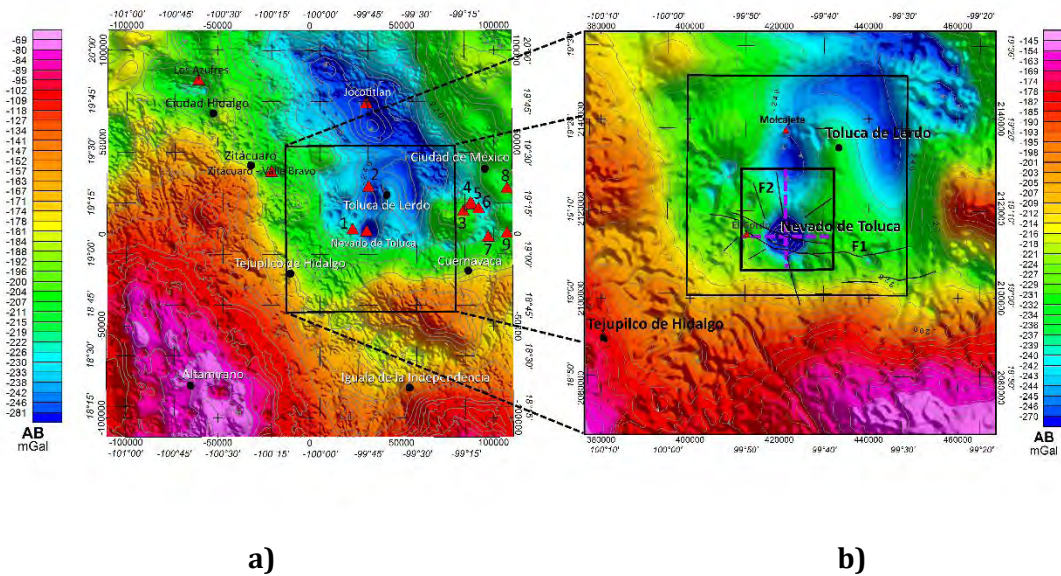


Figure: 2

Fig. 2 a) Complete Bouguer anomaly of the region surrounding the Nevado de Toluca (NT) volcano corresponding to the GGMplus model. Red triangles represent volcanoes: 1 El Gordo, 2 Molcajete, 3 Ajusco, 4 Xitle, 5 Cuautzontle, 6 Oloica, 7 Chichinautzin, 8 Tlaloc, 9 Xaltepec.

b) The black, larger rectangular polygon corresponds to the 1000 m resolution 3D inversion, and the smaller, black polygon to the 500 m resolution 3D inversion discussed ahead. The perpendicular, dashed magenta lines show the locations of the two sections trending N-S and E-W across the NT volcanic structure. F1 (Tenango-San Antonio Fault System) and F2 (Taxco-Querétaro Fault System) represent E-W and NNW-SSE trending fault systems through the volcano's structure (Torres-Orozco et al., 2017).

The Bouguer anomaly map (Figure 2) shows extended positive anomalies to the S and W of the NT volcano. An extended gravity low in the NE portion shows two trends. One is a SE-NW trend extending across the map in that direction; this major, SE-NW negative anomaly runs parallel to Sierra de Las Cruces consisting of an imbrication of volcanic edifices, lava flows, lahars, and pyroclastic deposits. The second, corresponding to the NT region, is located SW of the former and consists of a N-S, horseshoe-shaped anomaly whose western branch shows at its southern end the rounded, negative anomaly of NT. Two polygons (in black) enclose the NT area where the 3D gravity inversions were performed.

Negative gravity anomalies are often related to volcanic edifices associated with the presence of magma chambers and volcanic plumbing systems (e.g., Alvarez and Yutsis, 2015; Guevara et al., 2021; Alvarez and Camacho, 2023). The anomaly low associated with NT is circular and quite like the anomaly low immediately to the north; the difference is that the latter does not show an associated volcanic structure.

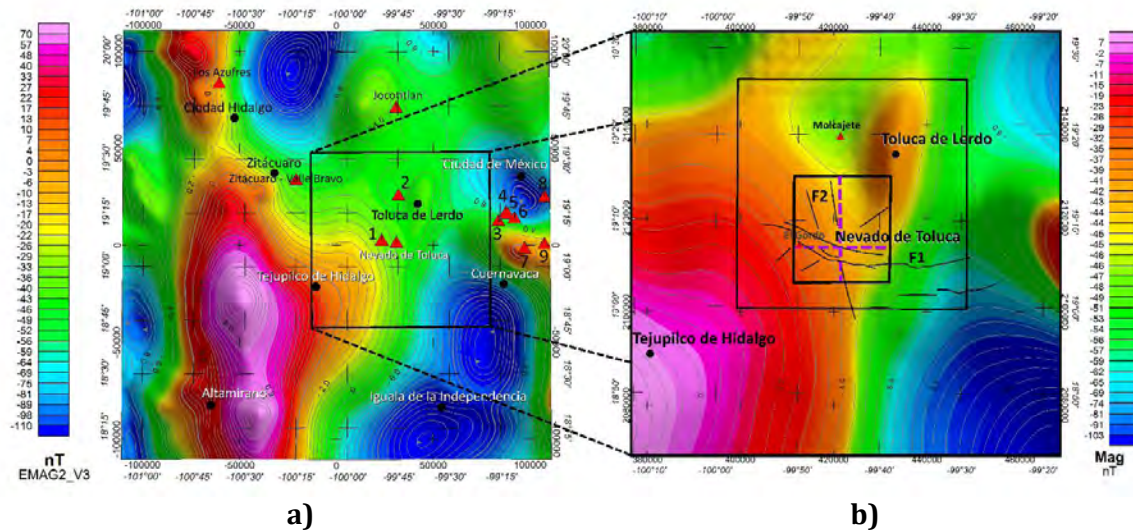


Figure: 3

Fig. 3 a) Magnetic anomaly map of the region surrounding the Nevado de Toluca volcano corresponding to EMAG2 data with a resolution of 2 arc-min ( $\sim 3700$  m), reduced to the pole according to the standard procedure (Baranod & Naudy, 1964),  $I=46.58^\circ$ ,  $D=5.88^\circ$ . Red triangles represent volcanoes: 1 El Gordo, 2 Molcajete, 3 Ajusco, 4 Xitle, 5 Cuautzontle, 6 Oloica, 7 Chichinautzin, 8 Tlaloc, 9 Xaltepec. b) Close up view of the magnetic anomaly around Nevado de Toluca volcano. The black, larger rectangular polygon corresponds to the 1000 m resolution 3D inversion, and the smaller, black polygon to the 500 m resolution 3D inversion discussed ahead. The perpendicular, dashed magenta lines show the locations of the two sections trending N-S and E-W across the NT volcanic structure. F1 (Tenango-San Antonio Fault System) and F2 (Taxco-Querétaro Fault System) represent E-W and NNW-SSE trending fault systems through the volcano's structure (Torres-Orozco et al., 2017).

The magnetic anomaly (Figure 3) was obtained from the satellite data set of EMAG2 (Meyer et al., 2017) with a resolution of 2 arc-min, and it was reduced to the pole. Owing to the difference in resolution with respect to that of the gravity data set, we used its 3D inversion to support the finer gravimetric results. We restricted the magnetic inversion to the smaller rectangle in **Figures 1** and **2**. The region of NT does not exhibit a distinctive magnetic anomaly, as in the case of the Bouguer anomaly; it is located between the two, dominating N-S highs in the magnetic map, showing some local disturbances.

## RESULTS

### 3D Inversions

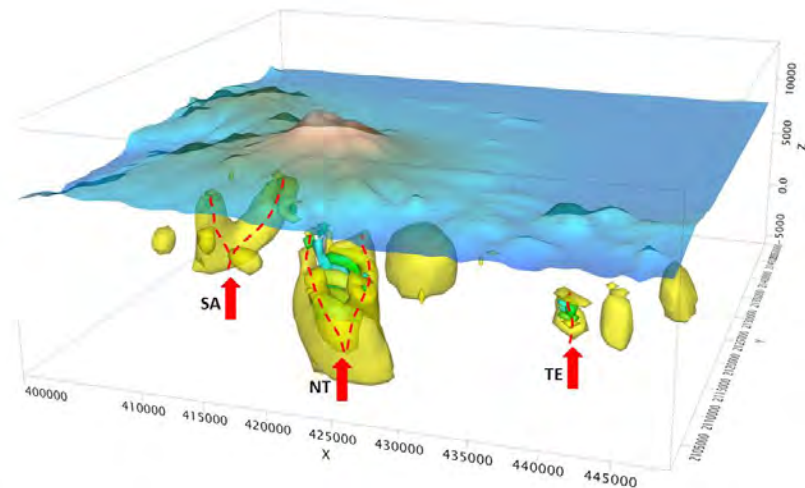
We performed the 3D gravity inversions using the method described by Macleod and Ellis (2013) based on the theoretical considerations of Ellis et al. (2012). The code was implemented in the Oasis Montaj program of Geosoft. The program uses a Cartesian Cut Cell algorithm (CCC) to represent geologic volumes and an Iterative Reweighting Inversion algorithm (IRI, Ingram et al., 2003) to match the observed results with the calculated ones within established error limits, that in these cases is 5% of the standard deviation. The inversion results are provided as densities in  $\text{g}/\text{cm}^3$  when making a gravity inversion, and magnetic susceptibility (SI units) when

performing a magnetic inversion. The depth of the inverted volume was proportional to the size of the basic volume selected for the calculation. Typically, choosing cubes of 500-m-long edges will attain depths of 5-6 km and greater depths can be obtained at the expense of the resolution. When referring to resolution we must bear in mind that there is the high-resolution of the data used to obtain the Bouguer anomaly in Figure 2, in the gravity data case, and there is the resolution of the model proper. Models may have different dimensions; in this study we used models of dimensions in the X-Y plane of 1000 and 500 m, which we call the model resolution. To optimize computation, a subset of the high-resolution data set is used, selected according to the model resolution, to perform the inversion. An example appears ahead (Figure 5b) of the set of stations used for the inversion.

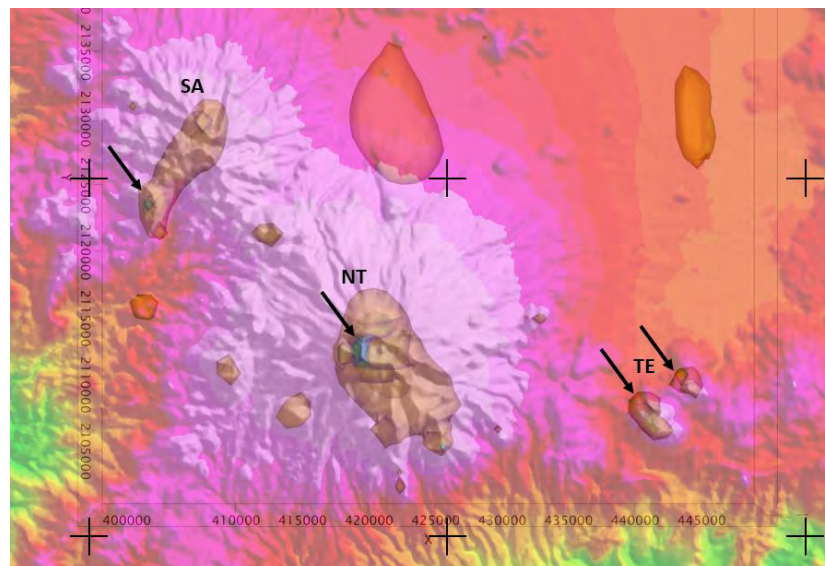
### 1000 m Resolution

The rectangle with the 1000 m resolution, the largest rectangle in Figures 1 and 2, was inverted first to learn about the volcanic sources in that area, before proceeding to the analysis of the NT structure. We performed the 3D inversion of the NT region in the 50 x 50 km area, as shown by the designated rectangles in Figures 1 and 2. In addition, the area included the San Antonio (SA) volcano in the NW of NT, and the Tenango (TE) region to the east containing fissure vent lava flows. From the density distribution obtained, we created geosurfaces, also called isosurfaces, to locate low-density regions. Figure 4a shows the geosurfaces enclosing regions with densities  $<2.56 \text{ g/cm}^3$  (yellow); these regions are associated with surface volcanic manifestations and are located directly underneath the volcanic structures or their manifestations (e.g., lava flows). The dashed, red lines indicate the possible trajectories of volcanic products towards the surface. The maximum depth of the inversion was -5000 m. The SA volcano is the oldest of the group; García-Palomo et al. (2000) assigned it a minimum age of  $3.0 \pm 0.2 \text{ Ma}$ , whilst suggesting that the volcano might have been formed as early as the Miocene. The yellow surface associated with SA (Figure 4a) bifurcates at an elevation of -830 m. The northern branch connects directly with the SA summit, indicating that it forms part of its plumbing system, whilst the southern branch outcrops 8 km SW of the SA summit (Figure 4b). Remarkably, both the yellow and green isosurfaces outcrop at that location. The peculiarity of this observation is that there are no clear associated volcanic structures, implying that the area should be studied in more detail. In contrast, the green surface does not outcrop at the summit of the SA volcano.

The golden surface under NT also shows a bifurcation close to the surface (Figure 4a), exhibiting a complicated pattern, and exposing the surface with a lower density (green) in the western portion of the summit (Figure 4b). Finally, a small deposit was identified as corresponding to the TE fissure-vent lava flows, apparently representing magma feeding through the TE fault system running E-W and reaching the NT volcano (García-Palomo et al, 2000). The green geosurface also outcrops at this location (Figure 4b). Other small, low-density regions will be discussed elsewhere.



a)

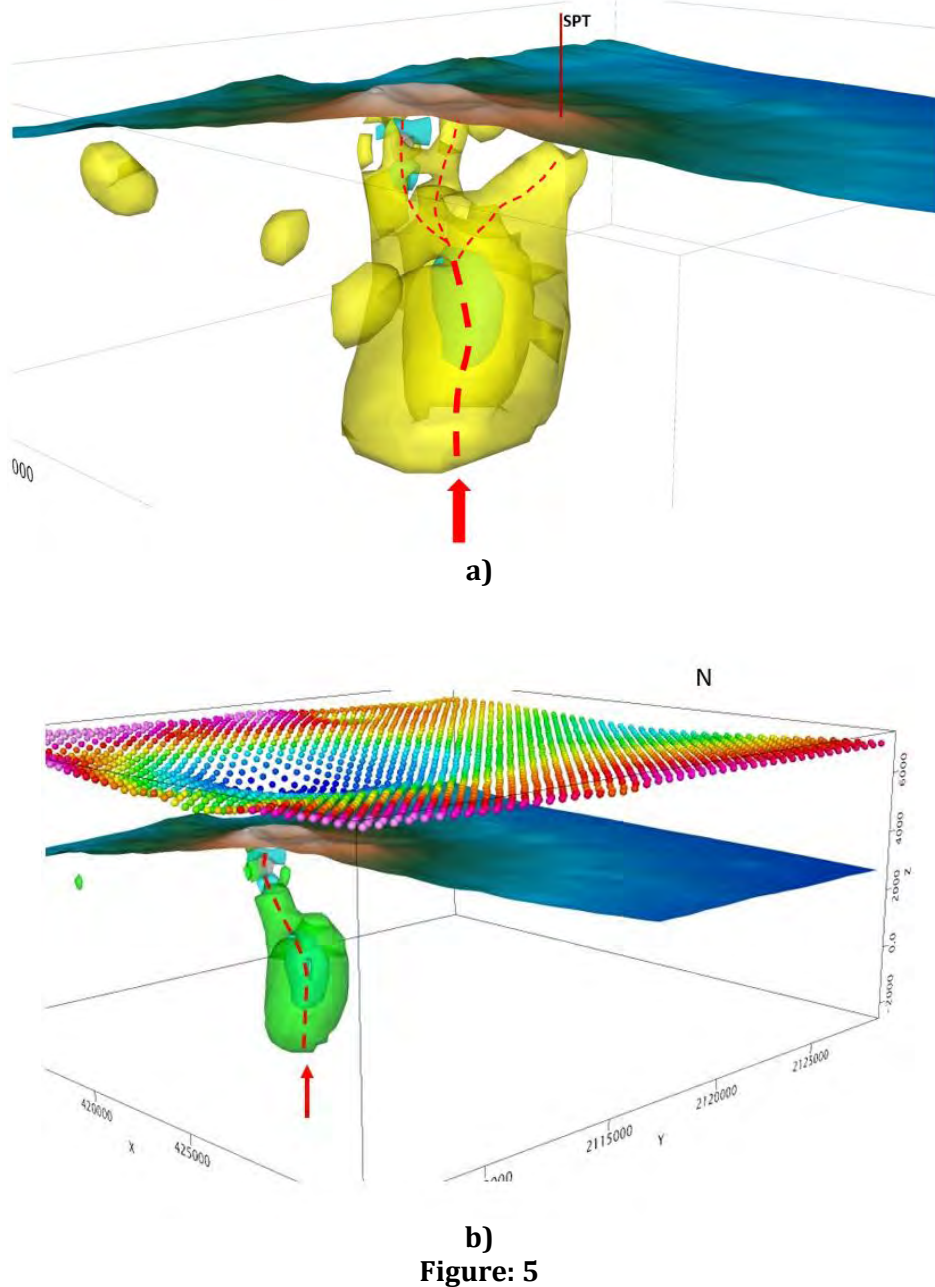


b)

Figure: 4

**Fig. 4** Geosurfaces obtained from the 1000 m resolution 3D inversion superposed onto the local topography. a) The golden surfaces represent the regions whose densities are between 2.12 and 2.56 g/cm<sup>3</sup>, and the green surfaces represent the regions with densities between 1.45 and 1.67 g/cm<sup>3</sup>. The red arrows indicate the flow of volcanic products towards the upper chambers/conduits of each structure. The dashed red lines indicate the trajectories of flow inferred from these results. The digital elevation model is shown as a transparent layer to allow the visualization of the low-density surfaces; the colors in the map correspond to topographic ranges, also discernible in the topographic map of Figure 1. Owing to the 3d perspective, the geosurfaces appear displaced from their corresponding volcanic structures. b) Vertical view of the superposition of the geosurfaces and the topography; the arrows show the locations where the green isosurfaces outcrop. We restricted the discussion to the three locations identified as the San Antonio volcano (SA), Nevado de Toluca volcano (NT), and Tenango lava flows (TE).

The apparent displacement of the geosurfaces toward the south is corrected in the present view.



**b)**  
**Figure: 5**

**Fig. 5** A closer view of the isosurfaces under NT obtained from the 3D inversion (Figure 4a) with a 1000 m resolution. Both figures extend vertically from the surface of NT volcano (+4600 m) to the bottom of the inversion (-2000 m). (a) An internal geosurface of lower density (blue) appears inside the translucent yellow one, corresponding to densities between 2.25 and 2.56  $\text{g}/\text{cm}^3$ . San Pedro Tlanixco (SPT) corresponds to a monogenetic volcano at that location. (b) By eliminating the outer, yellow layer close to the NT summit, a green geosurface is exposed, partially uncovering a gray one close to the surface, which we interpret as one of the exhaust



conduits of the volcano. The red arrow and dashed lines in a) and b) indicate the feeding and transport trajectories of volcanic materials. This geometry is inferred to represent the original plumbing system of the volcano. Both figures have the same depth and the same orientation; depth and north are indicated in Figure 5b. The colored dots on top of Figure 5b represent the location of the gravity stations selected to perform the 3D inversion; we note that this is a regularly distributed subset of the original, high-resolution data set. They are located on the surface of the ground, defined by the DEM reported above, and are selected by an algorithm of the program to optimize the inversion.

This preliminary analysis shows that low-density regions underlie the three main volcanic structures in the area. The inferred trajectories of volcanic materials from the interior to the surface are represented as red dashed lines in Figure 5. These geosurfaces present an onion-like structure, with the inner layers representing lower densities. We infer that volcanic activity at NT was initiated through the single western conduit shown in Figure 5b. The additional northern conduit shown in Figure 5a was subsequently activated where still another branch ending at SPT reaches the ground surface. We note that not all geosurfaces associated with surface volcanic manifestations contain the lowest density components (green and gray), perhaps indicating that they represent single expansion episodes of volcano-magmatic products. The lowest density trajectories should be the ones repeatedly used for the expulsion of such materials. According to Martínez-Serrano et al., (2004) volcanic activity at Nevado de Toluca (NT) volcano began 2.6 Ma ago with the emission of andesitic lavas; more recently (40 ka), eruptions have produced mainly lava flows and pyroclastic deposits of predominantly orthopyroxene–hornblende dacitic composition. One can assume that the andesitic lavas impregnated the conduits of the original plumbing system; whether the dacites modified the composition of the wall conduits cannot be ascertained in the present study.

### **500 m Resolution**

Next, we performed the inversion of the Bouguer anomaly on the 500 m resolution (smaller rectangle in Figure 2). The 3D inversion displayed in Figure 6 shows a slice along the 65° azimuth to highlight the density characteristics under the NT volcano; this azimuth direction cuts across two vents and the central dacitic dome, called Ombligo (García-Palomo et al. 2002). The voxel was overlain by the corresponding digital elevation model of the structure for correlation purposes; it is shown displaced upwards to allow the density volume to be visualized. The major low-density anomaly is exposed, extending from the surface to the deepest portion of the model (-2000 m). However, the uppermost portion of the negative anomaly appears divided by a small high-density region, corresponding to the dacitic dome. This region coincides with the highest portion of the volcanic structure.

The 3D magnetic inversion appears in Figure 7, also showing a slice of the inverted volume; a low-susceptibility zone corresponds to the low-density region of Figure 6. Since the magnetic model did not have the resolution of the density inversion, the results were not as accurate for defining near-surface details. The low-susceptibility region starts ~2 km below the surface and its shape appears to be circular, contrasting with the rectangular shape of the density anomaly. Both anomalies exhibit continuous increments of density/susceptibility when moving away from the anomalies.

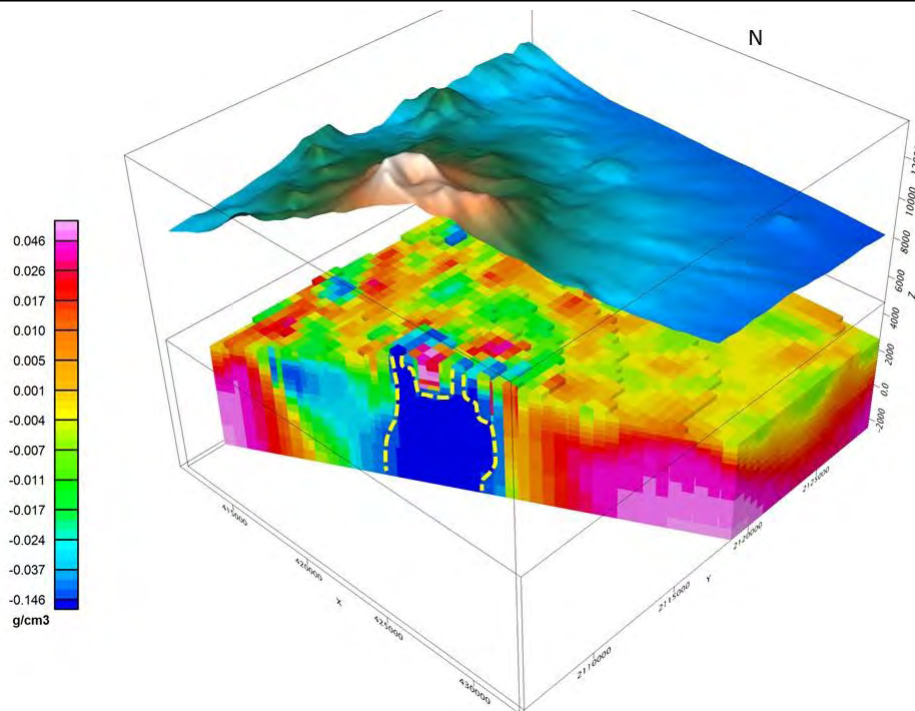


**Figure: 6**

**Fig. 6** The 3D gravity inversion of the smaller rectangle in Figure 2, in the volume delimited by the lower box whose approximate dimensions are 25 x 25 x 5 km was performed; the resolution of the mesh is 500 m. The volume was cut along an azimuth of 65 degrees across the volcanic edifice to exhibit the low-density anomaly (blue) under the NT volcano. The upper box displays the digital elevation model associated with the volcano. The yellow dashed lines indicate the limits of the volcano's plumbing system; notice its bifurcation at the surface.

Low-density volcanic anomalies accompanied by regions of low susceptibility are likely to be associated with a magma chamber or its conduits; close to the surface they typically tend to reveal a single conduit or chimney (e.g., Tibaldi, 2015; Alvarez, 2017; Guevara et al., 2021) normally associated with the plumbing system of the volcano; notwithstanding, the case of the Hunga Tonga Hunga Ha'apai volcano exhibits a group of low-density regions on the surface of the volcano, instead of a single chimney (Alvarez and Camacho, 2023). In the case of NT, two conduits close to the surface are exposed; these were linked with different eruptive periods associated with cataclysmic eruptions (García-Palomo et al., 2002).

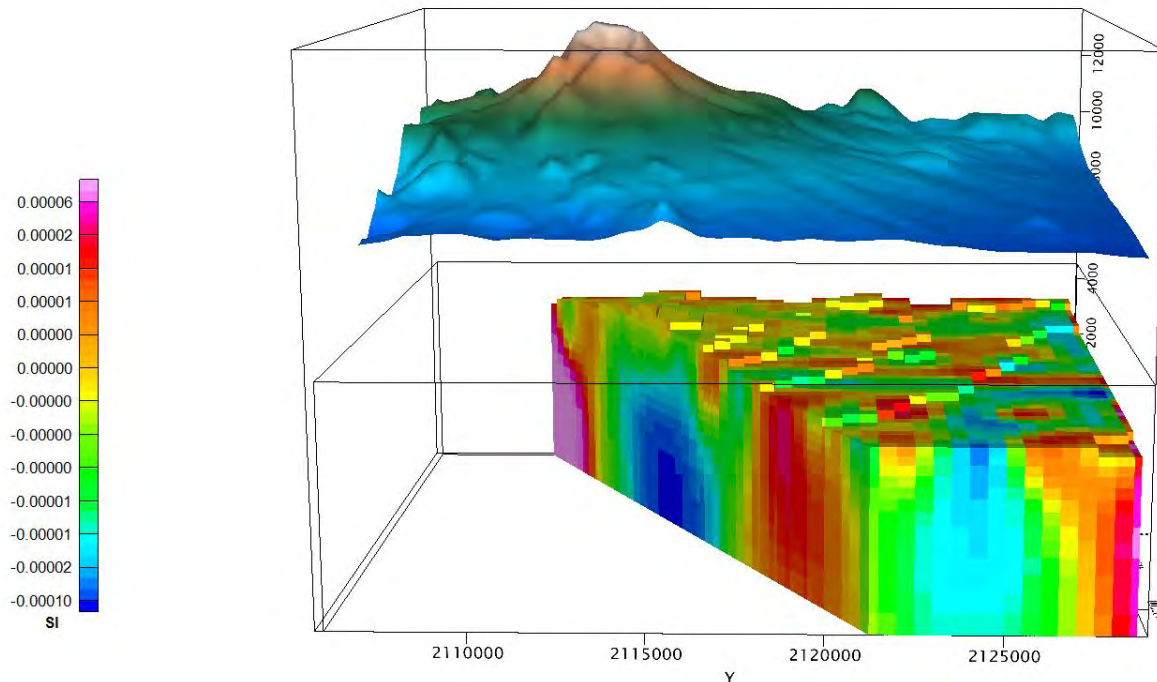


**Figure: 7**

**Fig. 7** 3D magnetic inversion of the data in Figure 3 showing the magnetic susceptibility results, where the constant  $+1.0 \times 10^{-3}$  SI is to be added to the values in the scale. A low-susceptibility region is located directly under the summit of the NT volcano. Although the resolution of the magnetic data set is considerably lower than that of the gravity data set, their general trends agree.

### NT Cross-Sections

To further explore the characteristics of these inversions, we extracted cross-sections from the 500 m resolution voxels. Figure 8 shows the N-S cross-section of the density voxel along with a topographic profile of the structure, in which a split negative anomaly reaching the surface is observed, suggesting there are two exhaust conduits. To the east, a large positive anomaly constrains the negative one vertically, while a low-density anomaly flanks the anomaly to the west. The low-density anomaly continues vertically downwards from the limit of the inversion (i.e., below -2000 m). The split character of the anomaly reaching the surface is maintained in two additional cross-sections, as will be shown below.

The low-density anomaly associated with the volcanic structure shows that its near-surface portion is divided, suggesting that these exhaust vents were partially responsible for the repeated destruction of the crater and the eruptions of debris avalanches (Cantagrel et al., 1981; García-Palomo et al., 2000). The base of the anomaly appears extended towards the south. This anomaly also revealed that it has the lowest values at depths ranging from +1.5 to -1.0 km and we infer that this may be associated with the location of the volcano's magma chamber which fed by deeper sources of magmatic material. The appearance of a density minimum supports the existence of the chamber. Below elevations of 0 to +1 km, the low-density anomaly is double the size of the upper portion in this N-S projection. Models of the

distribution of magma chambers in volcanoes usually locate several chambers distributed vertically in the crust (Magee et al., 2018; Cashman et al., 2017; Alvarez & Yutsis, 2015). Here, we only consider the uppermost chamber of the sequence at NT volcano.

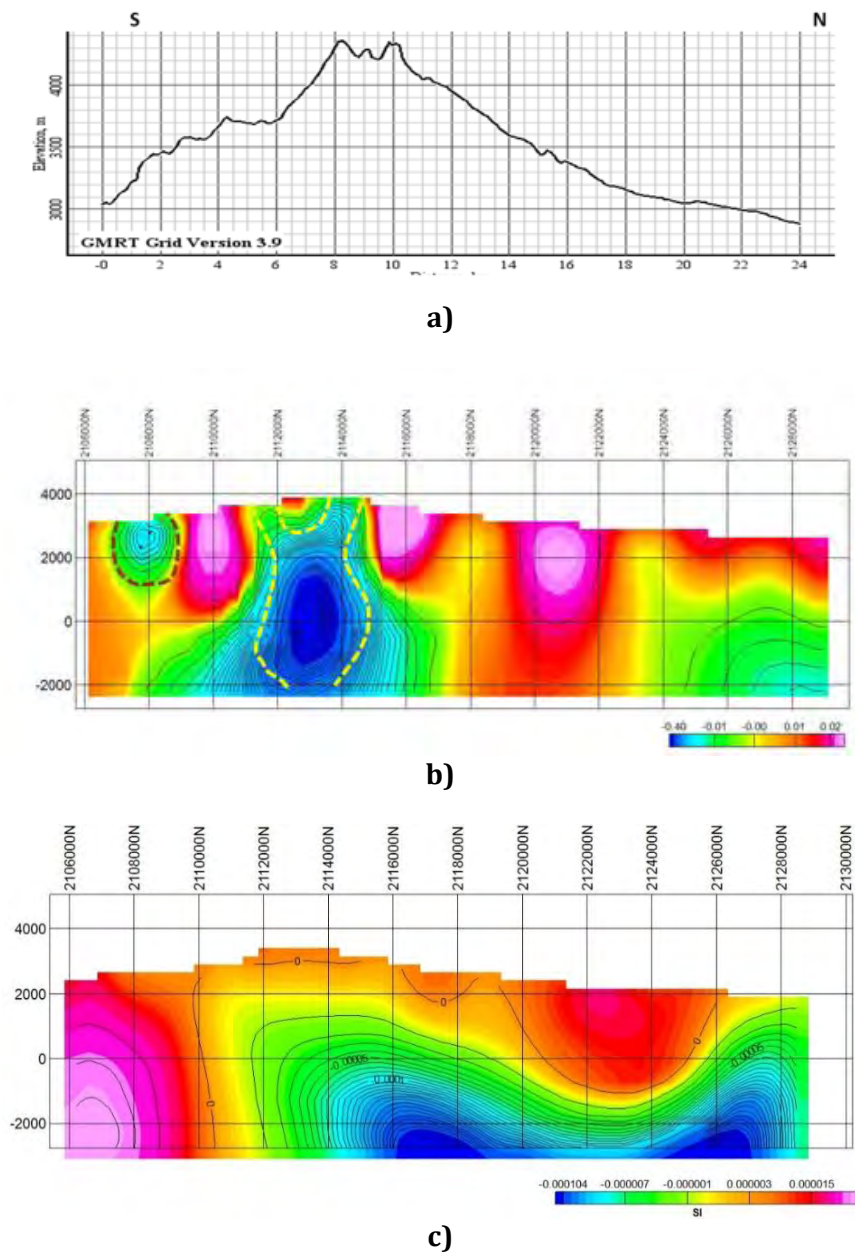


**Figure: 8**

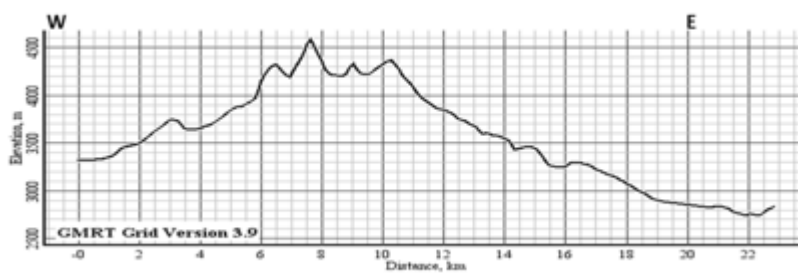
**Fig. 8** Vertical cross-sections along the N-S line in Figure 2 showing: a) the corresponding topographic profile, b) the density anomaly associated with NT (contours are included to enhance the characteristics of the anomalies and the scale shows density increments (+) or decrements (-) over the reduction density of  $+2.67 \text{ g/cm}^3$ , and c) the associated magnetic susceptibility (SI) cross-section, where the constant  $+1.0 \times 10^{-3} \text{ SI}$  is to be added to the values in the scale. The terrain profiles of the cross-sections were averaged according to the elevation of

the voxel elements involved. Model resolution 500 m. Topographic profile extracted from GeoMapApp ([www.geomapapp.org](http://www.geomapapp.org)) 209 / CC BY / CC BY (Ryan et al., 2009)

The N-S topographic profile is not symmetric (Figure 8a); it shows a bulge on the southern portion that is associated with the near-surface, low-density anomaly perched at the southern end of the line. It is worth noting that this local anomaly also shows a density minimum. The geometry of the main anomaly (Figure 8b) suggests that the perched anomaly is a result of magma injection directly from the lower portion of the main low-density anomaly.

The N-S cross-section resulting from the magnetic inversion corresponding to the magnetic susceptibilities is shown in Figure 8c. The cross-section displays a minimum value located to the north of the top of the volcanic structure, corresponding to a region where magnetization is minimal. Here, the two disconnected regions of minimum density shown in Figure 8b, one under NT and the other at the north end, appear connected at depths greater than the bottom depth (-2.5 km) of the inversion. Since low-susceptibility values are linked to temperatures near or above the Curie point, the probability of a deep, common magma feeder to the NT volcano and the associated region to the north is high. In the case of the volcanic structure, high-temperature materials have reached the surface, whilst in the anomaly to the north they seem to have been preserved at depth. The high-density region in the north portion of the profile (Between 2118000-2122000N) coincides with the high-susceptibility region (Figure 8c), indicating that this region functions as a local barrier to volcanic activity.

Figure 9 shows the E-W cross-section (Figure 2) across the crater of NT. The low-density anomaly associated with the volcanic structure most clearly shows the division in two of its uppermost volume. The extent of the anomaly at the surface is ~5 km across, including a central higher-density zone of ~1 km in diameter, and ~1.5 km deep. It clearly corresponds to the central dacitic dome called Ombligo which was emplaced between 10.5-9.0 ka (Aceves-Quezada et al., 2007). This higher-density zone exhibits different shapes in the two density cross-sections shown (N-S and E-W), either as the reason for, or a consequence of, the side deflection of the erupted materials. The crater has been described as having the form of a horseshoe (García-Palomo et al., 2002) since its eastern portion has been destroyed; this was likely associated with the magma ascent identified in Figure 9b which may have induced the explosive event. The identified magma chamber exhibits the same dimensions as those inferred for the N-S section, except that the bifurcation of the anomaly starts at the top of the proposed magmatic chamber. The center of the E-W anomaly is slightly deeper than the one appearing in the N-S cross-section (Figure 8b), highlighting structural differences in the central portion of the anomaly.



a)

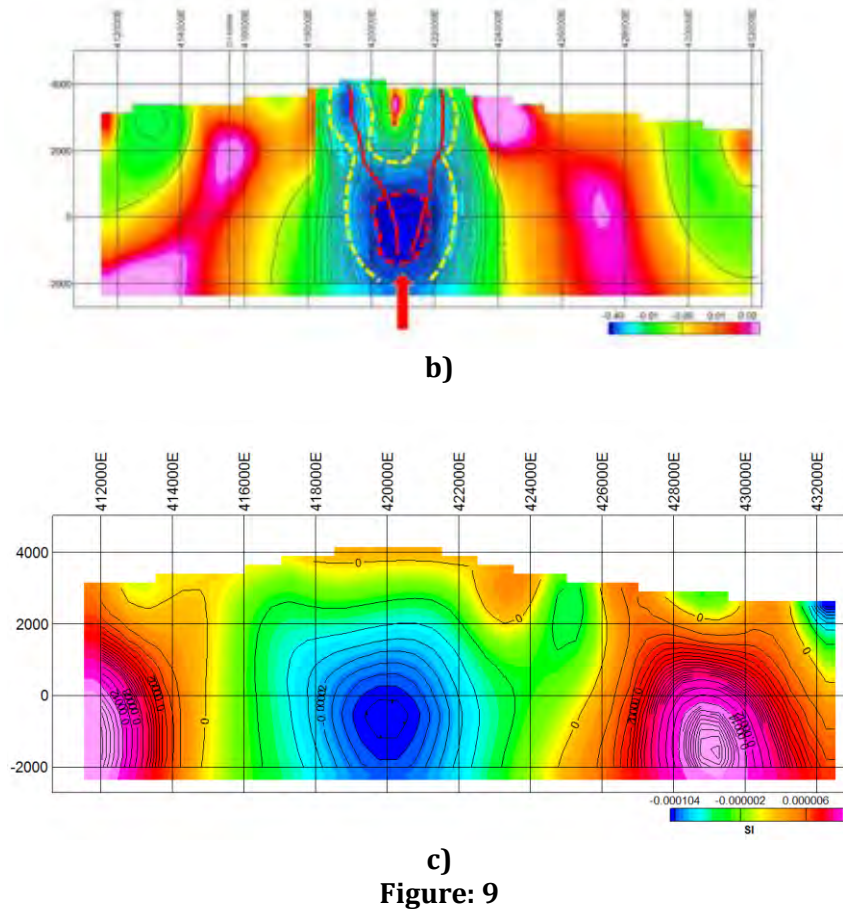


**Fig. 9** Vertical cross-section along the E-W line of Figure 1 showing: a) the topographic profile, b) the density distribution associated with the NT volcano (the scale shows density increments of  $+2.67 \text{ g/cm}^3$ ); notice the dacitic dome represented by the high-density, vertical region between the two exhaust trajectories, suggested by continuous, thin red lines, and c) the magnetic susceptibility cross-section in SI units, where the constant  $+1.0 \times 10^{-3} \text{ SI}$  is to be added to the values in the scale. The terrain profile of the cross-sections was averaged according to the elevation of the voxel elements involved; the contours are included to enhance the characteristics of the anomalies. Topographic profile extracted from GeoMapApp ([www.geomapapp.org](http://www.geomapapp.org)) 209 / CC BY / CC BY (Ryan et al., 2009)

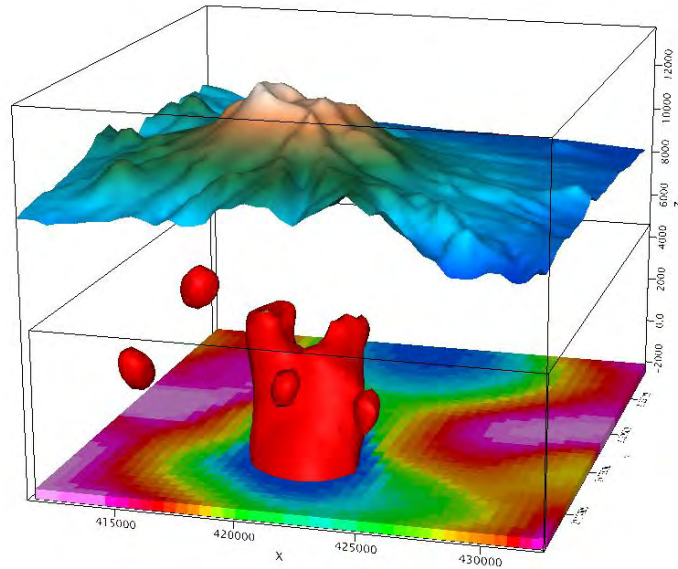
The repeated destruction of the crater summit seems to be directly related to the presence of the low-density anomalies near the surface. Of particular interest is the uppermost, low-density anomaly on the western side of the summit (Figure 9b). This anomaly contains a center which is absent in the corresponding anomaly on the eastern side of the summit, indicating the accumulation of low-density material in the form of a deposit with its center 500 m below the summit. This may constitute a potential hazard since it could give rise to a local flare up and we can only speculate that this type of activity could have contributed to some of the repeated destructions of the summit. The structural similarity with the perched anomaly in Figure 8b is worth mentioning.

The density and magnetic anomalies across the volcano's summit (Figures 8 and 9) show well-defined, coincident minima of density and magnetic susceptibility. Since the inversions were independent of each other, and involved different physical parameters, we considered this as a self-consistent system. We argue that the fact that we obtained minima in both physical properties indicates that this is a chamber in which material can be deposited. If it were just a conduit, we would not be observing minima of these properties. An accumulation of low-density, low-susceptibility (high-temperature) material could correspond to a mush at that location. We estimated the volume of this cylindrical reservoir as  $15.9 \text{ km}^3$ , considering a diameter of 2.2 km and a height of 4.2 km.

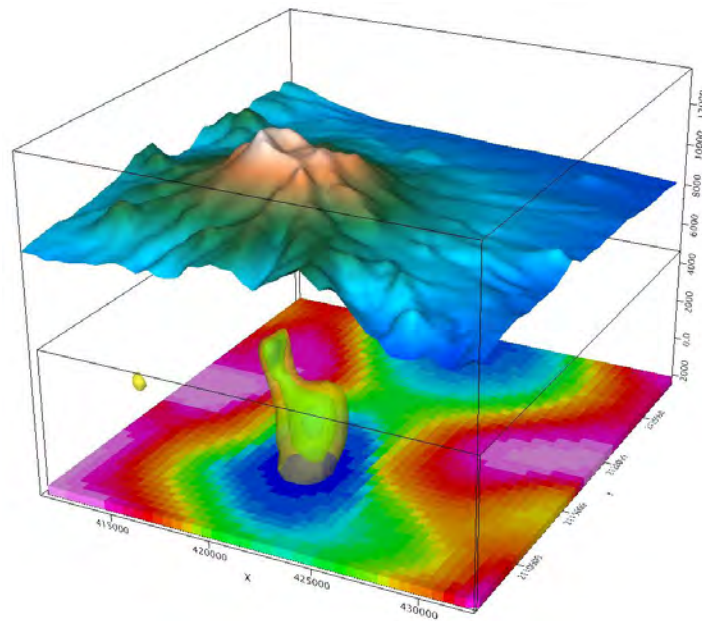
The inverted magnetic susceptibility (Figure 9c) exhibits a good correlation with the low-density zone. In particular, the regions of minimum density and minimum susceptibility coincide, reinforcing the notion that this may be the locus of the magma chamber of the NT volcano. Cantagrel et al. (1981) associated the abundant ash and pyroclastic flows with a shallow magma chamber. The distribution of the materials confining the low-density and low-susceptibility regions correspond to high-density and high-susceptibility zones, which also coincide in constraining them laterally (Figures 9b and 9c). Demagnetization can generally be explained by a change in mineral contents or by a rise in temperature. In the present case, we preferred the latter option, concluding that the regions of negative gravity anomalies are underlain by regions of low magnetic susceptibility.

### **Geosurfaces**

The geosurfaces obtained from the 1000 m resolution inversion were refined from the 3D inversion with a 500 m resolution (Figure 4). The prominent red surface in Figure 10a corresponds to a density value of  $1.784 \text{ g/cm}^3$ , delimiting the larger densities outside the volume of this surface from the lower densities within it. This surface clearly shows the split character of the anomaly close to the surface, indicating that low-density material reaches the upper portion of the volcanic structure. The western and eastern sides of this anomaly reach the surface or close to it, whilst the middle portion remains  $\sim 2 \text{ km}$  below. This surface was eliminated in Figure 10b, revealing surfaces with lower density values which we interpret to represent an older, initial stage of the volcanic plumbing system of the NT volcano. Like in many polygenetic volcanic structures, a single volcanic conduit formed during this earlier stage and located to the west of the summit is shown in Figure 10b. This suggests that a younger magmatic surge was responsible for the bifurcation of the volcanic conduits; one followed the earlier path and the other proceeded to the eastern side of the summit. The middle portion contains the Ombligo dome, as shown in Figure 8b. Further research may indicate whether the older and younger regions of magma ascent correspond to the two phases that built the NT structure, as suggested by Cantagrel et al. (1981).



a)



b)

**Figure: 10**

**Fig. 10** a) Surface enclosing the region of lowest densities (red), obtained from the 3D inversion with a 500 m resolution shown in Figure 6, extending vertically from elevations of +4210 to -2200 m. The top of the surface clearly shows the shape of the bifurcation. b) When the red surface is removed, the lower densities are exposed, showing a single volcanic conduit to the west of the summit



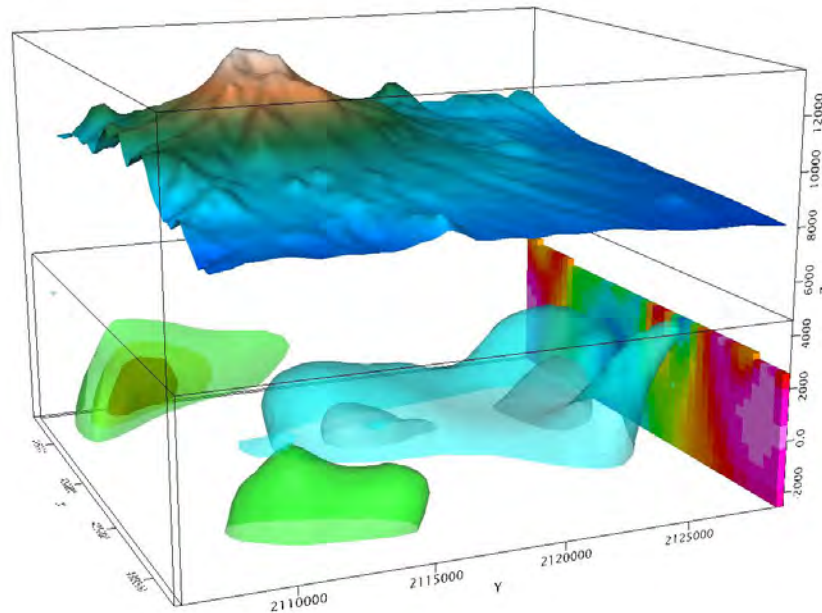


**Figure: 11**

**Fig. 11** Magnetic geosurfaces obtained from the inversion in Figure 7; the Y-axis corresponds to the N-S direction. The blue iso-surface encloses magnetic susceptibilities  $\leq -3.11 \times 10^{-5}$  SI, and the green geosurfaces enclose values  $\geq +12.0 \times 10^{-5}$  SI; the constant  $+1.0 \times 10^{-3}$  SI is to be added to the values in the scale.

The volume distribution of the magnetic material shown in cross-section in Figure 8c can also be observed as a volume in Figure 11, where the low-susceptibility region (light blue) extends in the N-S direction, getting closer to the surface in the north of the region. Out of the two separate lower-density regions (gray) enclosed in this volume, the southern one is associated with the NT structure.

### Volume Estimates

García-Palomo et al. (2002) reported on the oldest known materials ejected by the NT volcano which constitute the base upon which the volcanic edifice was built: 2.6 My-old light-gray porphyritic lava flows with a 100 m thickness, and 1.2-1.6 My-old primitive andesitic-dacitic lava flows with a 150 m thickness. The flows were overlain by a 200-m-thick stratigraphic column named the “Older Sequence” of the NT comprising interbedded debris flows, runout lahars, and minor lacustrine deposits. According to the geologic maps produced by Torres-Orozco et al. (2017) and Weber et al. (2020), we estimated the areal extent of the Old Nevado materials (2.6-1.2 Ma) to cover  $\sim 96 \text{ km}^2$ . The combined thickness of the initial lava flows is 250 m, yielding an approximate volume of  $24 \text{ km}^3$ , which can be compared with the dimensions of the uppermost magma deposit identified in this work as  $\sim 15.9 \text{ km}^3$ . To estimate volume recharge, we offer an illustration: We obtained a recharge volume of  $2.4 \text{ km}^3$ ; assuming that this volume is only replenished 15% in each recharge, this process should have occurred around ten times during the initial stages of construction of the volcanic edifice, assuming that these volumes did not change significantly during that period. Deeper deposits must have

intermittently replenished this upper magma chamber, constituting the main portion of NT uppermost plumbing system.

### CONCLUDING REMARKS

We found only one schematic description of the plumbing system of the NT volcano (Aceves-Quezada et al., 2007) in which a single chimney of the volcano was depicted, first during its early stages (Paleo-Nevado, about 1.4 Ma), and subsequently at the time of emplacement of the Ombligo dome between 10.5-9.0 ka. Neither stage showed the bifurcations of the upper plumbing system reported herein. The models presented here are based on the interpretation of the distributions of density and magnetic susceptibility of the rock formations constituting the volcanic edifice. They show that NT has a peculiar plumbing system, with two branches that surround, but do not completely enclose, the upper portions of the structure, conveying magmatic products to the volcano's summit. According to Figures 5 and 10, one can infer that the western branch is older than the eastern one, since there are no branches of lower density in the direction of the latter. Figure 8c shows the linking of a low-susceptibility region, below -2000 m, noting that in the same places, there are two independent gravimetric low-density anomalies separated by a region of high density that reaches the surface (Figure 8b). Figure 10a extends those results, showing that the low-susceptibility region has the shape of a deformed cylinder along the N-S direction; the northernmost portion rises towards the surface without reaching it. However, there is a group of volcanic edifices close to this region and along the N-S direction, some of which are clearly monogenetic and probably linked to this low-gravity and low-susceptibility anomaly. García-Palomo et al. (2000) reported that the latest deformation period in the region started during the late Pleistocene, ending in pure extension, and shifting  $\sigma_3$  to a N-S direction; the authors noted that these faults appear to control the local, late Pleistocene to Holocene monogenetic volcanism. Their observations and ours complement each other, reinforcing the idea of these faults controlling the monogenetic volcanic activity in this region. Based on the cross-sections across the summit of the volcano (Figures 8 and 9) and their density and magnetic susceptibility distributions, we estimated the center of the magmatic chamber to be located between elevations of 0 and -1 km, or between 5 and 6 km below the NT volcano's summit. Based on considerations of geothermometry Arce et al., (2012) concluded that dacitic magma was stored at 5.8 to 7.7 km below the volcano summit. Given the uncertainties in both estimates, we consider they coincide within reasonable limits. Regarding the study of Weber et al., (2020) that based on their petrologic model observes that very mafic clino- and orthopyroxene compositions are present in the erupted products of NT, indicative of two deep, separated magma sources feeding the volcano, we can only comment that they must be the magma sources replenishing the shallower chamber modeled in this work. The high-resolution gravity analysis performed here on the structure of the NT volcano could be extended to practically any volcanic structure in the world's continents within  $\pm 60^\circ$  latitudes where high-resolution GMMplus data is available, providing a powerful tool for analyzing volcanic formations.

### ACKNOWLEDGMENTS

During the development of this work, MC received support from the Consejo Nacional de Ciencia y Tecnología (CONACYT, México). This study was supported by IIMAS, UNAM; we acknowledge material support from both institutions. This research did not receive any specific grant from funding agencies in the public, commercial, or not-for-profit sectors.

## References

- Aceves-Quezada JF, Martin del Pozzo AL, López-Blanco J (2007) Volcanic hazard zonation of the Nevado de Toluca volcano, central Mexico. *Nat Hazards*, 41: 159-180. Doi: 10.1007/s11069-006-9029-6
- Alvarez R (2017) Mapping geologic interfaces that may alter seismic wave propagation in the Mexico City basin. *Geofísica Internacional*, 56-1: 37-56.  
Doi: 10.19155/geofint.2017.056.1.4
- Alvarez R, Yutsis V (2015) Southward migration of magmatic activity in the Colima Volcanic Complex, Mexico: an ongoing process. *Int. J. Geosciences*, 6: 1077–1099. <https://doi.org/10.4236/ijg.2015.69085>
- Alvarez, R. and Camacho, M. (2023). Plumbing System of Hunga Tonga Hunga Ha’apai Volcano. *Journal of Earth Science*, 34(3): 706–716. <https://doi.org/10.1007/s12583-022-1792-0>
- Arce JL, Macías JL, Vázquez-Selem L (2003) The 10.5 Ka Plinian eruption of Nevado de Toluca volcano, Mexico: stratigraphy and hazard implications. *Geol. Soc. Amer. Bull.* 115:230 – 248.
- Arce, J. L., Layer, P. W., Lassiter, J. C., Benowitz, J. A., Macías, J. L., and Ramírez-Espinosa, J. (2013a). 40 Ar/39 Ar dating, geochemistry, and isotopic analyses of the quaternary Chichinautzin volcanic field, south of Mexico City: implications for timing, eruption rate, and distribution of volcanism. *Bull. Volcanol.* 75 (12), 774.  
doi:10.1007/s00445-013-0774-6
- Arce JL, Gardner, and Macías, JL (2013b) pre-eruptive conditions of dacitic magma erupted during the 21.7 ka Plinian event at Nevado de Toluca volcano, Central Mexico. <http://dx.doi.org/10.1016/j.jvolgeores.2012.09.012>
- Baranod, V., Naudy, H., (1964). Numerical calculation of the formula of reduction to the magnetic pole. *Geophysics*, 29, 67-79.
- Bloomfield K (1974) The age and significance of the Tenango Basalt Central Mexico. *Bull. Volcanol.* 37: 585 – 595.
- Bloomfield K (1975) A Late-Quaternary monogenetic volcano field in central Mexico. *Geol. Rundsch.* 64: 476 – 497.
- Bloomfield K, Valastro S (1974) Late Pleistocene eruptive history of Nevado de Toluca, central Mexico. *Geol. Soc. Am. Bulletin*, 85: 901–906.
- Baranod, V., Naudy, H., (1964). Numerical calculation of the formula of reduction to the magnetic pole. *Geophysics*, 29, 67-79.
- Barthelmes, F., Kohler, W. (2016). International Centre for Global Earth Models (ICGEM), in: Drewes, H., Kuglitsch, F., Adam, J. et al., *The Geodesists Handbook*, 2016. *J. Geod.* 90 (10), 907–1205.  
<https://doi.org/10.1007/s00190-016-0948-z>.
- Bloomfield K, Valastro S (1977) Late Quaternary tephrochronology of Nevado de Toluca, central Mexico: Institute of Geological Sciences, *Overseas Geol. Min. Res.* 46: 1–15.
- Cashman, KV., Sparks, RSJ., Blundy, JD. (2017). Vertically extensive and unstable magmatic systems: A unified view of igneous processes. *Science* 355, eaag3055. DOI:10.1126/science. aag3055
- Camacho M, Alvarez R (2020) Gravimetric analysis of the rifts and volcanic fields of the Jalisco block, Mexico. *Tectonophysics*, 791, 228577. <https://doi.org/10.1016/j.tecto.2020.228577>
- Camacho M, Alvarez R (2021) Geophysical modeling with satellite gravity data: EIGEN-6C4 vs GGMplus. *Engineering*, 13, 690-706. <https://doi.org/10.4236/eng.2021.1312050>

- Camacho, AG, Prieto, JF, Ancochea, E, Fernández, J. (2018) Deep volcanic morphology below Lanzarote, Canaries, from gravity inversion: new results for Timanfaya and implications. *J. Volc. Geothermal Res.*, <https://doi.org/10.1016/j.jvolgeores.2018.11.013>
- Cantagrel JM, Robin C, Vincent P (1981) Les grandes étapes d'évolution d'un volcan andésitique composite: exemple du Nevado de Toluca. *Bull. Volcanol.* 44: 177 – 188.
- Capra L, & Macías JL (2000) Pleistocene cohesive debris flow at Nevado de Toluca volcano central Mexico. *J Volcanol Geotherm Res* 102: 149– 168.
- DeCserna Z, Fries C Jr (1981). Resúmen de la geología de la hoja Taxco, Estado de Guerrero, México y Morelos, Mapa con texto explicativo, Carta Geológica. Hoja Taxco 14Q-h (7), Serie 1:100,000, No. 15. Instituto de Geología, UNAM.
- Ellis RG, deWet B, Macleod IN (2012) Inversion of magnetic data for remnant and induced sources. Presented at the 2012 Australian Soc. Explor. Geophysicists (ASEG) 22nd Int Geophys Conf Exhibit, Brisbane, Australia, 26–29 February 2012.
- Ferrari, L., Orozco-Esquivel, M.T., Manea, V., Manea, M., (2012), The dynamic history of the Trans-Mexican Volcanic Belt and the Mexico subduction zone, *Tectonophysics*, 522-553, 122-149.
- García-Palomo, A., Macías, J.L., Arce, J.L., Espindola, J.M., (1996) Marco Geológico Estructural de la Región del Nevado de Toluca, Central México, Edo. de México. *Actas INAGEQ* 2, 115–120.
- García-Palomo A, Macías JL, Garduño VH (2000) Miocene to Recent structural evolution of the Nevado de Toluca volcano region central Mexico. *Tectonophysics*, 318: 281– 302.
- García-Palomo A, Macías JL, Arce JL, Capra L, Garduño VH, Espíndola JM (2002) Geology of Nevado de Toluca Volcano and surrounding areas, central Mexico. *Geol. Soc. Am. Map and Chart Series MCH089*, pp. 1– 48.
- Guevara R, Yutsis V, Varley N, Almaguer J, Calderón-Moctezuma A, Guevara-Mansilla O (2021) Geophysical determination of the Jalisco and Michoacán blocks boundary along the Colima graben. *J. South Am. Earth Sci.* 109, 103208. <https://doi.org/10.1016/j.jsames.2021.103208>
- Hildenbrand TG, Briesacher A, Flanagan G, Hinze, WJ (2002) Rationale and Operational Plan to Upgrade the US Gravity Database. USGS Open File Report, 1-12
- Hirt C, Claessens S, Fecher T, Kuhn M, Pail R, Rexer M (2013) New ultrahigh-resolution picture of Earth's gravity field. *Geophys Res Let*, 40(16): 4279–4283. <https://doi.org/10.1002/grl.50838>
- Ingram DM, Causon DM, Mingham CG (2003) Developments in Cartesian cut cell methods. *Math Comp Simulation*, 61 (3–6): 561–572.
- Jarvis A, Reuter HI, Nelson A, Guevara E (2008) Hole-filled SRTM for the globe Version 4. Available from the CGIAR-CSI SRTM 90m Database. Available at: <http://srtm.csi.cgiar.org/>.
- Kane MF (1962) A Comprehensive System of Terrain Corrections Using a Digital Computer. *Geophysics*, 27(4): 455-462. <https://doi.org/10.1190/1.1439044>
- Kauahikaua, J., Hildenbrand, T. and Webring, M. (2000) Deep magmatic structures of Hawaiian volcanoes, imaged by three-dimensional gravity models. *Geology* 2000;28;883-886 doi: 10.1130/0091 7613(2000)28<883: DMSOHV>2.0.CO;2
- Lafehr TR (1991) An exact solution for the gravity curvature (Bullard B) correction. *Geophysics*, 56(8):1179-1184. <https://doi.org/10.1190/1.1443138>

Li X, Götze HJ (1996) Topography and geoid effects on gravity anomalies in mountainous areas as inferred from the gravity field of the Central Andes. *Phys Chem Earth*, 21(4): 295–297. [https://doi.org/10.1016/S0079-1946\(97\)00051-7](https://doi.org/10.1016/S0079-1946(97)00051-7)

Macías JL, García-Palomo A, Arce JL, Siebe C, Espíndola JM, Komorowski JC, Scott KM (1997) Late Pleistocene–Holocene cataclysmic eruptions at Nevado de Toluca and Jocotitlán volcanoes, central Mexico. *In: Kowallis, B.J. (Ed.), Proterozoic to Recent stratigraphy, tectonic and volcanology, Utah, Nevada, Southern Idaho and Central Mexico. Buffalo Y U Geology Studies*, pp. 493–528.

Macleod IN, Ellis RG (2013) Magnetic vector inversion, a simple approach to the challenge of varying direction of rock magnetization. Presented at the 2013 Australian Society of Exploration Geophysicists–Petroleum Exploration Society of Australia (ASEG–PESA) 23rd International Geophysical Conference and Exhibition, 11–14 August 2013, Melbourne, Australia.

Magee, C., Stevenson, CTE., Ebmeier, SK., et al. (2018) Magma plumbing systems: a geophysical perspective. *J. Petrology*. 59-6: 1217-1251. doi: 10.1093/petrology/egy064

Martínez-Serrano RG, Schaaf P, Solís-Pichardo G, Hernández-Bernal MS, Hernández-Treviño T, Morales-Contreras JJ, Macías JL (2004) Sr, Nd and Pb isotope and geochemical data from the Quaternary Nevado de Toluca volcano, a source of recent adakitic magmatism, and the Tenango Volcanic Field, Mexico *J Volc Geothermal Res.* 138:77-110.

Meyer B, Saltus R, Chulliat A (2017) EMAG2v3: Earth Magnetic Anomaly Grid (2-arc-minute resolution). Version 3. NOAA National Centers for Environmental Information. <https://doi.org/10.7289/V5H70CVX>

Murcia H, Borrero C, Németh K (2019) Overview and plumbing system implications of monogenetic volcanism in the northernmost Andes' volcanic province. *J. Volcanol. Geothermal Res.* 383: 77-87. <https://doi.org/10.1016/j.jvolgeores.2018.06.013> 0377-0273/.

Nagy D (1966) The Gravitational Attraction of a Right Rectangular Prism. *Geophysics*, 31(2): 362-371. <https://doi.org/10.1190/1.1439779>

Norini, G., Gropelli, G., Lagmay, A.M.F., Capra, L., 2006, Recent left-oblique slip faulting in central Trans-Mexican Volcanic Belt: seismic hazard and geodynamic implications, *Tectonics*, 25, TC4012, Doi:10.1029/2005TC001877

Ryan, WBF, Carbotte SM, Coplan J, O'Hara S, Melkonian A, Arko R, Weissel RA, Ferrini V, Goodwillie A, Nitsche F, Bonczkowski J, Zensky R (2009) Global Multi-Resolution Topography (GMRT) synthesis data set, *Geochem. Geophys. Geosyst*, 10, Q03014, doi:10.1029/2008GC002332. Data doi: 10.1594/IEDA.0001000

Tibaldi A (2015) Structure of volcanic plumbing systems: A review of multiparametric effects. *J. Volcanol Geothermal Res.* 298: 85-135. <https://doi.org/10.1016/j.jvolgeores.2015.03.023>

Torres-Orozco R, Arce JL, Layer PW, Benowitz JA (2017) The Quaternary history of effusive volcanism of the Nevado de Toluca area, central Mexico. *J South Am Earth Sci*, 79:12-39. <http://dx.doi.org/10.1016/j.jsames.2017.07.008>

Weber, G., Caricchi, L., and Arce, J.L. (2020) The long-term life-cycle of Nevado de Toluca volcano (Mexico). *Front. Earth. Sci.* 8:563303. Doi:10.3389/feart.2020.563303

Wollard, G. P. (1979). New Gravity System - Changes in International Gravity Base Values and Anomaly Values. *Geophysics*, 44(8): 1352-1366. <https://doi.org/10.1190/1.1441012>


Capítulo 5: *Plumbing System of Hunga Tonga Hunga Ha 'apai  
Volcano.*

# Plumbing System of Hunga Tonga Hunga Ha'apai Volcano

Román Alvarez<sup>1</sup>\*, Miguel Camacho<sup>2</sup>

1. Instituto de Investigaciones en Matemáticas Aplicadas y en Sistemas (IIMAS), Universidad Nacional Autónoma de México, Coyoacán CDMX 04510, Mexico

2. Posgrado en Ciencias de la Tierra, Universidad Nacional Autónoma de México, Coyoacán CDMX 04510, Mexico

 Román Alvarez: <https://orcid.org/0000-0002-2606-0904>

**ABSTRACT:** The Hunga Tonga Hunga Ha'apai submarine volcano has experienced repeated eruptions in the latest decades. The recent one, in January 2022, released an enormous amount of energy inducing global perturbations, as tsunamis and atmospheric waves. The structure of the volcano is poorly understood, especially its internal structure. Deep-seated magmatic connections are difficult to define or visualize. We use a high-resolution gravity data set obtained via satellite to calculate the Bouguer anomaly over its structure, to perform a preliminary exploration of its interior. Executing 3D gravity inversions, we find a complex plumbing system with various exhaust trajectories and multiple surface pockets of low-density material within the volcanic edifice; some appear to be associated with ring fractures. This is in line with the report of the 2009 eruption, described as beginning from multiple vents. We found no signs of a magma chamber within 6 km depth, although several volcanic conduits are identified from such depth to the surface. Density variations occur within a plumbing conduit or may vary from one conduit to another in the same volcano. These models yield quantitative estimates for areas of magma-water interaction, constituting a baseline to compare with structural changes to be induced in future eruptions.

**KEY WORDS:** Hunga Tonga Hunga Ha'apai, satellite gravity data, 3D inversions, volcano, Tofua Island.

## 0 INTRODUCTION

The largest underwater volcano chain is generated by the Kermadec-Tonga subduction zone, with more than 3 000 km in length; the Tonga trench is one of the fastest subduction zones, with rates going up to 24 cm/yr (Smith and Price, 2006). The active volcanic islands and sea mounts are along a submarine ridge about 200 km west of the axis of the Tonga trench. These islands are the summits of volcanic cones aligned along the submarine ridge.

Although the arc is dominated by basalts and basaltic andesites, there is increasing evidence for significant proportions of silicic magmas erupted in recent times. Silicic volcanism is also evidenced in the presence of caldera structures. Triggering mechanisms postulated for highly explosive mafic eruptions frequently include water-magma interaction or basaltic intrusions into a storage chamber. Ensuing eruption progression and dynamics depend on the mechanism and rate of caldera collapse and resulting modification of the geometry of the plumbing system (Roche and Druitt, 2001).

Hunga Tonga Hunga Ha'apai (HTHH) is a submarine volcano (20° 52'40.82"S, 175° 25'38.18"W, Fig. 1) that belongs to

the Tonga-Kermadec ridge; it erupted on Jan. 15, 2022 releasing energy equivalent to an earthquake originally estimated at  $M$  5.8 (USGS, 2022), subsequently adjusted to  $M_w$  6.3 (Thurin et al., 2022) considering multiple events. This eruption followed another one that occurred on Jan. 15, 2015; after five weeks a new island was formed (GVP, 2015; The Watchers, 2015). Additional eruptions occurred in 1998 and 2009. The rate at which volcanic eruptions take place, implies frequent replenishing of the volcano's magma chamber and its active plumbing system; however, no detailed model of this system is available to date. New eruption models are emerging that require reliable descriptions of the plumbing system of the HTHH structure (Zheng et al., 2022) to improve on their parametrization. The purpose of this work is to establish a baseline for the size and geometry of HTHH volcano's plumbing system; this will allow comparison with modifications that may occur in the future. This study reflects the state of this volcanic structure in the period 2015 to 2022; at present the internal structure reflected here has been changed by the January 2022 eruption. When new satellite data is available for this region, an evaluation of the change will be possible, having the present study as a baseline.

The effects of volcanic eruptions on the Earth's climate are major, as documented by Sigl et al. (2015); they proposed that a cooling effect persisted up to ten years after some of the largest eruptive episodes. The recent eruption of HTHH induced worldwide atmospheric perturbations (Themens et al., 2022) and tsunamis that affected portions of the North, Central, and South American littorals (Yuen et al., 2022). A comparison

\*Corresponding author: roman.alvarez@iimas.unam.mx

© China University of Geosciences (Wuhan) and Springer-Verlag GmbH Germany, Part of Springer Nature 2023

Manuscript received October 6, 2022.

Manuscript accepted November 25, 2022.

of this recent eruption with another devastating eruption of Santorini, Greece in 1650 BC is available (Kusky, 2022).

Explosive volcanism in the Tonga-Kermadec arc appears to be common along its distance. An example is present in Tofua Island, 93 km NNE of HTHH. This island, classified as the largest emergent mafic volcano within the Tofua arc, in Tonga, has experienced paroxysmal explosive volcanism in which ignimbrite was emplaced in a radial fashion around the island, with associated Plinian fall deposits observed up to 40 km away (Caulfield et al., 2011; Bryan et al., 1972; Bauer, 1970). The latter authors conclude that the largest event analyzed was likely triggered by development of a H<sub>2</sub>O saturated dacitic magma; the rising body of magma interacting with external water may have enhanced explosivity. A subsequent event resulted in caldera-deepening because of chamber instability, accentuated by recharge of a chemically distinct magma. The explosive andesite-dacite eruptions may be derived from relatively shallow magma chambers that are cooling and giving rise to more fractionated liquids, the dilation of the volcanic conduits being achieved largely by expanding gases released by crystallization of the magma (Bryan et al., 1972). A new type of tsunami waves and the nature of phreatoplinian eruptions are listed among the phenomena associated with this extremely violent eruption in which supercritical fluids play a central role (Yuen et al., 2022).

Present-day imaging of deep magmatic interconnections

presents considerable difficulties; the problem reaches greater complexity levels in isolated areas. Here we use a high-resolution gravity data set, to perform an inversion of the complete Bouguer anomaly of the HTHH volcanic area. The inversion procedure essentially consists of a 3D inversion of the volcano's high-resolution gravity field (Bouguer anomaly) obtained from the satellite derived data (Hirt et al., 2013), which yields the density distribution in the volcano's interior. This distribution unveils the characteristics of the plumbing system.

## 1 METHODS

### 1.1 Data Acquisition

The gravimetric data set used for this investigation is the GGMplus. This gravimetric model has a resolution of 7.5 arc-sec (220 m); this data set is available in the latitudinal range of  $\pm 60^\circ$ , with a range of around 10 km from the line of coast, with coverage in some islands (Hirt et al., 2013). In this case, the dataset is available in a 10 km radius of the center island, making circular the data coverage of the GGMplus model (Fig. 2). In this work, we used the Gravity Observed ( $G_{obs}$ ) from the GGMplus satellite gravity model, to calculate the Bouguer anomaly (BA) according to the new gravimetric standard of the USGS (e.g., Hildenbrand et al., 2002).

To calculate the BA, it is necessary to obtain the theoretical gravity at each point of the data set (Eq. 1; Moritz, 2000; Woolard, 1979), where the coefficients are:  $g_e = 978\ 032.677\ 15$

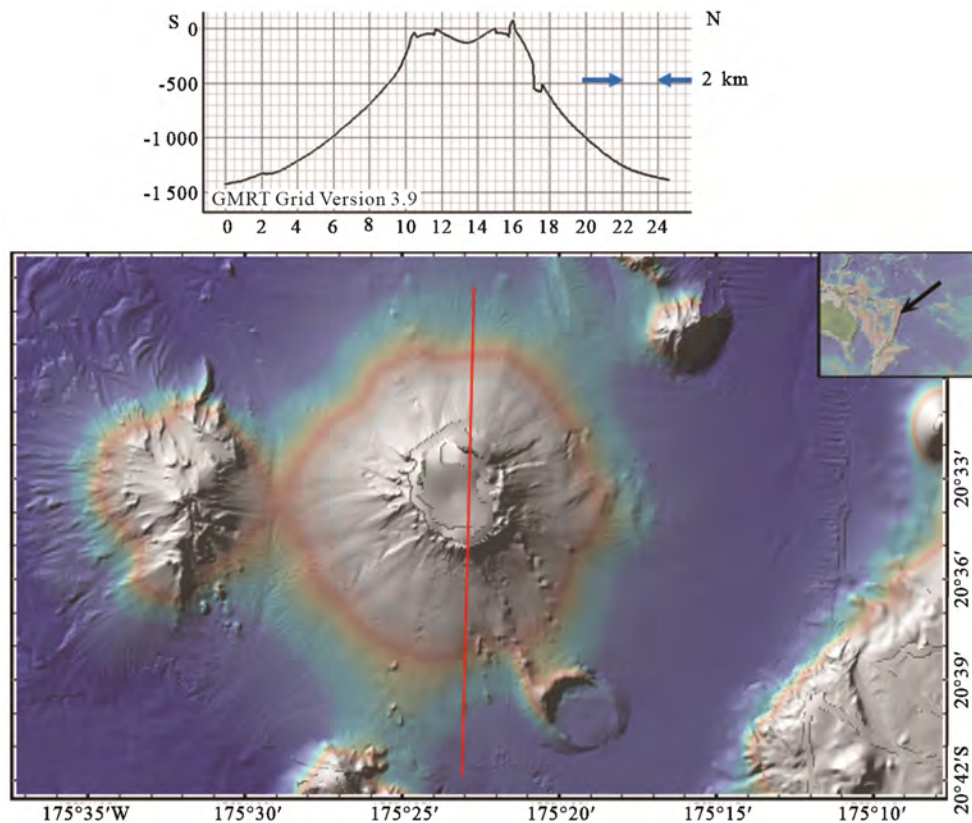


**Figure 1.** Location and bathymetric profile of Hunga Tonga Hunga Ha'apai volcano. Clearly, this bathymetry is now obsolete since it has been modified by the recent, intense explosion of the volcano. Two associated islands are barely seen at this scale; they conform the uppermost sections of the volcanic rim. The volcanic cone is regular, it rises ~1 480 m from the bottom of the ocean. In the profile (trace in red), only a small portion is above the water; this is one of the islands. It is to be expected that an eruption modifies the emerged portion, altering the islands' topography. Figure and bathymetric profile from GeomapApp (Ryan et al., 2009).



mGal;  $k = 0.019\ 318\ 513\ 53\ y$ ,  $e^2 = 0.006\ 693\ 800\ 229\ 0$ . Coefficients  $k$  and  $e$  are dimensionless, and  $\phi$  is the latitude at the point.

$$G_{\text{teo}} = g_e \frac{1 + k(\sin \phi)^2}{\sqrt{1 - e^2(\sin \phi)^2}} \quad (1)$$

The elevation at each point must be known; to accomplish this, we used the topographic model with a 15 arc-sec of resolution (450 m). This data is available from <https://download.gebco.net/> (Weatherall et al., 2021). Subsequently, the value of the ellipsoidal height ( $h_{\text{ellip}}$ ) and the value of the geoid height were taken to geoidal height ( $H_{\text{geo}}$ ) through Eq. (2) (Götze and Li, 1996). For the following formulas we will define geoidal height ( $H_{\text{geo}}$ ) as height ( $h$ ).

$$h_{\text{ellip}} = H_{\text{geo}} + N \quad (2)$$

where  $N$  is the geoid height.

Knowing the height at each point, we obtained the height correction ( $C_h$ ) through Eq. (3).

$$C_h = \left( (0.308\ 769\ 1 - 0.000\ 439\ 8 \sin(\phi)^2) h + 7.212\ 5 \times 10^{-8} h^2 \right) [\text{mGal/m}] \quad (3)$$

We then calculated the atmospheric correction ( $C_{\text{atm}}$ ); considering the gravimetric attraction produced by the mass of air over the point with Eq. 4 (Hildenbrand et al., 2002).

$$C_{\text{atm}} = 0.874 - 9.9 \times 10^{-5} h + 3.56 \times 10^{-9} h^2 \quad (4)$$

The Bouguer correction ( $C_{\text{Boug}_2^\circ}$ ), is the correction that eliminates the gravimetric attraction of the masses existing between the reference level and the point on the topographic surface (Eq. 5).

$$C_{\text{Boug}_2^\circ} = 2\pi G \rho h \left( \frac{\alpha}{2} - \eta \left( 1 + \frac{1}{2\alpha} \right) \right) [\text{mGal/m}] \quad (5)$$

where  $\alpha$  and  $\eta$  are coefficients defined by LaFehr (1991),  $G$  is the gravimetric constant and  $\rho$  the density of the medium.

For the topographic correction ( $C_{\text{topo}}$ ), we used the method implemented in the Oasis Montaj program of Geosoft, which uses the algorithm proposed by Kane (1962) and supplemented by Nagy (1966).  $AB$  is then calculated (Eq. 6)

$$AB = G_{\text{Obs}} - G_{\text{teo}} \pm C_{\text{alt}} \mp C_{\text{Boug}_2^\circ} + C_{\text{atm}} + C_{\text{topo}} \quad (6)$$

The result appears in Fig. 2, showing that the NW and the SE regions contain substantial negative anomalies.

## 1.2 Bouguer Anomaly Inversion

Volcanic plumbing systems are described in various ways (e.g., Corsaro et al., 2021; Trasatti et al., 2021; Tibaldi, 2015). In general, they are the conduits that store and transport magmatic products to the surface. The possibility to map those conduits based on their density relies in their low-density characteristics, arising from either gas-filled, porous paths, or low-density, high-temperature magma chambers. Volcanic density distributions can be obtained performing 3D inversions of the Bouguer anomaly (BA) that transforms gravity (mGal) determinations into density distributions ( $\text{g/cm}^3$ ). Satellite obtained, gravity data sets are available at different spatial resolutions,

which provide, through adequate processing, the required Bouguer anomaly of a given site. Camacho and Alvarez (2021) showed that the best resolution is obtained with the GGMplus gravity data set (Hirt et al., 2013). The high-resolution data sets play a definitive roll unveiling the characteristics of volcanic interiors.

The 3D inversion code we used is implemented in the Oasis Montaj program of Geosoft, following the method described by Macleod and Ellis (2013), based on the theoretical considerations of Ellis et al. (2012). To represent geologic volumes, the program uses a Cartesian cut cell algorithm (CCC); to match the observed result with the calculated one, within established error limits, the inversion program uses an iterative reweighting inversion algorithm (IRI, Ingram et al., 2003). Results of the gravity inversion are presented in the form of a voxel with a density distribution in  $\text{g/cm}^3$ . Correlations are then established between the inverted results and the volcanic structure.

The perimeter of the Bouguer anomaly in Fig. 2, shows positive gravity anomalies, whilst the central region, corresponding to the volcano, shows a changeable negative distribution, contrasting with the solid negative regions we have observed in other volcanoes; as will be shown, this distribution is directly connected to the volcano's plumbing system in the upper crustal layers. With the complete Bouguer anomaly calculated for the study area (Fig. 2), we proceeded to execute 3D inversions.

## 2 RESULTS

We perform two 3D inversions using the BA map of Fig. 2. The models have resolutions of 250 and 500 m, respectively. The former reaches depths of 5 km, whilst the latter reaches 6 km in depth; they complement each other.

### 2.1 Inversion 3D, 250 m

The result of the 3D inversion with a resolution of 250 m appears in Fig. 3; the inverted region corresponds to the smaller rectangle comprising lines 1 through 5 in Fig. 2. Exposed is a vertical, density cross-section reaching 5 km in depth. We highlighted (yellow dashes) the regions that we interpret as portions of the volcano's plumbing system. Along the exposed cross-section, the system shows at least two feeding conduits at the deepest portion of the section. A bifurcation occurs in this plane at elevations of  $\sim -2\ 500$  m, with one branch following a southward direction, and the other a northward one. In turn, each branch bifurcates again when approaching the surface. Thus, we identify four trajectories along which the motion of magmatic material could take place to the surface. The Bouguer anomaly map (Fig. 2) shows another important negative anomaly in the SE portion of the inverted area; from this and other cross-sections, we infer that the volcanic structure also concentrates many low-density regions. Figure 4 shows an E-W slice of the density distribution that confirms the existence in this region of deep conduits extending down beyond the bottom of the model; it also shows the distribution of high-resolution gravity stations used in the inversion.

This volcano presents a large quantity of low-density materials located at, or close to the surface, not common in other volcanic edifices. Exceptionally, we have found low-density

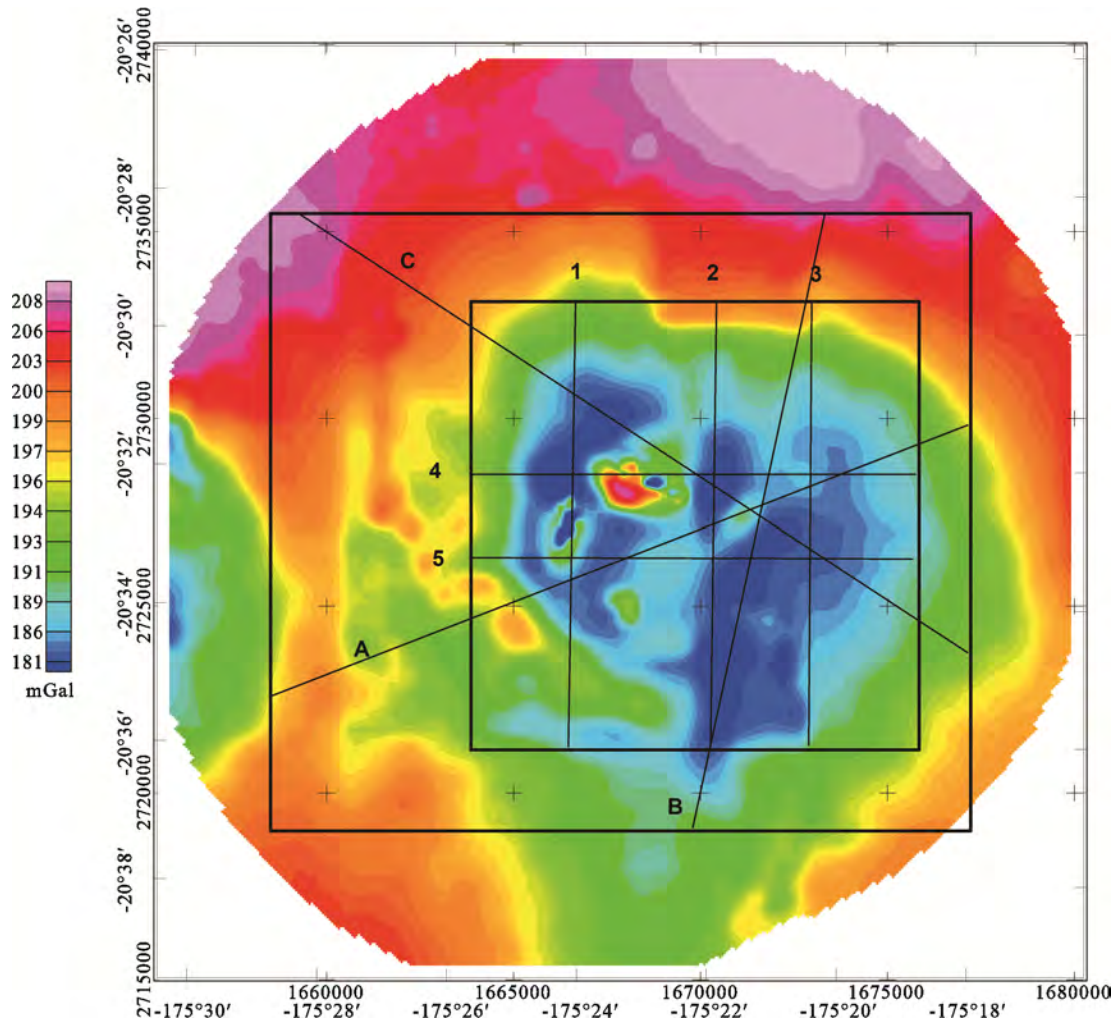


**Figure 2.** Complete Bouguer anomaly (mGal) of the study area; two rectangles (heavy lines) are used to delimit inverted regions; in the large rectangle three lines are used to obtain cross-sections: A, B, and C; the inversion has a resolution of 500 m. In the internal rectangle five lines (1–5) indicate the locations of the respective cross-sections obtained along their lengths, with 250 m resolution. The outstanding, positive Bouguer anomaly (region in red), close to the intersection of lines 1 and 4 corresponds to a bathymetric low.

pockets in volcanic surfaces (Camacho and Alvarez, 2021), contrasting with their common presence in HTHH volcano. The eruption of March 2009 from HTHH was reported as beginning from multiple vents on March 17 and ended after five days of activity on 21 March (Global Volcanism Program, 2009), which is in accordance with the surficial location of many low-density pockets, as observed in our model.

Exploring the characteristics of the low-density distributions, particularly those close to the surface (i.e., within 1.2 km depth), we identified a distribution in the form of an almost complete ring of low-density material, as shown in Fig. 5, surrounding the body of the volcanic structure. The ring is well defined with thicknesses between 500–750 m. Ring fractures have been observed in Tofua volcano, 93 km NNE of HTHH, also with explosive volcanism; Caulfield et al. (2011) reported a ring of circular fractures, attributed to magmatic chamber overpressure, resulting in roof failure. In the case of HTHH volcano the mechanism leading to the low-density ring can be attributed to invasion of light magmatic products through the ring faulted regions, prior to the eruption.

## 2.2 Geosurfaces

From the 3D inversion data, we can extract geosurfaces, in this case density surfaces that delimit defined density ranges, helping visualize and measure the associated volumes. To get an insight on the distribution of the regions with lowest density we extracted the geosurface in the 2.07–2.17 g/cm<sup>3</sup> density range; results appear in Fig. 6. It shows the abundant low-density materials near the surface, as well as a region that reaches to the bottom of the inverted volume, indicating it continues downward.

To complement the observations on the surficial low-density distributions, we obtain cross-sections designated 1 and 4 in Fig. 2; they were selected since their intersection occurs where we locate a large concentration of low-density material in the NW region of the volcano. Figure 7 shows their intersection as viewed from the NW; yellow, dashed lines highlight the regions where density is lowest, and dashed, brown lines limit regions of intermediate density which may also transport low-density materials to the surface (e.g., gases percolating to the surface, presumably at rates different than those in the lowest-density regions).

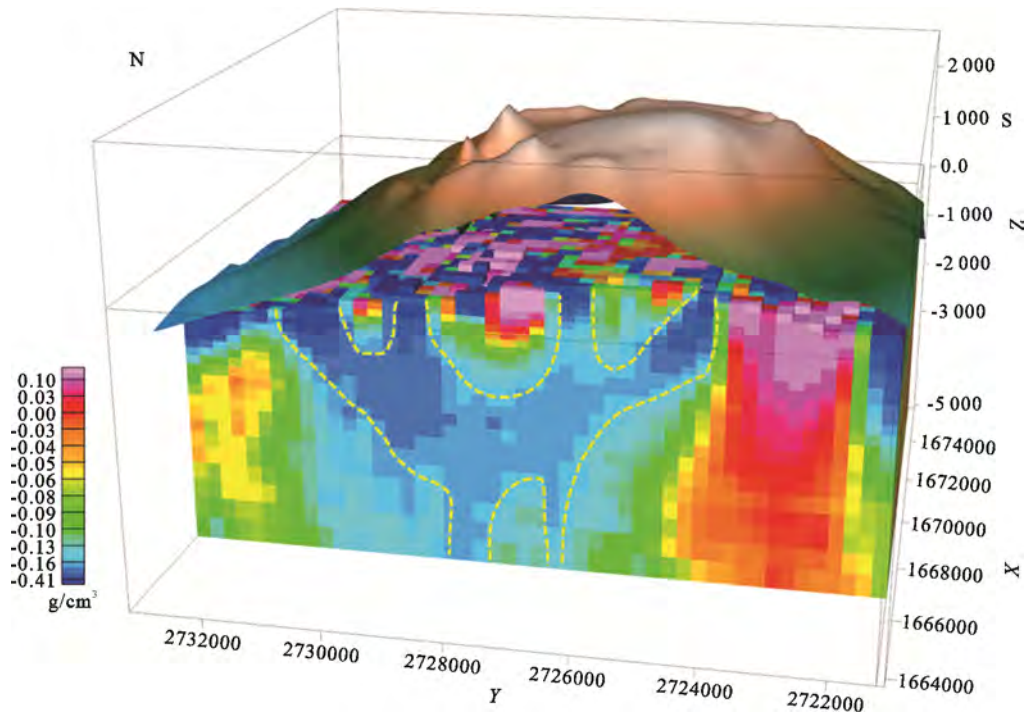


**Figure 3.** Volcano's bathymetry (brown surface) and vertical section across the inverted volume of the Bouguer anomaly of Fig. 2. The DEM (bathymetry) is displaced upwards, to make visible a portion of the surface of the inverted volume. The dashed, yellow lines indicate what we propose as the intersection of the plumbing system with this plane. Voxel resolution 250 m.

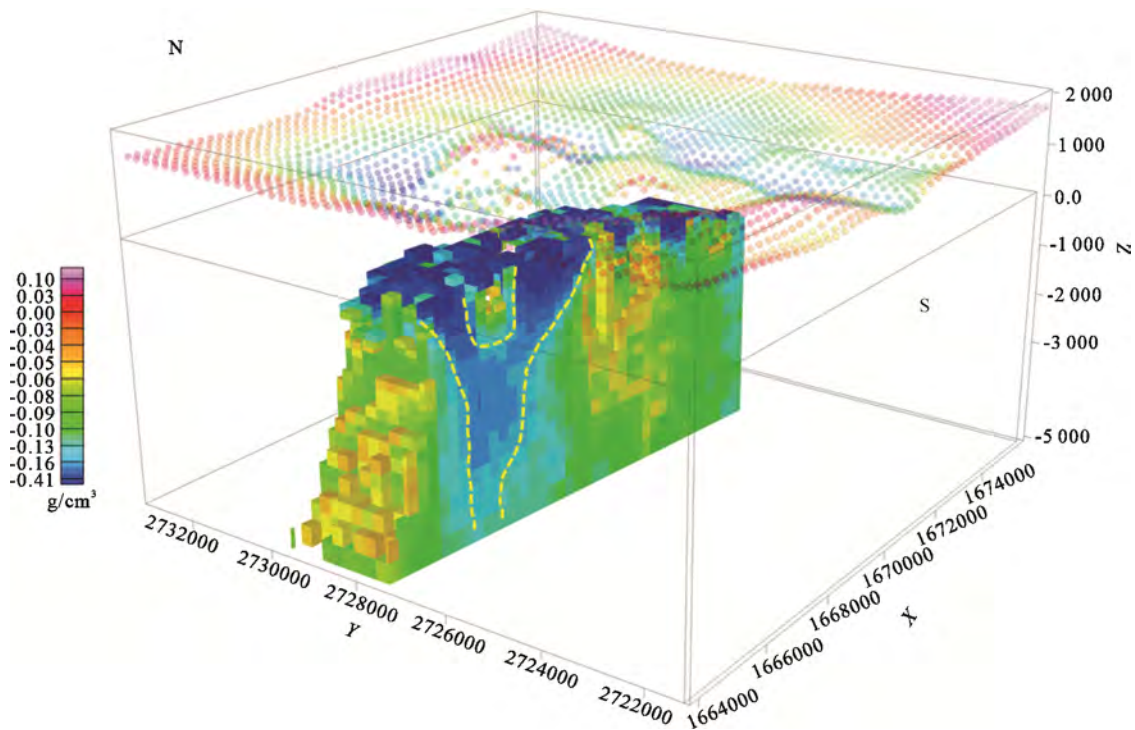


**Figure 4.** Slice in the E-W direction of the inverted volume in Fig. 3, with density filtered to allow only values  $< 2.61 \text{ g/cm}^3$ . The dashed, yellow lines indicate what we propose as the intersection of the plumbing system with the slice. Dots in the upper planes represent the distribution of the gravity stations involved in the inversion process; they are colored according to elevation ranges. Voxel resolution 250 m.

As an example, on the eastern portion of Section 4, we observe two surficial low-density pockets underlain by regions exhibiting intermediate density values (green), which may be the conduits through which these deposits were accumulated.

Dimensions of the low-density region at the intersection of the two lines (1 and 4) are measured at each cross-section as at  $X = 1.0 \text{ km}$ ,  $Y = 2.0 \text{ km}$ , and  $Z = 3.0 \text{ km}$ , or a volume of  $6.0 \text{ km}^3$  for this region. This is a first order estimate of the low-

density region in the vicinity of the intersections of those lines. The outstanding, low-density surface pockets are associated with regions (green) that connect with the bottom of the model, as highlighted by the dashed, brown lines. One must conclude that the materials forming those low-density pockets were fed laterally in the surface, or materials could have displaced along the green regions to accumulate at, or near the surface. Similar

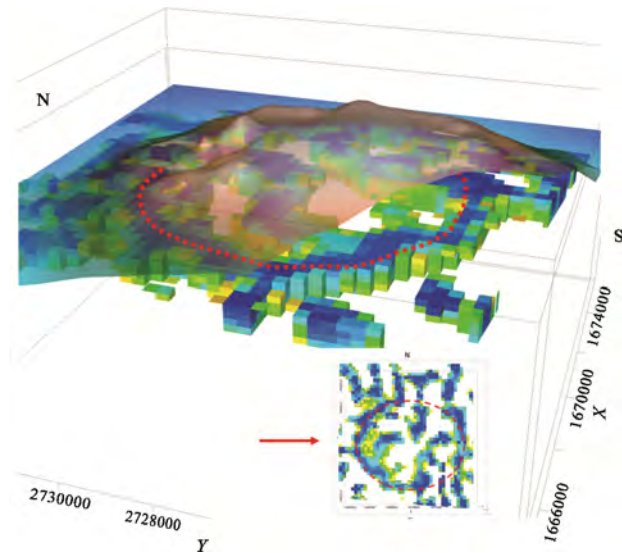


**Figure 5.** (a) Relationship between the DEM displaced upwards 1 000 m, scaled  $\times 2$ , and a transparency of 30%, and the circular distribution of low-density (material located at depths  $-1\ 190\ \text{m} < Z < -670\ \text{m}$ ) and density  $< 2.26\ \text{g}/\text{cm}^3$ . The volume is clipped at an elevation of  $-550\ \text{m}$ . (b) Vertical view of the low-density distribution with N on the top, showing the circular distribution of the low-density layer. Red dots indicate the location of the low-density ring in both figures.

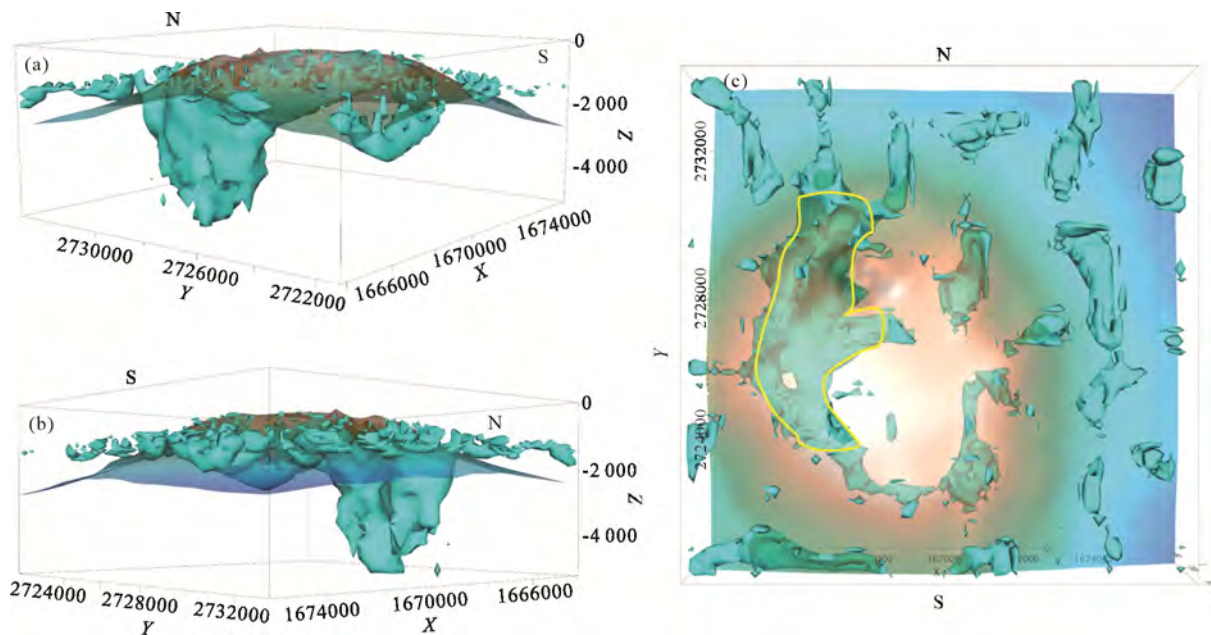


**Figure 6.** (a) View from the W of the geosurfaces enclosing densities  $2.07\text{--}2.17\ \text{g}/\text{cm}^3$ . The main surface reaches to the bottom of the inverted volume ( $-5\ 000\ \text{m}$ ), suggesting that this main conduit is fed from an underlying magma chamber. The DEM of the volcano is superposed. (b) View from the E of the geosurface enclosing densities  $2.07\text{--}2.17\ \text{g}/\text{cm}^3$ . (c) Top view of the geosurfaces enclosing densities  $2.07\text{--}2.17\ \text{g}/\text{cm}^3$ . The yellow polygon shows the surface extent of the low-density region estimated at  $\sim 12\ \text{km}^2$ .

pockets have been observed in volcanos, related to magmatic chambers at depths of 2 to 3 km, from which fluxes of low-density materials reach and concentrate close to the surface (e. g., Camacho and Alvarez, 2021). However, in the present case the feeder (magmatic chamber) is apparently below the bottom of our model and cannot be exposed in this inversion.

### 2.3 Inversion 3D, 500 m

The larger rectangle in Fig. 2 contains lines A, B, and C. We performed a 3D inversion at 500 m resolution on the area occupied by this rectangle to complement some of the observations made at 250 m resolution, as well as to reach deeper in the inverted region. One volume element of 500 m resolution averages four 250-m volume elements, and the density distribution reaches 1 km deeper.

Vertical, density cross-section A (Fig. 8a) reaches 6 km in depth; the main component of a major mid-density anomaly (green) can be appreciated between  $-2\ 500\ \text{m} < X < 10\ 000\ \text{m}$ . Additionally, between  $3\ 000\ \text{m} < X < 7\ 500\ \text{m}$  a low-density conduit is identified, extending vertically from the surface to an elevation of  $-6\ 000\ \text{m}$ , suggesting the connection with deeper magma sources. Line B intersects the Bouguer anomaly from S to N (Fig. 8b); a negative density anomaly in the south-central portion of the map was obtained. Given its position ( $-3\ 000\ \text{m} < X < 1\ 000\ \text{m}$ ) and depth we interpret it as one of the main conduits to the surface. It starts at the bottom of the model, passes through a narrow conduit at  $\sim -4\ 000\ \text{m}$ , to continue upwards, spreading considerably at the surface. Line C shows another connection to the deeper magma sources between  $5\ 000\ \text{m} < X < 7\ 500\ \text{m}$  (Fig. 8c). In summary, the 500-m resolution inversion indicates at least three major conduits from  $-6\ 000\ \text{m}$  elevation to the surface; we conclude that the magma chamber must be located below this depth.

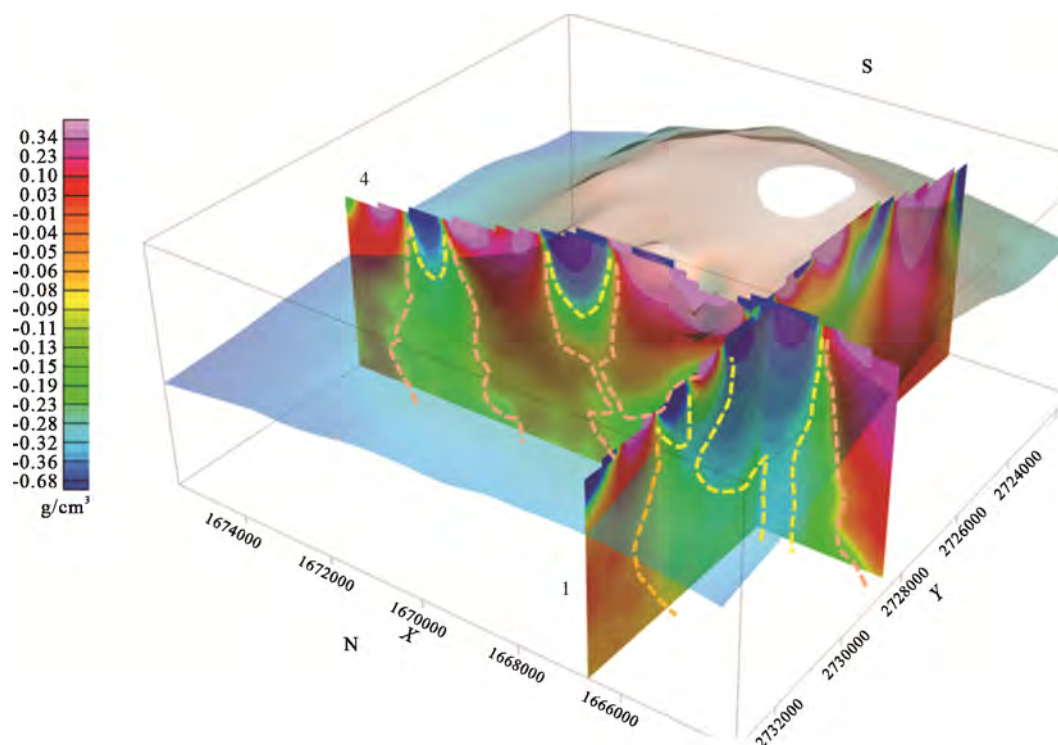


**Figure 7.** View from the NW of a 3D rendering of the intersection between cross-sections of lines 1 and 4 in Fig. 2, with a resolution of 250 m. A portion of the bathymetry (light blue to light brown) is included for reference. Dashed yellow lines highlight the lowest density regions, whilst dashed brown lines locate the regions surrounding them, which may also form part of the volcano's plumbing system.

A geosurface derived from the 500 m density distribution was also obtained. We explored various density ranges; the geosurface shown in Fig. 6 at 250 m resolution was replicated at the 500 m resolution with slightly different characteristics (not shown). In the density range from 2.47 to 2.57  $\text{g/cm}^3$ , a new important geosurface was obtained, as shown in Fig. 9a. This geosurface also reaches elevations of -6 km, and covers mostly the eastern portion of the structure, complementing the results obtained in the 250 m resolution inversion. The result confirms that plumbing conduits may vary in density from one location to another in the same volcano, in addition to the density variations occurring within the same volcanic conduit.

### 3 CONCLUDING REMARKS

One of the striking observations about Hunga Tonga Hunga Ha'apai volcano is the concentration of low-density materials at, or near its surface. The inversion at the highest resolution (250 m) allowed for the identification of a circular distribution of low-density material that we identified with ring fracturing, probably associated with overpressure from the magmatic chamber. Barth et al. (2019) observed that the rise and bursting of large, conduit-filling, over-pressurized gas slugs may lead to mush regions in the shallow plumbing system, where an exsolved volatile phase may also be abundant. Whether this mechanism operates in HTHH volcano cannot be discerned with the data presented at this point; however, it involves the concentration of low-density materials, as observed in here. Within the 5–6 km depths modeled we do not find a concentration of low-density material that we can identify with a magmatic chamber, in line with the conceptual model of the mag-

matic system of HTHH as an open system of a shallow (5–8 km depth) magma reservoir (Brenna et al., 2022). This contrasts with observations in other volcanos where low-density concentrations can be identified with magma chambers, owing to their density distributions and depths (e.g., Camacho and Alvarez, 2021; MacQueen et al., 2021; Alvarez and Yutsis, 2015).

Obtaining density geosurfaces helped isolate the deeper conduits that are probably the connection with the magma chamber feeding the upper volcanic conduits. Main conduits initiate at elevations of <-6 km, and as they progress upwards, they spread on the NW and SE sides of the volcanic structure. An estimate based on the yellow polygon of Fig. 6c yields an approximate area of 12  $\text{km}^2$  between depths of -400 to 0 m, which constitute the uppermost layers of the geosurface. This could be the contact area with sea water if volcanic effusions took place simultaneously in it, inducing the observed explosion. From the yellow polygon in Fig. 9b we estimate a contact area of 14  $\text{km}^2$  between depths of -1 200 to 0 m. These are preliminary estimates of contact areas with sea water. A more detailed location of actual discharge regions is out of the scope of this study. Forthcoming studies on gravity modeling will help shed light on the problem of rock fracturing in the surface of the volcano, by analyzing models of greater resolution than those used in the present study.

Similarly to what occurred in Tofua island, we infer that HTHH latest explosive eruption originated in the interaction of magma products with sea water. The interaction of emerging magma products with sea water guarantees violent reactions; since the volcanic structure is almost fully under water the abundant supply of this element is warranted. Any volcanic

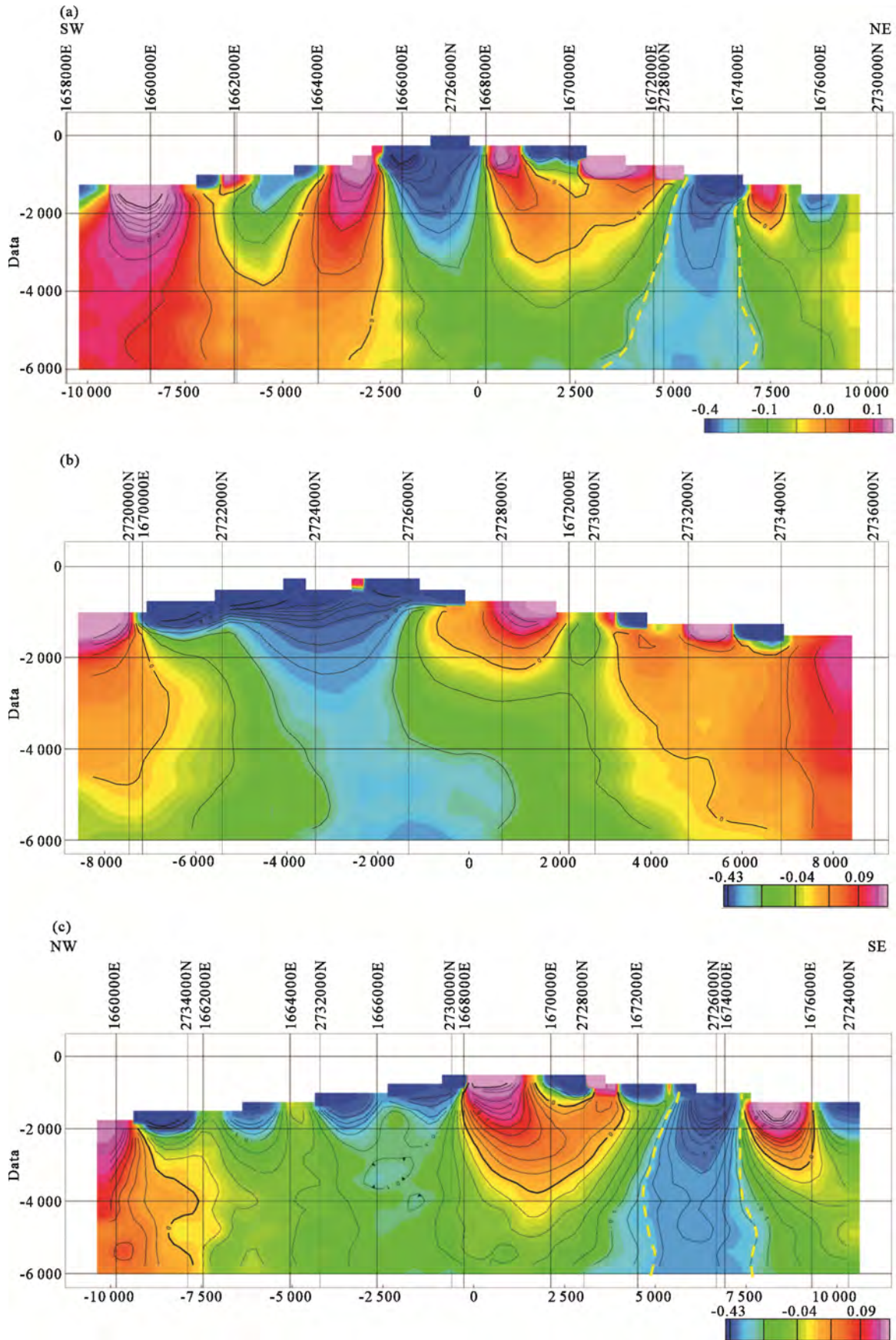


**Figure 8.** Sections A, B, and C, located in the larger rectangle of Fig. 2. Each section contains a vertical low-density column that we interpret as part of the plumbing system of the volcano. There are no signs of a magma chamber in the inverted volume; we conclude that the magma deposits feeding this volcano must be at depths greater than 6 km.

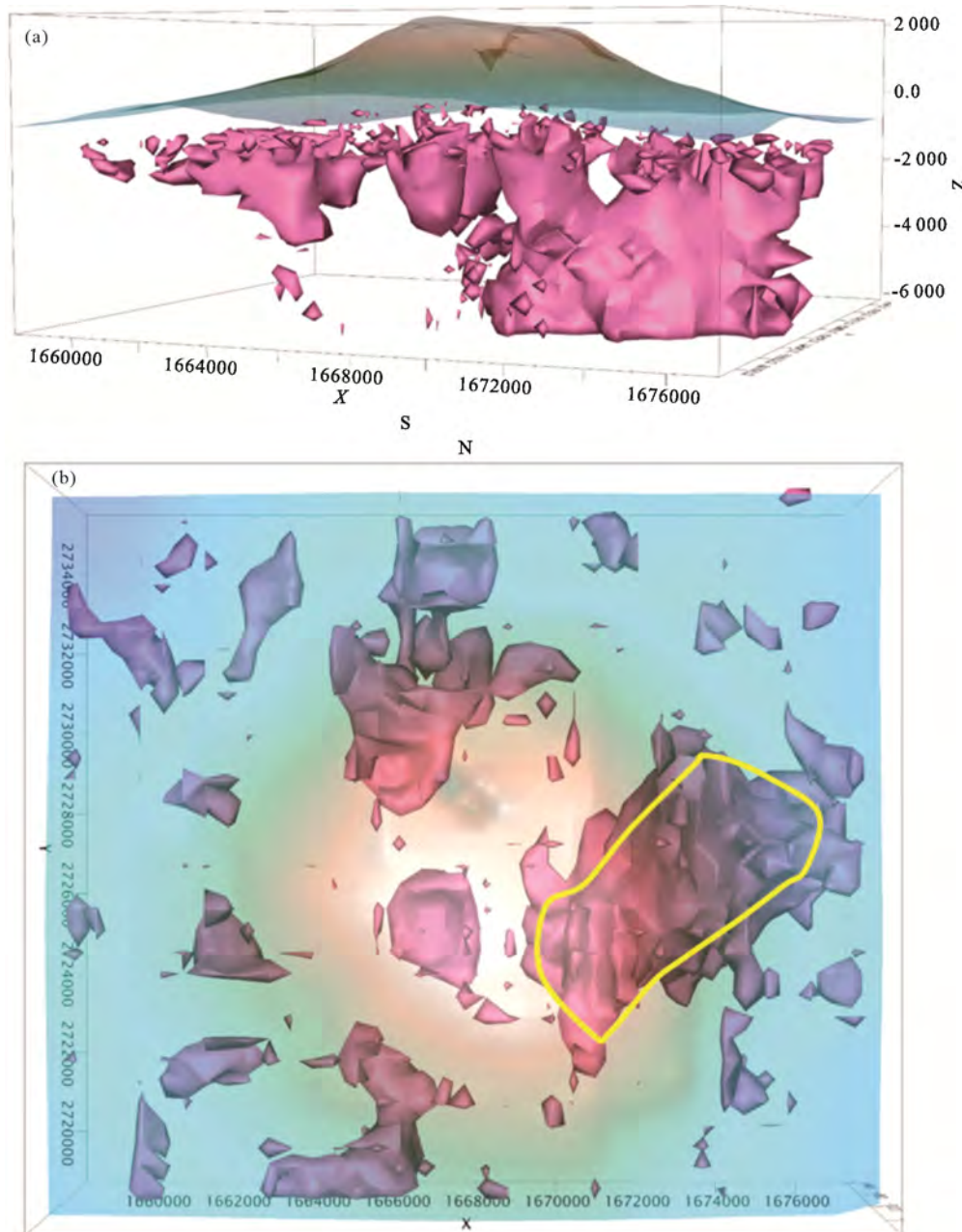


**Figure 9.** Geosurface obtained in the density range 2.47 to 2.57 g/cm<sup>3</sup> at 500 m resolution. (a) South view of the geosurface; it reaches to the bottom of the model (-6 000 m); (b) vertical view of the geosurface; it predominantly covers the central-eastern portion. The yellow polygon locates the area (14 km<sup>2</sup>) estimated of eruption products interacting with sea water.

products being ejected, necessarily will first interact with sea water. Injection of the volcanic products constituted a high energy event, producing enormous clouds that affected even the ionosphere (Themens et al., 2022). The observation of these authors, that smaller scale ionospheric waves continued to be present for up to six hours after the beginning of the eruption, suggests that ejection of magmatic materials may have continued in that lapse.

We extracted potential areas of contact with sea water from Figs. 6c and 9b, obtaining a total area of 26 km<sup>2</sup>; we note that those polygons are surface projections of the inclined planes of the geosurfaces involved, thus the actual contact areas are slightly larger. The quantitative observations derived from the present

study will help constrain new eruption models which, up to now, are using schematic descriptions of the volcano's plumbing system. For instance, Zheng et al. (2022) depicted a classical single-chimney volcano to explain their magma-hammer model in HTHH, whilst our results suggest that there may be at least two major exhaust trajectories, and probably more.

HTHH volcano has a continued history of explosions; its periodicity is indetermined, but ten-year lapses seem to be representative. The present analysis reflects the condition of the volcano between the 2015 and the 2022 eruptions, now modified by the latest eruption. When new gravity data on this structure is available, gravity inversions with those data may reflect the changes induced by the January 2022 explosion. In this re-

spect this study constitutes a gravimetric/density baseline for evaluating future modifications of the volcanic structure.

## ACKNOWLEDGMENTS

During the development of this work, Miguel Camacho received support from the Consejo Nacional de Ciencia y Tecnología (CONACYT, México). This study was supported by Instituto de Investigaciones en Matemáticas Aplicadas y en Sistemas, Universidad Nacional Autónoma de México; we acknowledge material support from both institutions. This research did not receive any specific grant from funding agencies in the public, commercial, or not-for-profit sectors. Upon request to the corresponding author, Bouguer anomaly data of HTHH will be provided. All other data is readily available from the cited references. The final publication is available at Springer via <https://doi.org/10.1007/s12583-022-1792-0>.

## REFERENCES CITED

- Alvarez, R., Yutsis, V., 2015. Southward Migration of Magmatic Activity in the Colima Volcanic Complex, Mexico: An Ongoing Process. *International Journal of Geosciences*, 6(9): 1077–1099. <https://doi.org/10.4236/ijg.2015.69085>
- Barth, A., Edmonds, M., Woods, A., 2019. Valve-Like Dynamics of Gas Flow through a Packed Crystal Mush and Cyclic Strombolian Explosions. *Scientific Reports*, 9: 821. <https://doi.org/10.1038/s41598-018-37013-8>
- Bauer, G. R., 1970. The Geology of Tofua Island. *Pacific Science*, 24(3): 333–350
- Brenna, M., Cronin, S. J., Smith, I. E. M., et al., 2022. Post-Caldera Volcanism Reveals Shallow Priming of an Intra-Ocean Arc Andesitic Caldera: Hunga Volcano, Tonga, SW Pacific. *Lithos*, 412/413: 106614. <https://doi.org/10.1016/j.lithos.2022.106614>
- Bryan, W. B., Stice, G. D., Ewart, A., 1972. Geology, Petrography, and Geochemistry of the Volcanic Islands of Tonga. *Journal of Geophysical Research*, 77(8): 1566 – 1585. <https://doi.org/10.1029/jb077i008p01566>
- Camacho, M., Alvarez, R., 2021. Geophysical Modeling with Satellite Gravity Data: Eigen-6C4 vs. GGM Plus. *Engineering*, 13(12): 690 – 706. <https://doi.org/10.4236/eng.2021.1312050>
- Caulfield, J. T., Cronin, S. J., Turner, S. P., et al., 2011. Mafic Plinian Volcanism and Ignimbrite Emplacement at Tofua Volcano, Tonga. *Bulletin of Volcanology*, 73(9): 1259 – 1277. <https://doi.org/10.1007/s00445-011-0477-9>
- Corsaro, R. A., Branca, S., De Beni, E., et al., 2021. Tales from Three 18th Century Eruptions to Understand Past and Present Behaviour of Etna. *Frontiers in Earth Science*, 9: 774361. <https://doi.org/10.3389/feart.2021.774361>
- Ellis, R. G., de Wet, B., Macleod, I. N., 2012. Inversion of Magnetic Data for Remnant and Induced Sources. In: Australian Society of Exploration Geophysicists (ASEG) 22nd International Geophysical Conference and Exhibition, Feb. 26–29, 2012, Brisbane
- Global Volcanism Program, 2009. Report on Hunga Tonga-Hunga Ha'apai (Tonga). *Bulletin of the Global Volcanism Network*, 34: 3. <https://doi.org/10.5479/si.GVP.BGVN200903-243040>
- Götze, H. J., Li, X., 1996. Topography and Geoid Effects on Gravity Anomalies in Mountainous Areas as Inferred from the Gravity Field of the Central Andes. *Physics and Chemistry of the Earth*, 21(4): 295 – 297. [https://doi.org/10.1016/s0079-1946\(97\)00051-7](https://doi.org/10.1016/s0079-1946(97)00051-7)
- GVP (Global Volcanism Program), 2015. Report on Hunga Tonga-Hunga Ha'apai (Tonga). *Bulletin of the Global Volcanism Network*, 40: 1. <https://doi.org/10.5479/si.gvp.bgvn201501-243040>
- Hildenbrand, T. G., Briesacher, A., Flanagan, G., et al., 2002. Rationale and Operational Plan to Upgrade the U.S Gravity Database. USGS Open File Report. Geology, Minerals, Energy and Geophysics Science Center, Moffett Field. 1–12. <https://doi.org/10.3133/ofr02463>
- Hirt, C., Claessens, S., Fecher, T., et al., 2013. New Ultrahigh-Resolution Picture of Earth's Gravity Field. *Geophysical Research Letters*, 40(16): 4279–4283. <https://doi.org/10.1002/grl.50838>
- Ingram, D. M., Causon, D. M., Mingham, C. G., 2003. Developments in Cartesian Cut Cell Methods. *Mathematics and Computers in Simulation*, 61(3/4/5/6): 561–572. [https://doi.org/10.1016/s0378-4754\(02\)00107-6](https://doi.org/10.1016/s0378-4754(02)00107-6)
- Kane, M. F., 1962. A Comprehensive System of Terrain Corrections Using a Digital Computer. *Geophysics*, 27(4): 455–462. <https://doi.org/10.1190/1.1439044>
- Kusky, T. M., 2022. DÉJÀ Vu: Might Future Eruptions of Hunga Tonga-Hunga Ha'apai Volcano be a Repeat of the Devastating Eruption of Santorini, Greece (1650 BC)? *Journal of Earth Science*, 33(2): 229–235. <https://doi.org/10.1007/s12583-022-1624-2>
- LaFehr, T. R., 1991. An Exact Solution for the Gravity Curvature (Bullard B) Correction. *Geophysics*, 56(8): 1179–1184. <https://doi.org/10.1190/1.1443138>
- Macleod, I. N., Ellis, R. G., 2013. Magnetic Vector Inversion, a Simple Approach to the Challenge of Varying Direction of Rock Magnetization. In: 2013 Australian Society of Exploration Geophysicists–Petroleum Exploration Society of Australia (ASEG–PESA) 23rd International Geophysical Conference and Exhibition, Aug. 11–14, 2013, Melbourne
- MacQueen, P., Gottsmann, J., Pritchard, M. E., et al., 2021. Dissecting a Zombie: Joint Analysis of Density and Resistivity Models Reveals Shallow Structure and Possible Sulfide Deposition at Uturuncu Volcano, Bolivia. *Frontiers in Earth Science*, 9: 725917. <https://doi.org/10.3389/feart.2021.725917>
- Moritz, H., 2000. Geodetic Reference System 1980. *Journal of Geodesy* 74: 128–133. <https://doi.org/10.1007/s001900050278>
- Nagy, D., 1966. The Gravitational Attraction of a Right Rectangular Prism. *Geophysics*, 31(2): 362–371. <https://doi.org/10.1190/1.1439779>
- Roche, O., Druitt, T. H., 2001. Onset of Caldera Collapse during Ignimbrite Eruptions. *Earth and Planetary Science Letters*, 191(3/4): 191–202. [https://doi.org/10.1016/s0012-821x\(01\)00428-9](https://doi.org/10.1016/s0012-821x(01)00428-9)
- Ryan, W. B. F., Carbotte, S. M., Coplan, J. O., et al., 2009. Global Multi-Resolution Topography Synthesis. *Geochemistry, Geophysics, Geosystems*, 10(3): Q03014. <https://doi.org/10.1029/2008gc002332>
- Sigl, M., Winstrup, M., McConnell, J. R., et al., 2015. Timing and Climate Forcing of Volcanic Eruptions for the Past 2, 500 Years. *Nature*, 523(7562): 543–549. <https://doi.org/10.1038/nature14565>
- Smith, I. E. M., Price, R. C., 2006. The Tonga-Kermadec Arc and Havre-Lau Back-Arc System: Their Role in the Development of Tectonic and Magmatic Models for the Western Pacific. *Journal of Volcanology and Geothermal Research*, 156(3/4): 315 – 331. <https://doi.org/10.1016/j.jvolgeores.2006.03.006>
- The Watchers, 2015. New Island Being Formed by Hunga Tonga-Hunga Ha'apai Eruption. (2015-1-17) [2022-3-4]. <https://watchers.news/2015/01/17/new-island-being-formed-by-hunga-tonga-hunga-hapai-eruption/>
- Themens, D. R., Watson, C., Žagar, N., et al., 2022. Global Propagation of Ionospheric Disturbances Associated with the 2022 Tonga Volcanic Eruption. *Geophysical Research Letters*, 49: e2022GL098158. <https://doi.org/10.1029/2022GL098158>



- doi.org/10.1029/2022gl098158
- Thurin, J., Tape, C., Modrak, R., 2022. Multi-Event Explosive Seismic Source for the 2022  $M_w$  6.3 Hunga Tonga Submarine Volcanic Eruption. *The Seismic Record*, 2(4): 217–226. <https://doi.org/10.1785/0320220027>
- Tibaldi, A., 2015. Structure of Volcano Plumbing Systems: A Review of Multi-Parametric Effects. *Journal of Volcanology and Geothermal Research*, 298: 85–135. <https://doi.org/10.1016/j.jvolgeores.2015.03.023>
- Trasatti, E., Tolomei, C., Wei, L. H., et al., 2021. Upward Magma Migration within the Multi-Level Plumbing System of the Changbaishan Volcano (China/North Korea) Revealed by the Modeling of 2018–2020 SAR Data. *Frontiers in Earth Science*, 9: 741287. <https://doi.org/10.3389/feart.2021.741287>
- USGS, 2022.  $M$  5.8 Volcanic Eruption-68 km NNW of Nuku 'alofa, Tonga. Earthquake Hazard Program. [2022-10-5]. <https://earthquake.usgs.gov/earthquakes/eventpage/us7000gc8r/executive>
- Weatherall, P., Tozer, B., Arndt, J. E., et al., 2021. The GEBCO\_2021 Grid a Continuous Terrain Model of the Global Oceans and Land. (2021-7-19) [2022-10-5]. <https://doi.org/10.5285/c6612cbe-50b3-0cffe053-6c86abc09f8f>
- Woollard, G. P., 1979. The New Gravity System—Changes in International Gravity Base Values and Anomaly Values. *Geophysics*, 44(8): 1352–1366. <https://doi.org/10.1190/1.1441012>
- Yuen, D. A., Scruggs, M. A., Spera, F. J., et al., 2022. Under the Surface: Pressure-Induced Planetary-Scale Waves, Volcanic Lightning, and Gaseous Clouds Caused by the Submarine Eruption of Hunga Tonga-Hunga Ha'apai Volcano. *Earthquake Research Advances*, 2(3): 100134. <https://doi.org/10.1016/j.eqrea.2022.100134>
- Zheng, Y. C., Hu, H., Spera, F., et al., 2022. Episodic Magma Hammers in the Recent Cataclysmic Eruption of Hunga Tonga-Hunga Ha'apai. (2022-6-1). *Research Square*. <https://doi.org/10.21203/rs.3.rs-1639007/v1>

## 7. CONCLUSIONES

### 7.1. Capítulo 1 (*Geophysical Modeling with Satellite Gravity Data: Eigen-6C4 vs. GGM Plus*)

La comparación entre los modelos Eigen-6C4 y el modelo GGMplus, planteada en el capítulo 1, destaca principalmente la utilidad y validez de los datos del modelo GGMplus para ser empleados en los estudios regionales y locales; demostrando que sus valores y comportamiento espectral son muy parecidos a los datos del EIGEN-6C4 en superficie y que poseen una resolución espacial 4 veces mayor.

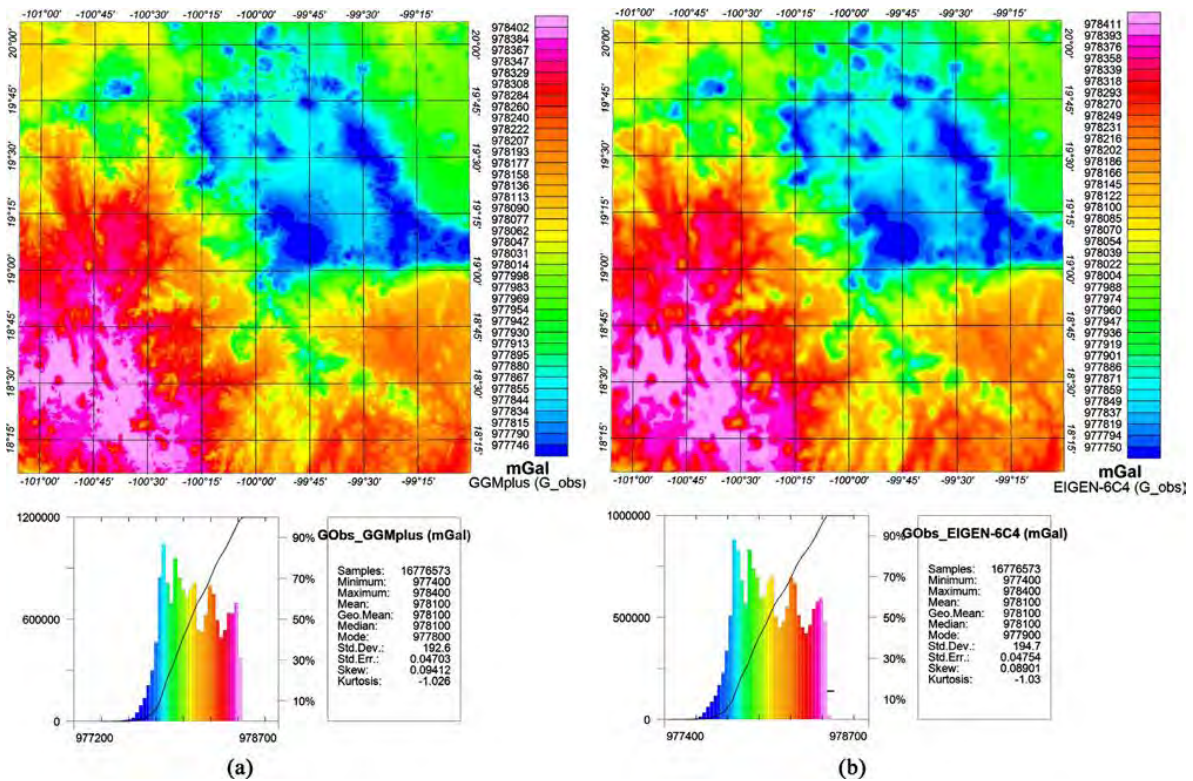


Figura 8. Comparación de G\_obs entre (a) GGMplus y (b) EIGEN-6C4. Observa la gran similitud entre los rangos de gravedad en ambos mapas. Tomado de Camacho y Alvarez (2021); Capítulo 1

También en este trabajo, se destaca la necesidad de usar DEMs topográficos de igual resolución a fin de evitar efectos de desenfoco o ruido por sobre muestreo sobre las anomalías. En la Figura 9, se presenta dos comparaciones de mallas de AB procesados con diferentes DEMs. En la malla a y en la malla b, se calculó la AB con el modelo EIGEN-6C4. La AB de la malla a, se calculó con un DEM de la misma resolución que el modelo EIGEN-6C4. En cambio, en la malla b, se calculó con el DEM STRM15

(de aprox. el doble de resolución), con lo cual se produce un efecto de ruido sobre la malla asociado al sobre muestreo de la topografía. En la malla c, se presenta una malla AB calculada con el modelo GGMplus y un DEM de igual resolución, mientras que en la malla d se tiene una malla de datos AB calculada con un DEM de la mitad de resolución, lo que genera un efecto de desenfoque de las anomalías.

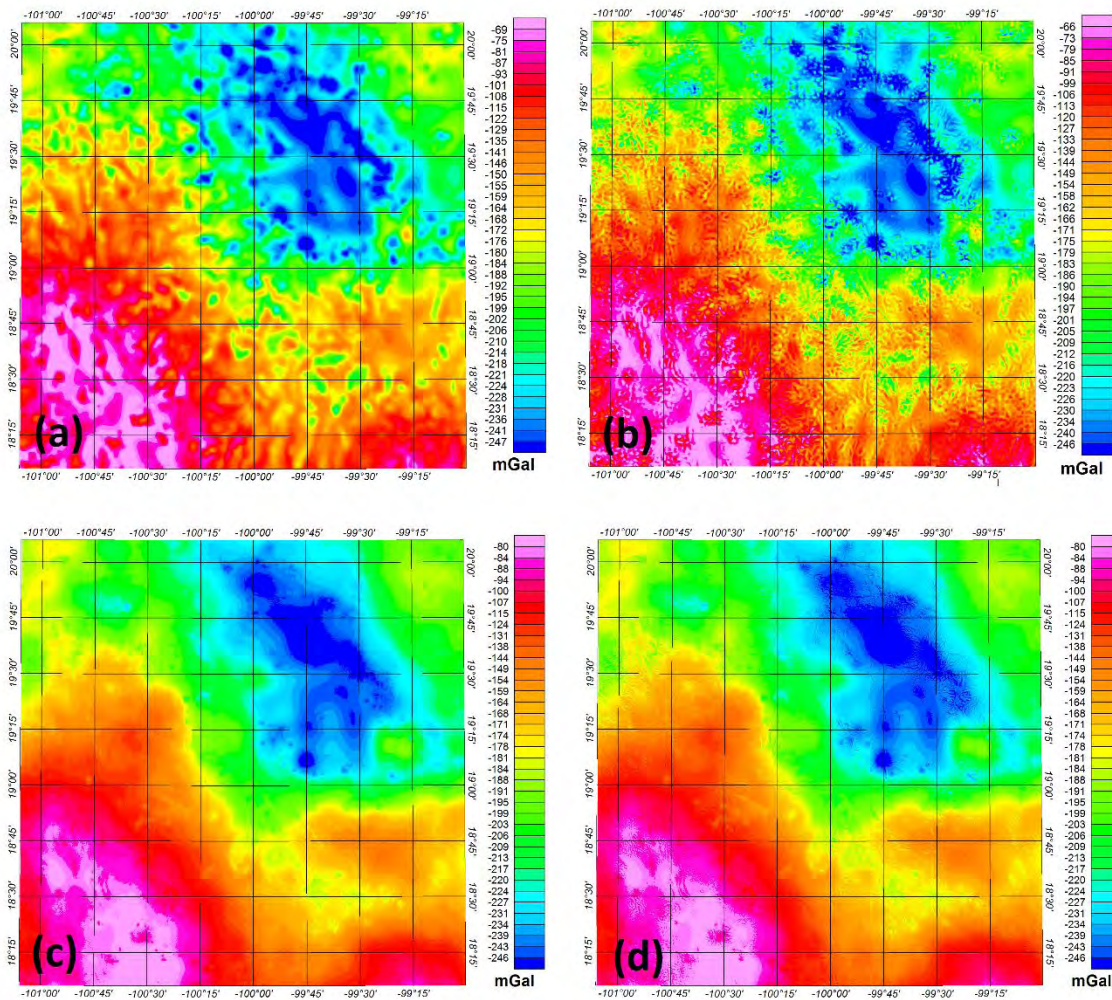


Figura 9. (a) Malla de AB calculada con el modelo EIGEN-6C4 y un DEM de igual resolución. (b) Malla de AB calculada con EIGEN-6C4 y con el SRTM15 (aproximadamente el doble de resolución). (c) En la malla (c) se observa una malla de AB calculada con el modelo GGMplus y un DEM de igual resolución. (d) Malla de AB calculada con el modelo GGMplus y un DEM de la mitad de resolución (SRTM15). Tomado y modificado de Camacho y Alvarez (2021); Capítulo 1.

Y finalmente, la comparación en el espectro de potencia de la AB de los dos modelos, demuestra que según su contenido espectral los datos del modelo GGMplus parecen ser mejores para estudios

donde la fuente gravimétrica está por encima de los 15 km de profundidad, mientras que los datos EIGEN-6C4 presentan un contenido espectral más nutrido para profundidades mayores a los 15 km de profundidad (Figura 10).

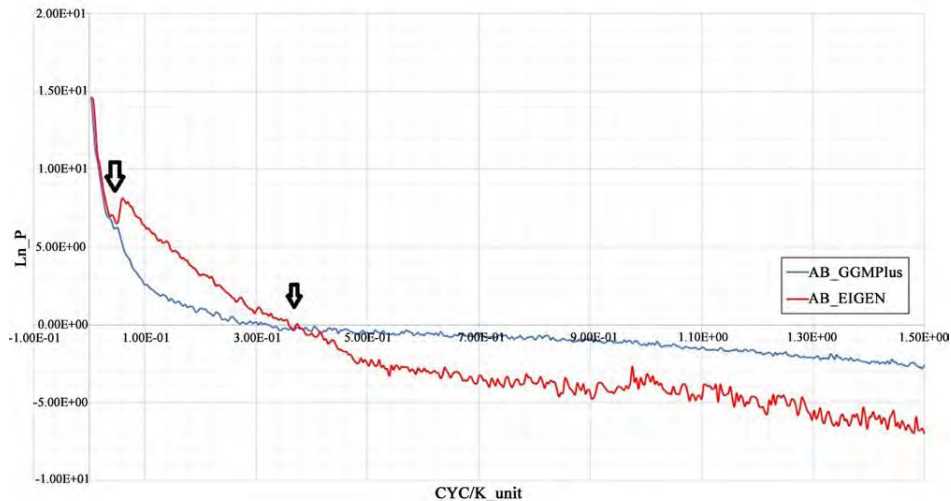


Figura 10. Comparación del espectro de potencia del modelo EIGEN-6C4 y el modelo GGMplus. Tomado de Camacho y Alvarez (2021); Capítulo 1

## 7.2. Capítulo 2 (*Delineation of the Boundaries of San Blas Basin, Mexico, Merging Gravity, Magnetic, and Seismic Data*; <https://doi.org/10.1016/j.jsames.2024.104818>)

En el capítulo 2, se emplearon datos gravimétricos de origen satelital del modelo EIGEN-6C4 para definir las fronteras de la Cuenca de San Blas (CSB). La anomalía de Bouguer calculada en el área de la CSB disminuye en una dirección N30°W aprox. casi paralelo a la costa de Nayarit. Se encontró que la gran cantidad de formas de relieve presentes en la zona, enmascara las características distintivas de la CSB, lo cual requirió de diversos procesos de filtrado en los datos gravimétricos para ser expuestas, como los aplicados en este estudio.

Los filtros de derivadas direccionales demuestran una correlación importante con los estudios sísmicos, lo cual resulta valioso para identificar áreas objetivo del estudio, mostrando que son una herramienta poderosa para complementar los resultados obtenidos de otros métodos geofísicos como: el tiempo de tránsito de ida y vuelta (TWTT) o líneas sísmicas interpretadas. En la Figura 11, se observa la delimitación propuesta en este trabajo (Camacho-Ascanio y Alvarez, 2024).

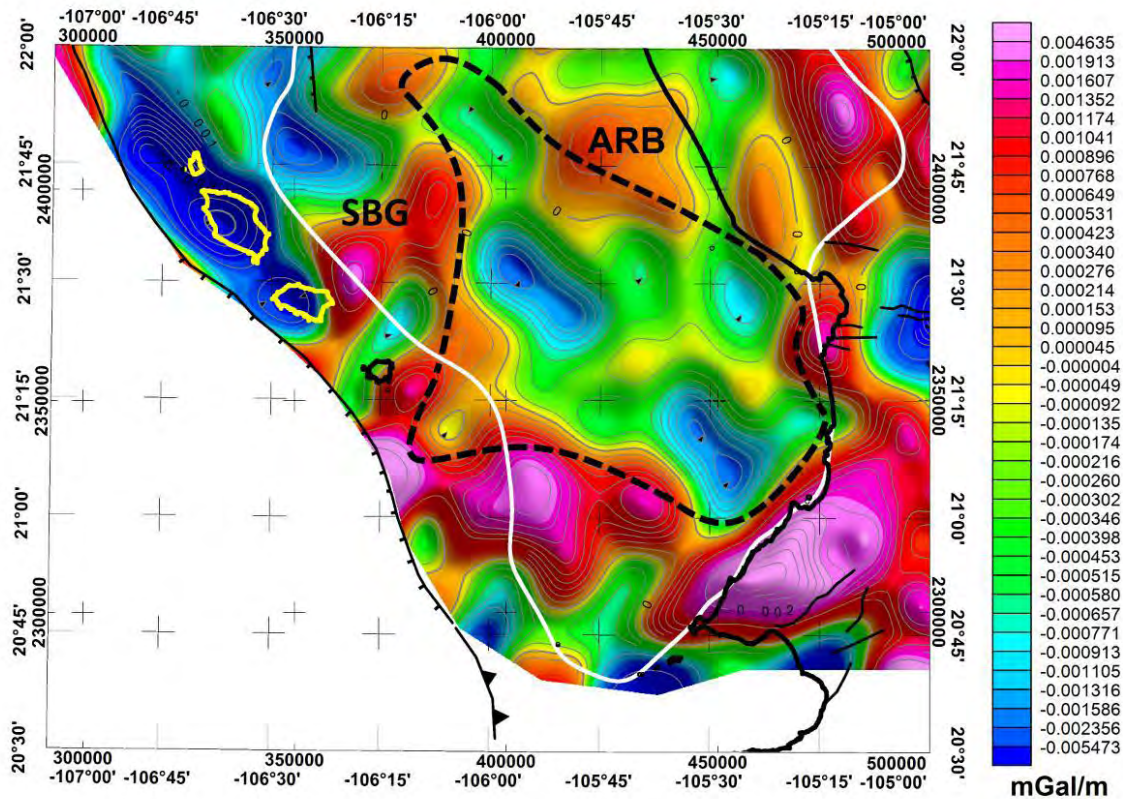


Figura 11. Mapa de AB\_Dz. En líneas grises, los contornos de la anomalía. En líneas delgadas negras, las fallas más representativas en la zona en tierra firme. La línea negra continua representa la línea de costa, y las líneas grises continuas representan los contornos de la AB. La línea blanca continua delinea la Cuenca de Mazatlán. SBG: Desfiladero de San Blas. ARB: Ensanchamiento de Aramara. La línea segmentada negra ubica los límites propuestos de la CSB. Tomado de Camacho y Alvarez (2024); Capítulo 2.

A partir de las inversiones 3D, se infiere que los procesos tectónicos más importantes en el área de la CSB siguen principalmente dos direcciones. Esto tiende a reafirmar el argumento de Sutherland et al. (2012), en el cual se sugiere que la CSB debió formarse antes de los 12 Ma. y podría estar relacionada con el período entre 30 y 18 Ma., propuesto por Ferrari et al. (2013) y ratificado por Ferrari et al. (2018), dado que muestra un desarrollo concordante en las orientaciones de los cuerpos de densidades anómalas encontrados. En consecuencia, el modelo de formación de la CSB propuesto por dichos autores en este estudio es coherente con tales observaciones.

Además, el modelo de inversión gravimétrica 3D obtenido, logró encontrar estructuras que pueden ayudar en el entendimiento del desarrollo de la apertura de Baja California, las cuales pueden ser vistas en la Figura 12.

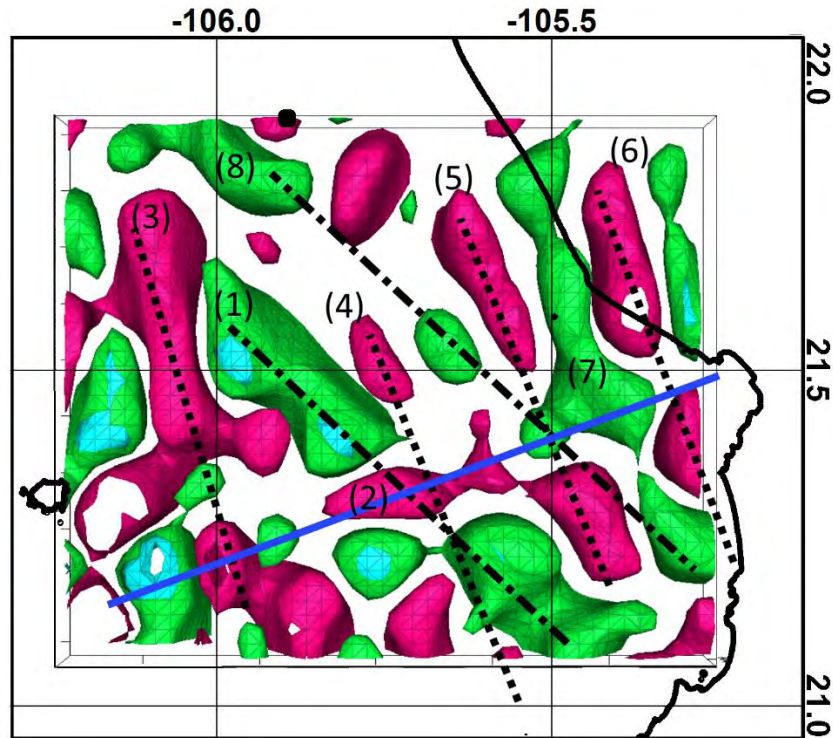


Figura 12. Mapa de geo-volúmenes de iso-densidades. En rojo, cuerpos con densidades de 0.025 g/cm<sup>3</sup>, en verde cuerpos con -0.025 g/cm<sup>3</sup> y en azul cuerpos con -0.050 (en relación con la densidad de reducción del medio de 2.67 g/cm<sup>3</sup>). En negro, la línea de costa. Las secciones en azul claro representan superficies dentro de las verdes. Tomado de Camacho y Alvarez (2024); Capítulo 2.

A través del estudio de estos cuerpos de densidades anómalas encontrados en la inversión gravimétrica 3D y sus posiciones, se planteó una posible reconstrucción de la evolución de los esfuerzos en la zona de la CSB (que puede ser visto en la Figura 13), mostrando evidencia concordante con el modelo de expansión propuesto por Ferrari et al. (2018).

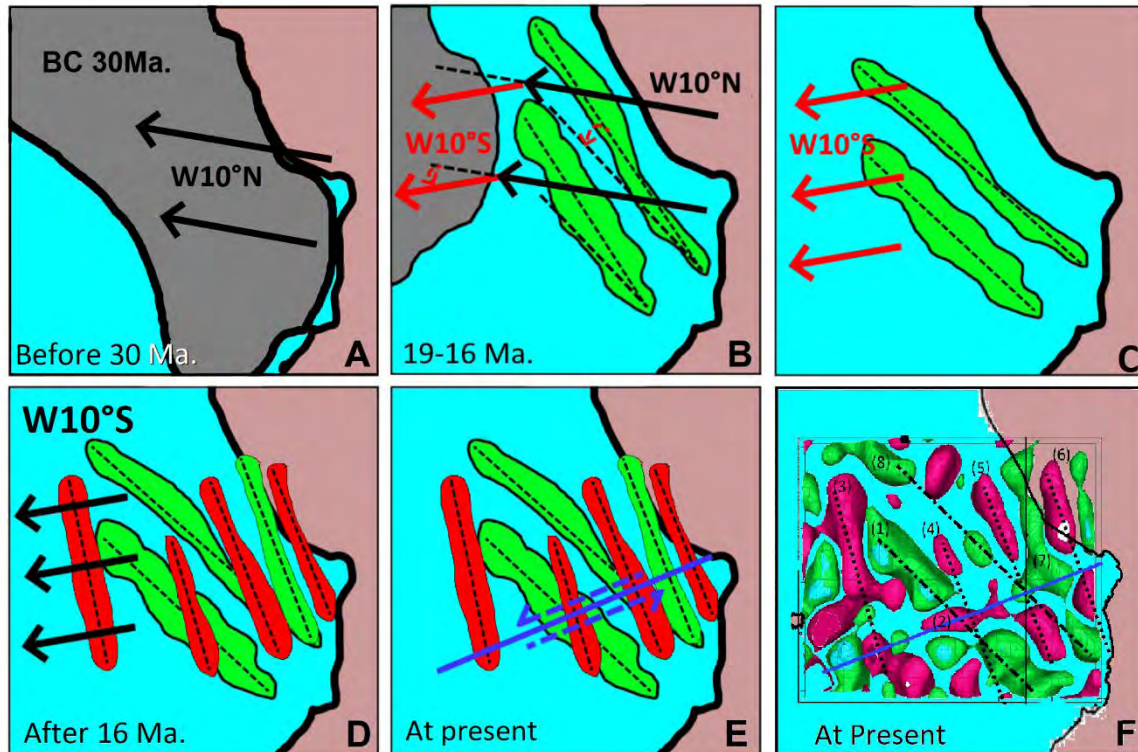


Figura 13. Desarrollo tectónico del área de la SBB entre 30 Ma y el presente. En el panel A, observamos la posición de la placa norteamericana cuando comenzó el movimiento de separación de la BC hace aprox. 30 Ma. El panel B se refiere al proceso de cambio en la dirección del movimiento, ocurrido entre 19 y 16 Ma atrás, sobre áreas de extensión y adelgazamiento cortical, causando su rotación. El panel C indica la consolidación del movimiento y la posición final rotada de los cuerpos asociados con zonas de adelgazamiento cortical. El panel D muestra la aparición de zonas de material de alta densidad asociadas con intrusiones formadas por el régimen continuo de extensión. En el panel E aparece un sistema de fallas sobre la zona, que la atraviesa. El panel F muestra la configuración actual del geo-volumen, obtenida a partir de la inversión. Tomado de Camacho y Alvarez (2024); Capítulo 2.

### 7.3. Capítulo 3 (*Gravimetric analysis of the rifts and volcanic fields of the Jalisco block, Mexico*)

En el estudio del Bloque de Jalisco, del capítulo 3. Los datos del modelo EIGEN-6C4, logran definir las principales estructuras del Bloque de Jalisco, de manera que hasta el momento no se había logrado, permitiendo así desarrollar una interpretación integral de su estructura y sus límites.

Estos límites tectónicos pueden ser observados en la Figura 14 y son: La Trinchera Mesoamericana para la región suroccidental; el Rift de Colima para la frontera oriental; el Graben del Gordo para el borde suroriental; el Rift de Tepic-Zacoalco para la región nororiental, y el Rift de Compostela-

Banderas para la región noroccidental. De esta forma, los límites del Bloque de Jalisco se confirman como las fallas Tepic-Zacoalco y las de Colima, y las tendencias de AB presentadas confirman la ubicación del límite noroeste del Bloque de Jalisco a lo largo de la falla Banderas-Compostela (Figura 14). Además, las fallas de Tepic-Zacoalco y el Valle de Banderas, se encuentran en un mínimo de AB el cual se asocia a un punto triple definido como el Punto Triple de Compostela.

Las fallas Tepic-Zacoalco, y la del N de Colima se encuentran y definen el Punto Triple de Guadalajara (PGT). En el trabajo, se identificaron dos tendencias estructurales adicionales representadas por secuencias alineadas de mínimos de AB, que comienzan en el PGT y continúan en direcciones suroeste a S15°O y S35°O; la primera termina en el puerto de Manzanillo y la segunda en la costa del Pacífico, cerca de la costa.

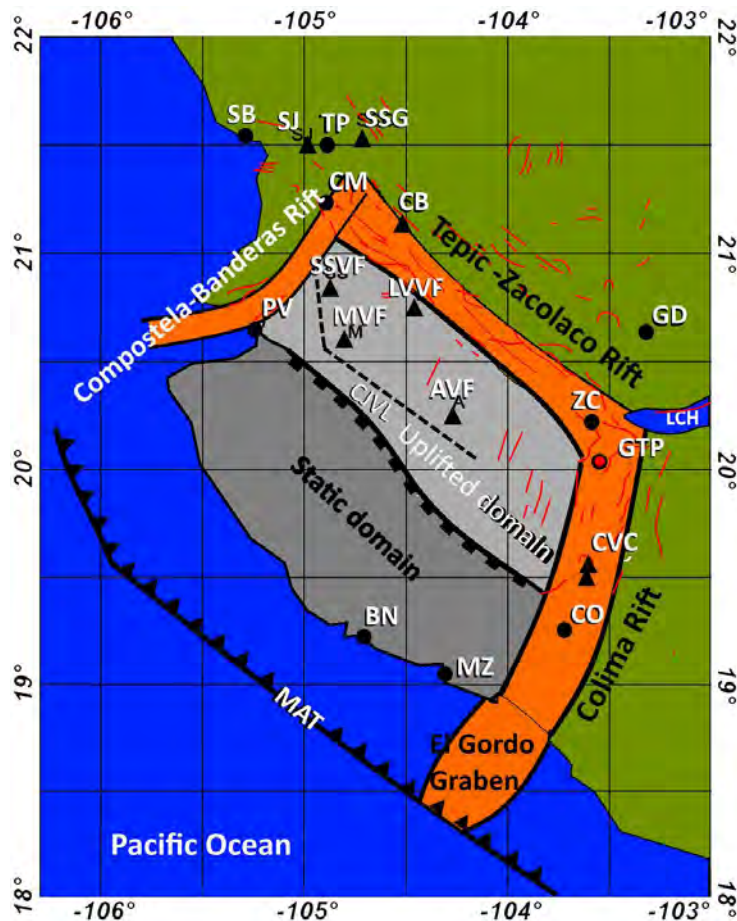


Figura 14. Principales elementos y límites tectónicos del Bloque de Jalisco, junto con los dominios topográficos (el estático y el levantado). En naranja se muestran los límites y las fallas geológicas. Los triángulos representan los campos volcánicos, incluyendo el Complejo Volcánico de Colima (CVC) y el Lineamiento Volcánico Central de Jalisco (CJVL, en línea negra), que abarca los campos volcánicos de San Sebastián (SSVF), Mascota (MVF), Ayutla (AVF) y Los Volcanes (LVVF). Otros



volcanes notables incluyen San Juan (SJ), Sangangüey (SGG), y Ceboruco (CB). Los puntos indican las ciudades principales, como San Blas (SB), Tepic (TP), Compostela (CM), Guadalajara (GD), Chamela (CH), Colima (CO), Manzanillo (MZ), Barra de Navidad (BN) y el Lago de Chapala (LCH). Los puntos rojos señalan el Punto Triple de Guadalajara (GTP) y el Punto Triple de Compostela (CTP). Tomado de Camacho y Alvarez (2020); Capítulo 3.

#### 7.4. Capítulo 4 (*Volcanic Plumbing Systems: The Case of Nevado De Toluca Volcano*)

En el estudio del volcán Nevado de Toluca (NT) realizado en el capítulo 4, se empleó el modelo de datos GGMplus para calcular la Anomalía de Bouguer en la zona, revelando características gravimétricas previamente no reportadas en la región. Los modelos de inversión gravimétrica 3D presentados se basan en la interpretación de las distribuciones de densidad y susceptibilidad magnética de las formaciones rocosas que conforman el edificio volcánico. La Figura 15 muestra el modelo generado, destacando el sistema de plomería del volcán, que en el NT presenta un sistema de conductos peculiar con dos ramas que rodean, pero no encierran completamente, las porciones superiores de la estructura, transportando productos magmáticos hacia la cima del volcán. Dentro de este estudio se determinó que la rama occidental es más antigua que la oriental, ya que no hay ramificaciones de menor densidad en la dirección de esta última.

Comparando estos resultados con la literatura, se observa que existe una descripción esquemática del sistema de conductos del volcán NT (Aceves-Quezada et al., 2007), en la cual se representaba una única chimenea del volcán, primero durante sus etapas tempranas (Paleo-Nevado, alrededor de 1.4 Ma), y posteriormente en el momento de la colocación del domo Ombligo entre 10.5 y 9.0 ka. Ninguna etapa mostró las bifurcaciones del sistema de conductos superiores informadas en este estudio.

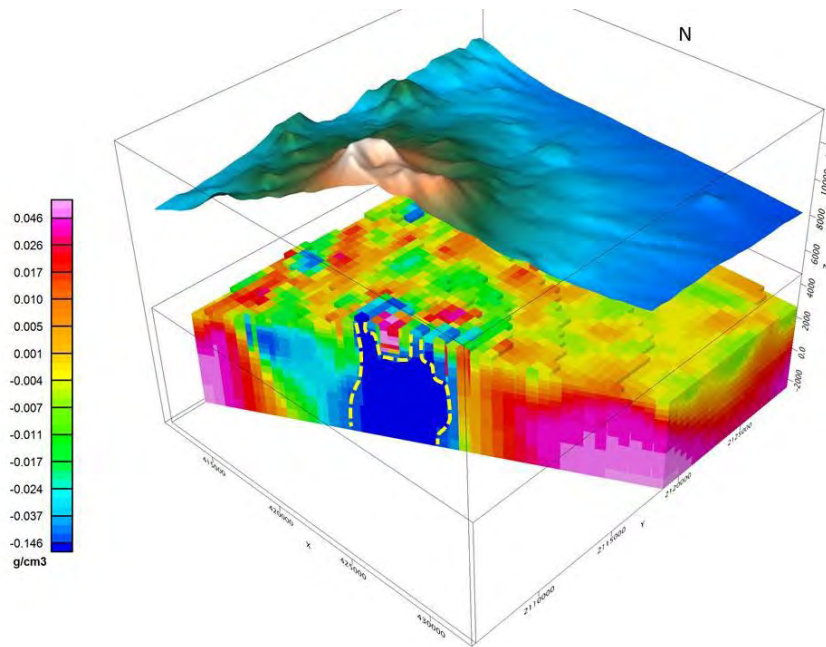


Figura 15. Inversión gravimétrica 3D de dimensiones aproximadas a 25 x 25 x 5 km; la resolución de la malla es de 500 m. El volumen fue cortado a lo largo de un azimuth de 65 grados a través del edificio volcánico para mostrar la anomalía de baja densidad (en azul) bajo el volcán NT. La caja superior muestra el modelo digital de elevación asociado al volcán. Las líneas punteadas amarillas indican los límites del sistema de conductos del volcán. Tomado de Alvarez y Camacho (2023a); Capítulo 4.

La Figura 15 amplía estos resultados, mostrando que la región de baja susceptibilidad tiene la forma de un cilindro deformado a lo largo de la dirección N-S; la porción más al norte se eleva hacia la superficie sin alcanzarla. Sin embargo, hay un grupo de edificios volcánicos cerca de esta región y a lo largo de la dirección N-S, algunos de los cuales son claramente monogenéticos y probablemente están vinculados a esta anomalía de baja gravedad y baja susceptibilidad. García-Palomo et al. (2000) informaron que el último período de deformación en la región comenzó durante el Pleistoceno tardío, terminando en una extensión pura y desplazando  $\sigma_3$  a una dirección N-S; esos autores (García-Palomo et al., 2000) notaron que estas fallas parecen controlar el vulcanismo monogenético local del Pleistoceno tardío al Holoceno. Sus observaciones y las encontradas en este estudio (Alvarez y Camacho, 2023a) se complementan, reforzando la idea de que estas fallas controlan la actividad volcánica monogenética en esta región. Basándonos en las secciones transversales en la cima del volcán y sus distribuciones de densidad y susceptibilidad magnética, se logró estimar que el centro de la cámara magmática superficial se encuentra entre elevaciones de 0 y -1 km, o entre 5 y 6 km debajo de la cima del volcán NT. Considerando la geo-termometría, Arce et al. (2013) concluyeron que el magma dacítico se almacenaba a 5.8 a 7.7 km debajo de la cima del volcán. Dadas

las incertidumbres en ambas estimaciones, consideramos que coinciden dentro de límites razonables.

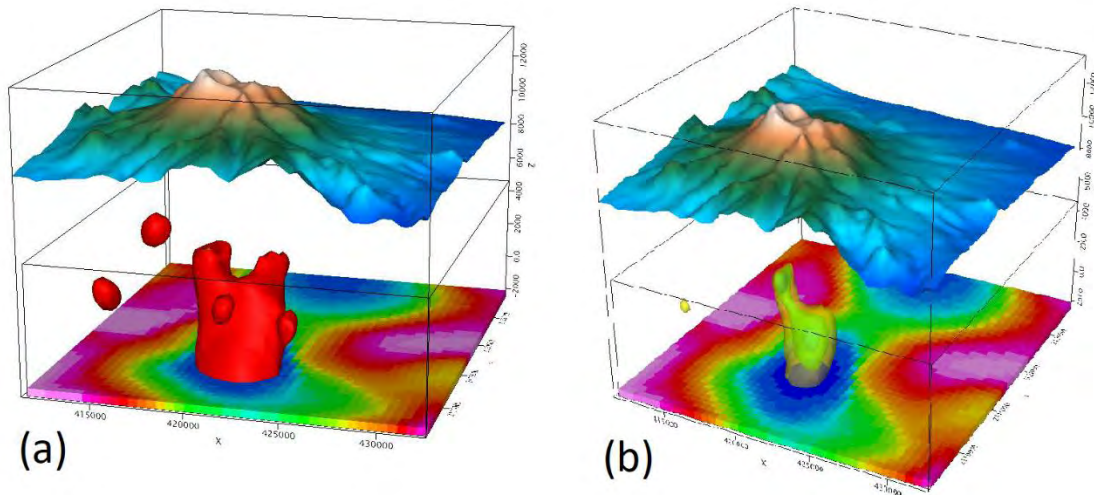


Figura 16. a) Superficie que encierra la región de densidades más bajas (en rojo), obtenida a partir de la inversión 3D con una resolución de 500 m, extendiéndose verticalmente desde elevaciones de +4210 hasta 2200 m. La parte superior de la superficie muestra claramente la forma de la bifurcación. b) Cuando se retira la superficie roja, se exponen las densidades más bajas, revelando un único conducto volcánico al oeste de la cima. Tomado de Alvarez y Camacho (2023a); Capítulo 4.

### 7.5. Capítulo 5 (*Plumbing System of Hunga Tonga Hunga Ha'apai Volcano*)

Con la gravimetría del GGMplus y el DEM del SRTM15+ (Tozer, 2019), se logró hacer el cálculo de Anomalía de Bouguer sobre el área circundante al volcán Hunga Tonga Hunga Ha'apai (HTHH) el cual se puede observar en la Figura 17.

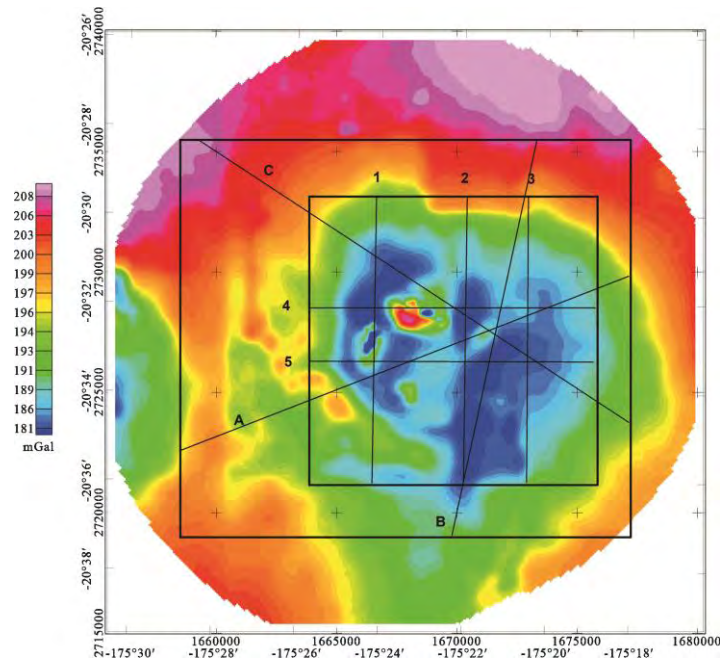


Figura 17. Anomalía de Bouguer del volcán Hunga Tonga Hunga Ha'apai Volcano. Tomado de Alvarez y Camacho (2023b); Capítulo 4.

La inversión 3D realizada sobre los primeros 5 km de la corteza, permitió determinar el sistema de plomería del volcán. En la Figura 18, se observa el modelo de inversión gravimétrica 3D del volcán. En ella se observa el sistema de plomería principal encontrado en el estudio. De este análisis una de las características más resaltantes encontradas es que el volcán presenta las mayores concentraciones de material cerca de su superficie, caso contrario a lo encontrado en otros estudios (e.g: Alvarez y Camacho, 2023a). Con una inversión más detallada se identificó una distribución circular de material de baja densidad que identificamos como fracturamiento en anillo, probablemente asociado con una sobrepresión proveniente de la cámara magmática. Dentro de las profundidades modeladas de 5 a 6 km, no encontramos una concentración de material de baja densidad que podamos identificar como una cámara magmática, en línea con el modelo conceptual del sistema magmático de HTHH como un sistema abierto de un reservorio de magma superficial (profundidad de 5-8 km) (Brenna et al., 2022). Esto contrasta con observaciones en otros volcanes donde se pueden identificar concentraciones de baja densidad con cámaras de magma, debido a sus distribuciones de densidad y profundidades (e.g: Camacho y Alvarez, 2021; MacQueen et al., 2021; Alvarez y Yutsis, 2015)."

La obtención de geo-superficies de densidad ayudó a aislar los conductos más profundos que probablemente estén conectados con la cámara magmática que alimenta los conductos volcánicos superiores. Los conductos principales se inician a altitudes inferiores a -6 km, y a medida que ascienden, se extienden en los lados noroeste (NW) y sureste (SE) de la estructura volcánica.

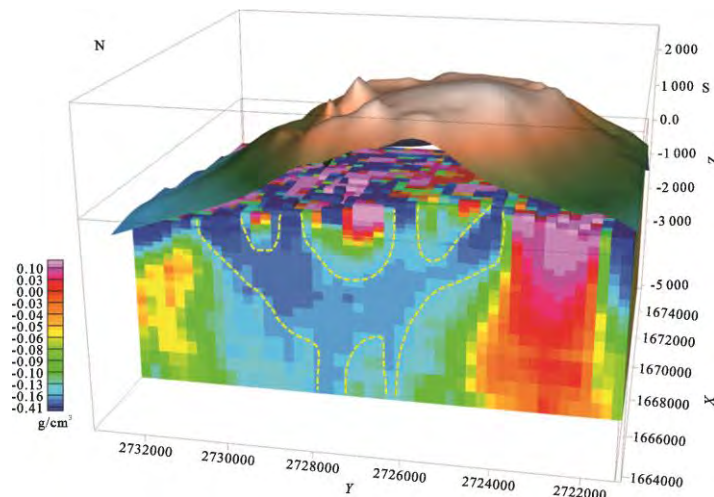


Figura 18. Modelo de inversión gravimétrica 3D del volcán Hunga Tonga Hunga Ha'apai Volcano. En la superficie 3D se encuentra la batimetría circundante al volcán. Resaltado en la línea respunteada blanca se señala el sistema de plomería encontrado. Tomado de Alvarez y Camacho (2023b); Capítulo 4.

A partir de las geo-superficies generadas en el modelo 3D, aislamos el principal volumen de materia presente cerca de la superficie (polígono amarillo; Figura 19). De este estimamos un área de contacto de  $26 \text{ km}^2$  con el agua del mar. Estas son estimaciones preliminares de áreas que hizo contacto con el agua de mar. Al momento de la erupción.

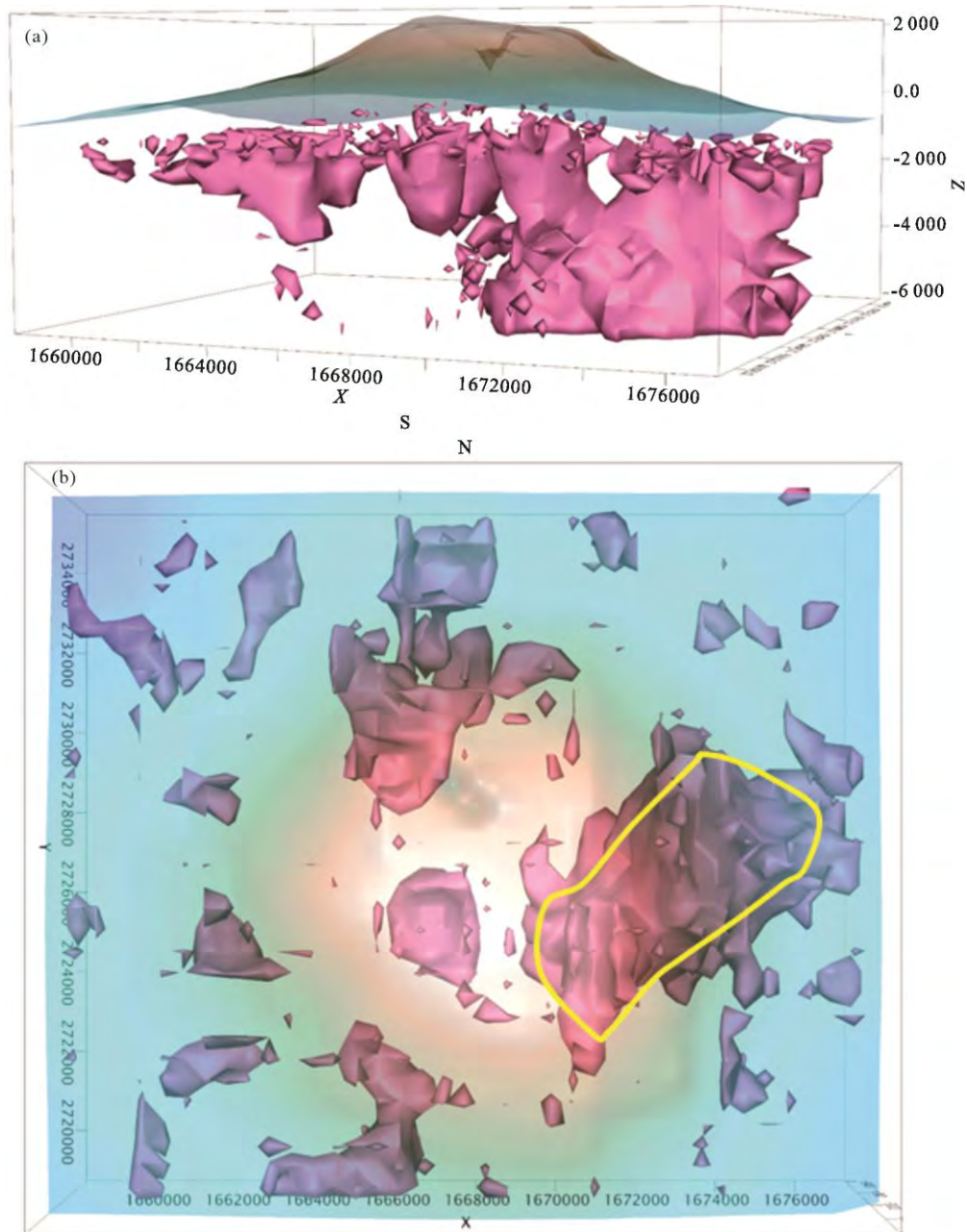


Figura 19. Modelo de inversión de 500 m de resolución. (a) Vista sur de la geo-superficie; alcanza hasta la parte inferior del modelo (-6,000 m); (b) vista vertical de la geo-superficie; cubre predominantemente la porción central-oriental. El polígono amarillo señala el área (14 km<sup>2</sup>). (b) Geo-superficie obtenida en el rango de densidad de 2.47 a 2.57 g/cm<sup>3</sup>, estimada de productos de erupción interactuando con agua de mar. Tomado de Alvarez y Camacho (2023b); Capítulo 4.

## REFERENCIAS

- Aceves-Quezada JF, Martin del Pozzo AL, López-Blanco J (2007) Volcanic hazard zonation of the Nevado de Toluca volcano, central Mexico. *Nat Hazards*, 41: 159-180. Doi: 10.1007/s11069-006-9029-6
- Alatorre-Zamora, M. y J. O. Campos-Enríquez, 1991. La Primavera Caldera (Mexico): structure inferred from gravity and hydrogeological considerations. *Geophysics*, 56 , 992-1002.
- Alatorre-Zamora, M.A., Campos-Enríquez, J.O., Fregoso-Becerra, E., Quintanar, L., Toscano-Fletes, R. and J. Rosas-Elguera, 2018, Gravity evidence for shaping of the crustal structure of the Ameca graben (Jalisco Block northern limit), Western Mexico, *Journal of South America Earth Sciences*, 82.
- Allan, J. F. (1986). Geology of the Northern Colima and Zacoalco Grabens, southwest Mexico: Late Cenozoic rifting in the Mexican Volcanic Belt. *Geological Society of America Bulletin*, 97(4), 473. [https://doi.org/10.1130/0016-7606\(1986\)97<473:GOTNCA>2.0.CO;2](https://doi.org/10.1130/0016-7606(1986)97<473:GOTNCA>2.0.CO;2)
- Alvarez, R. (2002). Banderas Rift Zone: A plausible NW limit of the Jalisco Block. *Geophysical Research Letters*, 29(20), 55-1-55-4. <https://doi.org/10.1029/2002GL016089>
- Alvarez, R., López-Loera, H., & Arzate, J. (2010). Modeling the marine magnetic field of Bahía de Banderas, Mexico, confirms the half-graben structure of the bay. *Tectonophysics*, 489(1-4), 14-28. <https://doi.org/10.1016/j.tecto.2010.03.012>
- Alvarez, Román y Yutsis, Vsevolod. (2015). The elusive Rivera-Cocos plate boundary: Not diffuse. Geological Society, London, Special Publications. <https://doi.org/10.1144/SP420.8>
- Alvarez, R., Corbo-Camargo, F., & Yutsis, V. (2021). The great tectonic discontinuity of Bahía de Banderas, Mexico. *Tectonophysics*, 803, 228762. <https://doi.org/10.1016/j.tecto.2021.228762>
- Alvarez, R., Camacho, M. (2023a) Plumbing System of Hunga Tonga Hunga Ha'apai Volcano. *J. Earth Sci.* 34, 706–716 (2023). <https://doi.org/10.1007/s12583-022-1792-0>
- Alvarez, R., & Camacho, M. (2023b). Applying High-Resolution Gravity Analysis to Volcanic Plumbing Systems: The Case of Nevado De Toluca Volcano, Mexico. *Transactions on Engineering and Computing Sciences*, 11(4), 184–207. <https://doi.org/10.14738/tecs.114.15392>
- Álvarez, O., Lincklinger, F., Sánchez, M., Weidmann, C., Ariza, J., & Giménez, M. (2016). Modelos globales de gravedad goce y egm2008: Su utilidad y complementariedad en la exploración geofísica. *Revista de la Asociación Geológica Argentina*, 73(1), 134-148.
- Arnaiz-Rodríguez, Mariano S., Rodríguez-Millán, Inírida, y Audemard, Franck. (2011). Análisis gravimétrico y flexural del occidente de Venezuela. *Revista mexicana de ciencias geológicas*, 28(3), 420-438.

- Arce JL, Gardner, and Macías, JL (2013b) pre-eruptive conditions of dacitic magma erupted during the 21.7 ka Plinian event at Nevado de Toluca volcano, Central Mexico. <http://dx.doi.org/10.1016/j.jvolgeores.2012.09.012>
- Arnaiz Rodríguez, M., y Garzón, Y. (2012). Nuevos mapas de anomalías gravimétricas del caribe. *Interciencia*, 37 (3), 176-182.
- Arzate, J. A. y otros, (2006). Geophysical modeling of Valle de Banderas graben and its structural relation to Bahía de Banderas, Mexic. *Revista Mexicana de Ciencias Geológicas*, 23(2), pp. 184-198.
- Atwater, T., & Stock, J. (1998). Pacific-north america plate tectonics of the neogene southwestern united states: An update. *International Geology Review*, 40(5), 375-402. <https://doi.org/10.1080/00206819809465216>
- Brenna, M., Cronin, S. J., Smith, I. E. M., et al., 2022. Post-Caldera Volcanism Reveals Shallow Priming of an Intra-Ocean Arc Andesitic Caldera: Hunga Volcano, Tonga, SW Pacific. *Lithos*, 412/413: 106614. <https://doi.org/10.1016/j.lithos.2022.106614>
- Brown, H. E. (2007). *Crustal rupture, creation, and subduction in the Gulf of California, Mexico and the role of gas hydrate in the submarine Storegga slide, offshore Norway*. University of Wyoming.
- Camacho, M., & Alvarez, R. (2020). Gravimetric analysis of the rifts and volcanic fields of the Jalisco block, Mexico. *Tectonophysics*, 791, 228577. <https://doi.org/10.1016/j.tecto.2020.228577>
- Camacho, M. and Alvarez, R. (2021) Geophysical Modeling with Satellite Gravity Data: Eigen-6C4 vs. GGM Plus. *Engineering*, 13, 690-706. doi: [10.4236/eng.2021.1312050](https://doi.org/10.4236/eng.2021.1312050).
- Camacho, A; Prieto, JF, Ancochea, E, Fernández, J. (2018) Deep volcanic morphology below Lanzarote, Canaries, from gravity inversion: new results for Timanfaya and implications. *J. Volc. Geothermal Res.*, <https://doi.org/10.1016/j.jvolgeores.2018.11.013>
- Camacho-Ascanio, M., & Alvarez, R. (2024). Delineation of the boundaries of San Blas basin, Mexico, merging gravity, magnetic, and seismic data. *Journal of South American Earth Sciences*, 136, 104818. <https://doi.org/10.1016/j.jsames.2024.104818>
- Campos-Enríquez J.O., Arroyo-Esquivel M.A., Urrutia-Fucugauchi J., 1990, Basement, Curie isotherm and shallow structure of the Trans-Mexican Volcanic Belt, from aeromagnetic data, *Tectonophysics* , 172, p.77-90.
- Campos-Enríquez, J. O., & Alatorre-Zamora, M. A. (1998). Shallow crustal structure of the junction of the grabens of Chapala, Tepic-Zacoalco and Colima, Mexico. *Geofísica Internacional*, 37(4), 263–282.
- DeMets, C., Gordon, R. G., Argus, D. F., & Stein, S. (1990). Current plate motions. *Geophysical Journal International*, 101(2), 425-478. <https://doi.org/10.1111/j.1365-246X.1990.tb06579.x>
- DeMets, C.y Wilson, D. (1997). Relative motions of the Pacific, Rivera, North American, and Cocos



- plates since 0.78 MA. *Journal of Geophysical Research*, 102, 2789–2806.
- Duque-Trujillo, J., Ferrari, L., Orozco-Esquivel, T., López-Martínez, M., Lonsdale, P., Bryan, S. E., Kluesner, J., Piñero-Lajas, D., & Solari, L. (2015). Timing of rifting in the southern Gulf of California and its conjugate margins: Insights from the plutonic record. *Bulletin of the Geological Society of America*, 127(5-6), 702-736. <https://doi.org/10.1130/B31008.1>
- Ekka, M. S., Sahoo, S. D., Pal, S. K., Singha Roy, P. N., & Mishra, O. P. (2022). Comparative analysis of the structural pattern over the Indian Ocean basins using EIGEN6C4 Bouguer gravity data. *Geocarto International*, 37(26), 14198–14226. <https://doi.org/10.1080/10106049.2022.2087748>
- Espinoza Celi, J. A., Cahuana-Yáñez, N. G., Martillo-Bustamante, C. E., & González-Bonilla, M. (2023). Bransfield Strait and South Shetland Islands sedimentary basement and upper crustal structure: An analysis of gravity and magnetic data at the northwestern area of the Antarctic Peninsula. *Tectonophysics*, 852, 229771. <https://doi.org/10.1016/j.tecto.2023.229771>
- Ferrari L., Conticelli S., Vaggelli C., Petrone C., and Manetti P., (2000). Late Miocene mafic volcanism and intra-arc tectonics during the early development of the Trans-Mexican Volcanic Belt. *Tectonophysics*, 318, 161-185.
- Ferrari L. and Rosas-Elguera J., (2000). Late Miocene to Quaternary extension at the northern boundary of the Jalisco block, western Mexico: the Tepic-Zacoalco rift revised. *Geological Society of America Special Paper #334*, chapter 03, p 42-64.
- Ferrari, L., López-Martínez, M., Orozco-Esquivel, T., Bryan, S. E., Duque-Trujillo, J., Lonsdale, P., & Solari, L. (2013). Late Oligocene to middle miocene rifting and synextensional magmatism in the southwestern sierra madre occidental, Mexico: The beginning of the Gulf of California rift. *Geosphere*, 9(5), 1161-1200. <https://doi.org/10.1130/GES00925.1>
- Ferrari, L., Orozco-Esquivel, T., Bryan, S. E., López-Martínez, M., & Silva-Fragoso, A. (2018). Cenozoic magmatism and extension in western Mexico: Linking the Sierra Madre Occidental silicic large igneous province and the Comondú Group with the Gulf of California rift. *Earth-Science Reviews*, 183(May 2017), 115-152. <https://doi.org/10.1016/j.earscirev.2017.04.006>
- Fletcher, J. M., Grove, M., Kimbrough, D., Lovera, O., & Gehrels, G. E. (2007). Ridge-trench interactions and the Neogene tectonic evolution of the Magdalena shelf and southern Gulf of California: Insights from detrital zircon U-Pb ages from the Magdalena fan and adjacent areas. *Bulletin of the Geological Society of America*, 119(11-12), 1313-1336. <https://doi.org/10.1130/B26067.1>
- Förste, C., Bruinsma, S., Abrikosov, O., Flechtner, F., Marty, J.-C., Lemoine, J.-M., Dahle, C., Neumayer, H., Barthelmes, F., König, R., Biancale, R., Förste, C., Bruinsma, S., Abrikosov, O., Flechtner, F., & Marty, J. (2014). EIGEN-6C4 - The latest combined global gravity field model including GOCE data up to degree and order 2190 of GFZ Potsdam and GRGS Toulouse. *EGU General Assembly*, 16, 3707. <https://doi.org/http://dx.doi.org/10.5880/icgem.2015.1>
- Gans, P. B. (1997). Large-magnitude Oligo-Miocene extension isouthern Sonora: Implications for the tectonic evolution of northwest Mexico. *Tectonics*, 16(3), 388-408. <https://doi.org/10.1029/97TC00496>.

- García-Palomo A, Macías JL, Garduño VH (2000) Miocene to Recent structural evolution of the Nevado de Toluca volcano region central Mexico. *Tectonophysics*, 318: 281– 302.
- Garduño-Monroy, V. H. y otros (1998). La Falla de Tamazula, limite suroriental del Bloque Jalisco, y sus relaciones con el con el Complejo Volcánico de Colima, México. *Revista Mexicana de Ciencias Geológicas*, 15(2), pp. 134-144.
- Garzón, Yaneth, González, Javier, y Orihuela, Nuris. (2011). Estadística básica y espacial comparativa entre datos gravimétricos satelitales y terrestres en la Faja Petrolífera del Orinoco, Venezuela. *Revista mexicana de ciencias geológicas*, 28(3), 459-473.
- Gastil, G., Krummenacher, D., & Minch, J. (1979). The record of Cenozoic volcanism around the Gulf of California. *Bulletin of the Geological Society of America*, 90(9), 839-857. [https://doi.org/10.1130/0016-7606\(1979\)90<839:TROCVA>2.0.CO;2](https://doi.org/10.1130/0016-7606(1979)90<839:TROCVA>2.0.CO;2)
- Gerardo León Soto, James F. Ni, Stephen P. Grand, Eric Sandvol, Raúl W. Valenzuela, Marco Guzmán Speziale, Juan M. Gómez González, Tonatiuh Domínguez Reyes, Mantle flow in the Rivera—Cocos subduction zone, *Geophysical Journal International*, Volume 179, Issue 2, November 2009, Pages 1004–1012, <https://doi.org/10.1111/j.1365-246X.2009.04352.x>
- Ghoms, Franck & Pham, Luan & Steffen, Rebekka & Ribeiro-Filho, Nelson & Tenzer, Robert. (2022). Delineating structural features of North Cameroon using the EIGEN6C4 high-resolution global gravitational model. *Geological Journal*. 57. 10.1002/gj.4544
- Goguitchaichvili, A., L. Alva-Valdivia, J. Rosas-Elguera, J. Urrutia-Fucugauchi, A. M. Soler and C. Caballero (2007). Combined Paleomagnetic and Petromagnetic study of the Upper Cretaceous Volcanic sequence in western Mexico: Implications for Tectonics and Magnetostratigraphy of the Jalisco block. *International Geology Review*, 45, 10, 886-897.
- Guevara R, Yutis V, Varley N, Almaguer J, Calderón-Moctezuma A, Guevara-Mansilla O (2021) Geophysical determination of the Jalisco and Michoacán blocks boundary along the Colima graben. *J. South Am. Earth Sci.* 109, 103208. <https://doi.org/10.1016/j.jsames.2021.103208>
- Guevara-Betancourt, R., Yutis, V., Varley, N., Almaguer, J., Alvarez, R., Calderón-Moctezuma, A., & Sieck, P. (2023). Insights into the plumbing system of Colima Volcanic Complex from geophysical evidence. *Journal of Volcanology and Geothermal Research*, 433, 107711. <https://doi.org/10.1016/j.jvolgeores.2022.107711>
- Hirt, C., Claessens, S., Fecher, T., Kuhn, M., Pail, R., & Rexer, M. (2013). New ultrahigh-resolution picture of Earth's gravity field. *Geophysical Research Letters*, 40(16), 4279-4283. <https://doi.org/10.1002/grl.50838>

- Hutton W., C. DeMets, O. Sánchez, G. Suárez and J. Stock (2001). Slip kinematics and dynamics during and after the 1995 October 9, Mw=8.0, Colima-Jalisco earthquake, Mexico, from GPS geodetic constrains. *Geophys. J. Int.*, 146, 3, 637-658.
- Karig, D. E., & Jensky, W. (1972). The proto-Gulf of California. *Earth and Planetary Science Letters*, 17(1), 169-174. [https://doi.org/10.1016/0012-821X\(72\)90272-5](https://doi.org/10.1016/0012-821X(72)90272-5)
- Kauahikaua, J., Hildenbrand, T., & Webring, M. (2000). Deep magmatic structures of Hawaiian volcanoes, imaged by three-dimensional gravity models. *Geology*, 28(10), 883. [https://doi.org/10.1130/0091-7613\(2000\)28<883:DMSOHV>2.0.CO;2](https://doi.org/10.1130/0091-7613(2000)28<883:DMSOHV>2.0.CO;2)
- Klokočník, J., Cílek, V., Kostelecký, J., & Bezděk, A. (2020). Gravity aspects from recent Earth gravity model EIGEN 6C4 for geoscience and archaeology in Sahara, Egypt. *Journal of African Earth Sciences*, 168, 103867. <https://doi.org/10.1016/j.jafrearsci.2020.103867>
- Linares, Fabian & Orihuela, Nuris & García-Reyes, Andreína & Audemard, Franck. (2014). Generación del mapa de basamento de la Cuenca de Falcón a partir de datos gravimétricos de modelos combinados. *Geociencias Aplicadas Latinoamericanas*. 1. 9-19. 10.3997/2352-8281.20140002.
- Linares, Fabian & Arraiz, Daniel & Orihuela, Nuris. (2016). Mapa de anomalías de Bouguer de Venezuela derivado del modelo combinado EIGEN-6C4. *Geociencias Aplicadas Latinoamericanas*. 1. 10.3997/2352-8281.20150006
- Lonsdale, P. (1991). Structural patterns of the Pacific floor offshore of Peninsular California. *The Gulf and Peninsula Province of the Californias*, 87-125.
- MacQueen, P., Gottsmann, J., Pritchard, M. E., et al., 2021. Dissecting a Zombie: Joint Analysis of Density and Resistivity Models Reveals Shallow Structure and Possible Sulfide Deposition at Uturuncu Volcano, Bolivia. *Frontiers in Earth Science*, 9: 725917. <https://doi.org/10.3389/feart.2021.725917>
- Melbourne, T., I. Carmichael, C. DeMets, K. Hudnut, O. Sánchez, J. Stock, G. Suárez, and F. Webb (1997). The geodetic signature of the M8.0 Oct. 9, 1995, Jalisco subduction earthquake, *Geophys. Res. Lett.*, 24, 6, 715-718.
- Moore, D. G. (1973). Plate-Edge deformation and crustal growth, gulf of California structural province. *Bulletin of the Geological Society of America*, 84(6), 1883-1906. [https://doi.org/10.1130/0016-7606\(1973\)84<1883:PDACGG>2.0.CO;2](https://doi.org/10.1130/0016-7606(1973)84<1883:PDACGG>2.0.CO;2)
- Nieto-Obregón J., J. Urrutia-Fucugauchi, E. Cabral-Cano and Guzmán de la Campa (1992). Listric faulting and continental rifting in western Mexico A paleomagnetic and structural study, *Tectonophysics*, 208, 365-376.

- Núñez-Cornú, F. J. (2004). *Sismotectónica del norte y oeste del Bloque de Jalisco usando datos sísmicos regionales*. <https://www.researchgate.net/publication/235910499>
- Ortega-Gutiérrez, F., Elías-Herrera, M., Morán-Zenteno, D. J., Solari, L., Luna-González, L., & Schaaf, P. (2014). A review of batholiths and other plutonic intrusions of Mexico. *Gondwana Research*, 26(3-4), 834-868. <https://doi.org/10.1016/j.gr.2014.05.002>
- Pacheco J. F, W. Bandy, G. A. Reyes-Dávila, F. J. Núñez-Cornú, C. A. Ramírez-Vázquez, and J. R. Barrón (2003). The Colima, México, Earthquake (Mw 5.3) of 7 de March 2000: Seismic activity Along the Southern Colima Rift. *Bull. Seism. Soc. Am.*, 93, 4, 1458-1467.
- Pardo, M., y Suárez, G. (1993). Steep subduction geometry of the Rivera Plate beneath the Jalisco Block in western Mexico. *Geophysical Research Letters*, 20(21), 2391–2394. doi:10.1029/93gl02794
- Pardo, M. y Suarez, G. (1995). Steep subduction geometry of the Rivera plate beneath the Jalisco block in western Mexico. *Geophysical Research Letters*, 20, 2391–2394.
- Ryan, F. Carbotte, W. B., Coplan S. M., J. O., Melkonian, A., Arko, R., Weissen, R. A., Ferrini, V., Goodwillie, A., Nitsche, F., Bonczkowski, J., & Zemsky, R. (2009). Global Multi-Resolution Topography synthesis. *Geochemistry, Geophysics, Geosystems*, 10(3). <https://doi.org/10.1029/2008GC002332>
- Sánchez-Barra, A. C., González-Escobar, M., & Ferrari, L. (2022). Subsurface structure of the Mazatlán basin, southeastern Gulf of California, Mexico, from seismic reflection and well data. *Tectonophysics*, 838, 229505. <https://doi.org/10.1016/j.tecto.2022.229505>
- Schaaf, P., Morán-Zenteno, D., Hernández-Bernal, M.S., 1995, Paleogene continental margin truncation in southwestern Mexico; Geochronological evidence: *Tectonics*, 14, 1339-1350.
- Schmitt S. V., Charles De Mets, J. Stock, O. Sánchez, B. Márquez-Azúa y G. Reyes (2007). A geodetic study of the 2003 January 22 Tecoman, Colima, Mexico earthquake. *Geophys. J. Int.*, 169, 389-406.
- Stock, J. M., & Hodges, K. (1989). Pre-Pliocene Extension around the Gulf of California and the transfer of Baja California to the Pacific Plate. *Tectonics*, June 2014. <https://doi.org/10.1029/TC008i001p00099>
- Stock, J. M., (1993). Tectónica de placas y evolución del Bloque Jalisco, México, *GEOS, Bol. U. Geofís. Mex.* 13(3), 3-9.
- Sutherland, F. H., Kent, G. M., Harding, A. J., Umhoefer, P. J., Driscoll, N. W., Lizarralde, D., Fletcher, J. M., Axen, G. J., Holbrook, W. S., González-Fernández, A., & Lonsdale, P. (2012). Middle Miocene to early Pliocene oblique extension in the southern Gulf of California. *Geosphere*, 8(4), 752-770. <https://doi.org/10.1130/GES00770.1>
- Tozer, B. , D. T. Sandwell, W. H. F. Smith, C. Olson, J. R. Beale, and P. Wessel, Global bathymetry and topography at 15 arc seconds: SRTM15+, *Accepted Earth and Space Science*, August 3, 2019.

- Ughi, A. (2014). Estudio de la estructura cortical en la zona centro norte de Venezuela mediante el análisis de flexión de placas. *Revista mexicana de ciencias geológicas*, 31(1), 93-103.
- Wallace J. Paul y Ian S. E. Carmichael (2004). Petrology of Volcán Tequila, Jalisco, México: desequilibrio phenocryst assemblages and evolution of the subvolcanic magma system. *Contrib. Min. and Petrol.*, 117, 4, 345-361
- Yang, T., S. P. Grand, D. Wilson, M. Guzman-Speziale, J. M. Gómez-González, T. Dominguez-Reyes and J. Ni (2009). Seismic structure beneath the Rivera subduction zone from finite-frequency seismic tomography, *J. Geophys. Res.*, 114, B01302. W.M. Telford, L. P. G. and R. E. S. (1991). *Applied geophysics (second edition)*. Cambridge University Press (Vol. 69). [https://doi.org/10.1016/0031-9201\(91\)90163-C](https://doi.org/10.1016/0031-9201(91)90163-C)